UNIVERSIDAD COMPLUTENSE DE MADRID

FACULTAD DE CIENCIAS FÍSICAS

TESIS DOCTORAL

A VLT-SINFONI study of local Luminous and Ultraluminous infrared galaxies

MEMORIA PARA OPTAR AL GRADO DE DOCTOR

PRESENTADA POR

Javier Piqueras López

Directores

Luis Colina Robledo
Santiago Arribas Mocoroa

Madrid, 2014

The importance of Luminous and Ultraluminous Infrared Galaxies in the context of galaxy evolution has been clearly established since their discovery in the early 70's. (U)LIRGs are valuable candidates to study extreme cases of compact star-formation and coeval active galactic nuclei, as well as their impact on the interstelar medium in terms of feedback processes. Taking advantage of the high spatial resolution and S/N that can be achieved in local samples, the study of nearby (U)LIRGs provides with a unique oportunity to perform detailed analysis of these physical processes, and is a fundamental piece to understand their more distant counterparts.
This thesis presents, for the first time, a comprehensive near-IR study of local LIRGs and ULIRGs based on seeing-limited VLT-SINFONI observations, and focused on the emitting gas structure, dust morphology and star-formation. In addition, we present the detailed analysis of the spatially resolved kinematics of the central regions of the nearby galaxy M83, focusing on the role of supernovae in shaping the gas kinematics at scales of tens of parsecs.

La importancia de las Galaxias Luminosas y Ultraluminosas en el Infrarrojo en el contexto de la evolución de las galaxias ha quedado claramente establecido desde su descubrimiento, durante los primeros años de la década de los 70. Las (U)LIRGs locales son objetos especialmente útiles para el estudio de los casos más extremos de formación estelar en regiones compactas, coexistiendo con núcleos galácticos activos, así como su impacto en el medio interestelar. Haciendo uso de la alta resolución espacial y S/N que proporcionan las muestras locales, el estudio de (U)LIRGs cercanas proporciona una oportunidad única para llevar a cabo análisis detallados de estos procesos físicos, y es una pieza fundamental en la comprensión de sus correspondientes homólogos más distantes.
Esta tesis presenta, por primera vez, un estudio exhaustivo de LIRGs y ULIRGs locales en el infrarrojo cercano, basado en observaciones realizadas con el instrumento VLT-SINFONI, y centrado en la estructura del gas en emisión, la morfología del polvo y la formación estelar. Además, presentamos el estudio detallado de la cinemática del gas en las regiones centrales de la galaxia M83, centrado en analizar el papel que juegan las supernovas en "moldear" la cinemática del gas a escalas de decenas de párseces.

CAB
ASTROBIOLOGY INSTITUTE
CSIC
CONSEJO SUPERIOR DE INVESTIGACIONES CIENTÍFICAS
UNIVERSIDAD COMPLUTENSE
MADRID

A VLT-SINFONI Study of Local Luminous and Ultraluminous Infrared Galaxies
Javier Piqueras López

A VLT-SINFONI Study of Local Luminous and Ultraluminous Infrared Galaxies

Estudio de Galaxias Luminosas y Ultraluminosas en el Infrarrojo con VLT-SINFONI

Javier Piqueras López

A VLT-SINFONI study of local Luminous and Ultraluminous infrared galaxies

CENTRO DE ASTROBIOLOGÍA
ASOCIADO AL NASA ASTROBIOLOGY INSTITUTE

GOBIERNO DE ESPAÑA

CSIC
CONSEJO SUPERIOR DE INVESTIGACIONES CIENTÍFICAS

Instituto Nacional de Técnica Aeroespacial

UNIVERSIDAD COMPLUTENSE MADRID

Javier Piqueras López

Centro de Astrobiología (CAB, INTA-CSIC)

Universidad Complutense de Madrid

Directors

Dr. Luis Colina Robledo

Dr. Santiago Arribas Mocoroa

A thesis submitted for the degree of

PhilosophiæDoctor (PhD) in Astrophysics

2014

A mi abuelo, Antonio.

Agradecimientos

Como en toda empresa a largo plazo, hay cabida para momentos buenos y no tan buenos. Pero supongo que, como en casi todo, el tiempo termina por difuminar los contornos, y que, pasado unos años, volviendo la vista atrás, cuando ojee esta tesis en casa de mis padres o al sacarla de una caja en alguna mudanza, no pueda evitar la sonrisa de satisfación por todo el trabajo e ilusión que hay puesto entre estas páginas. Nadie se acordará entonces de aquellos momentos puntuales de frustración, de las horas delante del ordenador o de las temporadas fuera de casa, cuando ves que la vida que dejaste no te espera. Creo que es ahora, cuando todos esos pequeños momentos están frescos, cuando realmente puedo escribir estos agradecimientos que tanto tiempo llevan rondando por mi cabeza.

No puedo empezar sino agradeciendo a mis directores, Luis Colina y Santiago Arribas, por su confianza desde el primer momento de este proyecto. Su apoyo y dedicación a lo largo de todos estos años de tesis, así como su espíritu crítico han sido fundamentales para llevar este trabajo a buen puerto. Me tranquiliza saber que es posible mantener esa inquietud tan necesaria a lo largo de los años. Por otro lado, quisiera agradecer a Miguel Mas y a Bjorn Emonts por la lectura final del manuscrito. Sus comentarios y sugerencias han contribuido enormemente a mejorar el resultado final de esta tesis. Asimismo, quiero agradecer a María José Fernández Figueroa por toda su ayuda en la tramitación de la tesis, facilitándome en gran medida todo el proceso.

Una parte fundamental de este trabajo se ha llevado a cabo durante mis estancias en el Max-Planck-Institut für extraterrestrische Physik (MPE). Debo

agradecer a los miembros del Departamento de Astrofísica Infrarroja y Submilimétrica su hospitalidad y cordialidad, y el hacerme mi estancia tan fácil y agradable. En particular, quiero agradecer a Ric Davies su dedicación desinteresada, así como su ayuda y consejos, no sólo durante los meses de estancia, sino siempre que lo he necesitado. En el terreno más personal, agradecer a Javier Graciá por hacerme la vida mucho más sencilla desde los primeros días, que fueron los más duros. Gracias por enseñarme una ciudad a la que siempre querré volver, ¡aunque me hubiese venido muy bien que me enseñases a usar el S-bahn! Quiero también agradecer a Martin Mahl por acogerme en su tierra, por esas tardes de Champions o de Schwimmhalle. Gracias por abrirme las puertas de tu casa. Ya sabes, ¡te esperamos en Pozorrubio!

Y de vuelta a Madrid, no podemos ir al CAB sin pasar por Serrano. Supongo que siempre echaremos de menos esos cafés en la Residencia de Estudiantes, o los *tanios* (café doble, cortado, con leche fría en vaso) después de comer. Gracias a Fabián por acordarse siempre de mí, incluso después de tanto tiempo; a Ruyman, por tan buenos ratos de supertropicalidad (no sólo Enrica, Sara o yo, ¡Madrid y Malasaña también te echan de menos!); a Alejandro, por ayudarme con mis primeros pinitos con SINFONI...

Y la nave... Porque siempre nos quedará la nave. Nuestra cueva particular en *Dagobah*, las trincheras de la astronomía. Todos los que pasamos por allí llevaremos "la marca"... porque entrar por la ventana a tu lugar de trabajo te marca, de un modo u otro. Aquí aparecen dos "personajes" a los que tengo mucho que agradecer en el plano científico, pero casi más en el personal. Muchas gracias a Javier y a Álvaro por acoger a un tierno estudiante en la "élite" post-doctoral, por todos los buenos ratos dentro y fuera del trabajo (entrenamientos, conciertos, ensayos...), que han sido y espero serán muchos.

Finalmente, después de un largo camino, a la derecha del Monte del Destino, llegamos al CAB. Todos sabemos que si J.R.R. Tolkien hubiese elegido el CAB en lugar de Mordor, *El Señor de los Anillos* hubiese dado para un cuento y un corto. Los hobbits nunca hubiesen destruido el Anillo, y Sauron hubiese arrasado con todos los pueblos libres. Punto. Afortunadamente, nosotros no somos hobbits, y el peregrinaje al CAB se ha convertido finalmente en nuestra rutina de todos los

días. En este punto de la historia, quiero agradecer a Sara por mantener siempre su sonrisa en el despacho, no tiene que ser fácil el armarse de valor para hacer preguntas a alguien que está escribiendo la tesis... y, cómo no, a Miguel y Enrica, que me han acompañado en este largo peregrinaje desde el principio.

Esta historia también tiene una precuela, que tuvo lugar hace varios años, en el departamento de importación de una naviera. Allí tuve el placer de conocer a buenos amigos, muchos de los cuales se han quedado en el camino por las exigencias del guión. Quiero agradecer a muchos de ellos, pero especialmente a Miguel, Giampiero, Álvaro, Paula, Nerea y Raúl, por animarme a tomar la díficil decisión de dejar el shipping para retomar "el sendero de la Fuerza".

A partir de aquí, los agradecimientos, como los vinos, van ganado algo de 'cuerpo' para dejar un ligero gusto a "disculpa" en el paladar. Empezando por mis compañeros-amigos de *Voodoo Tales*: Armando, David (muchas gracias por ayudarme con la impresión de la tesis, ¡me has quitado un gran peso de encima!), y por supuesto a Distor y Julián, que también han "sufrido" todo el proceso, por todas esas ausencias a ensayos y no-ensayos. Otra parte muy importante en este camino son mis amigos de Pozorrubio, especialmente Joaquín, Álvaro, Pablo y Víctor, que han estado siempre muy pendientes de mí durante los últimos y complicados meses de tesis. ¡Prometo retomar mi *noche Fraguel* en septiembre!

Y las últimas líneas de estos agradecimientos no pueden ir sino a mi familia. Agradecer a mi tía y a mis primos, especialmente a Miguel Ángel, por aquella conversación en una tarde lejana, en una habitación de hospital. Y a mis "cuñados", Pepe y Héctor, porque ya debe de ser difícil tener como cuñado a un tío tan serio como yo, como para que encima se ponga a escribir una tesis... Gracias por las tardes de fútbol y las carreras por el parque. A mis hermanas, Elena y Laura, por las tardes de repostería y Wii/PS3 (¿debería agradecer también a Miyamoto?), las compras, y por aguantar todos los gruñidos desde el otro lado de la puerta de la habitación, al fondo del pasillo. Gracias a mis padres, José y Mª Dolores, grandes protagonistas en esta historia, que me/nos han dado todo lo que han podido y más para, entre otras cosas, terminar con buen pie esta tesis. Aunque no entendáis mucho de lo que está escrito, siempre podréis ojearla y ver que una parte, grande y pequeña a la vez, de todos los sacrificios que habéis hecho por

nosotros, está entre estas páginas. Y finalmente, María Fernanda, la persona que probablemente más haya sufrido con esta tesis... cuántos kilómetros, aviones, trenes, carreteras hay aquí escondidos. Creo que necesitaría otra docena de tesis para agradecerte la paciencia que has tenido, los sacrificios que has hecho y el apoyo que me has dado, pero te haré un regalo mejor: ¡no escribir ninguna más! Ahora ya sí, éste es un punto y aparte en nuestra historia...

Javier Piqueras López

En Madrid, Marzo de 2014

Este trabajo ha sido financiado por el Ministerio de Ciencia e Inovación, bajo los proyectos BES-2008-007516, ESP2007-65475-C02-01, y AYA2010-21161-C02-01. Basado en observaciones obtenidas en ESO (European Organisation for Astronomical Research in the Southern Hemisphere), Chile. Hemos hecho uso de la base de datos NASA/IPAC Extragalactic Database (NED) operada por el Jet Propulsion Laboratory, en el California Institute of Technology, bajo el contrato de la National Aeronautics and Space Administration. Parte de los datos presentados en este trabajo se han obtenido a través del archivo Multimission Archive at the Space Telescope Science Institute (MAST), y del proyecto Two Micron All Sky Survey. Algunas de las figuras se han realizado mediante el paquete jmaplot, *desarrollado por Jesús Maíz-Apellániz (http://jmaiz.iaa.es/software/jmaplot/current/html/jmaplot_overview.html)*

Abstract

The importance of Luminous (LIRGs) and Ultraluminous (ULIRGs) infrared galaxies in the context of galaxy evolution has been clearly established since their discovery in the early 70's. This new class of "infrared galaxies" is characterised by emitting more energy in the mid- and far-infrared than at all other wavelengths combined (see the review of Sanders & Mirabel 1996). Despite (U)LIRGs are not very common in the local Universe, they happen to be the most luminous galaxies locally. They have been detected in large quantities at high-z in deep mid- and far-infrared surveys, where they dominate the energy density of the Universe beyond z $\sim$ 1.5 (e.g. Le Floc'h et al. 2005, Pérez-González et al. 2005, Lonsdale et al. 2006, Nardini et al. 2008, Sargent et al. 2012, Magnelli et al. 2013).

(U)LIRGs are valuable candidates to study extreme cases of compact star-formation and coeval active galactic nuclei (AGN), as well as their impact on the interstelar medium in terms of feedback processes. Taking advantage of the high spatial resolution and S/N that can be achieved in local samples, the study of nearby (U)LIRGs provides with a unique opportunity to perform detailed analysis of these physical processes, and is a fundamental piece to understand their more distant counterparts.

This thesis project is part of a larger program, that covers the whole range of LIRG and ULIRG luminosities and the different morphologies observed, and presents, for the first time, a near-IR study of local LIRGs and ULIRGs based on seeing-limited VLT-SINFONI observations. In addition, we present the study of the spatially resolved kinematics of the central regions of the nearby galaxy M83, focusing on the role of supernovae in shaping the gas kinematics at scales of tens of parsecs. The main results and conclusions of this thesis are:

- **Spatially resolved kinematics of the central regions of M83**

  The detailed study of the kinematics of M83 (Piqueras López et al., 2012b) is based on adaptive optics assisted VLT-SINFONI observations on the H+K band. The inner regions of M83 are sampled with an unprecedented spatial resolution of $\sim 0\farcs2$, and their analysis shows that the gas kinematics are unsuitable to estimate dynamical properties of the central regions of M83. Although the stellar kinematics trace the global velocity field of uniform rotation, the kinematics of the gas at small scales of tenths of parsecs seem to be dominated by shocks and inflows, and totally unrelated to the stellar kinematics.

  We also address the controversial issue of the 'true' nucleus of M83, and argue that the optical nucleus of M83 is a star cluster of $\sim$100 Myr with its own coherent internal kinematics, and a dynamical mass of $M_{dyn} = (1.1 \pm 0.4) \times 10^7 M_\odot$. We suggest that the 'true' nucleus of M83 is located at the photometric and kinematic centre of the galaxy, where we found a modest enhancement of the K-band continuum.

- **Mapping the emitting gas structure of local (U)LIRGs**

  The analysis of the sample of local LIRGs and ULIRGs is based on seeing-limited near-infrared H- and K-band VLT-SINFONI observations. We present the atlas of the ionised, partially ionised and warm molecular gas 2D flux distributions and kinematics of the galaxies of the sample (Piqueras López et al., 2012a). The analysis of the emission maps of (U)LIRGs shows that the more luminous star-forming regions are located typically in star-forming rings or spiral arms in LIRGs, and at the nucleus of the ULIRGs. On the contrary, the peak of the H_2 emission coincides with the stellar nucleus in all the sources. In addition, although the Brγ and H_2 peaks are usually not spatially coincident, their luminosities are very similar.

  In LIRGs, all the phases of the gas (i.e. ionised, partially ionised and molecular) appear to share the same large scale kinematics in terms of velocity fields, although we find signatures of radial flows in some of the objects. The kinematics in ULIRGs are very complex due to their interacting nature, and show features like coherent velocity gradients that can be associated with the progenitors or dynamical structures like tidal tails.

- **Characterisation of the visual extinction and dust clumpiness in local (U)LIRGs**

  We also analysed in detail the 2D extinction structure of the galaxies of the sample, based on the Brγ/Brδ and Paα/Brγ line ratios (Piqueras López et al., 2013). We present the visual extinction maps, and the spaxel-by-spaxel A_V distributions and radial profiles of the individual sources. The dust distribution in LIRGs and ULIRGs shows a patchy structure on sub-kpc scales, and the spaxel-by-spaxel A_V distributions of the individual objects reveals no clear evidence of any dependence of extinction with L_{IR}[8–1000μm]. However, the combined spaxel-by-spaxel distributions of LIRGs and ULIRGs as separated classes show that ULIRGs present a slightly higher median value of A_V= 6.5 mag, compared to the median value of A_V= 5.3 mag measured in LIRGs.

- **Sub-kpc study of the star formation in local (U)LIRGs**

  Taking advantage of the spatially resolved A_V maps derived from the line ratios, we study in detail the observed and extinction-corrected 2D structure of the star-formation rate (SFR) and surface density of the star-formation rate (Σ_{SFR}) in our sample of (U)LIRGs. When we compare regions of the same physical extend, LIRGs and ULIRGs seem to have similar median values of their observed (i.e. not corrected from extinction) Σ_{SFR} ($\Sigma^{obs}_{LIRGs} = 1.16\,M_\odot\,yr^{-1}\,kpc^{-2}$, and $\Sigma^{obs}_{ULIRGs} = 1.38\,M_\odot\,yr^{-1}\,kpc^{-2}$). The difference between the median values of the Σ_{SFR} distributions increases when the extinction corrections are applied ($\Sigma^{corr}_{LIRGs} = 1.72\,M_\odot\,yr^{-1}\,kpc^{-2}$ and $\Sigma^{corr}_{ULIRGs} = 2.90\,M_\odot\,yr^{-1}\,kpc^{-2}$).

  We find that the spatial sampling, i.e. the physical scale per spaxel, of the emission maps has direct implications in deriving physical quantities like A_V and Σ_{SFR}, even more in high-z studies. Using a first-order approximation, we simulated the emission maps of LIRGs at increasing distances and found that the median of the A_V distribution of LIRGs is decreased by a $\sim$20 % at the average distance of the ULIRG subsample, and that it can be reduced in a factor $\sim$40 % beyond 800 Mpc. When we consider this effect on the Σ_{SFR} measurements, we observe that the medians of the LIRG Σ_{SFR} distributions (observed and extinction-corrected) are increased by a factor $\sim 2-3$.

In agreement with previous studies, we observe a tight correlation between our near-IR measurements and the SFR derived from *Spitzer* 24 μm data, and a reasonable agreement with SFR measurements from L_{IR}. When we compare our SFR values with optical measurements from Hα emission, we find that the near-IR measurements are a factor $\sim$3 larger than the optical, even when the extinction corrections are applied.

Together with the spaxel-by-spaxel analysis of the Σ_{SFR}, we identified a sample of 95 individual star-forming clumps in our set of (U)LIRGs, with sizes that range within $\sim$60–400 pc and $\sim$300–1500 pc, and Paα luminosities of $\sim10^5$–10^7 $L_\odot$ and $\sim10^6$–10^8 $L_\odot$ in LIRGs and ULIRGs, respectively. The derived properties of these clumps show that local star-forming regions, specially in ULIRGs, are more similar to high-z clumps in terms of luminosity and Σ_{SFR} than local regions from 'normal' galaxies.

Resumen

La importancia de LIRGs y ULIRGs en el contexto de la evolución de las galaxias ha quedado claramente establecido desde su descubrimiento, durante los primeros años de la década de los 70. Esta nueva clase de "galaxias infrarojas" se caracteriza por emitir más energía en el infrarrojo medio y lejano que en el resto de longitudes de onda juntas (ver la revisión de Sanders & Mirabel 1996). Pese a que las (U)LIRGs no son muy comunes en el Universo local, estos objetos resultan ser las galaxias más luminosas localmente. Se han detectado en grandes números a alto desplazamiento al rojo mediante estudios sistemáticos en el infrarrojo medio y lejano, donde dominan la densidad de energía del Universo más allá de $z \sim 1.5$ (Le Floc'h et al. 2005, Pérez-González et al. 2005, Lonsdale et al. 2006, Nardini et al. 2008, Sargent et al. 2012, Magnelli et al. 2013).

(U)LIRGs son objetos especialmente útiles para el estudio de casos extremos de formación estelar compacta, evolucionando coetáneamente con AGN (Núcleos Galácticos Activos, en sus siglas en inglés), así como su impacto en el medio interestelar mediante procesos de "feedback" o retro-alimentación. Aprovechando la alta resolucón espacial y S/N que proporcionan las muestras locales, el estudio de (U)LIRGs cercanas proporciona una oportunidad única para llevar a cabo análisis detallados de estos procesos físicos, y es una pieza fundamental en la comprensión de sus correspondientes homólogos a mayores distancias.

Este proyecto de tesis se engloba en un programa más amplio, que cubre todo el rango de luminosidades correspondientes a LIRGs y UIRGs, así como los diferentes tipos morfológicos observados. Presenta, por primera vez, un estudio de LIRGs y ULIRGs locales en el infrarrojo cercano, basado en observaciones limitadas por "seeing" realizadas con el instrumento VLT-SINFONI. Asimismo, se presenta el estudio de la cinemática, resuelta espacialmente, de las regiones centrales de la galaxia cercana M83, centrado principalmente en analizar el papel que juegan las explosiones de supernova en "moldear" la cinemática del gas a escalas de decenas de pársecs. Los resultados y conclusiones generales de esta tesis son:

- **Estudio de la cinemática espacialmente resuelta de las regiones centrales de M83**

  El estudio detallado de la cinemática de M83 (Piqueras López et al., 2012b) se basa en observaciones en banda H+K realizadas con VLT-SINFON,I en combinación con su módulo de óptica adaptativa. Las regiones internas de M83 se han muestreado con una resolución espacial sin precedentes de $\sim 0\farcs2$, y su posterior análisis muestra que la cinemática del gas no es adecuada para estimar las propiedades dinámicas de las regiones centrales de M83. Mientras que la cinemática estelar traza el campo de velocidades global correspondiente a una rotación uniforme, la cinemática del gas, a escalas pequeñas de unas decenas de parsecs, parece estar dominada por ondas de choque y flujos de gas, sin relación alguna con la cinemática de las estrellas.

  Asimismo, hemos abordado la cuestión de la controvertida localización del núcleo de M83, y proponemos que el núcleo óptico de M83 es en su lugar un cúmulo estelar de 100 millones de años, con su propia y coherente cinemática interna y una masa dinámica de $M_{dyn} = (1.1 \pm 0.4) \times 10^7 M_{\odot}$. Además, sugerimos que el núcleo de M83 se encuentra situado en el centro fotométrico y cinemático de M83, donde hemos encontrado un ligero aumento de la emisión en la imagen de continuo en banda K.

- **Trazado de los mapas de la estructura del gas en emisión en (U)LIRGs locales**

  El análisis de la muestra local de LIRGs y ULIRGs se basa en observaciones en el infrarrojo cercano, limitadas por "seeing", realizadas con el instrumento VLT-SINFONI en bandas H y K. Presentamos el atlas 2D de las distribuciones de flujo y cinemática del gas ionizado, parcialmente ionizado y gas molecular templado de las galaxias de la muestra (Piqueras López et al., 2012a). El análisis de los mapas de emisión de LIRGs y ULIRGs muestra que las regiones de formación estelar más luminosas se localizan típicamente en las estructuras de anillos o brazos espirales en las LIRGs, mientras que en las ULIRGs coinciden generalmente con los núcleos de las fuentes. Por el contrario, el pico de emisión de H_2 coincide con el núcleo estelar en todas

las galaxias. Asimismo, mientras que los picos de Brγ y H_2 generalmente no coinciden, sus luminosidades son muy similares.

En las LIRGs, todas las fases del gas (ionizada, parcialmente ionizada y molecular) parecen presentar la misma cinemática a gran escala en cuanto a los campos de velocidad, aunque encontramos indicios de flujos de gas radiales en algunos de los objetos. La cinemática en ULIRGs es muy compleja debido a que la mayoría de estos objetos son sistemas en interacción. Además, muestran características como gradientes de velocidad coherentes que se pueden identificar con los progenitores o con estructuras dinámicas como colas de marea.

- **Caracterización de la extinción visual y de la distribución del polvo en (U)LIRGs locales**

  Hemos analizado en detalle la estructura bidimensional de la extinción en las galaxias de la muestra, basándonos en los cocientes de líneas Brγ/Brδ y Paα/Brγ (Piqueras López et al., 2013). Presentamos los mapas y las distribuciones spaxel a spaxel de la extinción, así como los perfiles radiales de las fuentes individuales. La distribución del polvo en LIRGs y ULIRGs muestra una estructura irregular en escalas inferiores al kilopársec, mientras que las distribuciones spaxel a spaxel de la extinción en fuentes individuales no revelan ninguna evidencia clara de alguna posible dependencia de la extinción con la L_{IR}. No obstante, las distribuciones spaxel a spaxel globales de LIRGs y ULIRGs, como clases de luminosidad, muestran que las ULIRGs presentan una mediana de $A_V = 6.5$ mag, ligeramente más alta que el valor mediano en las LIRGs, de concretamente $A_V = 5.3$ mag.

- **Estudio de la formación estelar en (U)LIRGs a escalas inferiores al kiloparsec**

  Haciendo uso de los mapas espacialmente resueltos de la extinción, obtenidos a partir de los cocientes de líneas, hemos estudiado en detalle la estructura bidimensional, tanto observada como corregida de extinción, de la tasa de formación estelar (SFR, en sus siglas en inglés) y de la densidad de tasa de formación estelar (Σ_{SFR}) en nuestra muestra de (U)LIRGs. Al comparar regiones con la misma extensión física, LIRGs y ULIRGs muestran

valores medianos muy similares en cuanto a la densidad superficial de tasa de formación estelar observada, es decir, no corregida de extinción. Estos valores medianos son $\Sigma^{\rm obs}_{\rm LIRGs} = 1.16\,{\rm M}_\odot\,{\rm yr}^{-1}\,{\rm kpc}^{-2}$, and $\Sigma^{\rm obs}_{\rm ULIRGs} = 1.38\,{\rm M}_\odot\,{\rm yr}^{-1}\,{\rm kpc}^{-2}$. La diferencia entre estos valores medianos de las distribuciones de $\Sigma_{\rm SFR}$ aumenta al tener en cuenta los efectos de la extinción, siendo $\Sigma^{\rm corr}_{\rm LIRGs} = 1.72\,{\rm M}_\odot\,{\rm yr}^{-1}\,{\rm kpc}^{-2}$ y $\Sigma^{\rm corr}_{\rm ULIRGs} = 2.90\,{\rm M}_\odot\,{\rm yr}^{-1}\,{\rm kpc}^{-2}$.

Hemos encontrado que la resolución espacial con la que se muestrean los mapas de emisión, es decir, la escala física por spaxel, tiene implicaciones directas al derivar magnitudes físicas como la extinción y la $\Sigma_{\rm SFR}$, siendo estos efectos más importantes a alto desplazamiento al rojo. Usado una aproximación de primer orden, hemos simulado los mapas del subconjunto de LIRGs a distancias cada vez mayores, y hemos encontrado que la mediana de las distribuciones de A_V en las LIRGs disminuye en $\sim$20 % a la distancia promedio de la submuestra de ULIRGs, y que puede verse reducida en $\sim$40 % a partir de los 800 Mpc. Cuando se considera este efecto en las medidas de la $\Sigma_{\rm SFR}$, observamos que las medianas de las distribuciones de las LIRGs se ven incrementadas en un factor $\sim 2-3$.

En la línea de estudios previos, hemos observado una estrecha relación entre nuestras medidas en el infrarrojo cercano y la SFR derivada a partir de datos de *Spitzer* en 24 μm, así como un acuerdo razonable con medidas obtenidas a partir de la $L_{\rm IR}$. Cuando comparamos nuestros valores de la SFR con medidas en el óptico, obtenidas a partir de la emisión en Hα, encontramos que las medidas en el infrarrojo cercano son $\sim$3 veces mayores que las ópticas, incluso después de haber aplicado las correciones de extinción.

Junto con el análisis spaxel a spaxel de la $\Sigma_{\rm SFR}$, hemos identificado una muestra de 95 regiones de formación estelar individuales en nuestro conjunto de (U)LIRGs, con tamaños que oscilan entre los $\sim$60–400 pc y $\sim$300–1500 pc, así como luminosidades en Paα de $\sim 10^5$–$10^7\,{\rm L}_\odot$ y $\sim 10^6$–$10^8\,{\rm L}_\odot$ en LIRGs y ULIRGs, respectivamente. Las propiedades de estas regiones muestran que, localmente y especialmente en ULIRGs, se asemejan más a las regiones de formación estelar en objetos a alto desplazamiento al rojo, en términos de luminosidad y $\Sigma_{\rm SFR}$, que a aquellas regiones procedentes de galaxias locales "normales".

Contents

1

Introduction

"Begin at the beginning," the King said gravely, "and go on till you come to the end: then stop."
— Lewis Carroll, *Alice in Wonderland*

In this chapter we present a brief summary of the main properties of the Luminous (LIRGs) and Ultraluminous (ULIRGs) Infrared Galaxies and their key role on the study of galaxy evolution. We also briefly discuss the actual stage of the integral field spectroscopic (IFS) studies of this class of objects, and describe the main physical mechanisms responsible for the spectral features observed in the near-IR spectra of (U)LIRGs. Finally, we present a summary of this thesis project.

1.1. Luminous and Ultraluminous Infrared Galaxies

Infrared bright galaxies were first discovered in the early 70's with the first mid-infrared observations of extragalactic sources (Low & Kleinmann 1968, Kleinmann & Low 1970a, 1970b, Rieke & Low 1972), that already highlighted the dominant infrared emission of several objects, including starburst, Seyferts and QSOs. Mid-infrared photometry of larger samples of starburst, Seyfert and bright spiral galaxies (Rieke & Low 1975, Neugebauer et al. 1976, Rieke & Lebofsky 1978, Rieke 1978) revealed that this infrared excess was a common property of these sources, and that the shape of their infrared continuum was better explained in terms of models of thermal re-radiation from dust.

The early results from the *Infrared Astronomical Satellite* (*IRAS*, Neugebauer et al. 1984) revealed a new class of "infrared galaxies" characterised by emitting more energy in the mid- and far-infrared than at all other wavelengths combined (Soifer et al. 1984, and the

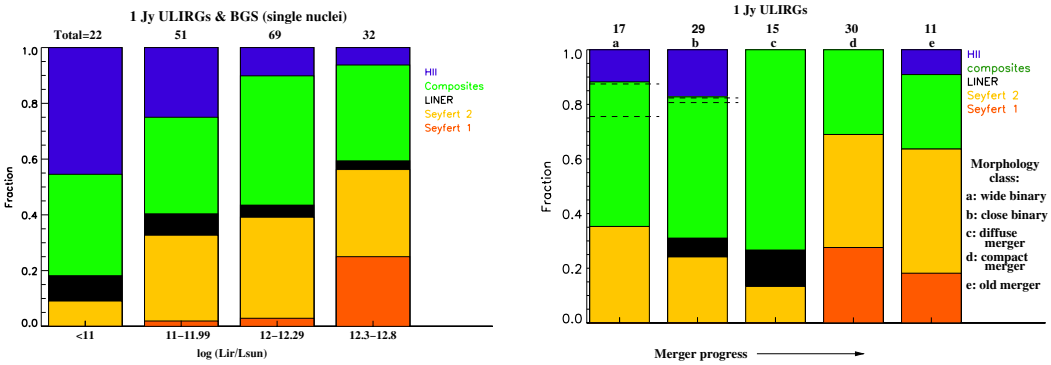

Figure 1.1: Optical spectroscopic classification of (U)LIRGs - *Left:* Spectral type as a function of L_{IR} for the 1 Jy ULRIG sample (Veilleux et al., 1999) and the LIRGs in the Bright Galaxy Survey (BGS, Veilleux et al. 1995). The luminosity bins are labeled at the bottom. *Right:* Optical spectroscopic classification as a function of merger morphology for the 1 Jy ULIRG sample. The merger progresses from left to right, from wide binary to old merger. In both panels, the number of galaxies contained in each bin is marked on top of the histograms. (Figure adapted from Yuan et al. 2010)

Sanders & Mirabel 1996 review). As one of the most important discoveries from extragalactic mid- and far-infrared observations, this new population of infrared bright galaxies (LIRGs, $10^{11}L_{\odot}<L_{IR}<10^{12}L_{\odot}$; and ULIRGs, $10^{12}L_{\odot}<L_{IR}<10^{13}L_{\odot}$) happens to be the most luminous galaxies in the local Universe, and dominates the galaxy population at $z \sim 1.5$ (Pérez-González et al. 2005, Lonsdale et al. 2006, Sargent et al. 2012).

These early studies already related the role of interaction, as triggering mechanism of extreme nuclear activity and large-scale starbursts, with the infrared excess of the newly discovered extragalactic sources. Nevertheless, it was not until the first all-sky survey carried out by *IRAS* when the importance of these objects to galaxy evolution was clearly established. The survey covered $\sim 96\,\%$ of the sky, and observed $\sim$ 20000 galaxies on 12 μm, 25 μm, 60 μm and 100 μm. Most of these sources were not previously catalogued, since they were modest emitters in the optical wavelengths and went undetected in optical surveys.

1.1.1. Power source

Since their discovery, there is a wide consensus that interactions and mergers of gas-rich galaxies are the trigger mechanisms for the most luminous (U)LIRGs (e.g. Sanders & Mirabel 1996). However, there is less agreement on the nature of the power source of these objects. The IR luminosity in (U)LIRGs could be explained as the output from reprocessed radiation from dust of either extreme star-formation activity, AGN, or a combination of both. Studies of large samples of (U)LIRGs suggested that the dominant power source of the low-luminosity

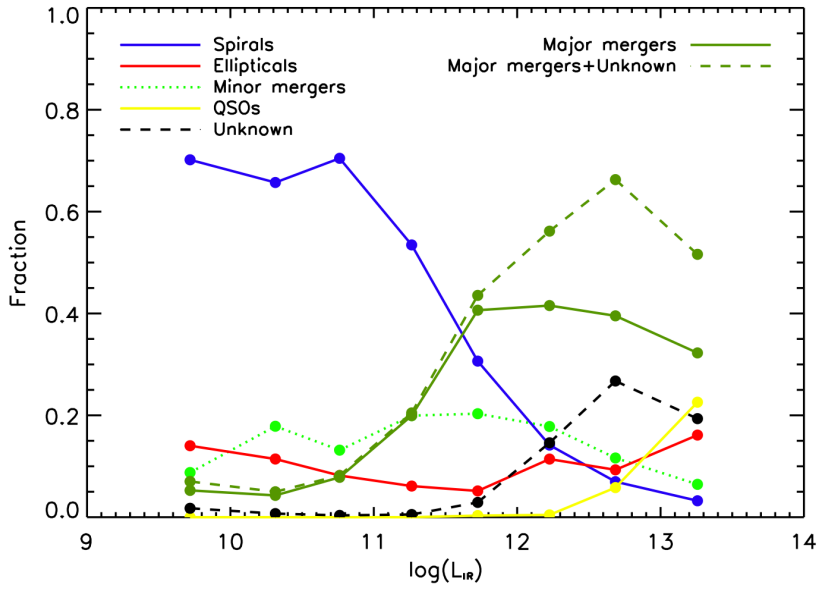

Figure 1.2: Morphological class as a function of L_{IR} - Fraction of COSMOS 70 μm sources that are morphologically classified as spiral (blue line), elliptical (red line), minor mergers (light green dotted line), major mergers (dark green line), QSOs (yellow line), unknown (black dashed line), or major mergers+unknown (dark green dashed line) as a function of L_{IR}. (Figure adapted from Kartaltepe et al. 2010)

objects is likely to be extended star-formation activity, whereas the contribution of AGN increases with bolometric luminosity in the more luminous sources (see Fig. 1.1, Nardini et al. 2010, Yuan et al. 2010, Alonso-Herrero et al. 2012).

Due to the large amount of dust in these objects, extinction plays a key role, especially in ULIRGs. Optical and near-IR studies (e.g. Veilleux et al. 1995, Murphy et al. 2001, Alonso-Herrero et al. 2006) showed that extinction in LIRGs could be as high as $A_V \sim 12$–15 mag, and ULIRGS could reach even higher values of $A_V \sim 20$–30 mag. Therefore, dust could completely obscure a large fraction of the recent star formation activity and, in extreme cases, there would be no indication of an AGN in the optical.

The advent of mid-IR space telescopes like *Spitzer* or *Herschel* contributed to the study of larger samples of (U)LIRGs in wavelengths that are relatively unaffected by dust obscuration. These studies confirmed that most of the luminosity in ULIRGs is produced by star formation, and, although AGN signatures are present in most of them ($\sim$70 %), its contribution dominates the IR emission only in $\sim$20 % of the objects (Nardini et al. 2008, 2010, Farrah et al. 2007, Alonso-Herrero et al. 2012).

1.1.2. Morphology and the role of interactions

From the early work of Toomre & Toomre (1972), galaxy mergers are considered a key mechanism in driving galaxy evolution, and are the base to explain the morphological features like tails or bridges observed in close pairs of galaxies. There are multiple evidences that a large fraction of LIRGs and almost all the ULIRGs show signatures of recent interactions (e.g. Murphy et al. 1996, Borne et al. 2000, Veilleux et al. 2002, Haan et al. 2011), and most of the studies agree that strong interactions and mergers of gas-rich galaxies are the trigger for the more luminous ULIRGs.

However, numerical simulations showed that the idea that mergers transform disk galaxies into ellipticals is more complex than initially expected, and highlighted the key role of the mass ratio of the progenitors, their number, the gas fraction and feedback processes in galaxy interactions (e.g. Bournaud et al. 2005b and references therein). In those mergers where the progenitors are systems of similar masses (major mergers), the resulting products are massive, elliptical galaxies through induced dissipative collapse (e.g. Toomre & Toomre 1972, Barnes & Hernquist 1991, 1996, Mihos & Hernquist 1996, Naab & Burkert 2003). On the other hand, mergers where the mass ratio of the progenitors are within the range 4:1 and 3:1 lead to disk-like remnants (e.g. Bournaud et al. 2005b).

Optical and IR studies showed that the merger fraction increases with L_{IR} (see Fig. 1.2, Kartaltepe et al. 2010), and that approaches the 80–90 % for samples of ULIRGs (e.g. Murphy et al. 1996, Veilleux et al. 2002). ULIRGs are then observed across the entire merging process, from close binary systems with distinct nuclei to compact objects with signs of past interactions. Local LIRGs, on the other hand, are mostly spiral galaxies, with morphologies that are less disturbed than of ULIRGs, typical of an early stage of interaction.

1.1.3. LIRGs and ULIRGs in the cosmological context

The importance of LIRGs and ULIRGs in the context of galaxy evolution has been clearly established in the last decades. They have been detected in large quantities at high-z ($z > 1$) in deep surveys with *Spitzer* and *Herschel* (e.g. Le Floc'h et al. 2005, Nardini et al. 2008, Magnelli et al. 2013), and dominate the energy density of the Universe beyond $z \geq 1.5$, although contribute only with a $\sim$3 % locally (Soifer & Neugebauer, 1991). LIRGs have slightly higher spatial densities than the most powerful optically selected starburst and Seyfert galaxies at similar luminosities, whereas ULIRGs have $\sim$ 2 times the volume density of

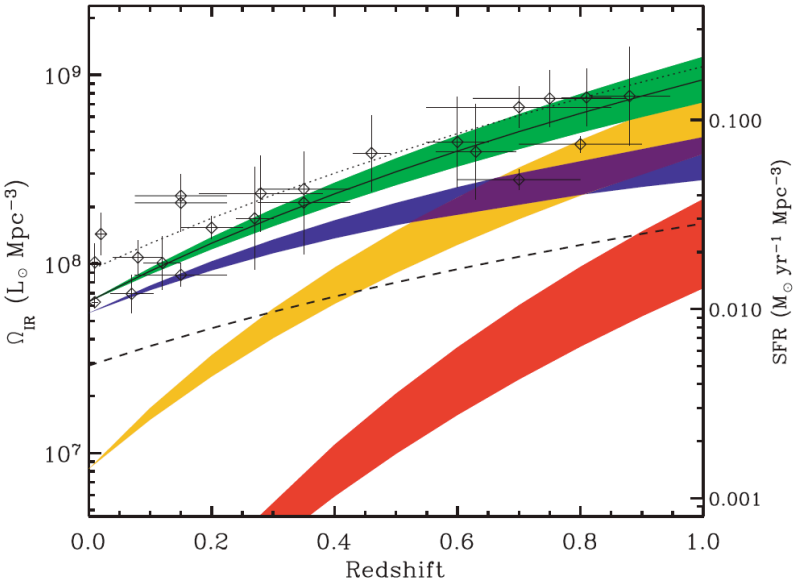

Figure 1.3: Evolution of the comoving energy density - The green filled area shows the evolution of the comoving IR energy density up to z = 1, and the respective contributions from low-luminosity galaxies ($L_{IR} < 10^{11}\,L_\odot$, blue filled area), LIRGs (yellow-filled area) and ULIRGs (red-filled area). The dashed line corresponds to the SFR measured from the UV luminosity not corrected from extinction. The dotted line represents the best estimate of the total SFR density as the sum of this uncorrected UV contribution and the best fit of the IR-SFR (solid line). Open diamonds represent integrated SFR densities and their uncertainties estimated within various redshift bins and taken from the literature (see Le Floc'h et al. 2005 for details). (Figure adapted from Le Floc'h et al. 2005)

optically selected QSOs (Soifer et al., 1987), the only other previously known population of objects with comparable bolometric luminosities.

There are evidences that LIRGs and ULIRGs have undergone strong evolution in their luminosity function (see Fig. 1.3; Le Floc'h et al. 2005, Pérez-González et al. 2005). At $z \sim 1$, (U)LIRGs are responsible for $\sim$70 % of the comoving IR energy density, and dominate the star-forming activity beyond $z \sim 0.7$, where they are responsible for half of the newly born stars. ULIRGs starts to play a significant role on the star-formation cosmic history of the Universe beyond $z \sim 1$ (Pérez-González et al., 2005). Previous studies based on *Spitzer* 24 μm data concluded that the relative contribution of ULIRGs to the star formation rate (SFR) density of the Universe increases with redshift, and may even be the dominant component at $z \geq 2$. However, these conclusions still need to be confirmed since there are large uncertainties at high-redshift in transforming observed 24 m flux densities to far-infrared luminosities (Magnelli et al. 2011, 2013).

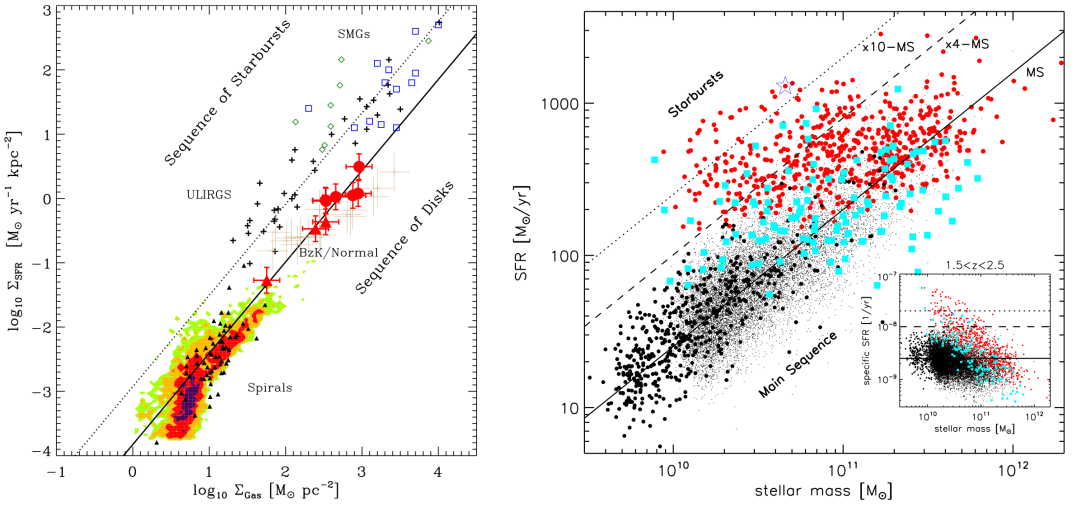

Figure 1.4: Kennicutt-Schmidt law and stellar mass vs star formation rate relation - *Left:* Star-formation rate surface density (Σ_{SFR}) as a function of the gas (atomic and molecular) surface density. The empty blue squares and green diamonds are sub-millimetre galaxies (SMGs) from Bouché et al. (2007) and Bothwell et al. (2009), respectively, whereas crosses and filled triangles are (U)LIRGs and spiral galaxies from Kennicutt (1998). The lower solid line is a fit to local spirals and z = 1.5 *BzK* galaxies, and the upper dotted line is the same relation shifted up by 0.9 dex to fit local (U)LIRGs and SMGs. (Figure adapted from Daddi et al. 2010). *Right:* Stellar mass-SFR relation at $1.5 < z < 2.5$ for different samples. Red filled circles correspond to PACS-COSMOS sources, cyan squares are objects from the PACS-GOODS South survey, whereas the BzK-GOODS and BzK-COSMOS samples are plotted as black filled circles and dots, respectively. The solid black line represents the main sequence for star-forming galaxies at z∼2 defined by Daddi et al. (2007), while the dotted and dashed lines mark the loci 10 and 4 times above the main sequence (along the SFR axis), respectively. The small inset shows the same data as the main panel, using the specific SFR instead the SFR. (Figure adapted from Rodighiero et al. (2011))

1.2. The role of local (U)LIRGs in the study of galaxy evolution

Despite LIRGs and ULIRGs are not very common in the local Universe, the detailed analysis of local samples of these objects is essential to understand not only the formation and evolution of galaxies in a cosmological context, but also the local physical processes that take place in such extreme environments. (U)LIRGs are hence valuable candidates to study extreme cases of compact star-formation and coeval AGN, as well as their impact on the ISM in terms of feedback processes (outflows, quenching of the star-formation, etc). The study of local samples provides with a unique opportunity to perform these detailed analysis, due to the high spatial resolution and S/N that can be achieved.

A basic question on the theory of galaxy evolution is whether the mechanism that transforms the cold molecular gas into stars is or not universal, and whether it is dominated by

the global dynamics or by local processes. Kennicutt (1998) presented the empirical relation (Kennicutt-Schmidt law, or KS law), already proposed by Schmidt (1959, 1963), between the star-formation rate surface density (Σ_{SFR}) and the gas surface density in spirals. The derived relation is a power law of index $N = 1.40 \pm 0.15$, similar to the one found locally for other classes of galaxies like LIRGs (Yao et al., 2003). Recent studies showed that not all galaxies follow the same relation, and seem to be forming stars at higher ratios. Fig.1.4 shows that high-z sub-millimetre galaxies (SMG) and ULIRGs lay above the spiral and star-forming disks relation, suggesting that stars are formed more efficiently in these objects.

This 'enhanced' mode of forming stars has been also observed when comparing the specific SFR (sSFR, i.e. SFR per unit of stellar mass, M$\star$) with the stellar mass. In recent years, a tight correlation between these two quantities has been observed (the so-called 'main sequence', Fig. 1.4, right panel) out to $z \sim 7$ (e.g. Daddi et al. 2007, Elbaz et al. 2007, 2011, Rodighiero et al. 2011, Wuyts et al. 2011). The slope and normalisation of the SFR-M$\star$ relation play a crucial role in the growth of galaxies and in the evolution of their mass function (Rodighiero et al., 2011). In this plot, local ULIRGs and high-z SMGs show higher sSFR than 'normal' star-forming (SF) galaxies at the same stellar mass, and appear to be in different star formation regimes: a quasi-steady, long-lasting mode for disks and a more rapid, starburst mode in major mergers or in the densest SF regions. The nature of this bimodality is not clear yet, and the local study of extreme starburst is essential to shed some light in this question.

Given that (U)LIRGs are extreme examples of starburst and coeval AGN, they are perfect candidates to study in detail the feedback processes of both driving mechanisms. There is a growing number of studies that has revealed the important role of outflows in LIRGs and ULIRGs (Rupke & Veilleux 2005, Rupke et al. 2005a, 2005b, Spoon et al. 2009, Westmoquette et al. 2012, Rodriguez-Zaurín et al. 2013, U et al. 2013). These studies showed that outflows of gas seem to be ubiquitous in LIRGs and ULIRGs, with independence of their driven mechanisms (AGN or starburst), and are observed in different phases of the gas, from highly ionised (Rodríguez-Ardila et al. 2006, Bedregal et al. 2009) and ionised gas (e.g. Westmoquette et al. 2012, Bellocchi et al. 2013) to neutral (e.g. Rupke & Veilleux 2005, Rupke et al. 2005a, 2005b, Martin 2005, 2006) and molecular gas (e.g. Feruglio et al. 2013, Morganti et al. 2013, Rupke & Veilleux 2013a, Cicone et al. 2014). These extended outflows, with sizes from a few hundred of parsecs to several kiloparsecs (Feruglio et al. 2013, Cicone et al. 2014), show mass outflowing rates with typical values of 10-100 $M_\odot\,yr^{-1}$. These values compete with the observed SFR in LIRGs and ULIRGS, and suggest that the star-formation

could be quenched by the depletion of molecular gas (Rupke & Veilleux 2013a, Cazzoli et al. 2014, in prep.). Although the importance of these local processes is well stablished, there is still lack of a deeper understanding of the geometry and spatially resolved kinematics, and accurate measurements of the mass loading factors (i.e. amount of gas expelled in the wind per unit of solar mass of stars formed), from a multi-phase perspective.

1.3. The IFS perspective of (U)LIRGs

During the first decades since the discovery of LIRGs and ULIRGs, a great effort was made to understand their nature and physical properties. The first comprehensive studies on these objects were made using spectroscopic and imaging observations from ground-based and space telescopes (e.g. Goldader et al. 1995, Kim et al. 1995, Veilleux et al. 1995, Murphy et al. 1996, Borne et al. 2000, Scoville et al. 2000, Alonso-Herrero et al. 2006 among others), and covered from the optical to mid-IR wavelengths. These studies laid the foundations of our current understanding of the power source of LIRGs and ULIRGs, and unveiled the complexity and interacting nature of these objects.

The advent of modern IFS facilities, in combination with adaptive optics (AO) techniques, has offered a brand-new range of possibilities to study in detail the physical processes in LIRGs and ULIRGs. The great advantage of these techniques is that they allow to obtain spectroscopic and imaging measurements of the sources simultaneously, and allow to perform spectrally and spatially-resolved studies of the emission and kinematics of the gas and stars in a wide range of redshifts, with an unprecedented level of detail.

The first IFS studies of local LIRGs and ULIRGs in the last decades have been mainly focused on individual or small samples of sources, and usually oriented towards the optical analysis of the most luminous nearby objects (e.g. Colina et al. 1999, Arribas et al. 2000). More recently, the development of new near-IR integral field units (IFUs) like SINFONI (*Spectrograph for INtegral Field Observations in the Near Infrared*, Eisenhauer et al. 2003) or OSIRIS (*OH-Suppressing Infra-Red Imaging Spectrograph*, Larkin et al. 2006), has extended the study of these objects towards longer wavelengths (e.g. Bedregal et al. 2009, U et al. 2013).

In recent years, optical IFS studies of representative samples of local sources have been performed, covering the whole range of the LIRG and ULIRG luminosities and the different morphologies observed in this class of objects (e.g. Arribas et al. 2008, Alonso-Herrero et al.

2009, García-Marín et al. 2009b, 2009a, Monreal-Ibero et al. 2010, Rodriguez-Zaurín et al. 2011, Bellocchi et al. 2013). These optical studies have been focused in a wide range of topics, from investigating the ionisation sources or the structure of the star-forming regions, to the comprehensive analysis of the spatially resolved gas kinematics at sub-kpc scales.

In parallel with the study of local samples, a great effort has been made to investigate the nature and physical properties of star-forming galaxies at early stages of their evolution (e.g. the SINS survey, Förster Schreiber et al. 2006, 2009, 2011a; MASSIV, Epinat et al. 2012, Vergani et al. 2012, among others). Although these surveys are focused on optical/UV selected galaxies, some of these sources have been proposed as the high-z counterparts of local ULIRGs. Such studies map the morphology and kinematics of the gas using the Hα emission, redshifted towards near-IR wavelengths.

1.4. A new near-IR IFS approach to local (U)LIRGs

Most of the recent IFS studies of LIRGs and ULIRGs have been mainly focused on rest-frame optical wavelengths, not only locally but also at higher redshifts, and typically biased towards the high-luminosity objects. The main advantage of the optical wavelengths is that they have been traditionally deeply studied, and a wide variety of physical properties can be constrained from the optical spectroscopic features. In addition, Hα is the brightest line in the optical, and allows to trace, with great amount of detail, the kinematics of the ionised gas in high-z sources.

However, early studies like Goldader et al. (1995) already showed the large number of emission lines and stellar absorption features that offer the near-IR wavelengths. Figure 1.5 shows an example of the synthetic H- and K-band spectra of local LIRGs and ULIRGs. The abundance of spectroscopic features, specially in the K-band, allow to perform comprehensive studies of a wide variety of physical processes, and trace the kinematics of the different phases of the gas and stars using a single, self-contained dataset. In addition, the IR wavelengths are less affected by dust extinction, which make them very appropriate to study dusty environments like LIRGs and ULIRGs.

If we focus only on the brightest spectral features of the H and K bands, i.e. [FeII] at 1.644 μm, Paα at 1.876 μm, HeI at 2.059 μm, H_2 1-0S(1) at 2.122 μm and Brγ at 2.166 μm, and the deepest CO stellar absorption bands, i.e. CO (2–0) at 2.293 μm, CO (3–1) at 2.323 μm or CO (4-2) at 2.354 μm, we could almost completely characterise a wide variety

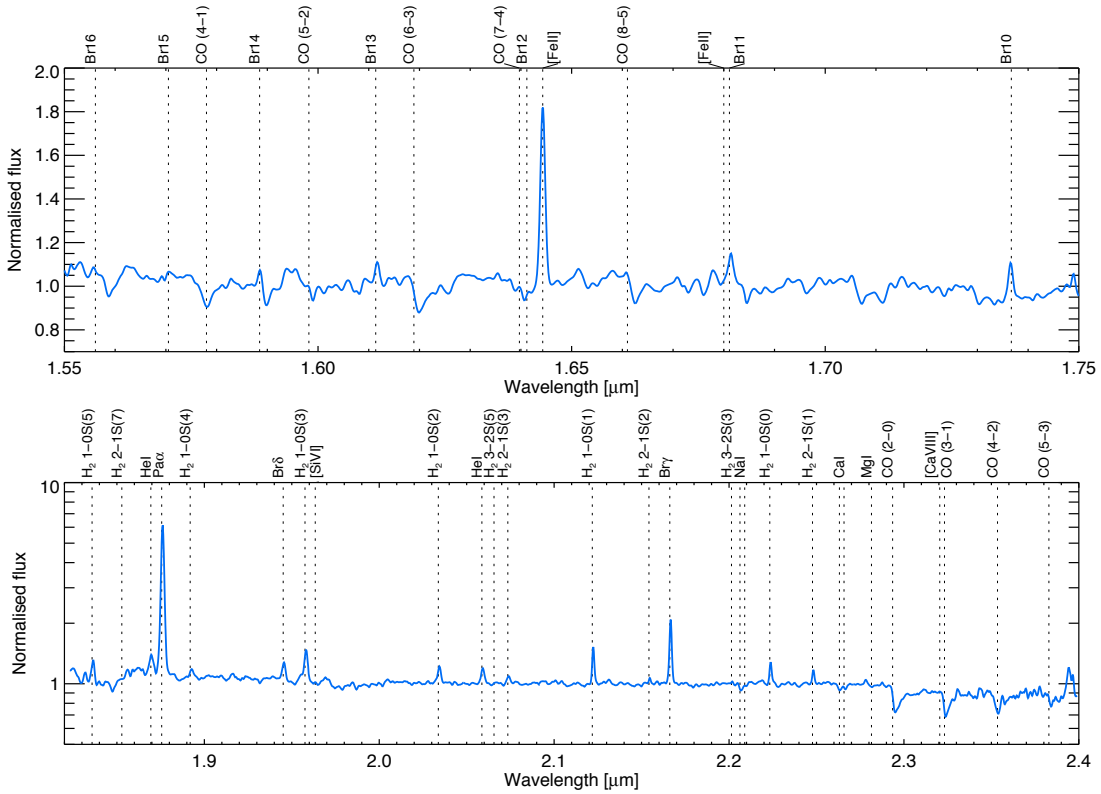

Figure 1.5: H- and K-band sample spectra - Synthetic spectra along the H (top) and K (bottom) bands obtained by stacking and combining the data from local LIRGs and ULIRGs (Piqueras López et al., 2012a). The more relevant spectral features have been labeled to illustrate the riches of the near-IR wavelengths.

of physical properties of the system, as well as its kinematics and dynamics. These spectral features, for which high S/N can be achieved, allow to trace emission and kinematic maps of a large number of the ISM phases, e.g. the ionised and partially ionised gas, the warm molecular phase or the stellar component of the ISM. In addition, other fainter emission lines like the [SiVI] at 1.963 μm or [CaVIII] at 2.321 μm are excellent tracers of AGN activity.

Although further details will be given in the following chapters of this project, we will briefly describe some of the most important physical processes that produce the emission and absorption features in the H and K bands:

- **Ionised gas and star-formation from near-IR emission lines**

  The structure and kinematics of the ionised gas can be traced accurately by the hydrogen recombination lines Paα and Brγ. In particular, the Paα line at 1.876 μm is the brightest line across the H and K bands, and it is particularly useful at increasing

distances since it is only a factor ∼8 fainter than Hα. For nearby objects (z$\lesssim$0.04), the atmospheric absorption between ∼1.8-2.0 μm due to water vapour precludes accurate measurements of the Paα emission from the ground. In this case, the Brγ line at 2.166 μm, a factor ∼12 fainter than Paα, is also an excellent tracer of the ionised phase of the ISM.

Therefore, the Paα and Brγ lines are excellent indicators of the recent star-formation activity, where the more massive, young stars keep the gas in an ionised state (e.g. Kennicutt & Evans 2012 and references therein). These lines will allow us to map the SFR in LIRGs and ULIRGs at sub-kpc scales.

Besides the Paα and Brγ lines, used as primary indicators of the SFR, the HeI line at 2.059 μm is also associated to very young star-forming complexes. Although its interpretation is not as straight-forward as the hydrogen recombination lines (Shields, 1993), the HeI emission traces the younger OB stars, given its high ionisation potential.

Finally, the [FeII] line at 1.644 μm has been widely used to estimate the supernova rate in starbursts (e.g. Colina 1993, Alonso-Herrero et al. 2003), since it is usually associated with regions where the gas is partially ionised by shocks. In combination with the Paα or Brγ measurements, it can be used to constrain the age of the stellar populations in synthesis models.

- **Spatially-resolved extinction measurements**

  As mentioned before, the detailed characterisation of the extinction is essential to understand the properties of dusty environments like LIRGs and ULIRGs, and to obtain accurate measurements of physical quantities like the SFR or the SFR surface density (Σ_{SFR}). The quantitative study of the extinction of the gas can be performed using the Paα/Brγ line ratio, or, when the Paα line is not available, the Brγ/Brδ ratio by measuring the Brδ line at 1.945 μm.

- **Molecular warm gas and excitation mechanisms**

  The roto-vibrational transition H_2 1-0S(1) at 2.122 μm is the brightest H_2 line in the H and K bands, and traces the warm molecular phase of the gas. Its typical brightness is similar to the Brγ line, which allows to study both lines with similar S/N, and given that both are very close in wavelength, with almost no bias by extinction.

However, one of the advantages of the K-band IFS regarding the H_2 is that it allows to study in detail the excitation mechanisms of the molecular hydrogen. These mechanisms involve radiative processes like fluorescence due to the excitation by UV photons in photon-dominated regions (PDR), and thermal processes like collisional excitation by supernova (SN) shocks or X-rays (e.g. Davies et al. 2003, 2005). The study of these processes requires measurements of several lines, since the different mechanisms rise to similar intense and thermalised H_2 1-0S(1) emission. As shown in Fig. 1.5, there are several H_2 lines within 1.9–2.4 μm that can be measured with enough S/N on the integrated spectra of local sources. Using the relative fluxes of these transition to the 1-0S(1), it is possible to obtain population diagrams of the emitting regions, and, in some cases, to distinguish between thermal and non-thermal processes.

- **Ionisation mechanisms**

  The three of the brightest lines in the H and K bands, i.e. [FeII] at 1.644 μm, H_2 1-0S(1) at 2.122 μm and Brγ at 2.166 μm, are tracers of three different ionisation states of the ISM. Since all of them present very similar intensities, they can be studied achieving similar S/N ratios. Their respective line ratios, i.e. [FeII]/Brγ and H_2 1-0S(1)/Brγ, allow to distinguish different ionisation mechanisms and efficiencies (e.g. Rodríguez-Ardila et al. 2005, Riffel et al. 2010, 2013 and references therein). The advantage of the near-IR IFS data is that this analysis could not only be performed in terms of integrated measurements, but could also be perform in an spaxel-by-spaxel basis, to obtain the spatially-resolved 2D maps of the line ratios (i.e. 2D BPT near-IR diagrams).

- **Near-IR tracers of obscured AGNs**

  There are two coronal lines in the K-band, i.e. the [SiVI] line at 1.963 μm and the [CaVIII] line at 2.321 μm, that can be used as AGN indicators. Given the high ionisation potential of both lines, they are usually associated to the outskirts of the broad-line region, and to extended narrow-line regions. Although the coronal emission is usually rather compact and unresolved, there are some examples of Seyfert galaxies where [SiVI] extended emission has been observed. In particular, Bedregal et al. (2009) presented the detection of a cone of [SiVI] emission in NGC 5135, extending $\sim$600 pc ($\sim$2 arcsec) from its AGN, using the same SINFONI data as presented in this work.

- **Absorption features and stellar populations**

  Besides the large number of emission features along the near-IR, there are different absorption features that lie within the K-band, such as the NaI doublet at 2.206 μm and 2.209 μm, the CaI doublet at 2.263 μm, and 2.266 μm and the CO absorption bands CO (2–0) at 2.293 μm, CO (3–1) at 2.323 μm or CO (4-2) at 2.354 μm. The strongest feature among the stellar signatures is the CO (2–0) band, that is typical of late stellar types (K or later), and traces the red giant and supergiant populations. The measurements of the equivalent width (EW) of this first CO band (or the equivalent CO index defined as the ratio of the flux densities at 2.37 μm and 2.22 μm), combined with the equivalent width of the Paα or Brγ lines, are widely use by the stellar population synthesis models to constrain the ages of the stellar populations (e.g. Leitherer et al. 1999, Maraston 1998, 2005).

- **Gas and stellar kinematics**

  In addition to the morphology, luminosity and physical properties, the IFS data allow to extract the kinematics of the different constituents of the ISM. It is possible to obtain spatially-resolved maps of the velocity and velocity dispersion of the different phases of the gas using the brightest emission lines present across the H and K bands (i.e. [FeII], H_2 1-0S(1) and Brγ), and trace the kinematics of the stars using the stellar absorption bands at 2.293 μm and beyond. The analysis of the global kinematics of the different phases of the ISM provides with a very robust way to study whether the kinematics of gas and stars are coupled, and whether they are located at the same dynamical structures. In addition, it is possible to derive the dynamical masses of the objects, and distinguish between rotation- and dispersion-dominated systems (e.g. Epinat et al. 2012, Bellocchi et al. 2013)

- **Outflows signatures in different phases of the ISM**

  IFS techniques allow to study not only the global kinematics of the objects, but also local processes such as that associated with mass flows or turbulence. AGN- and SF-induced outflows have been detected in multiple phases of the ISM, from highly ionised to molecular gas, and are almost ubiquitous in LIRGs and ULIRGs (e.g. Rupke et al. 2005a, 2013b, Westmoquette et al. 2012, Cicone et al. 2014, Rodriguez-Zaurín et al. 2013). The near-IR IFS data allow to performed spatially and spectrally resolved

multi-phase analysis of gas outflows, and study their spatial structure, kinematics, outflows rates and mass loading factors in all different phases using an homogeneous dataset.

1.5. Thesis project

The advent of IFS facilities allowed to perform spatially and spectrally resolved morphological and kinematical studies of (U)LIRGs, not only locally, but also at early stages of their evolution. In parallel with other projects for investigating the nature of star-forming galaxies at high-z, a large survey of local LIRGs and ULIRGs has been performed using different IFS facilities (Arribas et al., 2008). This thesis project is part of this larger program, that covers the whole range of LIRG and ULIRG luminosities and the different morphologies observed, and presents, for the first time, a near-IR study of local LIRGs and ULIRGs based on seeing-limited VLT-SINFONI observations. Throughout this work we consider H_0 =70 km s^{-1} Mpc^{-1}, Ω_Λ = 0.70, Ω_M = 0.30.

This thesis is divided as follows:

- **Data reduction and calibration of VLT-SINFONI data**

  In Chapter 2, we present a brief description of SINFONI and the science data and calibration products from seeing-limited and AO observations. We also describe in detail the reduction and calibration techniques that has been used to perform the calibration of the datasets used in this thesis, together with some of the techniques implemented to improve the final products.

- **Spatially resolved kinematics of the central regions of M83** (Piqueras López et al., 2012b)

  Chapter 3 presents the study of the spatially resolved kinematics of the central regions of the nearby galaxy M83, based on AO-assisted VLT-SINFONI observations on the H+K band. The inner regions of M83, that correspond to the central $\sim$235$\times$140 pc, are sampled with an unprecedented spatial resolution of $\sim$0.″2 ($\sim$4 pc). The detailed study of the gas and stellar kinematics, and the role of supernovae in shaping the gas kinematics are discussed. We also present the photometric and kinematic analysis of the optical nucleus of M83, and discuss whether it is suitable for hosting a supermassive black hole.

- **Mapping the emitting gas structure of local LIRGs and ULIRGs** (Piqueras López et al., 2012a)

  We present the detailed study of the sample of local ($z < 0.1$) LIRGs and ULIRGs, based on near-infrared H- and K-band VLT-SINFONI. Chapter 4 corresponds to the atlas of the ionised, partially ionised, and warm molecular gas two-dimensional flux distributions and kinematics over a FoV of $\sim 3 \times 3$ kpc (LIRGs) and $\sim 12 \times 12$ kpc (ULIRGs) and with average linear resolutions of $\sim$0.2 kpc and $\sim$0.9 kpc, respectively. We include an overview of the data and physical processes of the line emitting gas and stellar populations, together with the emission and kinematic maps of the main spectral features (i.e. Brγ, Paα, H_2 1-0S(1) and [FeII] lines), and a brief discussion of their general properties.

- **Characterisation of the visual extinction and dust clumpiness** (Piqueras López et al., 2013)

  In Chapter 5, we present the detailed 2D analysis of the extinction in the galaxies of the sample, based on the Brγ/Brδ and Paα/Brγ line ratios. We describe the general properties of the A_V maps, and analyse the spaxel-by-spaxel A_V distributions and radial profiles of the individual sources. We investigate the possible effect of the spatial sampling of the maps in the derived extinction values, and their implications in the derivation of subsequent physical properties.

- **Sub-kpc study of the star formation rate** (Piqueras López et al., 2014, in prep.)

  In Chapter 6, we study in detail the observed and extinction-corrected 2D structure of the SFR and Σ_{SFR} in our sample. We also compare our near-IR measurements of the SFR with other tracers like Hα, mid-IR continuum and L_{IR}, and investigate the implications of the spatial scale of the emission maps on the Σ_{SFR} measurements. Besides the spaxel-by-spaxel Σ_{SFR} distributions and maps, we analyse a sample of 95 star-forming regions in terms of their size, luminosity and velocity dispersion, and compare them with other local and high-z samples of star-forming clumps.

- **Conclusions and future work**

  Finally, in Chapter 7, we present the general conclusions of our analysis, together with a brief discussion of the ongoing work and future prospects that follow from this thesis project

2

Data reduction and calibration

"Devil is in the detail."

— Anonymous proverb

In this chapter we briefly describe the characteristics of SINFONI, as well as the resulting science and calibration products for both AO and seeing-limited observations. We explain in detail the data reduction process using the standard ESO pipeline, EsoRex, and the absolute flux calibration of the intermediate products, prior to the final reconstruction of the coadded data cubes. Finally, we also discuss some techniques that could be implemented to improve the quality of the final data, and ease the ulterior analysis of the cubes.

2.1. SINFONI observations

2.1.1. Instrument description

SINFONI is a near-infrared (1.1–2.45 μm) integral field spectrograph (IFS) installed at the Cassegrain focus of the ESO VLT UT4 telescope, which can be fed by an adaptive optics module. The instrument can operate with four different gratings, J, H, K and H+K (see Table 2.1) and three setups (250, 100 and 50 mas) that allow to chose the pixel scale of the observations (see Table 2.2).

There are two main operation modes available for SINFONI, seeing-limited and AO-assisted observations. In the seeing-limited mode, the spatial resolution is determined by the natural seeing conditions, and the recommended configuration of the instrument is the 250 mas setup that achieves a field of view (FoV) of 8" $\times$8". In the AO-assisted mode, the system performs the correction of wavefront errors induced by the atmospheric turbulence. These corrections are sent to the deformable mirror of the instrument and, together with

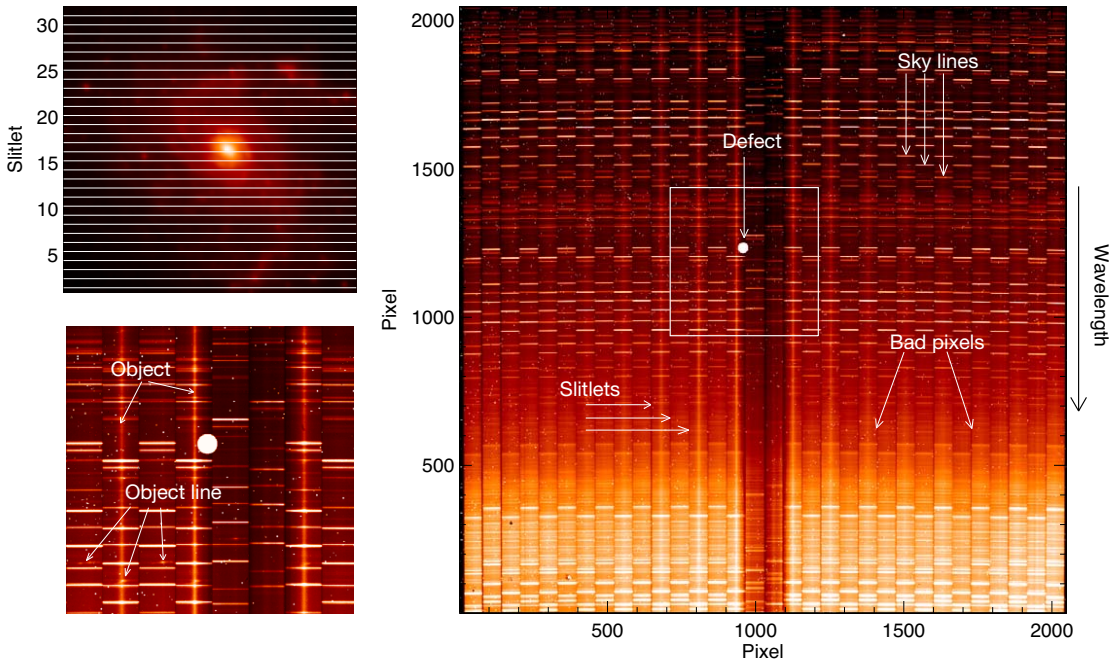

Figure 2.1: SINFONI raw frames - Example of a SINFONI science raw frame. The top left panel shows the distribution of the slices over a 8"×8" HST-NICMOS F160W image of NGC 3110. The right panel shows a complete raw frame of the same object. The slitlets are distributed along the detector following an interleaved pattern. The bottom left panel shows a zoomed view of the 500×500 pixel region marked as a white square on the right frame, where the sky lines and the object continuum are clearly visible.

the active optics system of the telescope, allows to reach spatial resolutions close to the diffraction limit of the telescope (∼0.05 arcsec).

The wavefront is measured from a guide star, either a natural guide star (NGS) or a laser guide star (LGS), although it could also be an extended object that provides enough contrast. The NGS should be a bright star ($m_R \gtrsim 14$ mag), ideally as close as possible to the scientific target ($\lesssim 30''$) to provide accurate measurements of the wavefront. The availability of a suitable NGS severely limits the fraction of sky over the AO can be used. In that sense, the LGS mode allows to extend the use of the AO to a wider number of scientific targets. The LGS consists on an artificial star, created by a Na laser beam, that is used to measure the wavefront. However, it still needs a natural star, a tip-tilt star (TTS), fainter than a NGS ($m_R \gtrsim 18$ mag) and reasonably close to the target, to correct from the motion of the image (tip-tilt).

SINFONI works as a image slicer, i.e. its FoV is sliced in the image plane into 32 slitlets, that are dispersed and rearranged on different locations on the detector plane. The pixel

Band	Wavelength range	Resolution
J	1.10–1.40 μm	$\sim$2000
H	1.45–1.85 μm	$\sim$3000
K	1.95–2.45 μm	$\sim$4000
H+K	1.45–2.45 μm	$\sim$1500

Table 2.1: SINFONI spectral bands. The spectral resolution is approximate since it depends on the particular plate scale setup.

FoV	Spaxel scale	Mode
8" $\times$8"	0.″250$\times$0.″125 spaxel^{-1}	Seeing-limited
3" $\times$3"	0.″100$\times$0.″050 spaxel^{-1}	Seeing-limited / AO
0.″8$\times$0.″8	0.″050$\times$0.″025 spaxel^{-1}	Seeing-limited / AO

Table 2.2: SINFONI plate scale setups and available observation modes.

scale setup determines the angular size of the slices on the sky, each one projected onto 64 pixels of the 2048$\times$2048 detector.

Figure 2.1 shows an example of a K-band 0.″250$\times$0.″125 spaxel^{-1} raw science frame. The top-left panel shows a 8" $\times$8" FoV with the positions of the slitlets overplotted. The 32 slitlets are aligned to form a pseudo-slit that is then dispersed and projected onto the 2048 pixels of the detector. The raw image from the spectrometer is shown in the right panel of Fig. 2.1, where the position of the slitlets are clearly visible along the detector.

2.1.2. AO-SINFONI observations of M83

The M83 AO-assisted SINFONI observations were carried out in service mode using the SINFONI AO module fed by a LGS. The data were taken using the H+K grating and the 100 mas setup for the plate scale, that yields a FoV of $\sim$3" $\times$3". The wavelength coverage of the H+K configuration is $\sim$1.45–2.45 μm with an average spectral resolution of R$\sim$1500.

The total integration time per pointing was $\sim$3400 s, splitting the observations into individual exposures of 300 s. In addition, four sky frames were taking every two on-source exposures following a pattern OOSOOSOO. Further details of each of the four pointings will be discussed in Chapter 3.

Using the same setup as the science data, a set of six spectroscopic standard stars was observed, using shorter exposures between 2-10 s, and following a typical OS pattern (one on-source exposure followed by a sky acquisition).

2.1.3. Seeing-limited SINFONI observations of local LIRGs and ULIRGs

The seeing-limited observation of our sample of local LIRGs and ULIRGs were obtained in service mode, using the same plate scale configuration of 250 mas for all the objects, that yields a nominal FoV of $\sim$8"$\times$8". The whole sample was observed in the K-band ($\sim$1.95–2.45 μm), whereas the subsample of LIRGS was also observed in the H-band ($\sim$1.45–1.85 μm), with spectral resolutions of R$\sim$4000 and R$\sim$3000, respectively.

The average integration time per pointing and per band for each object is $\sim$2800 s, splitted into short exposures of 150 s (see Chapter 4). The observations were carried out following a jittering OSSO pattern for sky and on-source frames, i.e., two sky frames were taken between two on-source exposures.

Two sets of standard stars were also observed, for both H and K bands, using the same configurations as for the scientific data. As for M83, a pair of on-source and sky frames was taken, using integration times of $\sim$2-30 s per frame, every $\sim$2 hours of science data acquisition, yielding an average of 1–3 stars per observing night.

2.2. Data reduction

Besides the intrinsic difficulty of the near-IR observations (sky lines, background emission, etc.), the reduction process of SINFONI IFS data also implies an additional effort to reconstruct the final data from the images of the slitlets on the detector. In addition to the common techniques of dark subtraction, flat-fielding or wavelength calibration, it is also necessary to account for the geometrical distortion of the images and to determine the correct position of the slitlets on the detector.

The SINFONI reduction and calibration processes could be divided as follows:

- Correct from the telescope, instrument and detector signatures: bad pixels, background emission, pixel to pixel gain variations and geometrical distortions.
- Wavelength calibration of the data.
- Cube reconstruction from the 32 slices to recover the spatial and spectral information.
- Calibration of the data: correct from the strong near-IR sky emission and translate the information of the cubes into physical units.

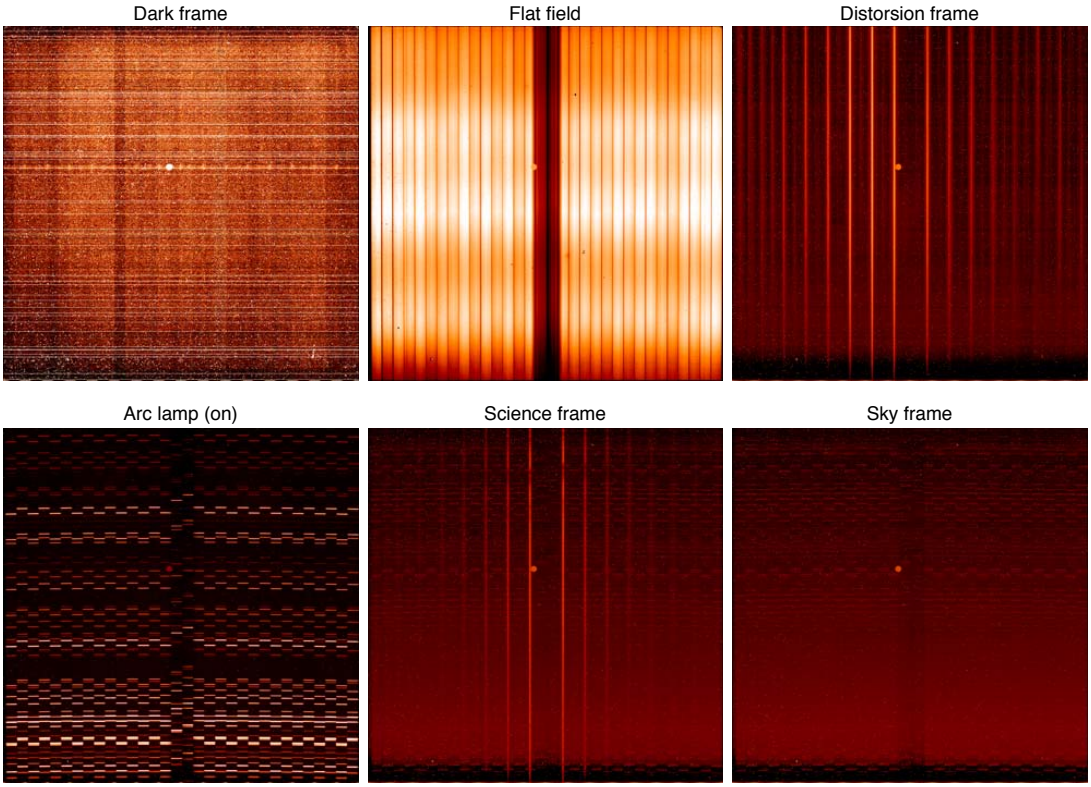

Figure 2.2: Set of SINFONI science and calibration frames - *From top to bottom and left to right:* example of a dark frame of 150 s of exposition; a flat field used to calculate the response of the detector; a distortion frame to compute the geometrical distortion of the slitlets across the detector; an arc lamp frame to perform the wavelength calibration; and a science and sky frames.

The standard ESO pipeline, EsoRex, allows to integrate almost all the reduction and calibration tasks into data reduction scripts for the automation of the process. We now describe briefly the reduction process, and the EsoRex recipes and calibration frames involved in the different steps. An example of the calibration and science frames is shown in Fig. 2.2.

The pipeline is based on a set of stand-alone recipes that performs the different steps of the reduction cascade. Each recipe has an input ASCII file, a set-of-frames (SOF), that consists on a list of calibration and/or science FITS frames. The filenames must be listed together and tagged using a label assigned to each data type. For a detailed description of the recipes and the calibration frames, please see the SINFONI pipeline user manual at http://www.eso.org/sci/software/pipelines/.

An example of a SOF used to reconstruct an spectroscopic standard star is as follows:

```
/file_path/SINFO.2008-07-16T09:53:34.153.fits      STD
/file_path/SINFO.2008-07-16T09:56:02.374.fits      SKY_STD
```

```
/file_path/MASTER_BP_MAP_K_250.fits          MASTER_BP_MAP
/file_path/MASTER_FLAT_LAMP_K_250.fits       MASTER_FLAT_LAMP
/file_path/WAVE_MAP_K_250.fits               WAVE_MAP
/file_path/SLITLETS_DISTANCE_K.fits          SLITLETS_DISTANCE
/file_path/SLIT_POS_K_250.fits               SLIT_POS
/file_path/DISTORTION_K.fits                 DISTORTION
```

The SINFONI data reduction typically follows the next sequence:

1. The first step of the reduction chain is generate a master dark frame using the recipe *sinfo_rec_mdark*, from a set of raw dark frames.

2. Then, the recipe *sinfo_rec_detlin* calculates the response of the detector as a function of the pixel intensity, and determines when it becomes non linear. The input SOF consists on a set of flat field images, with increasing intensity/exposition time.

3. The next step of the reduction is to compute the optical distortion of the system, and the relative distances of the slitlets from the first one, using the recipe *sinfo_rec_distortion*. The recipe needs a set of $\sim$75 fibre flat frames that covers all the slitlets. These fibre flats are taken with a calibration fibre that moves perpendicular to the image slices and illuminates only the first detector column of each slitlet.

4. The recipe *sinfo_rec_mflat* is then used to calculate the master bad pixel map and the master flat frame from a set of standard flat fields. This step and the previous one (the distortion correction) could be exchanged, since the input of both routines only depend on the first two steps of the reduction chain.

5. Before the final data cube is reconstructed, the wavelength calibration frames have to be created. This task is performed by the recipe *sinfo_rec_wavecal* on a set of arc lamp frames and the slitlet edge position table. This calibration could also be performed based on OH lines from an input sky frame, improving the accuracy of the data reduction. However, although for the J and H bands the OH based wavelength calibration may work, the absence of OH lines beyond 2.3 μm makes it less robust for the K band (see Fig. 2.3). For this reason, we performed the wavelength calibration of our sample using the arc lamp frames.

6. The final step of the reduction cascade is performed by the recipe *sinfo_rec_jitter*. This routine reduces not only the science frames, but also the standard stars for the flux calibration. It subtracts the sky emission (see Sec. 2.3), correct from the flat-field, and resamples the science and sky frames to construct wavelength calibrated data cubes. It also builds a final mosaic from the individual data cubes by reconstructing the jittering pattern. However, as we will discuss later, we perform the reconstruction of the final cube using an additional routine, *sinfo_utl_cube_combine*, after the individual data cubes are flux calibrated.

The reduction of the spectrophotometric standard stars is performed following the same reduction cascade as the science data. Almost the totality of the sub-products of the reduction process are common for both stars and science targets, and could be skipped. The final result of the standard star reduction process is an individual cube of the star, that is later used to perform the flux calibration of the scientific targets and to correct from the atmospheric transmission (see Sec. 2.4).

2.3. Sky emission

One of the key issues of the reduction of near-IR data (1.0-2.5 μm) is the correction from the sky emission. The airglow emission is originated by OH radicals which are created by reactions between the hydrogen and the ozone in an atmospheric layer of 6-10 km thickness at an altitude of $\sim$87 km. Fig. 2.3 shows the stacked spectrum of the sky emission extracted from SINFONI H- and K-band observations. These emission lines are the dominant source of noise in fully processed data, since their flux is typically several orders of magnitude above from other sources (Rousselot et al., 2000). Thus, in most cases, to correct from this emission, it is mandatory to obtain separate frames of the sky field using identical setups and similar conditions than science frames.

Besides the OH lines, that dominate the near-IR spectrum below $\sim$2.3 μm, the sky emission has also a thermal contribution that dominates beyond 2.3 μm in the K-band (see Fig.2.3). This thermal component consists of both atmospheric and telescope emission, and has to be subtracted from the raw data during the reduction process.

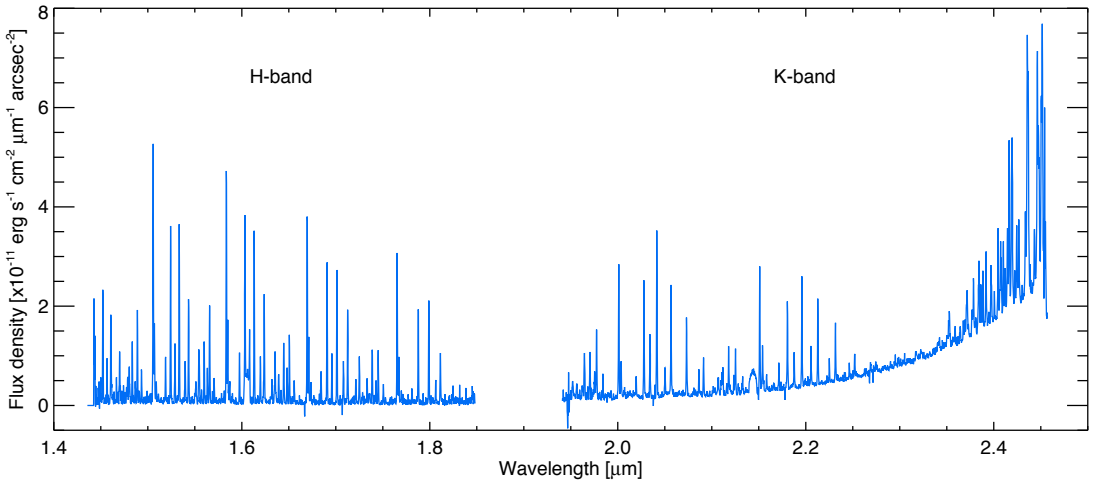

Figure 2.3: H- and K-band sky spectra - Stacked spectrum of the sky emission extracted from H- and K-band SINFONI sky cubes.

2.3.1. Sky lines subtraction

The standard 'first-order' approach to deal with the sky emission is to subtract a 'sky' spectrum from an 'object' spectrum. This procedure implies two sources of error, i.e. from the statistical photon noise, that can only be improved by longer integration times, and a systematical source of noise that comes from the strong and rapid variability of the sky lines. This variability of the line fluxes is specially problematic in IFS observations, since the limited FoV does not allow to measure both the object of interest and the sky emission simultaneously, as in long-slit spectroscopy. Even more, in such instruments the line profile can vary across the FoV due to image distortions, flexures or off-axis aberrations, and can lead to significant and characteristic 'P-Cygni' residual profiles when subtracting an sky frame.

To deal with all these issues, the SINFONI pipeline includes a method developed by Richard Davies (Davies, 2007) to remove residual OH emission. This method takes into account both the variation in the absolute and relative fluxes of the OH lines together with the instrumental flexures, and allows to reduce significantly the time spent on sky acquisition.

This technique is based on finding a scaling at each position of the sky cube, as a function of wavelength, in order to match optimally the sky background of an object cube. This scaling is then applied to the sky cube to obtain a modified sky cube that is subtracted from the object cube, and that takes the possible variations of the line fluxes into account. To compensate for the instrumental flexures, the routine measures iteratively the relative wavelength shifts of the sky lines in both the sky and object cubes, removing outliers which

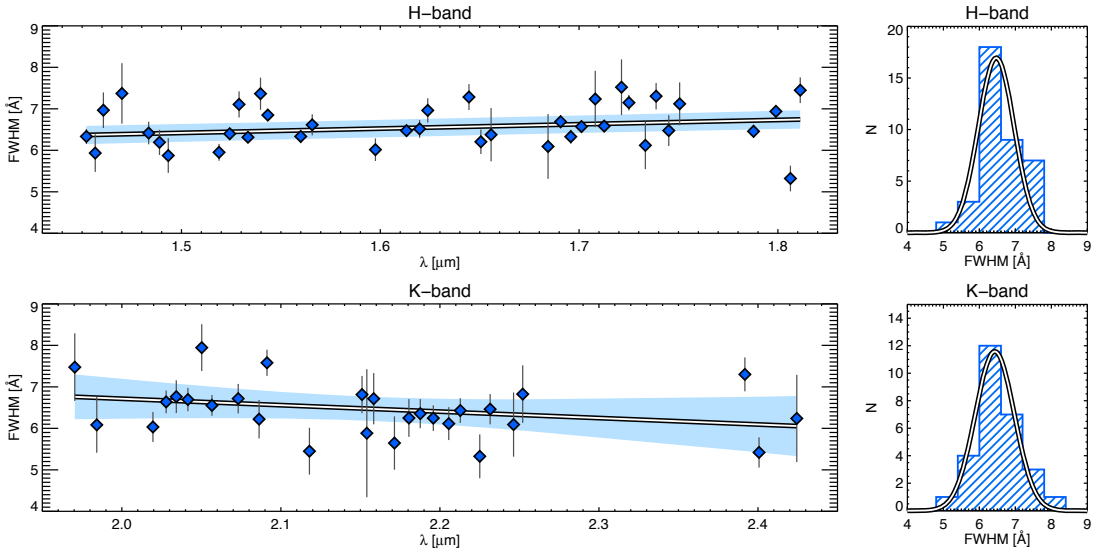

Figure 2.4: Spectral resolution from sky line measurements - H- (top panels) and K-band (bottom panels) sky line FWHM measurements. The left panels show the variation of the line width with wavelength. Blue diamonds show measurements of individual sky lines, and grey bars represent 1-σ uncertainties. The white lines are linear fits to the data points, and the blue shaded area represents the 98 % confidence interval of the fitting. The right panels show the distributions of the FWHM of each set of lines.

deviate significantly. A final average shift is then calculated and applied to the modified sky cube.

2.3.2. Spectral resolution measurements using the sky emission lines

As discussed in Sec. 2.2, the sky emission, although could be a nuisance as an additional source of noise, could be of useful reference for the wavelength calibration of the data. In that sense, since the sky frames are usually observed using the same instrument configuration as the science frames, they are a valuable option to characterise the spectral resolution of the processed data. Even more, since the sky lines are present all along the J, H and K bands, with the exception of a small window at $\sim$2.3 μm in the K-band, they provide with useful information of a possible dependence of the spectral resolution with wavelength within the cubes.

To measure the spectral resolution of our data cubes, we extracted a stacked spectrum from both a H- and K-band sky cubes (Fig. 2.3). We identified as much lines as possible that were strong enough to be fitted by a single Gaussian profile unambiguously, i.e., were no sign of blended lines. We found a mean value of the FWHM (full width at half maximum) of

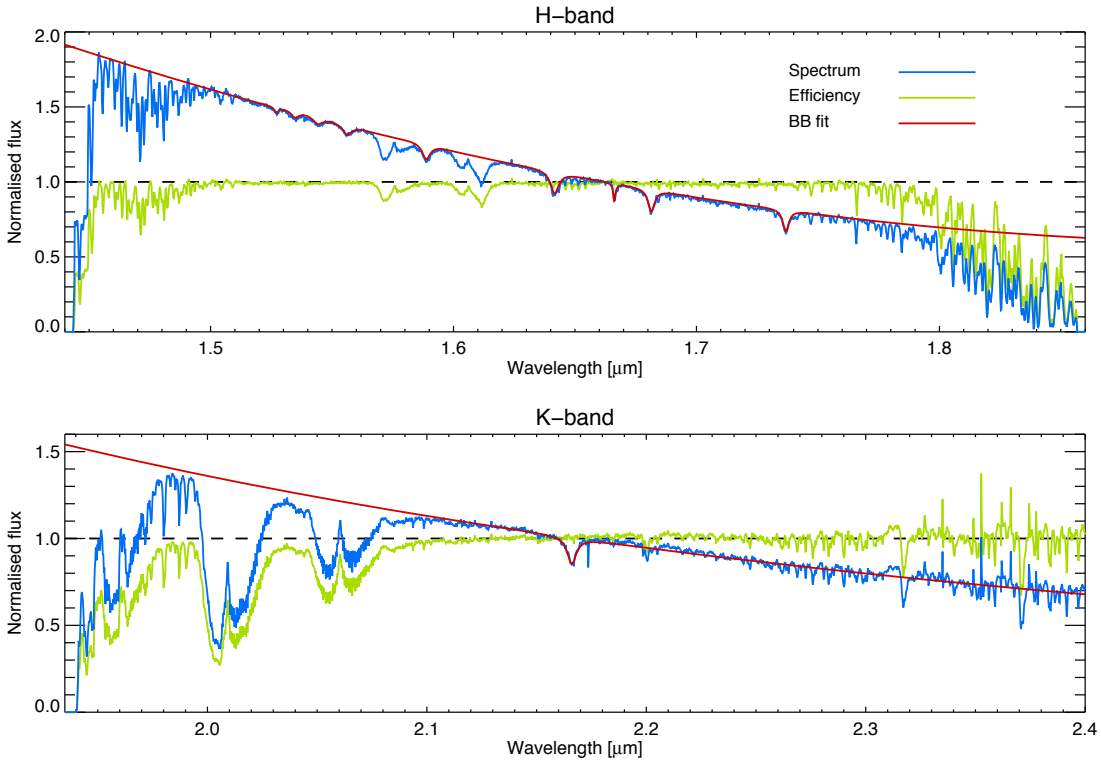

Figure 2.5: H- and K-band spectra of spectrophotometric standard stars - H- (top) and K-band (bottom) normalised spectra of two standard stars using for the flux calibration of the data cubes (blue curves). The red lines correspond to the fits of a black body (BB) profile, that include the stellar absorption features of the stars, whereas the green lines are the resulting efficiency curves.

the lines of 6.6 ± 0.5 Å for the H-band and 6.4 ± 0.6 Å for the K-band, respectively. Fig. 2.4 shows the distributions of the FWHM of the lines for each band, together with the variation of the width with wavelength, and a linear fit to the data. In both bands, the linear fits are compatible with an almost constant spectral resolution across each wavelength range, although the K-band data suggest a mild decrease of the line width at larger wavelengths.

2.4. Flux calibration

The final product of the reduction pipeline is a wavelength calibrated and sky-subtracted data cube, built by combining the individual cubes of each on-source exposures, following the pre-determined jittering pattern of the observations. This cube still has to be corrected from the atmospheric absorption and to be flux-calibrated using the spectrophotometric standard star data.

It is common that SINFONI observations to be carried out in service mode, and thus

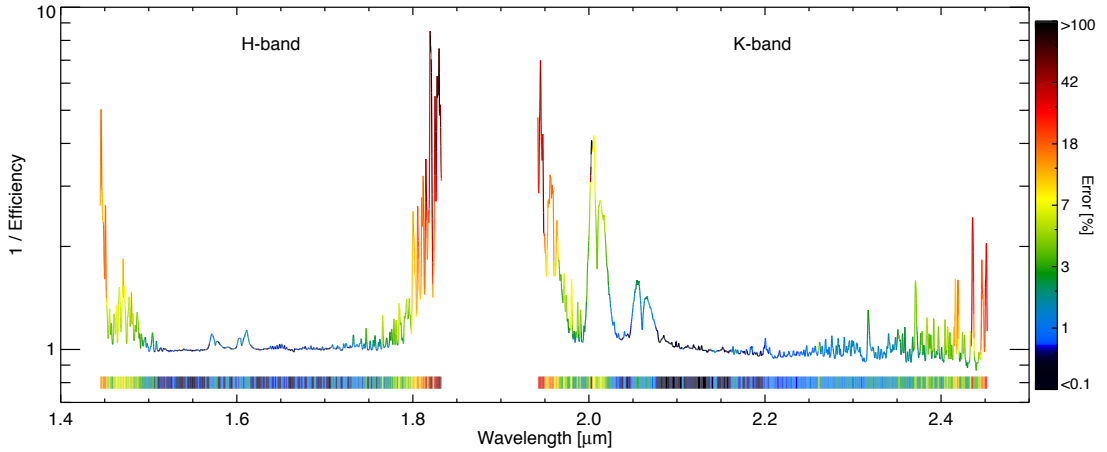

Figure 2.6: H- and K-band efficiency - H- and K-band median efficiency curves obtained from the sample of standard stars. The colour code indicate the relative error calculated as the standard deviation of the set of curves at each wavelength point.

that the final data cube to be the result of combining different individual observations taken during different days or weeks. Hence, instead of combining the un-calibrated exposures in a single cube, it is advisable to calibrate the individual cubes separately prior to the final reconstruction, for a more accurate calibration. In this way, each individual cube is calibrated using the closer standard star exposure to its observing date, assuring the most similar atmospheric conditions as possible to the science cube acquisition.

2.4.1. Atmospheric absorption. Efficiency curves

The first step of the flux calibration is to correct each individual cube from the atmospheric absorption. It is well known that the water vapour present in the atmosphere absorbs the electromagnetic radiation from outside the Earth along well-defined bands, that correspond to rotational and vibrational transitions of the molecule. In particular, at near-IR wavelength, the vibrational transitions of the water vapour dominate the absorption of the atmosphere. Although the H and K-bands take advantage of two windows where the atmosphere is almost transparent, both bands are still affected by the atmospheric absorption, specially the K-band.

To characterise the transmission of the atmosphere, we use the imprint of the absorption bands on the spectrum of the standard stars. We extract an stacked spectrum from the star data cube, by integrating all the flux within a 3σ radius aperture, where σ is measured from a 2D Gaussian fit of a collapsed image of the star. This ensures that almost all the flux of the star is included in the spectrum.

The spectrum of the standard star is then normalised with a black body profile, calculated with the corresponding T_{eff} listed in the Tycho-2 Spectral Type Catalog (Wright et al., 2003), and scaled at the central wavelength of the spectroscopic band (1.675 μm and 2.175 μm for H and K bands, respectively). The presence of stellar absorption features in the spectra of the stars, in particular along the H-band, needs to be taken into account, to avoid artificial artefacts on the final processed data. These features, mainly lines from the Brackett series, are fitted independently using a Lorentzian profile, and added to the black body fit of the stellar continuum (see Fig. 2.5).

The resulting curve, after the normalisation of the spectrum, is the *efficiency* or *sensitivity curve* that accounts for the atmospheric transmission. We obtain one efficiency curve per standard star cube, that would be used to correct each science data cube on an spaxel-by-spaxel basis. Fig. 2.6 shows the median efficiency curves for the H and K bands, obtained by combining the whole set of curves for each band. Due to the variability of the atmospheric conditions, and the different airmasses of the observations, the uncertainties of the curves at the extremes of the bands are significant, and, in most of the cases, make these wavelength regions almost unsuitable for analysis purposes.

2.4.2. Absolute flux calibration

To find the conversion factor from counts to physical units, we performed synthetic photometry on the stacked spectra of the standard stars. We use the H- and K-band response curves of the 2MASS filters (Cohen et al., 2003) to obtain the total flux of the stars on each band, and compare the values with the H- and K-band magnitudes of the stars from the 2MASS catalogue (Skrutskie et al., 2006).

We obtain a flux conversion factor for each standard star cube. Figure 2.7 shows the distributions of the flux conversion factor for each band, where the average factors are $(1.91\pm0.08)\times10^{-17}$ and $(1.60\pm0.07)\times10^{-17}$ for H and K bands, respectively, in units of $[\mathrm{erg\,s^{-1}\,cm^{-2}\,\mu m^{-1}\,count^{-1}}]$.

In this way, each individual science data cube is divided by the sensitivity curve and multiplied by the conversion factor of the standard star which is closest to the observing time of the cube. Once all the cubes for a certain pointing are fully calibrated, they are combined by reconstructing the jittering pattern of the observations.

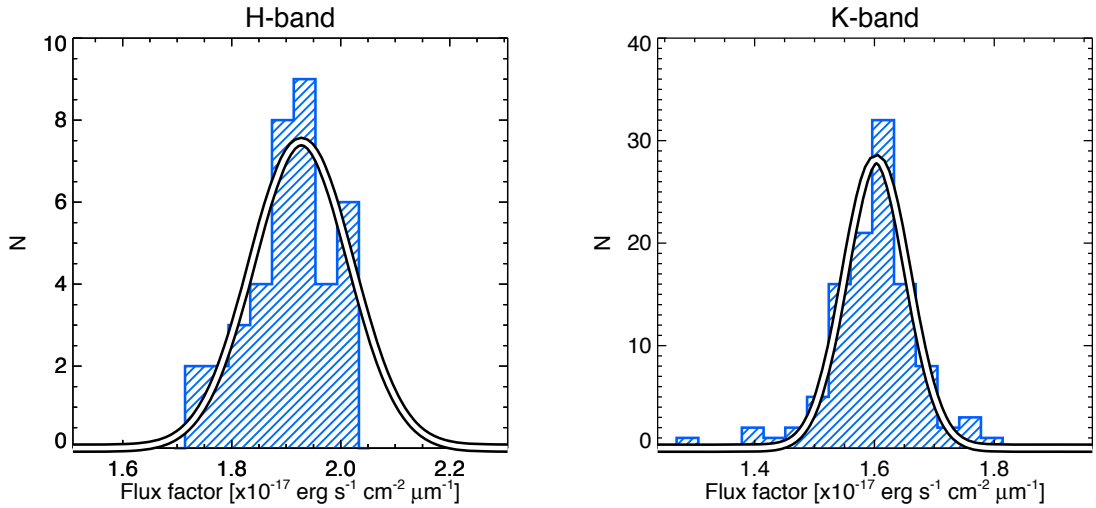

Figure 2.7: H- and K-band flux factor distributions - H- and K-band flux factor distributions obtained from the sample of standard stars.

2.5. Improving the data cubes: The La3D and background-match methods

Before reconstructing the final cubes, we perform additional tasks to the individual cubes, not included on the standard ESO pipeline, to improve the quality of the resulting cubes by reducing the noise on both spatial and spectral dimensions.

2.5.1. The 3D Laplacian Edge Detection method

The 3D Laplacian Edge Detection method (La3D) is a procedure kindly provided and developed by Richard Davies, that is a generalisation of the cosmic-ray rejection algorithm developed by Pieter G. van Dokkum (van Dokkum, 2001). This procedure detects and corrects bad pixels on the data cubes using a variation of a Laplacian edge detection method. This is widely used for edge detection in digital images, and allows to identify the bad pixels of the data cube and their surroundings by the sharpness of their edges.

In the Laplacian edge detection method, the image is convolved with the Laplacian of a 2D Gaussian function. In the convolved image, the location of the edges of the spatial defects is identified as the zero-crossings, and using different values of the Gaussian σ, it is possible to detect both sharp and smooth defects in the image.

Figure 2.8 shows an example of the results of applying the La3D method to a SINFONI data cube of NGC 3110. The top panels show the different steps of the procedure, from a

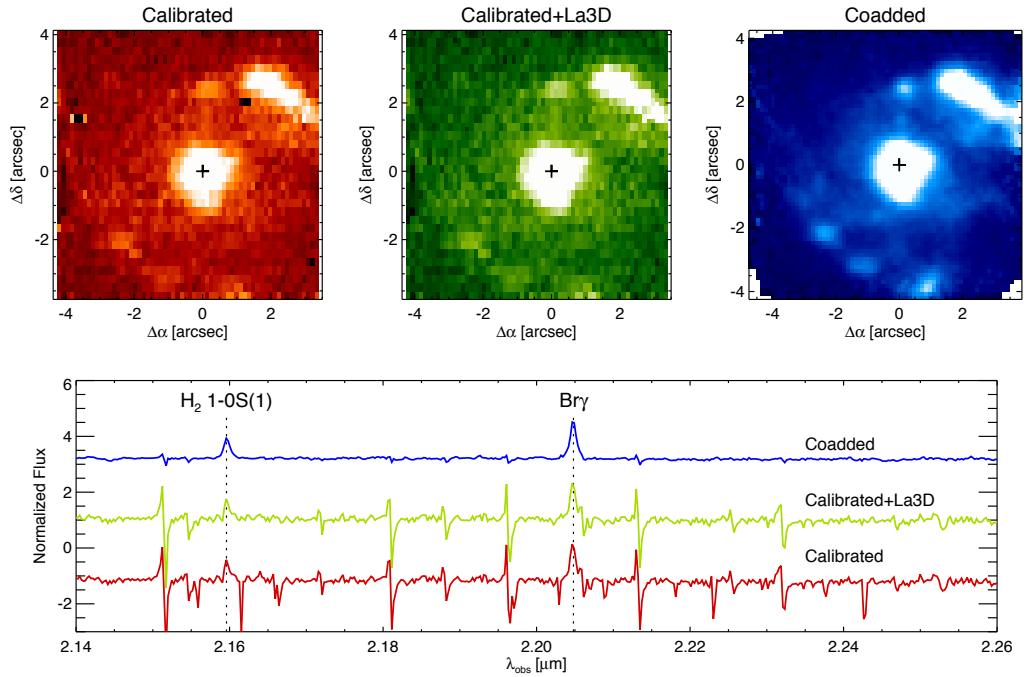

Figure 2.8: The 3D Laplacian Edge Detection method - Example of the 3D Laplacian Edge Detection method applied on a single cube of NGC3110. The top panels show, from left to right, a single wavelength plane (at $\sim$2.21 μm) of a calibrated cube before (red) and after (green) the La3D correction; and the same plane of the final coadded cube (blue) after the combination of all the corrected cubes. The bottom panel shows the spectra of each cube, extracted over a 10$\times$10 spaxel aperture, using the same colour code as in the top panels.

calibrated frame before and after the La3D correction to the coadded final cube, built from the individual, corrected cubes. The bottom panel shows the effect of the algorithm on the spectral dimension, using the same cubes than the top panels. In both cases, the spatial and spectral dimensions, the improvement of the data is clearly visible, with a significant decrease of spatial defects and sky line residuals.

2.5.2. The background-match method

Although the individual cubes are background-corrected from both, the thermal background and the atmospheric transmission (that also modifies the slope of the spectra), it is possible to find some scatter among the background levels of the set of cubes of a particular pointing. This scatter is translated into a higher dispersion of the flux on an spaxel-by-spaxel basis, and is clearly visible in some of the coadded cubes, and in the collapsed images in the form of dark and bright stripes along the FoV (see Fig. 2.9).

To minimise this scatter of the background level among the individual cubes, we developed

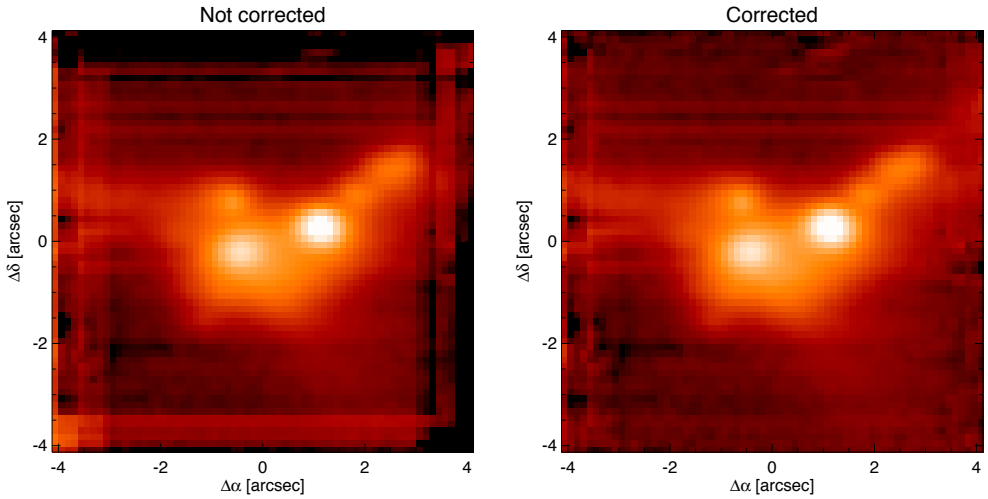

Figure 2.9: Background-match method results - Collapsed images of IRAS 22491-1808 from a coadded cube with no background-matching (left) and after applying the correction (right).

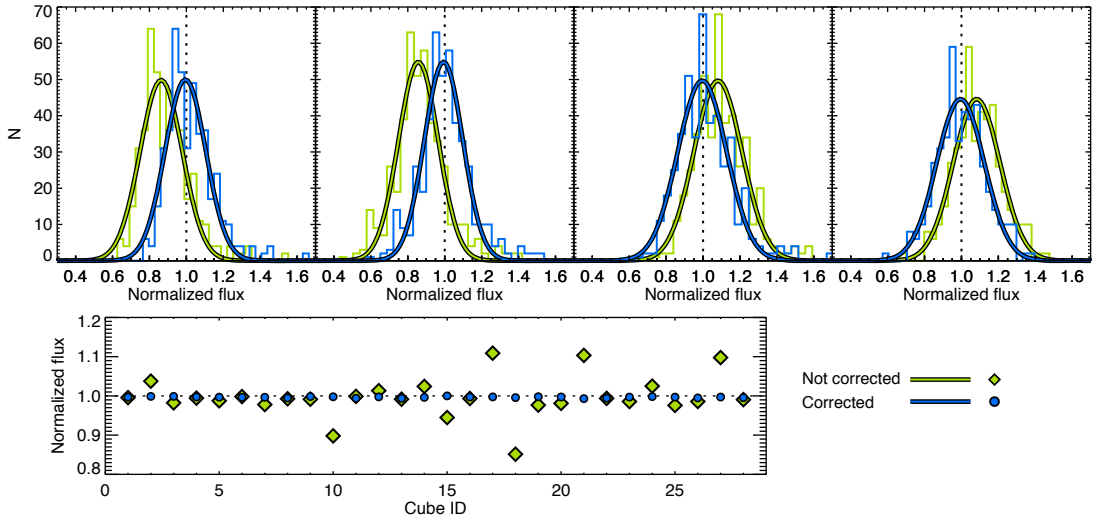

Figure 2.10: Background-match method - Example of the background-match correction. The top panels show the spaxel-by-spaxel flux distributions of the same common region on a single wavelength slice from four individual cubes of IRAS 22491-1808, before (green) and after the correction (blue). The bottom panel shows the median of the non-corrected (green diamonds) and corrected (blue circles) distributions of individual data cubes, normalised to the median of the whole set of cubes.

a routine that could be applied, not only before combining individual cubes to form a coadded one, but also when combining coadded cubes to build larger mosaics. The routine is a generalisation of a similar algorithm provided by Richard Davies, that evaluates the level of background of a set of cubes along the spectral dimension, and calculates the relative offsets among the cubes as a function of wavelength.

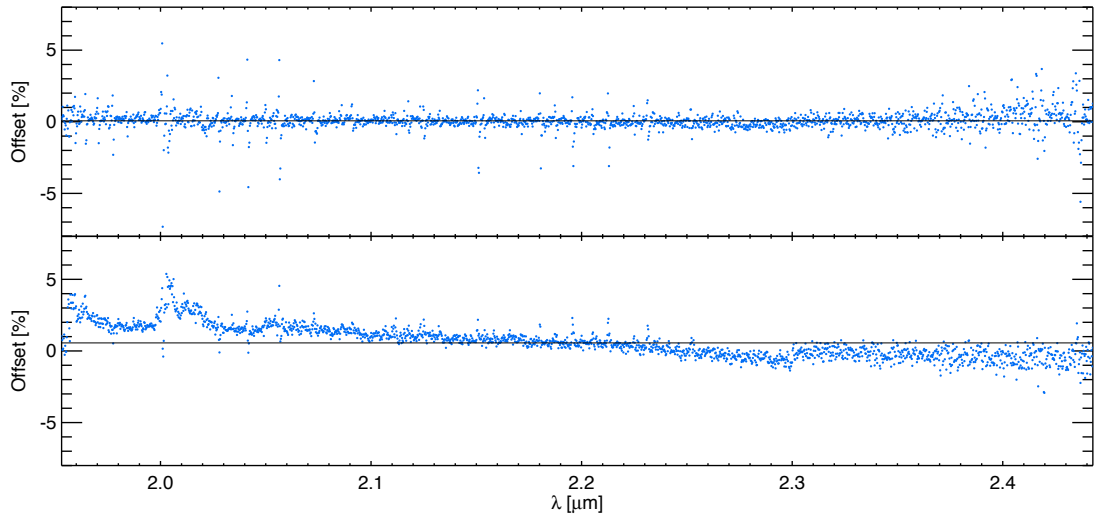

Figure 2.11: Examples of background-match method wavelength variability - Variation of the relative offsets from the background-match method with wavelength for two individual cubes of IRAS 22491-1808. The top panel shows a cube with no clear wavelength dependence of the offset, whereas the bottom panel shows a cube where the relative offsets have a strong dependence with wavelength, probably due to an inaccurate fit of the slope of the standard star spectrum.

The algorithm identifies the overlapping region of the set of cubes, and measures, in a particular wavelength slice, the spaxel-by-spaxel flux distribution of the region. It calculates the median of the flux distributions of all the cubes at this particular wavelength, and derives the relative offsets of each cube (see Fig. 2.10). This procedure is repeated at each wavelength slice, obtaining a set of relative offsets as a function of wavelength for each individual data cube.

Figure 2.11 shows the offsets of a couple of individual cubes of IRAS 22491-1808. Although in one of the cubes the relative offsets are almost constant and close to zero, one of the cubes shows a strong dependence with wavelength, that clearly indicates an inaccurate correction of the atmospheric transmission. This source of error is usually consequence of an inaccurate fit of the standard star continuum. As discussed in Sec. 2.4, the slope of the black body profile used to fit the stellar continuum is calculated by the T_{eff} of the star, obtained from the Tycho-2 Spectral Type Catalog. In those stars where the temperature is not well determined, the normalisation of the spectrum by the black body yields efficiency curves that are not flat, and might change the slope of the cube spectra.

This technique provides a correction for individual data cubes that is typically less than $\sim$5 % in most of the cases. However, we found that the method is particularly useful when combining coadded cubes to build a mosaic.

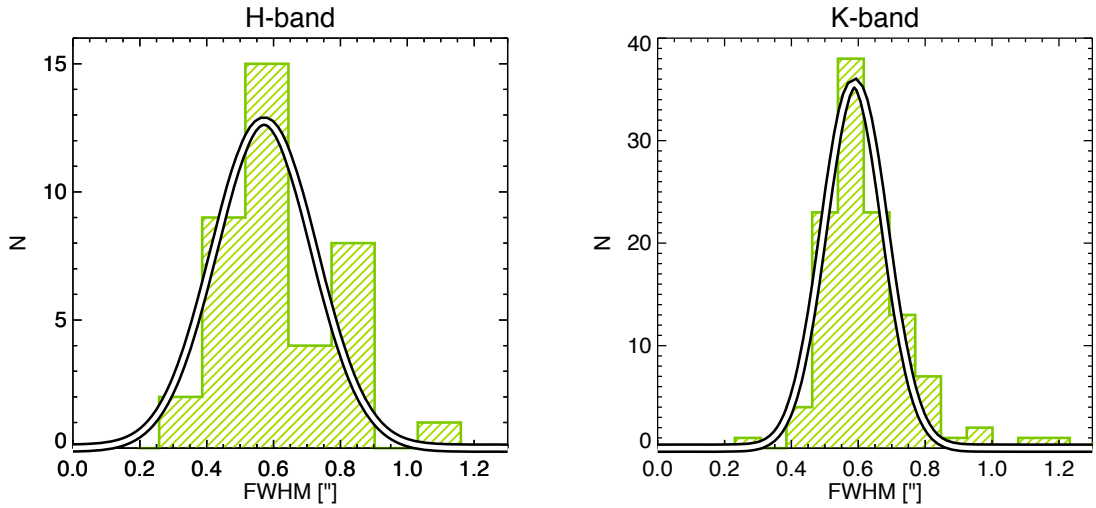

Figure 2.12: H- and K-band seeing distributions - H- and K-band seeing (FWHM) distributions obtained from the sample of spectrophotometric standard stars.

2.6. PSF estimation. Seeing-limited vs AO observations

The point spread function (PSF) of the seeing-limited observations could be easily measured using the standard star cubes. As mentioned in Sec. 2.4, during the flux calibration of the cubes, a collapsed image of each standard star is obtained. The image is then fitted using a 2D Gaussian profile, and the PSF radius is calculated as the quadratic mean of the widths of the Gaussian function, $\sigma_{x'}$ and $\sigma_{y'}$, where x' and y' are the canonical axes of the ellipse.

Figure 2.12 shows the distribution of the FWHM of the sets of standard stars, for H and K bands, respectively. The average values of the distributions are 0.61 ± 0.17 arcsec for the H-band and 0.63 ± 0.15 arcsec for the K-band, respectively.

An accurate measurement of the PSF for AO-assisted data is, nevertheless, not such straight forward, due to its temporal and spatial variability. Although the shape of the PSF could be estimated using reference stars, in a similar way as in seeing-limited observations, it could be misleading due to anisoplanaticism (i.e. shape of the PSF is not constant across the detector).

Although different methods have been proposed (Davies, 2008), here we discuss one method that consists on estimating the PSF by comparison with high resolution data. The main drawback of this method is clear, the availability of additional data at similar wavelengths and at higher spatial resolution. However, in the particular case of our AO data, M83 was

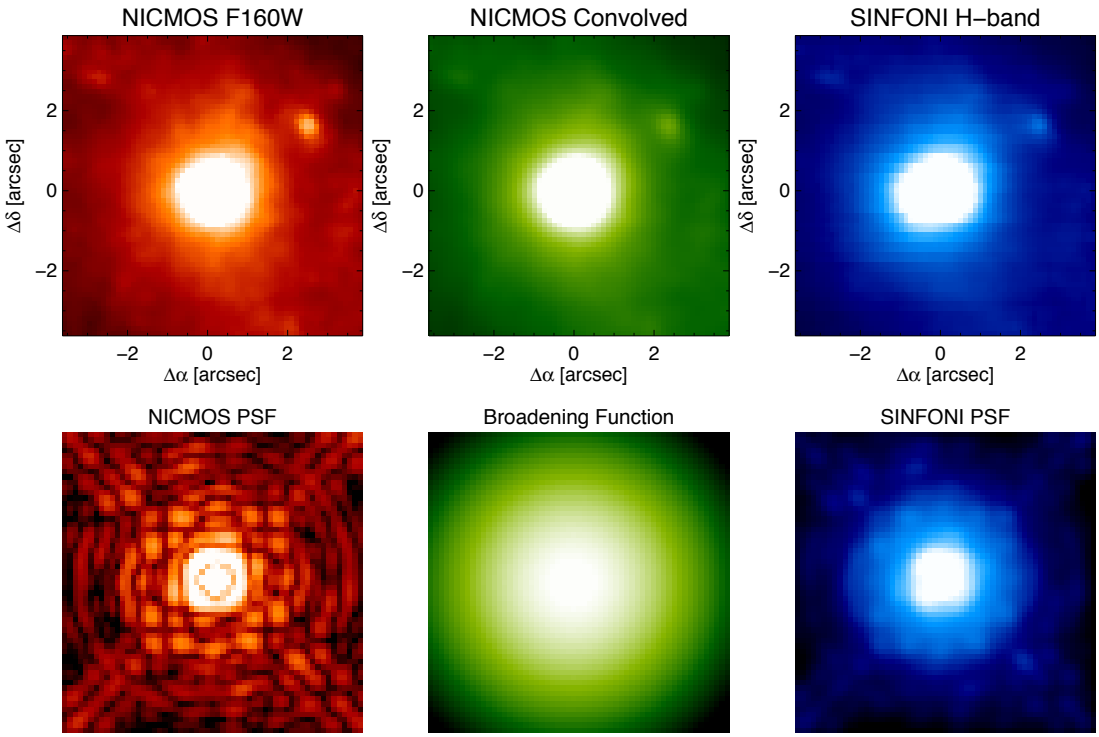

Figure 2.13: Estimation of the AO-SINFONI PSF using HST-NICMOS images - Top panels show the optical nucleus of M83 observed with NICMOS F160W filter (left), the same region after convolving the image with the broadening function B (centre) and the corresponding AO-SINFONI H-band image (right). Bottom panels show the NICMOS PSF (left), the broadening function B obtained from convolving the original NICMOS image to match the AO-SINFONI data (centre), and the SINFONI PSF that results from convolving the NICMOS PSF with B (right)

also observed using HST-NICMOS NIC2 camera, and the F160W and F222M filters. These setups achieve a slightly higher spatial resolution than our 100 mas SINFONI data, and have well defined, stable PSFs.

The aim of the procedure is to find a broadening function, B, that satisfies $I_{SINFONI} = I_{NICMOS} \otimes B$. The NICMOS PSF is well known, and can be easily modelled using the PSF simulator *Tiny Tim* (Krist et al., 2011). Using this model, we can estimate the SINFONI PSF as $PSF_{SINFONI} = PSF_{NICMOS} \otimes B$, where the resulting PSF is dominated by the broadening function. Fig. 2.13 shows the different steps of the process to calculate B for one of our M83 pointings, in the H-band. The top panels show the original NICMOS image of the optical nucleus of M83, together with the same region after being resampled to the SINFONI resolution and convolved with the broadening function. The resulting PSFs and B are shown on the bottom panels.

As discussed in Davies (2008), the correction provided by the AO is limited for extragalactic

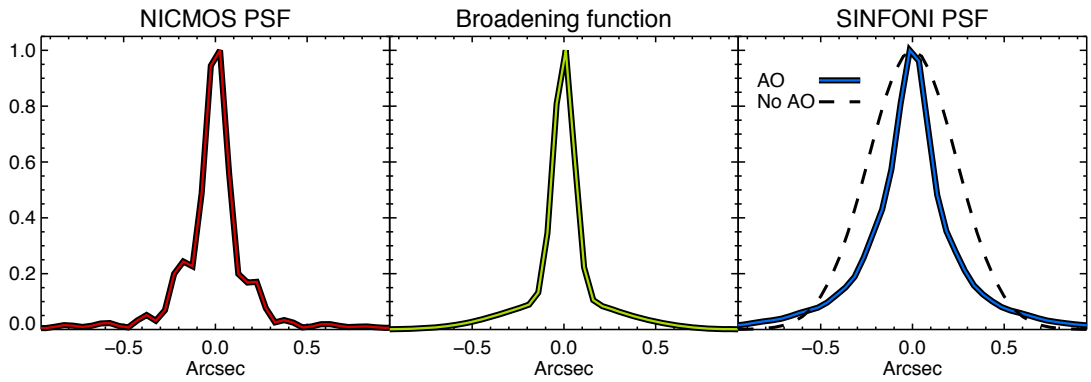

Figure 2.14: PSF profiles - Comparison among the NICMOS PSF profile (left), the broadening function B profile (centre), and the H-band SINFONI PSF profiles (right), where the blue line corresponds to the AO observations whereas the black line corresponds to the median PSF profile of the seeing-limited data.

sources, and a simple model of B is sufficient for a proper representation of the PSF. In this particular case, we use a symmetric double 2D Gaussian function to account for the core of the PSF, and for the wings of the seeing-limited halo. Fig. 2.14 shows the profiles of the NICMOS and SINFONI (AO and seeing-limited) PSFs, together with the B profile. The resulting broadening function is composed by a narrow component of $\sim$1 pixel FWHM and another wide but fainter component of $\sim$4–6 pixel FWHM.

2.7. The Voronoi binning

After the cubes are calibrated and coadded, and before extracting the kinematics and flux maps, the cubes/mosaics are binned to increase the average S/N across the FoV. We use the Voronoi binning, developed by Cappellari & Copin (2003), an adaptive spatial binning method that uses a Voronoi tessellation with a nearly hexagonal lattice.

The method follows a recursive approach to bin the data. Firstly, it generates an initial set of bins that satisfies certain topological and morphological general criteria, e.g. there have to be no holes or bin overlapping, the bins have to be as round as possible to maximise the spatial resolution, and the S/N scatter has to be minimal but not at expenses of an extreme degradation of the spatial resolution. Secondly, the algorithm tries to improve the binning of the previous stage, according to the previous criteria of optimal binning.

The binning method employs bins of approximate circular shape to divide the space, described in terms of a set of points called *generators*. The algorithm starts from the spaxel with the highest S/N and keeps accreting its closest spaxels until the target S/N threshold is reached. Thus, in those regions where the S/N is higher than the threshold, bins are reduced

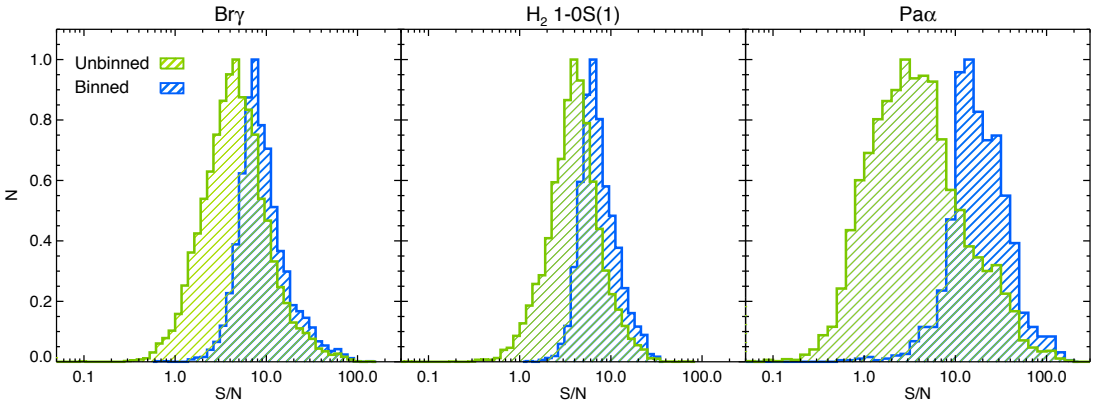

Figure 2.15: Voronoi binning - S/N spaxel-by-spaxel (green) and bin-by-bin (blue) normalised distributions of the IC 5179 Brγ (left) and H_2 1-0S(1) (centre) maps, and the IRAS 14348-1447 Paα map (right).

to individual spaxels. The process continues on an spaxel-by-spaxel basis, until the whole frame has been processed. Finally, the method computes the centroids of all good bins, that are then used as generators for the Voronoi tessellation.

Figure 2.15 shows the S/N distributions of three example maps, before and after the binning process. Although in all cases the improvement of the average S/N is clear, it is specially significant on the Paα map of IRAS 14348-1447, where there is a larger number of spaxels with low surface brightness. However, since the optimal binning criteria have to be satisfied, some bins might not reach the desired S/N threshold.

Although most of the applications of the Voronoi binning use a S/N criterium, it is also possible to bin the data according to other quantity of interest. For example, the data could be binned according to the error of the measured flux, or use more sophisticate quantities as the error in some extracted parameter like kinematics.

3

Spatially resolved kinematics of the central regions of M83

Hidden mass signatures and the role of supernovae

"There is nothing like looking, if you want to find something. You certainly usually find something, if you look, but it is not always quite the something you were after."

— J.R.R. Tolkien, *The Hobbit*

The barred grand-design spiral M83 (NGC 5236) is one of the most studied galaxies given its proximity, orientation, and particular complexity. Nonetheless, many aspects of the central regions remain controversial conveying our limited understanding of the inner gas and stellar kinematics, and ultimately of the nucleus evolution.

In this Chapter, we present AO VLT-SINFONI data of its central $\sim 235 \times 140$ pc with an unprecedented spatial resolution of $\sim$0.2 arcsec, corresponding to $\sim$4 pc. We have focused our study on the distribution and kinematics of the stars and the ionised and molecular gas by studying in detail the Paα and Brγ emission, the H_2 1-0S(1) line at 2.122 μm and the [FeII] line at 1.644 μm, together with the CO absorption bands at 2.293 μm and 2.323 μm. Our results reveal a complex situation where the gas and stellar kinematics are totally unrelated. Supernova explosions play an important role in shaping the gas kinematics, dominated by shocks and inflows at scales of tens of parsecs that make them unsuitable to derive general dynamical properties.

We propose that the location of the nucleus of M83 is unlikely to be related to the off-centre 'optical nucleus'. The study of the stellar kinematics reveals that the optical

nucleus is a gravitationally bound massive star cluster with $M_{dyn} = (1.1 \pm 0.4) \times 10^7\,M_\odot$, formed by a past starburst. The kinematic and photometric analysis of the cluster yield that the stellar content of the cluster is well described by an intermediate age population of $\log T(yr) = 8.0 \pm 0.4$, with a mass of $M^\star \simeq (7.8 \pm 2.4) \times 10^6\,M_\odot$.

3.1. Introduction

M83 (NGC 5236) is a nearby (D = 4.6 Mpc, 22 pc arcsec^{-1}, $z = 0.0017$ from the NASA/IPAC Extragalactic Database, NED) barred grand-design spiral galaxy with a nuclear starburst. The galaxy has been object of intense study during the last decade, given the complexity of its central regions, its proximity and the fact that it is almost face-on, with an inclination of $i = 24^\circ$ (Comte, 1981). This makes it a good candidate on which to make use of high spatial resolution IFS to study the controversial aspects of its innermost regions.

The general morphology of the galaxy shows a pronounced bar and well-defined spiral arms where star formation is intense. On the other hand, the central regions of M83 in the infrared are rather complex. The J–K images of the inner region show two non-concentric circumnuclear dust rings, which are associated with two inner Lindblad resonances (Elmegreen et al., 1998). These two rings are connected by an inner bar, almost perpendicular to the main stellar bar. The general shape of the extended emission traces an arc between these two dust rings, where the star formation is concentrated.

The location of the nucleus of M83 remains unclear. Thatte et al. (2000) first reported the existence of a 3.4 arcsec ($\sim$ 75 pc) offset between the optical nucleus and the centre of symmetry of the bulge K-band isophotes. The centre of symmetry of these external isophotes is coincident with the dynamical centre proposed by Sakamoto et al. (2004), based on two-dimensional CO spectroscopy, and confirmed later by Rodrigues et al. (2009) and Knapen et al. (2010). Different locations of hidden mass concentrations were proposed to host the supermassive black hole of M83, mainly based on studies of the gas kinematics (Mast et al. 2006, Díaz et al. 2006, Rodrigues et al. 2009 and Knapen et al. 2010).

In this paper, we present new integral field VLT-SINFONI spectroscopy in H+K bands, with an unprecedented spatial resolution, covering the central $\sim 235 \times 140$ pc of the galaxy. We study the stellar and gas kinematics of the inner parts and address some of the open questions regarding the hidden mass concentrations at off-nuclear locations (Thatte et al. 2000, Mast et al. 2006, Díaz et al. 2006) and the origin of the steep velocity gradients in the

gas kinematics (Rodrigues et al., 2009), revealing a complex scenario where supernovae play a key role in the kinematics.

3.2. Observations

3.2.1. Observations and Data Reduction

The M83 observations are divided into four different pointings, labeled as A, B, C and D in Fig. 3.1. These pointings were chosen to cover the stellar nucleus of the galaxy, that is identified with the optical nucleus of M83, covered by pointing A; the centre of symmetry of the bulge K-band isophotes (Thatte et al., 2000), that corresponds to pointing B; the proposed location of a hidden mass by Mast et al. (2006), by pointing C; and the putative massive black hole location given in Díaz et al. (2006) sampled by pointing D. The first three, A, B and C, were carried out between April and June 2009 in service mode, using the AO module fed by a LGS. The fourth was performed in July 2011, also in service mode. The data were taken in the H+K configuration, using a scale plate of 0.05×0.1 arcsec pixel^{-1} that yields a nominal field of view (FoV) of $\sim$3.2" $\times$ 3.2" then enlarged by dithering. The wavelength range covered is from 1.45 μm to 2.46 μm with a spectral resolution of R$\sim$1500.

Although a total of four pointings were programmed, the main analysis in this work has been performed on three of them, A, B and C. The observations for pointing D could not be completed and there was only 1 usable object frame. Taking into account the vast difference of quality in the data, we decided not to include the new data in the main analysis, but use it instead to support some of the results. The first three pointings cover an area of $\sim$8"$\times$6" around the nucleus of the galaxy, while the fourth pointing covers $\sim$ 3" $\times$ 3". The footprints of the observed pointings are shown in Fig. 3.1. The total integration time was 3300 s for pointing A and 3600 s for each of pointings B and C, split into individual exposures of 300 s. In addition, four sky frames of 300 s were taken for every pointing every two on-source exposures to subtract the sky emission, following the pattern OOSOOSOO. In the same way, a total of five standard stars (Hip066957, Hip069230, Hip070506, Hip071136 and Hip098641) were observed in order to perform telluric and flux calibration. The fourth pointing is a single on-source exposure of 300 s with a matching sky frame. The standard star used for the calibration was Hip001115.

The reduction of the data was performed using the standard ESO pipeline. An individual cube was built from each frame, from which the background sky emission was subtracted

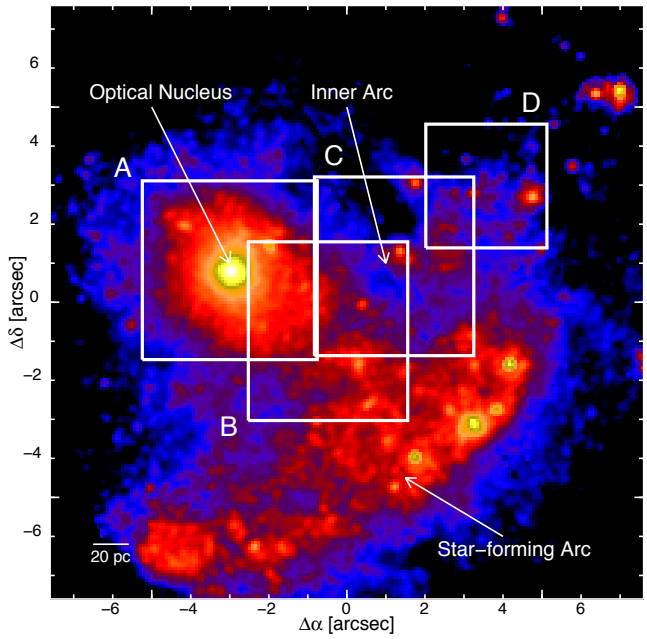

Figure 3.1: Central region of M83 - HST NICMOS F222M image with the fields covered by the four SINFONI pointings superimposed. The location of the optical nucleus and the arc of star formation mentioned in the text are also shown. Although the inner arc is not visible in the continuum map, it is clearly visible in the western part of the FoV in the flux panels in Fig. 3.4. The total coverage of our SINFONI observations is $\sim 235 \times 140$ pc.

using the method outlined in Davies (2007). We performed the telluric and flux calibration on each cube individually to improve the results. Taking into account the relative shifts of the jitter pattern, we then combined the data to create a single cube for each pointing. Finally, these were combined to build a single mosaic.

The telluric and flux calibration were performed in two steps. First, each individual star was normalised to the continuum level, using a blackbody profile at the T_{eff} listed in the Tycho-2 Spectral Type Catalog (Wright et al., 2003). To remove the absorption features in the spectra of the stars, we used a solar template, convolved and binned to match the resolution of the SINFONI data. The result is a 'sensitivity function' that takes into account the atmospheric transmission. Secondly, we used the H and K magnitudes of the stars from the 2MASS catalog (Skrutskie et al., 2006) to convert our spectra from counts to physical units. We made use of the response curves of 2MASS filters, as defined in Cohen et al. (2003), to obtain the values in counts of our spectra at their effective wavelengths. Using the above mentioned magnitudes, we obtained two conversion factors for each star (one for H-band and one for K-band). These factors were almost identical for both bands in every star, which verifies the calibration. We adopted the mean value to scale our curves. The flux-calibrated

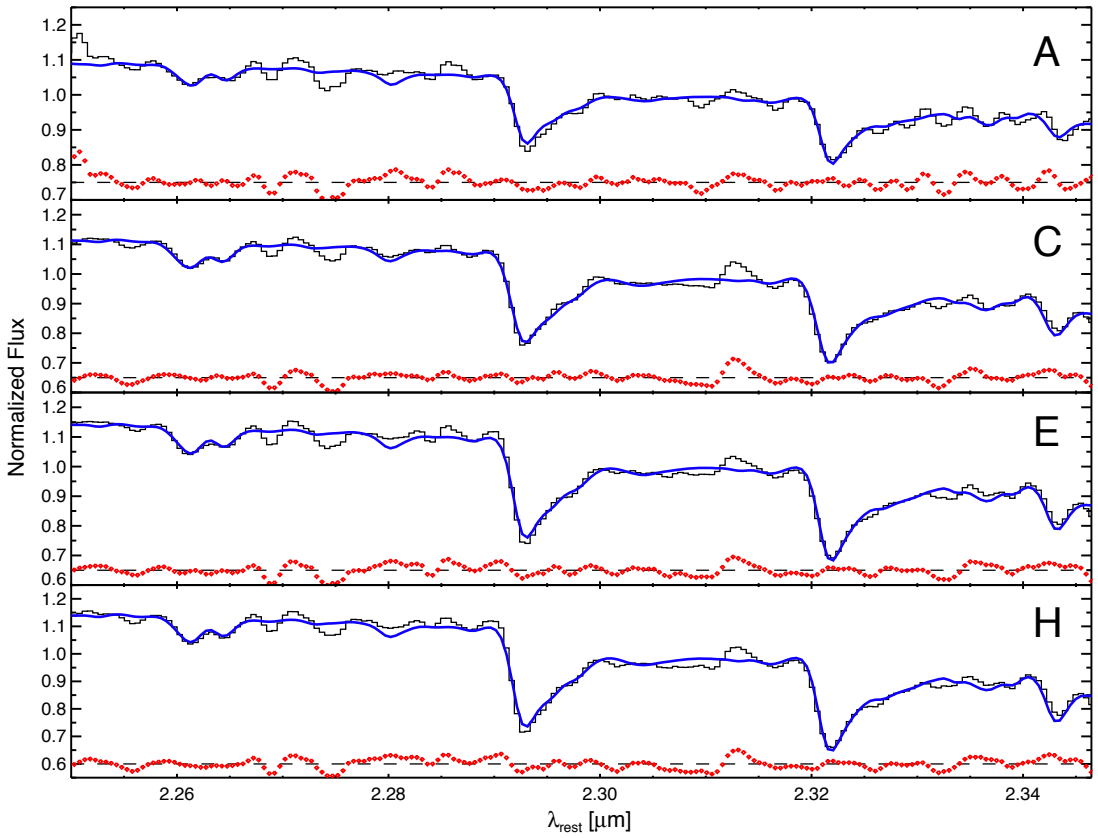

Figure 3.2: Fitting of the stellar CO bands - Integrated spectra of apertures A, C, E and H, represented in Fig. 3.4) and the result from fitting template spectra to the stellar absorption features. The normalised spectra are shown in black, and the results from the fitting are plotted as a thick blue line. The red dotted lines show the residuals from subtracting the fit.

cubes were obtained by dividing the individual cubes by the 'sensitivity function', to correct from the atmospheric transmission, and by multiplying them by the conversion factor.

3.2.2. Gas and Stellar Kinematics

The gas kinematics were extracted by fitting a gaussian profile to the most relevant emission lines, using the code *LINEFIT* described in Davies et al. (2011) (see also Förster Schreiber et al. 2009). During the extraction, the OH sky line at 2.18 μm is used to remove the instrumental broadening, measured to be 13 Å FWHM.

To extract the stellar kinematics, we focused on the two most prominent CO bands, CO (2 – 0) at 2.293 μm and CO (3 – 1) at 2.323 μm, and used the Penalized Pixel-Fitting (pPXF) software developed by Cappellari & Emsellem (2004) to fit a library of stellar templates to our data (see Fig. 3.2). We made use of the near-IR library of spectral templates from Winge et al.

(2009), which covers the wavelength range of 2.15 μm – 2.43μm with a spectral resolution of $R \sim 5600$ and sampled at 1 Å pixel^{-1}. The library contains a total of 23 late-type stars, from F7III to M3III, and was previously convolved to our SINFONI resolution.

The uncertainty in the gas and stellar kinematics is highly dependant on the S/N and how well resolved the line is. For the gas kinematics, the uncertainties could range from $\sim 1\%$ of the resolution element in those regions with high S/N up to more than $\sim$10% in the regions with poorer S/N. The kinematic precision achievable with the stellar absorption features also depends on the S/N, although it is typically lower than the precision in the gas kinematics mainly due to uncertainties in the template matching uncertainties. As shown in Fig. 3.2, the quality of the template fitting indicates that the precision we achieved in the stellar kinematics is high, less than $\sim$40 km s^{-1} in those regions with high S/N, and that offsets of $\gtrsim$30 km s^{-1} would be clearly visible in the residuals of the fitting.

In order to compare the velocity fields of the different phases of the gas and the stellar component, we have established a reference value of $cz = 589.6$ km s^{-1} for the velocity that has been used as a zero-point for the velocity maps. This reference value for the velocity has been chosen as the mean value of the stellar velocity in a small aperture of 5 spaxel radius centred in the dynamical centre of the galaxy proposed by Sakamoto et al. (2004).

3.2.3. Voronoi Binning

Before the extraction of the kinematics, the data were binned to achieve a minimum value of S/N on the whole field. We used the Voronoi binning method implemented by Cappellari & Copin (2003) to maintain the maximum spatial resolution of our maps while constraining the minimum S/N ratio.

The Voronoi tessellation employs bins of approximate circular shape to divide the space, described in terms of a set of points called *generators*. Every bin encloses all the points that are closer to its generator than any other generator. The algorithm finds an initial set of generators by selecting the spaxel with highest S/N ratio and accreting spaxels to that bin, until the required threshold is reached. Then, it moves downwards to lower S/N spaxels until all the points are assigned to a proper bin. This set of generators is then refined to satisfy both topological and morphological criteria and to ensure that the scatter of the S/N among all the bins is reduced to a minimum (see Cappellari & Copin 2003 for further details).

This binning of the data does not affect those spaxels with high S/N ratio, preserving the original spatial resolution of these regions. The maps obtained for each line and the continuum

Feature	S/N
Paα	50
Brγ	45
H_2 1-0S(1)	15
[FeII]	25
Stellar	50

Table 3.1: S/N thresholds used for the Voronoi binning

are then binned independently, since their flux distributions are totally different. We have therefore defined different S/N thresholds for each line, in order to obtain appropriately sampled maps. The S/N cutoff used for each line and for the stellar continuum are shown in Table 4.3. We selected these values to achieve roughly the same number of bins in each map.

3.2.4. PSF Determination

The measurement of the PSF has been done by comparing the SINFONI data to higher resolution HST NICMOS data. As discussed in Davies (2008), we can use a higher resolution image with a well known PSF to estimate the PSF of a lower resolution image. After resampling the NICMOS image to our SINFONI pixel scale, the aim is to find a broadening function, B, that satisfies $\mathrm{I_{SINFONI}} = \mathrm{I_{NICMOS}} \otimes \mathrm{B}$. Since the NICMOS PSF is well known, we can estimate the SINFONI PSF as $\mathrm{PSF_{SINFONI}} = \mathrm{PSF_{NICMOS}} \otimes \mathrm{B}$. The shape of the resulting PSF is dominated by the broadening function.

We performed independent fittings of the broadening function for each pointing and each band. The NICMOS images were obtained with the NIC2 camera, using the F160W and F222M filters for H and K band respectively, with a pixel scale of 0.075 arcsec pixel^{-1}. After trying different models for the broadening function B, we find that it is better described as a symmetric double Gaussian with a narrow component of $\sim$1 pixel FWHM and another wide but fainter component of $\sim$4–6 pixel FWHM that takes into account the seeing-limited halo. The different values of the FWHM of the resulting PSF are shown in Table 3.2.

We note that the resolution of our data is limited by the pixel scale chosen for the observations rather than the LGS-AO performance since, in order to cover a wider FoV ($\sim$3 arcsec), we chose the $0\farcs05 \times 0\farcs1$ pixel scale from the three configurations available for SINFONI.

Pointing	H Band			K Band		
	FWHM (pixel)	FWHM (")	FWHM (pc)	FWHM (pixel)	FWHM (")	FWHM (pc)
A	3.66	0.18	4.03	4.05	0.20	4.45
B	3.76	0.19	4.14	4.18	0.21	4.60
C	2.95	0.15	3.24	4.09	0.20	4.50

Table 3.2: FWHM of the PSF for each pointing. The values are measured after convolving the broadening function, B, obtaining from the fitting with the PSF of NICMOS images.

3.3. Overview of Data

The inner $\sim$190 $\times$ 130 pc of M83 are covered by pointing A centred on the optical nucleus of the galaxy, pointing B on the photometric centre, and pointing C on the off-nuclear black hole location proposed by Mast et al. (2006).

The wide spectral coverage of the H+K band configuration of SINFONI allows us to study in detail a large number of emission lines and stellar absorption features (see Fig. 3.3). In order to achieve a good level of S/N in the whole FoV, we focussed our study of the gas kinematics on the brightest emission lines, i.e. Brγ 2.166 μm for the ionised gas, the roto-vibrational transition H_2 1-0S(1) at 2.122 μm for the warm molecular gas and the [FeII] line at 1.644 μm. We have extracted surface brightness, velocity dispersion and velocity maps of these three lines, represented in Fig. 3.4, that allow us to study different phases of the interstellar medium.

Although the Paα line is the brightest in the wavelength range covering the H and K bands, it lies at a wavelength where the atmospheric transmission is very low. Here, the strong variability of the sky absorption makes it very difficult to perform a good correction of the transmission, which translates into an increase of the noise compromising the results of the kinematics extraction. However, given the brightness of the Paα line, we were able to obtain a map of the emission that can be compared with HST/NICMOS archive images of the same region.

As noted above, we make use of the H_2 1-0S(1) line to trace the warm molecular gas in the whole FoV. However, the detection of additional H_2 transitions allows us to study in more detail, in Sec. 3.4, the excitation mechanisms of the H_2 in the inner regions of M83, and distinguish collisional excitation in shocks from radiative fluorescence. To improve the S/N ratio of the weaker transitions, we have integrated the signal of all the spaxels from the

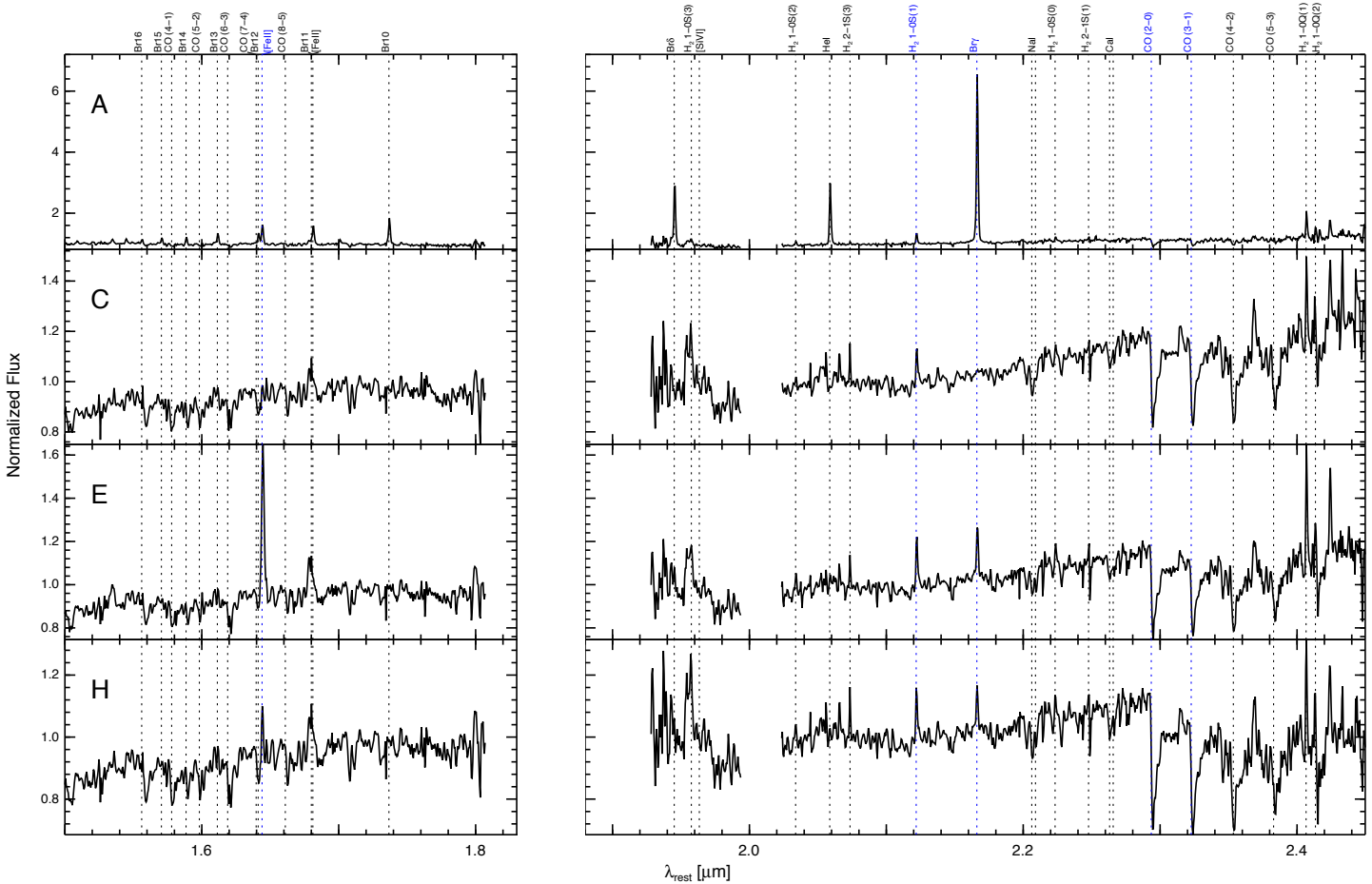

Figure 3.3: Normalised H+K spectra of selected apertures - Normalised H+K spectra of the apertures A, C, E and H (see Fig. 3.4 for reference). Aperture A is located at the maximum of the Brγ emission, aperture C covers the centre of the optical nucleus, aperture E corresponds to one of the bright spots of [FeII] emission next to the optical nucleus and aperture H is located at the position of one of the SNR listed in Dopita et al. (2010). The wavelengths of a number of lines and features are identified, and those studied in this paper are identified in blue. These spectra clearly illustrate the wide variety of excitation conditions that are occurring in the inner regions of M83.

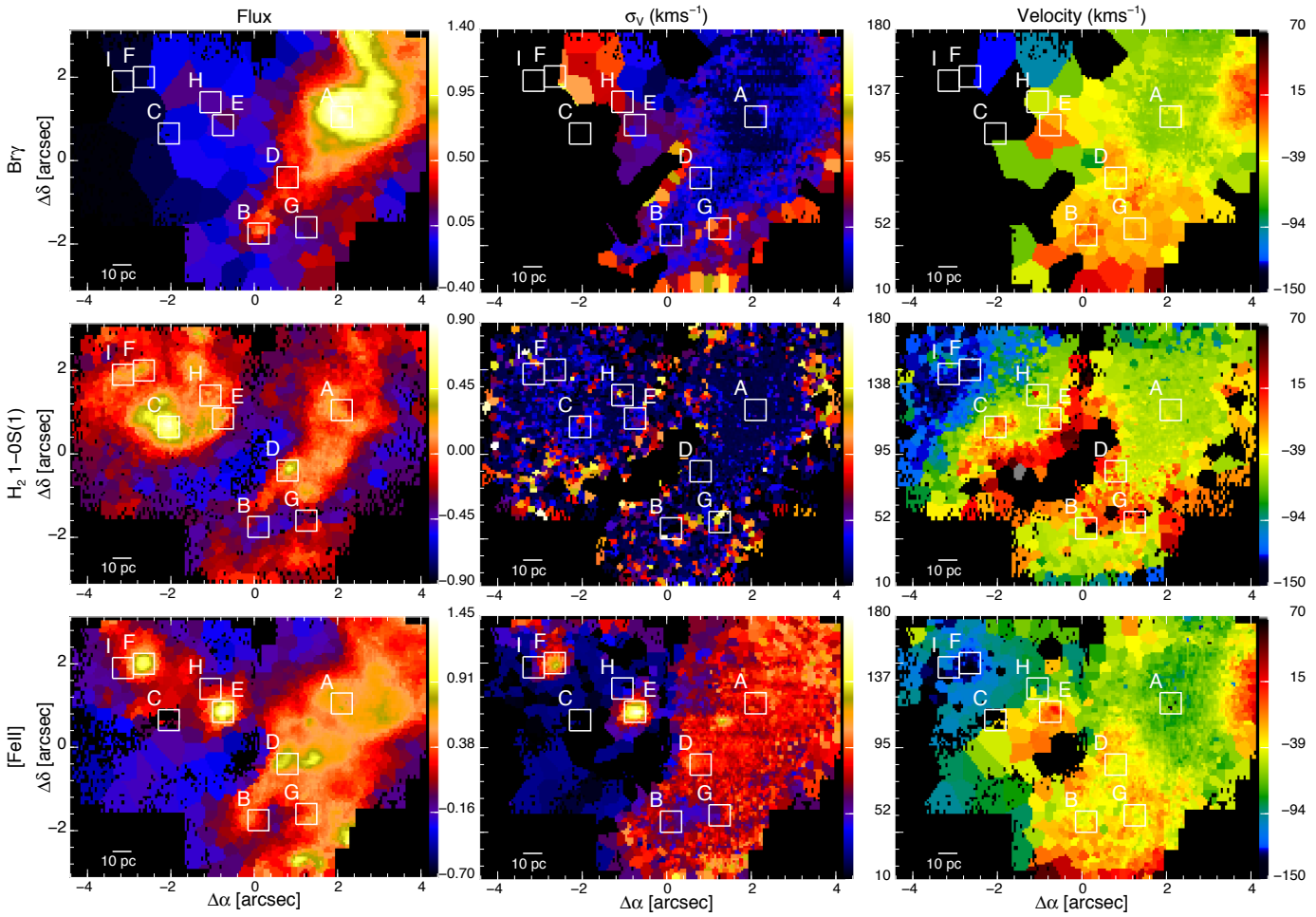

Figure 3.4: M83 flux and kinematics maps - Flux and kinematics maps of the main emission lines. From top to bottom, the Brγ , H_2 1-0S(1) and [FeII] maps, and from left to right, flux, velocity dispersion and velocity field. The boxes indicate the apertures used to extract spectra, some of which are shown in Fig. 3.3. These also act as reference points with respect to the discussion in the text. Flux maps are scaled with a factor 3×10^{-18} erg s^{-1} cm^{-2}.

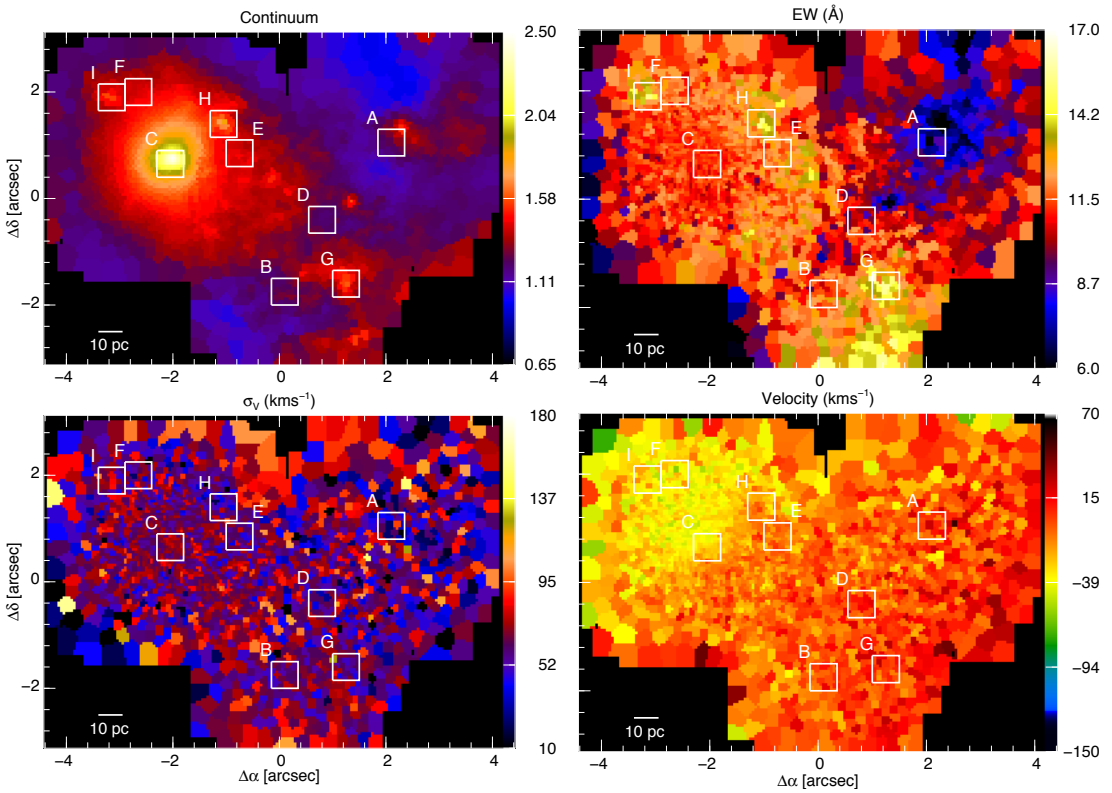

Figure 3.5: M83 stellar maps - Maps of the stellar continuum flux (top left), equivalent width (top right), velocity dispersion (bottom left) and velocity field (bottom right) for the nuclear region of M83. These were obtained by fitting the first two CO absorption bands, CO (2 – 0) at 2.293 μm and CO (3 – 1) at 2.323 μm. The boxes indicate the same apertures as in Fig. 3.4. Flux map is scaled with a factor 3×10^{-18} erg s^{-1} cm^{-2}.

inner star-forming arc (those above a certain flux level) and those from the optical nucleus (see Fig. 3.1). This allows us to measure the fluxes of six different transitions with good level of confidence. The different lines measured are listed in Table 3.3.

In addition to the numerous emission lines available, we detect a variety of stellar features in our spectra, most notably the NaI, CaI and CO absorption bands. As mentioned previously, we have focussed on the first two CO bands, CO (2 – 0) at 2.293 μm and CO (3 – 1) at 2.323 μm to study the stellar kinematics (Fig. 3.5).

3.3.1. Morphology and Kinematics of the Gas

As shown in Fig. 3.4, the morphology and, to some extent, the kinematics of the distinct phases of the gas are rather different. The Brγ emission is mainly associated with the inner star-forming arc towards the west side of the FoV. The global velocity gradient of $\sim$60 kms^{-1} from northwest to southeast is consistent with an inflow of gas along the spiral arms and

through the inner bar (Elmegreen et al. 1998, Crosthwaite et al. 2002, Fathi et al. 2008) to the photometric centre of the galaxy. Superimposed on this, there is a ring that is on and around aperture A in Fig. 3.4. One of the most remarkable properties of this ring-like feature is that it shows no velocity gradient and has a low velocity dispersion that, together, argue against it being a dynamical structure. We discuss this feature in detail in Sec. 3.5.

The H_2 emission is mainly associated with the inner arc along the western part of the FoV and with the optical nucleus. The kinematics are very similar to those exhibited by the ionised gas. Around region A in Fig. 3.4, the velocity is the same as that of the Brγ emission, where no dominant velocity gradient is observed. Moreover, the emission of the molecular gas resembles the observed ring-like feature of the ionised gas. However, the strong emission of the optical nucleus allowed us to trace the velocity field across this region in more detail. The velocity gradient measured from northeast to southwest is $\sim$200 km s^{-1} in $\sim$45 pc, significantly steeper than the gradient measured from the stellar kinematics (see Fig.3.5). The velocity dispersion shows a similar picture as the Brγ emission, where the low values measured along the inner arc suggest that the gas is confined to a thin plane, presumably a disk supported by rotation.

The [FeII] emission is highly extended along the inner arc, showing various knots of strong emission. Two of the brightest spots are located in the outskirts of the optical nucleus, labeled as E and F in Fig. 3.4, at radial distances of $\sim$ 30 pc and $\sim$ 32 pc respectively. These two knots also exhibit a high velocity dispersion ($\sim$ 150 km s^{-1} in region E and $\sim$ 115 km s^{-1} in region F, both taking into account the spatial resolution of our data) and are probably tracing individual supernovae. We return to this issue in Sec. 3.5. Although the velocity field of the [FeII] is very similar to those traced by the Brγ and H_2 emission, the velocity dispersion is systematically higher along the inner star-forming arc. As we discuss in Sec. 3.5, this higher velocity dispersion may be a sign of recent supernovae explosions, and would set a constraint on the age of the stellar populations along the arc.

3.3.2. Stellar Component

The stellar continuum derived from the first two CO absorption bandheads is mainly concentrated in the optical nucleus and, unsurprisingly, shows a similar morphology to that of the K-band image. On the other hand, the stellar kinematics show a completely different picture to that traced by the gas. Whereas the gas kinematics appear to be completely dominated by shocks and outflows at small scales, the stars show a smooth velocity gradient

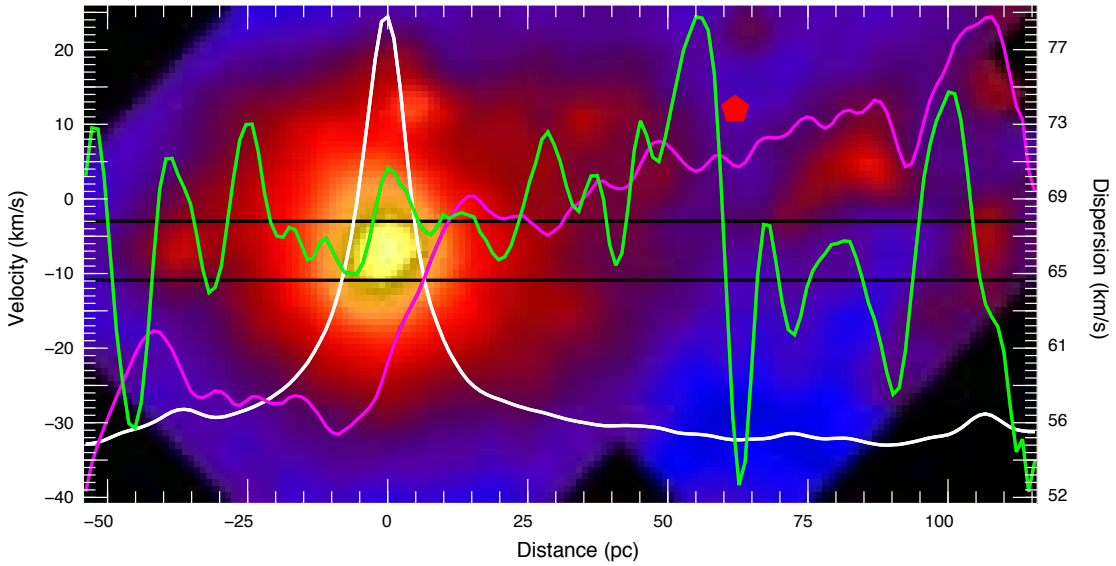

Figure 3.6: Optical Nucleus stellar profiles - Flux (white), velocity dispersion (green) and velocity (magenta) profiles of the stellar component along a pseudo-slit traced to include the optical nucleus along the direction of maximum variation of the velocity field. The location of the photometric centre of Thatte et al. (2000) is marked as a red dot. The pseudo-slit is plotted in black over the stellar continuum map for reference.

from northeast to southwest, typical of a rotating disk. Superimposed on this, the stellar continuum emission from the optical nucleus is dominated by a coherent internal rotation, as highlighted in Fig. 3.6. The amplitude of the projected velocity field, measured peak to peak, is $\sim 32\,\mathrm{km\,s^{-1}}$ within $\sim 24\,\mathrm{pc}$. The de-projected rotation velocities for an adopted inclination of $i = 24^{\circ}$ would be a factor 2.5 higher. Although the uncertainties in the stellar kinematics are comparable to this value (in an spaxel basis), Fig. 3.6 shows a very clear jump in the projected velocity (magenta line) across the optical nucleus.

As shown in Fig. 3.5, we detect two bright spots of continuum emission (apertures H and I) in the outskirts of the optical nucleus, with a substantially high equivalent width. Given the spatial resolution of our data, these bright sources in the stellar continuum could be identified as individual stars – late type giants or supergiants – in a post main sequence phase. This is consistent with the main scenario proposed for the optical nucleus, discussed in Sec. 3.6, where the UV photons of a population of non-ionising stars would excite the molecular gas, explaining the overpopulation of the $J_l = 3$ levels shown in Fig. 3.8. Such a population of stars would be consistent with the age of the cluster derived from the CO absorption bands, as discussed in Sec.3.6.

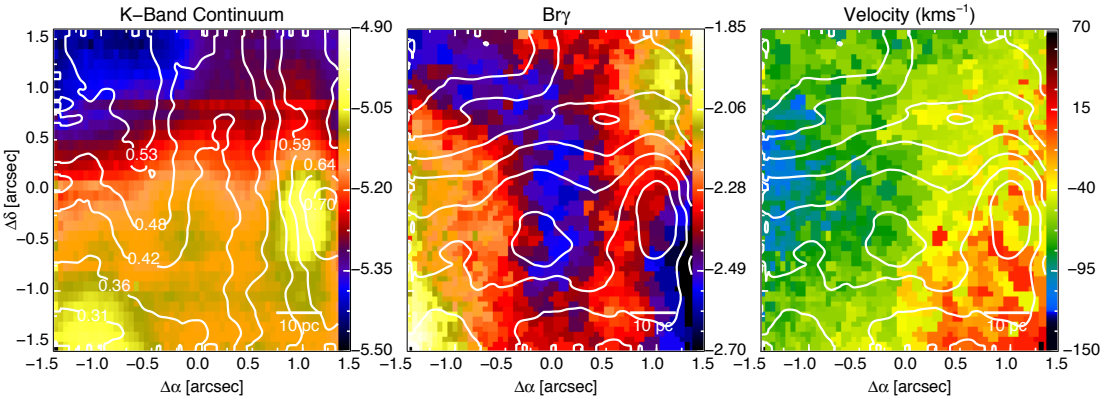

Figure 3.7: M83 maps of pointing D - Maps of the K-band continuum emission (left), Brγ surface brightness (centre) and velocity (right) from SINFONI data at pointing D. The white contours in the left panel correspond to the H-K colour obtained from the SINFONI data; the contours in the centre and right panels show the K-band continuum emission. The values of the Brγ velocity are in the same colour scale as those shown in Fig. 3.4 for the other three pointings.

3.3.3. Pointing D

Because of the different integration time for the SINFONI data from pointing D, we have not included them in the general analysis of the emission and kinematics of the nuclear regions of M83. However, we can draw some conclusions about the hidden mass location proposed by Díaz et al. (2006). As shown in Fig. 3.7, we have extracted a K-band continuum image, H–K colour map and Brγ surface brightness and velocity maps of the $\sim 65 \times 65$ pc region. The H-K values obtained lie within the range $\sim 0.2 - 0.7$, in good agreement with those derived by Wiklind et al. (2004) using NICMOS F160W and F222W images. The dust lane that crosses from north to south in the central region of M83 is just at the east of our field of view, although the extinction gradient is clearly visible towards the western part of the map. The Brγ map shows the north-west end of the ring feature seen in Fig. 3.4, and the smooth velocity field that continues beyond pointing C. The velocity gradient does not show any evidence of a hidden mass in this position, but simply reflects the difference in velocity between two regions, the ring-like structure observed in pointing C and the bright lane of Brγ emission at the west of pointing D (see Fig. 3.7).

3.4. Warm molecular gas: H_2 transitions

There are two very distinct areas of strong H_2 emission, one associated with the optical nucleus and the other with emission from the inner arc at the western part of the FoV (see Fig. 3.4). We have extracted integrated spectra from both the optical nucleus and the arc,

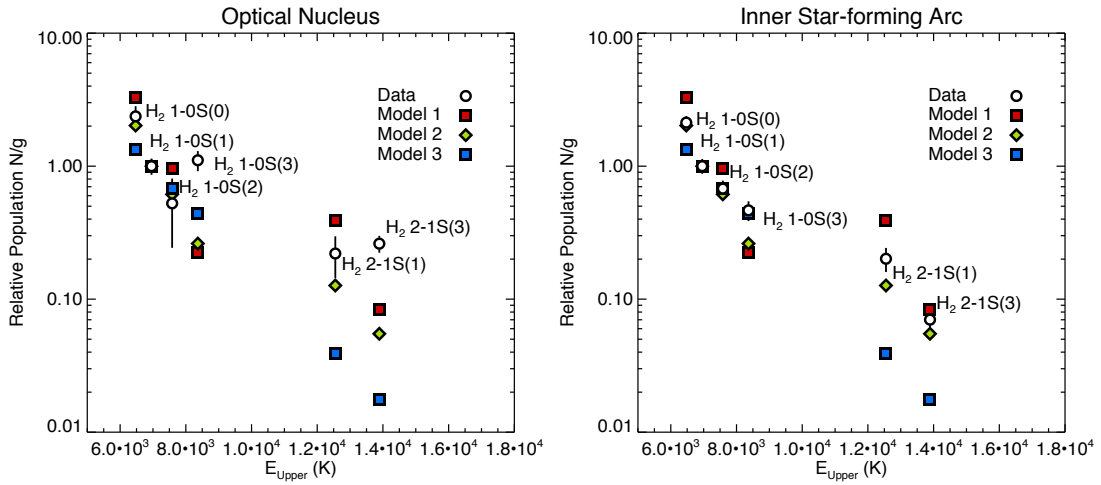

Figure 3.8: H_2 excitation diagrams - H_2 excitation diagrams relative to 1-0S(1) for the optical nucleus (left panel) and the inner star-forming arc (right panel). The lines from which the population levels are derived, are indicated. Overplotted are three of the five PDR models discussed in Davies et al. (2003). Models 1 and 2 consist of moderate and high density gas respectively where the main excitation process is UV fluorescence, while model 3 describes a fully thermalised region. As mentioned in the text, the error bars are obtained by a *bootstrap* method of N = 1000 simulations of the spectra. The diagram of the optical nucleus shows a strong overpopulation of the $J_u = 5$ transitions that points to non-thermalised excitation mechanisms like radiative fluorescence, whereas the populations of the inner arc are consistent with a dense PDR where the $\nu = 1$ levels are thermalised by collisions while the $\nu = 2$ overpopulation is characteristic of fluorescent excitation.

including all the spaxels from each region above a given flux threshold. This threshold has been chosen to be 15% of the brightness of the H_2 peak, and allows us to reject most of the weakest spaxels that contribute mostly to increase the noise. We have measured the fluxes of the different transitions by fitting a Gaussian profile, and derived the uncertainties using a Monte Carlo technique. The method consists of measuring the noise in the spectra as the rms of the residuals after subtraction of the Gaussian profile. Taking into account this estimation of the noise, we construct a total of N = 1000 simulations of our spectra where the lines are again fitted. The uncertainty of our measurements is defined as the standard deviation of the fluxes for each line. The values obtained for the fluxes of the different transitions and their uncertainties are listed in Table 3.3.

Using these fluxes, we can calculate the various populations of the upper H_2 levels associated with each transition. As shown in the population diagrams in Fig. 3.8, we found that the emission on both regions has an important contribution from non-thermal processes. We have compared the population of the different levels of both regions with three of the PDR models discussed in Davies et al. (2003), where the excitation is dominated by far-UV photons.

Line	λ (μm)	Optical Nucleus Flux (erg s^{-1} cm^{-2}) $\times 10^{-15}$	Star-forming Arc Flux (erg s^{-1} cm^{-2}) $\times 10^{-15}$
1-0S(3)	1.958	4.24 ± 0.73	1.19 ± 0.20
1-0S(2)	2.034	0.50 ± 0.27	0.43 ± 0.06
2-1S(3)	2.073	1.30 ± 0.19	0.23 ± 0.05
1-0S(1)	2.122	1.85 ± 0.26	1.24 ± 0.15
1-0S(0)	2.223	0.73 ± 0.14	0.44 ± 0.05
2-1S(1)	2.248	0.55 ± 0.19	0.34 ± 0.07

Table 3.3: Integrated fluxes of the H_2 lines for the optical nucleus and the inner arc.

In Fig. 3.8, model 1 and 2 consist of moderate and high density gas, $n_H = 10^3\,cm^{-3}$ and $n_H = 10^4\,cm^{-3}$ respectively, where the main excitation process is UV fluorescence, whereas model 3 describes a fully thermalised region with $n_H = 10^4\,cm^{-3}$ and $T = 2 \times 10^3\,K$.

The emission from the inner arc shows that the lowest ($\nu = 1$) transitions are thermalised while the higher ($\nu = 2$) transitions are slightly overpopulated. This is a clear sign of fluorescent excitation mechanisms, that tend to excite the highest levels. The values are consistent with model 2 of a dense PDR in which the $\nu = 1$ levels are thermalised and the $\nu = 2$ levels are overpopulated by fluorescence. Intriguingly, the optical nucleus shows a stronger contribution of radiative processes, most notably in terms of an overpopulation of the $J_u = 5$ levels (equivalently stronger S(3) lines).

Although these results do not allow us to quantify the contribution from the different mechanisms, it is clear that the dominant processes are rather different in both regions: while the inner arc seems to be dominated by thermal processes compatible with episodes of recent supernova activity, the contribution from radiative processes in the optical nucleus associated to fluorescent excitation mechanisms is highly significant.

3.5. Emission and Kinematics of the Gas: Evidence for Supernovae

As shown in Fig. 3.4, the kinematics of the gas is totally unrelated to the stellar kinematics (Fig. 3.5). There is no clear evidence of a single uniform velocity gradient, as seen for the stars, in any of the emission line maps. Together with the dispersion, this suggest that the gas kinematics are at small scales dominated by shocks and flows. In this section we argue that these characteristics are related to the presence of supernovae.

The nature of the Brγ ring-like feature noted in Sec. 3.3.1 could be explained in terms of a light echo from a recent type II supernova explosion. This would be consistent with the low velocity dispersion and the presence of the complete Brackett series in the spectrum (see the spectrum of aperture A in Fig. 3.3). The projected radius of the ring is ~ 23 pc, which means that, if its origin was a supernova event, the explosion would have occurred ~ 75 yr ago. If it is indeed a light echo, one might expect to see changes on a timescale of 10 years, for example between the NICMOS data from 1998 and our data from 2009. We have compared the Paα luminosity profiles of the ring measured by NICMOS with our data to confirm a possible evolution with time. We first matched the PSFs, and then extracted horizontal and vertical profiles centred in the centre of symmetry of the ring feature in both images. We applied a single scaling and normalisation to the profiles, derived to match the background of the emission far from the Paα ring. The two resulting profiles of the Paα emission are shown in Fig. 3.9. Considering the expansion rate of a light echo, the difference in size of the ring between the two datasets is expected to be of $\sim$3.4 pc, which is less than a resolution element in our coarse sampling (see Table 3.2). However, there is a significant relative decrease of $\sim$6% in brightness between the two epochs that cannot be explain as a PSF or AO effect. This decrease in the emission supports the hypothesis of a transient event like a supernova explosion.

In Sec. 3.3.1 we also pointed out two bright [FeII] spots located at the outskirts of the optical nucleus, labeled as E and F in Fig.3.4, which are associated with high velocity dispersion and are probably tracing individual supernovae. The spectrum of one of these sources (E) is shown in Fig. 3.3. The region labeled as D in Fig. 3.4 corresponds to the source M83-SNR-N-01 identified in Dopita et al. (2010) in their Table 3, and shows some characteristics expected for a recent supernova, i.e. strong [FeII] and H_2 emission.

There are also a few other supernova remnant (SNR) candidates that lie within our FoV, but none of them are obviously detected. The reason why there is no sign of most of these sources is because the selection criteria of the SNR candidates in Dopita et al. (2010) is in terms of the [OII] emission at 3727 Å and 3729 Å. To achieve high [OII]/Hα ratios, a radiative shock of $\sim$300–500 kms^{-1} is needed (Dopita & Sutherland 1995, 1996), so it is the ionized pre-shock that actually emits in [OII]. Therefore, the temperature and the shock speed are too high to expect [FeII] or H_2 emission (see Burton et al. 1990). We have also assessed the list of individual X-ray sources of Soria & Wu (2002) but only three of them lie within our FoV (sources 37, 40 and 43). Source 43 corresponds to the optical nucleus, source 37 is

shifted by $\sim$0.7″ to the west and by $\sim$0.5″ to the south of our aperture A and source 40 is shifted $\sim$0.5″ to the west and $\sim$0.6″ to the south of aperture B. Taking into account the uncertainties in the position of the X-ray sources, source 37 could be tentatively associated with the ring of Brγ emission.

As proposed by Raymond (2001), the width of the [FeII] and H_2 lines is a good estimation for the velocity of the shock speed in SNRs. The [FeII] line is clearly broadened with an intrinsic width of $\sim$100–180 kms^{-1}. In contrast, the H_2 line width is no more than $\sim$40 kms^{-1}, indicating it is barely resolved. These values are in good agreement with the values derived in Burton et al. (1990) for fast J shocks (i.e. "jump" shocks, exhibiting discontinuous transition; in contrast to "continuous" shocks showing continuous transition in velocity, density and temperature) where the [FeII] emission is expected to be stronger, and slow J or fast C shocks for the molecular hydrogen emission. Given the size of these regions of $\sim$4 pc or less and the velocity dispersion of $\sim$100–180 kms^{-1}, and assuming a constant expansion rate, we obtain an upper limit to their age of $\sim 4 \times 10^4$ yr which supports the argument that they are recent events.

The global velocity gradient in the [FeII] emission of $\sim$60 kms^{-1} along the arc is very similar to that observed for the Brγ line. However, the extended [FeII] emission throughout the inner arc and the high velocity dispersion are rather different compared to the Brγ and H_2. Both are consistent with a scenario where the most massive stars have already exploded as supernovae. These explosions would blow up the gas of a thin quiescent disk in the perpendicular direction.

This would provide a natural explanation for the systematically higher velocity dispersion observed for the [FeII] emission along the inner arc: the shocks of the supernovae would be fast enough to dissociate the H_2 molecules and enhance the gas-phase Fe abundance as well as to generate singly ionised Fe, but not to fully ionise the H.

A scenario in which many stars have recently exploded as supernovae, or may soon do so, is supported by the strong radio continuum found by Saikia et al. (1994) and the diffuse X-ray emission detected in the arc (see Soria & Wu 2002). These authors also found a high abundance of Ne, Mg, Si and S with respect to Fe. This suggest that the interstellar medium would have been enriched due to type-II supernova explosions in the recent past. This scenario would also provide an origin for the radiative fluorescence excitation of the H_2 molecules. It can be explained in terms of a population of stars of $\sim$5–8 $M_\odot$ that have not

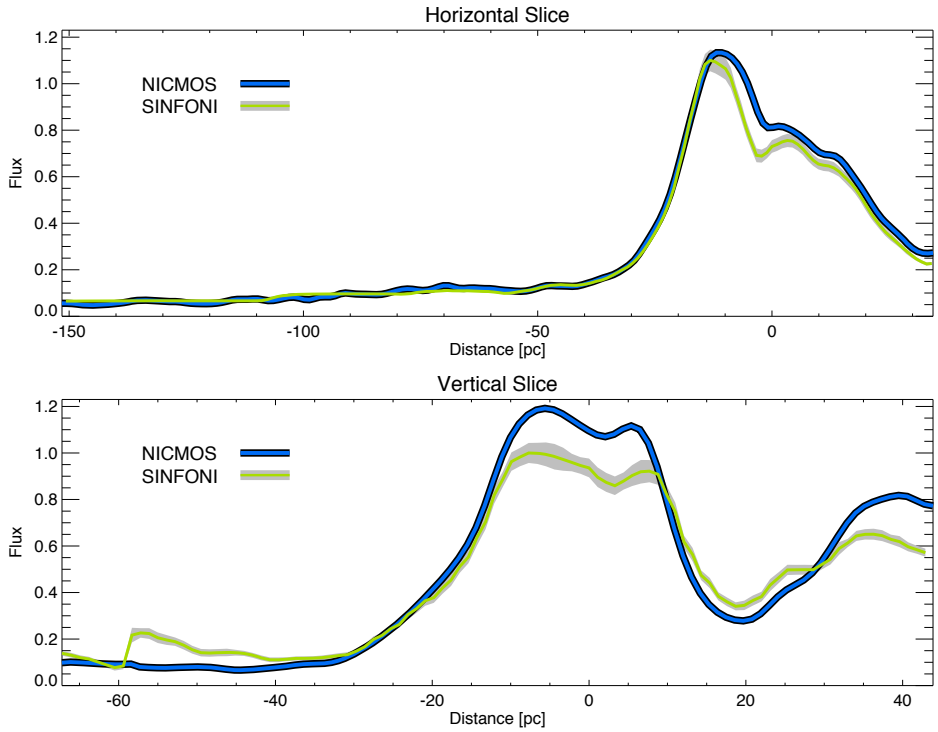

Figure 3.9: Paα profiles of the ring-like emission - Flux profiles in arbitrary units of the Paα ring-like emission from NICMOS and SINFONI. Distances are measured from the centre of the ring. Both images were previously PSF-matched and normalised to the background of the emission before comparing the data. There is a significative relative decrease of $\sim$6% in flux between the two epochs.

exploded yet as supernovae (and may not do so), but emit enough UV radiation to excite the H_2 (Puxley et al., 1990).

This scenario would also be in good agreement with the ages of optically-selected star clusters inferred in Harris et al. (2001). Based on HST WFPC2 observations, these authors studied the star formation history of the southern star-forming arc and found that more than $\sim$75 % of the more massive clusters ($M \gtrsim 2 \times 10^4\,M_\odot$) have ages less than 10 Myr. They found a sharp cutoff in the age distribution of the star clusters, and proposed a recent burst of star formation activity that began $\lesssim$10 Myr ago, suggesting an outward propagation across the arc.

We can make a rough estimate of the age of the youngest stellar population along the inner star-forming arc under the assumption that the [FeII] emission originates in supernovae. The STARBURST99 stellar population synthesis models (Leitherer et al. 1999, SB99 hereafter) predict that this emission would reach its maximum at $\sim$10 Myr (see Fig. 3.10). On the other hand, the Brγ emission also appears to be dominated by a supernova event. It shows

little ionised gas emission from the stars themselves and it is probably part of the tail end of the supernovae for the same burst of star formation that will be discussed in Sec. 3.6. This implies that there are few OB stars left and that the star formation episode was consequently a short burst. Compared to the arc, the optical nucleus shows more H_2 emission and less [FeII] while still having very little Brγ emission. This is also suggestive of a short burst of star formation. Both regions therefore appear to have experienced an episode of star formation around $\gtrsim$10 Myr ago. More detailed assessments of the age of the star formation in the optical nucleus, based on dynamics as well as spectral features, are presented in Sec. 3.6.

3.6. Optical Nucleus: An Evolved Massive Off-Nuclear Star Cluster

In order to shed some light on what one should consider to be the nucleus of M83, we have studied in more detail the kinematic and photometric properties of the optical nucleus. We made use of NIC2 F222M K-band continuum image to fit the brightness profile of the cluster. We adopted a model of a symmetric Sérsic profile convolved with the PSF to fit the core of the nucleus, combined with an asymmetric Gaussian to take care of the extended emission. The fits reveal a strongly peaked nucleus of $R_{eff} = 2.97 \pm 0.15$ pc (with a Sérsic index of $n = 2.7$), clearly unresolved in the SINFONI data, which sits on a more extended emission of size $\sim$50 pc. Given that the core of the cluster appears point-like and is not resolved in the AO data, we use this value as an upper limit for the effective radius of the cluster.

3.6.1. Age and Mass Estimation from Stellar Kinematics

We have extracted an integrated spectrum of the core of the nucleus using an aperture of radius R_{eff}, and performed a similar analysis as for the stellar kinematics, making use of the pPXF code to fit it with a library of stellar templates. The results of the fitting yield a velocity dispersion of $\sigma_{R_{eff}} \simeq 71 \pm 14\,\mathrm{km\,s^{-1}}$. We have adopted this value to provide an estimate of the dynamical mass of the cluster, given by the following relation:

$$M_{dyn} = \eta \frac{\sigma^2 R_{eff}}{G} \tag{3.1}$$

where η is a geometric constant, σ is the velocity dispersion, R_{eff} is the effective radius of the cluster and G is the gravitational constant. The geometrical constant η is determined

by the density and velocity distribution of the cluster, and is commonly assumed to be ∼10 when R_{eff} is used (McCrady & Graham, 2007; Walcher et al., 2005) to obtain the total mass of the cluster. However, different values from 3 to 10 could be adopted (see Hägele et al. 2009, Barth et al. 2009 and Basu-Zych et al. 2009). As shown in Fig. 3.6, the optical nucleus has its own internal velocity gradient, distinct from the main velocity gradient of the galaxy, that suggests that the cluster is virialised. Using the lowest value of $\eta = 3$ that assumes an isotropic velocity field, yields $M_{dyn} = (1.1 \pm 0.4) \times 10^7\,M_\odot$ for the mass of the cluster, a value consistent with an earlier stellar kinematic estimate by Thatte et al. (2000).

Using both NICMOS F222M image and our SINFONI data, we have obtained the K band luminosity of the star cluster. In order to perform synthetic photometry in our IFU data, we made use of the K band response curve of 2MASS as defined in Cohen et al. (2003) to obtain a synthetic K-band image. We have used the same aperture of radius 2.97±0.15 pc to measure the luminosity of the star cluster in both images. The values obtained are $L_{K,SINFONI} = 6.03 \times 10^5\,L_\odot$[1] and $L_{K,NICMOS} = 5.43 \times 10^5\,L_\odot$ from the SINFONI and NICMOS data respectively.

We can thus derive a mass-to-light ratio M_{dyn}/L ratio based on the dynamical mass obtained above, which is $M_{dyn}/L \sim 0.29 \pm 0.12\ M_\odot/L_{K,\odot}$ (where the denominator is in units of monochromatic solar K-band luminosity $L_{K,\odot} = 2.150 \times 10^{25}$ W). In order to make a first estimation of the age of the cluster, we have used the stellar population synthesis models of Maraston (2005, M05 hereafter). The age that corresponds to the mass-to-light ratio derived above according to these models is $\log T(\mathrm{yr}) = 8.17^{+0.08}_{-0.36}$.

3.6.2. Age and Mass Estimation From Spectral Diagnostics

In addition to the age derived from stellar kinematics and photometry, we can put further constrains on the age via the CO stellar absorption. We have measured the equivalent width of the first CO bandhead as well as its CO index (defined as the ratio of the flux densities at 2.37μm and 2.22μm) to compare the values with the prediction from the SB99 and the M05 synthesis models respectively. The value obtained for the CO equivalent width is $W_{CO} = 11.06 \pm 0.25$ Å, where uncertainties are calculated by a Monte Carlo method of N = 1000 simulations of the spectrum.

To compare the equivalent width with the SB99 models (assuming a Salpeter initial mass function, IMF, and solar metallicity), we have considered an instantaneous burst of

[1] $L_\odot = 3.826 \times 10^{26}$ W.

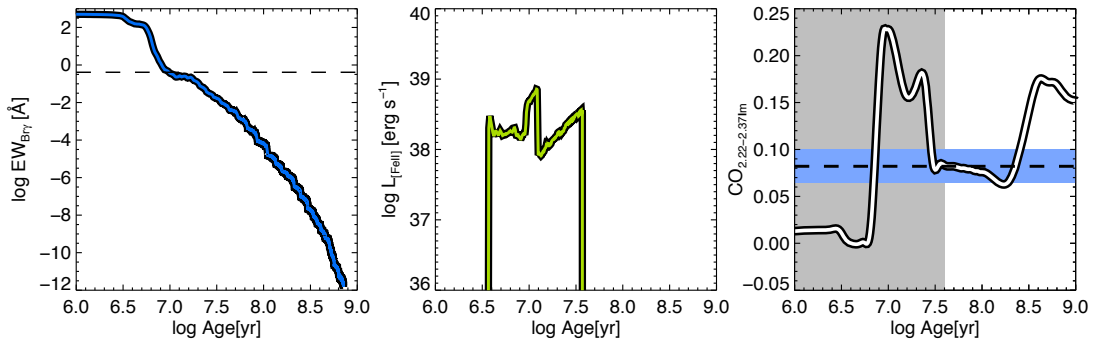

Figure 3.10: Stellar population synthesis models - Evolution of the Brγ equivalent width (left) and [FeII] flux (centre) from SB99 models, and $CO_{2.22-2.37\mu m}$ index (right) from M05 models. The dotted line in the left panel shows the upper limit of the Brγ equivalent width at the optical nucleus. We have assumed the theoretical ratio from Colina (1993) to convert the [FeII] 1.26 μm flux predictions to [FeII] 1.64 μm fluxes. The upper limit for the [FeII] luminosity at the optical nucleus is $\log[\mathrm{FeII}](\mathrm{erg\,s^{-1}}) \lesssim 33$, far below the expected luminosity of a ~ 10 Myr population. In the right panel, the region incompatible with the low Brγ and [FeII] fluxes is shown in grey. The blue strip shows the range of $CO_{2.22-2.37\mu m}$ index allowed by our data to 1σ confidence.

star formation as implied by the low Brγ emission from the cluster. It is compatible both with a young population of less than $\log \mathrm{T(yr)} \sim 7.17$ or with an evolved population older than $\log \mathrm{T(yr)} \sim 7.70$. On the other hand, according to the models, the lack [FeII] emission suggests a lower limit of $\log \mathrm{T(yr)} \sim 7.55$ for the age of the star cluster. Combining the constraints from the [FeII] emission and the W_{CO} yield an estimate for the age of the cluster of $\log \mathrm{T(yr)} = 7.97^{+0.12}_{-0.33}$.

In contrast to SB99, the M05 models use the CO index. The integrated spectrum of the optical nucleus yields $CO_{2.22-2.37\mu m} = 0.082 \pm 0.018$. Using the M05 models with the same constraints as discussed above from the Brγ and [FeII] emission, the resulting age is $\log \mathrm{T(yr)} = 7.98^{+0.43}_{-0.37}$.

It is notable that the ages estimated here from the CO equivalent width and index are very similar to that calculated previously from the mass-to-light ratio using the dynamical mass. Instead of comparing ages derived using the different methods, we can instead compare masses. To do this, we first estimate the mass-to-light ratio $M^\star/L$ from the M05 model associated with the age derived from the CO index. We can then derive the stellar (rather than dynamical) mass for the core of the star cluster. Again adopting a Salpeter IMF and solar metallicity, we find $M^\star/L \simeq 0.22 \pm 0.08$. Since the luminosity is measured within R_{eff} (which by definition contains half the light), we set the luminosity of the cluster to be twice that given in Sec. 3.6.1. Thus the stellar mass is $M^\star \simeq (7.8 \pm 2.4) \times 10^6\,M_\odot$.

This value is a factor of a few higher than the photometric mass estimate from Thatte et al. (2000) and rather similar to that given in Wiklind et al. (2004). We note that, within the inevitable uncertainties, it is also remarkably consistent with the dynamical mass we estimated previously.

These ages (from 3.6.1 and 3.6.2) are a little higher, but not inconsistent with that discussed at the end of Sec. 3.5 and all point to an age approaching, but perhaps a little less than $\sim 100\,\mathrm{Myr}$. We have considered only instantaneous star formation, since continuous models are clearly ruled out by the low Brγ equivalent width. However, a short but finite burst length of, for example, $\sim 50\,\mathrm{Myr}$ could plausibly reconcile the small differences between the estimates.

3.6.3. Could the Optical Nucleus Host a Supermassive Black Hole?

As a particularly massive star cluster, and potentially the nucleus of M83, the optical nucleus is a suitable candidate for hosting a supermassive black hole. We have therefore estimated the mass of the supermassive black hole that one might expect to find in the inner regions of M83. Using GALFIT (Peng et al., 2010), we fitted a three component model to the 2MASS K-band image (Skrutskie et al., 2006), that allows us to separate the contribution of the disc, bar and bulge to the total flux distribution. The K-band luminosity of the bulge derived from the fit is $\log L_{K,bulge} = 9.705$ in $L_{K,\odot}$ units. Taking into account the $M_{BH}/L_{K,bulge}$ relation from Marconi & Hunt (2003), we estimate that the mass of the central black hole should be around $\sim 3.9 \times 10^6\,M_\odot$. This value for the BH mass is also similar to that obtained from the $M_{BH} - \sigma$ relation (Tremaine et al., 2002), if we take $100\,\mathrm{kms}^{-1}$ from Fig. 3.5 to be the velocity dispersion of the stars in the bulge. Although this mass is less than the dynamical mass of the optical nucleus, it seems unlikely that a supermassive black hole should make up more than $\sim 35\%$ of the dynamical mass of a star cluster.

On the other hand, the measurements from *Chandra* presented in Soria & Wu (2002) show that the optical nucleus is one of the brightest sources in X-rays within the nuclear regions of M83. They fit the nuclear spectra to a power-law model with total X-ray luminosity (0.3–8 keV) of $L_X \sim 2.6 \times 10^{38}\,\mathrm{erg\,s}^{-1}$ and a photon index of $\Gamma \sim 1.15$ (see their Table 3). The total luminosity is compatible with the X-ray emission from either a low luminosity AGN or a stellar-mass black hole candidate in a binary system (Grimm et al., 2003). However, the lack of any other AGN signature (e.g. [SiVI] emission at $1.96\,\mu$m) indicate that if a

supermassive black hole were present, it would not be in an AGN phase at the present epoch. It is likely then that the X-ray emission comes from X-ray binaries in the hard state.

3.7. Location of the Nucleus

The location of the nucleus of M83 has been topic of an intense debate over the last decade. Thatte et al. (2000) first reported the discovery of a double nucleus in M83 based on long-slit measurements of the velocity dispersion of stars. They found two peaks in the velocity dispersion, one coincident with the optical nucleus, and another associated with the centre of symmetry of the bulge isophotes, both enclosing a dynamical mass of $\sim 1.3 \times 10^7\,M_\odot$. However, the lack of two-dimensional information did not allow them to obtain the precise position of this second mass concentration.

Mast et al. (2006) made optical integral field spectroscopic observations of the inner $12'' \times 21''$ of the galaxy that allow them to study in more detail the velocity field of the ionised gas. Their results support the conclusion about the presence of a second mass concentration of $\sim 1.0 \times 10^7\,M_\odot$ (although it is possible that its position was misplaced due to an incorrect spatial scaling).

Díaz et al. (2006) pointed out the position of a mass concentration at the northernmost part of the southern star-forming arc. They estimated that this hidden concentration would enclose a total mass of $\sim 1.6 \times 10^7\,M_\odot$, derived from the ionised gas kinematics. They also found that the position of this hidden mass corresponds to a peak of emission in the mid-IR continuum at $10\,\mu$m.

More recently, Houghton & Thatte (2008) combined near-IR long-slit spectroscopy with HST imaging to study the $20'' \times 20''$ central region of M83. They looked at the stellar kinematics for dynamical signatures of putative hidden mass concentrations at locations indicated in previous work. Their results show no evidence of obscured masses and they conclude that the velocity gradients observed in the gas kinematics are a consequence of shocks.

Making use of near-IR integral field spectroscopy and numerical simulations, Rodrigues et al. (2009) presented a detailed study of the ionised gas kinematics in the inner $5'' \times 13''$ of the galaxy, covering the wavelength interval from $1.2\,\mu$m to $1.4\,\mu$m with a spatial sampling of $0\farcs36$. They focused on the dynamical properties and evolution of the optical nucleus, the CO kinematic centre (similar to the photometric centre) and the putative mass concentration

proposed by Díaz et al. (2006) that is coincident with the 10μm continuum emission peak. Based on the ionised gas kinematics, they derived dynamical masses of $\sim 6.0 \times 10^7\,M_\odot$, $\sim 4 \times 10^6\,M_\odot$ and $\sim 2.0 \times 10^7\,M_\odot$ for the kinematic centre, the optical nucleus and the hidden mass concentration respectively.

Finally, Knapen et al. (2010) analysed in detail the ionised gas kinematics, making use of Paβ IFU observations with a spatial sampling of 0$''$.36, confirming the results found by Thatte et al. (2000) that the photometric centre coincides with the kinematic centre, and this location is offset by $\sim$4$''$ ($\sim$90 pc) from the optical nucleus. They proposed two possible options for the location of the true nucleus of M83. One option is the presence of an obscured hidden mass in the kinematic and photometric centre, that would require a dust extinction of $A_V = 3 - 10$ mag. However, authors consider this option unlikely, because no other signatures – such as a peak in the velocity dispersion or in the near-IR emission – of a hidden mass are found. Their other option was that the optical nucleus is the true nucleus, and it is displaced from the kinematic centre as a result of some past interaction.

Our results clearly show that on scales of tens of parsecs, the gas kinematics are dominated by shocks and outflows. But we have also seen there is a global gradient of $\sim$60 kms^{-1} along the inner arc which is totally unrelated to the stellar velocity field. Given the orientation of the galaxy, these gas kinematics appear to be tracing an inflow of gas along the inner bar to the photometric centre. We would expect such a bar-driven gas inflow to terminate at the nucleus, and the location of the end of the inflow does coincide with the photometric centre. We also emphasise that there is an increase of the stellar continuum at this point, consistent with the centre of the bulge. But this continuum, primarily from older stars, is mostly swamped by the stronger continuum from the young stars in the surrounding star-forming ring. The lack of a very recent starburst in the photometric centre would explain the low stellar continuum emission in this region.

As mentioned before, we have not found any evidence or signature of a hidden mass near the kinematic centre. However, the velocity dispersion expected due to random motions around such a black hole, given the spatial resolution of our AO data, would be $\sigma_{BH} \sim 60$ kms^{-1}. Taking into account the instrumental resolution of our data (R $\sim$ 1500, or an instrumental broadening of $\sigma_{instr} \sim 85$ kms^{-1}) and the dispersion of the stars of $\sigma_\star \sim 100$ kms^{-1} measured almost everywhere, the effective enhancement of the dispersion expected to be observed for this BH would be of $\sim$10 kms^{-1}, making our data insensitive to such a compact object. Thus,

the lack of a kinematic signature of a supermassive BH does not equate to the absence of such a BH at the location of the kinematic and photometric centre of M83.

We also considered the possibility that the $\sim 3.4''$ offset of optical nucleus from the kinematic centre could be the result of an $m = 1$ perturbation in the gravitational potential, as suggested by Knapen et al. (2010). As shown in Bournaud et al. (2005a), an $m = 1$ perturbation of the potential could be explained by asymmetric accretion of gas towards the inner regions of the galaxy, which would be in agreement with the unperturbed spiral pattern revealed at mid-infrared wavelengths for M83 (Dale et al., 2009). Alternatively, as discussed in Hopkins & Quataert (2010), an eccentric pattern resulting from a past interaction could persist up to $\sim 10^4$ dynamical times. However, a model of an eccentric disk as used by Tremaine (1995) to explain the double nucleus of M31 is probably not appropriate to explain the offset in here. It is caused by the high density of stars near apocenter in their elliptical orbits: the combination of their slow velocities at this point together with the fact that their velocity is along the line of sight, create the illusion of a secondary nucleus. In M83, the compactness of the optical nucleus and the presence of a coherent internal velocity gradient (see Fig. 3.6) are inconsistent with the rather diffuse appearance expected for such a gravitational perturbation. Furthermore, the presence of an apparent secondary nuclei as in M31 is favoured by the close edge-on sightline. In principle, the eccentric disk could obscure the radiation from the black hole, even at X-ray wavelengths, and would explain the lack of signature of a compact object near the kinematic centre of M83. However, the low inclination of the galaxy and the fact that the optical nucleus lies within the rather symmetric circumnuclear ring traced by the molecular gas (see Sakamoto et al. 2004) make it unlikely.

3.8. Conclusions

We have presented new and detailed near infrared adaptive optics integral field spectroscopic data for the innermost $\sim$200 pc of M83, and studied the kinematics and distribution of the stars as well as molecular and ionised gas. Our conclusions are as follows:

- The stellar kinematics show a smooth global velocity field typical of uniform rotation. They reveal an independent and coherent velocity gradient intrinsic to the optical nucleus with an amplitude of $\sim$30 $\mathrm{km s^{-1}}$. The velocity dispersion across the whole region also shows a smooth distribution, with values in the range $\sim$ 50–100 $\mathrm{km\,s^{-1}}$.

- The ionised and molecular gas reveal a complex situation in which their kinematics are completely dominated by shocks and inflows at small scales but trace globally an inflow along the nuclear bar to the kinematic centre. This, and the fact that they are totally unrelated to the stellar kinematics, make them unsuitable to estimate dynamical properties of the central regions.

- There is plentiful evidence for recent supernovae. A bright ring-like Brγ feature, which dominates the inner star-forming arc, has low dispersion and no measurable velocity gradient. It can be explained in terms of a light echo from a recent supernova explosion. The [FeII] emission has high dispersion along the arc suggestive of shocks from supernova remnants; and in the optical nucleus shows two bright locations where the dispersion is high, which are likely to be individual supernova remnants. A comparison of the gas and stellar kinematics indicates that the off-nuclear mass concentrations, which had been proposed on the basis of ionised gas kinematics, are instead regions where there are complex kinematics associated with recent supernova events.

- A spatial study of the excitation mechanisms of the warm H_2 suggest that the inner arc is dominated by collisional mechanisms, consistent with an episode of recent supernova events, while H_2 in the optical nucleus has a higher contribution from radiative processes.

- The $\sim 3\,$pc effective radius of the optical nucleus together with its coherent internal kinematics yield a dynamical mass of $M_{dyn} = (1.1 \pm 0.4) \times 10^7\,M_\odot$. Its K-band luminosity is $L_K = 5.7 \times 10^5\,L_\odot$. The resulting mass-to-light ratio implies an age of $\sim 100\,$Myr that is fully consistent with that implied independently by the CO index and equivalent width. Similarly, the age implied by the CO index yields a stellar mass for the cluster of $M^\star \simeq (7.8 \pm 2.4) \times 10^6\,M_\odot$, consistent with the dynamical mass.

- We show that the optical nucleus cannot be an $m = 1$ perturbation, and is not the 'true' nucleus of M83. Instead, we argue that this is indeed located at the photometric and kinematic centre of M83's bulge, where there is a measurable peak in the K-band continuum (albeit swamped by the bright surrounding star forming ring). We also show that, for the expected black hole mass in the centre of M83, one would not expect to see a dynamical signature at currently attainable spatial resolutions.

4

Mapping the emitting gas structure of local LIRGs and ULIRGs

Spatially resolved emission and kinematic maps

"Well, I feel that we should always put a little art into what we do. It's better that way."
— Jules Verne, *From the Earth to the Moon*

We present an atlas of a sample of local ($z < 0.1$) LIRGs (10) and ULIRGs (7) covering the luminosity range $\log(L_{IR}/L_{\odot}) = 11.1 - 12.4$. The atlas is based on near-infrared H (1.45 - 1.85 μm) and K-band (1.95 - 2.45 μm) VLT-SINFONI integral field spectroscopy. The atlas presents the ionised, partially ionised, and warm molecular gas two-dimensional flux distributions and kinematics over a FoV of $\sim 3 \times 3$ kpc (LIRGs) and $\sim 12 \times 12$ kpc (ULIRGs) and with average linear resolutions of $\sim$0.2 kpc and $\sim$0.9 kpc, respectively. The different phases of the gas show a wide morphological variety with the nucleus as the brightest Brγ source for $\sim$33% of the LIRGs and $\sim$71% of the ULIRGs, whereas all the LIRGs and ULIRGs have their maximum H_2 emission in their nuclear regions. In LIRGs, the ionised gas distribution is dominated by the emission from the star-forming rings or giant HII regions in the spiral arms. The Brγ and [FeII] line at 1.644 μm trace the same structures, although the emission peaks at different locations in some of the objects, and the [FeII] seems to be more extended and diffuse. The ULIRG subsample is at larger distances and contains mainly pre-coalescence interacting systems. Although the peaks of the molecular gas emission and the continuum coincide in $\sim$ 71% of the ULIRGs, regions with intense Paα (Brγ) emission tracing luminous star-forming regions located at distances of 2–4 kpc away from the nucleus

are also detected, usually associated with secondary nuclei or tidal tails. LIRGs have mean observed (i.e. uncorrected for internal extinction) SFR surface densities of about 0.4 to 0.9 $M_\odot$ yr^{-1} kpc^{-2} over large areas (4–9 kpc^2) with peaks of about 2−2.5 $M_\odot$ yr^{-1} kpc^{-2} in the smaller regions (0.16 kpc^2) associated with the nucleus of the galaxy or the brightest Brγ region. ULIRGs do have similar average SFR surface densities for the integrated emitting regions of $\sim$0.4 $M_\odot$ yr^{-1} kpc^{-2} in somewhat larger areas (100−200 kpc^2) and for the Paα peak ($\sim$ 2 $M_\odot$ yr^{-1} kpc^{-2} in 4 kpc^2). The observed gas kinematics in LIRGs is primarily due to rotational motions around the centre of the galaxy, although local deviations associated with radial flows and/or regions of higher velocity dispersions are present. The ionised and molecular gas share the same kinematics (velocity field and velocity dispersion) to first order, showing slight differences in the velocity amplitudes (peak-to-peak) in some cases, whereas the average velocity dispersions are compatible within uncertainties. As expected, the kinematics of the ULIRG subsample is more complex, owing to the interacting nature of the objects of the sample.

4.1. Introduction

The *Infrared Astronomical Satellite* (*IRAS*) discovered a population of galaxies with their bolometric luminosities dominated by its mid- and far-infrared emission (Soifer et al. 1984, Sanders & Mirabel 1996). Although the number density of these luminous (LIRGs; $10^{11}L_\odot < L_{IR} < 10^{12}L_\odot$) and ultraluminous (ULIRGs; $10^{12}L_\odot < L_{IR} < 10^{13}L_\odot$) infrared galaxies is low locally (Sanders & Mirabel 1996), their number increases steadily up to redshift of $\sim$ 2.5 and dominates at redshifts $\sim$ 1.5 and above (Pérez-González et al. 2005, Lonsdale et al. 2006, Sargent et al. 2012). The energy output of the local (U)LIRGs is now established as mainly due to massive starbursts with a small AGN contribution for LIRGs, whereas the contribution from the AGN increases with L_{IR} and dominates bolometrically at the very high L_{IR} end of ULIRGs (e.g. Nardini et al. 2010, Alonso-Herrero et al. 2012 and references therein). Morphological studies show that most/all local ULIRGs show clear signs of on going interactions or recent mergers between two or more gas-rich spirals (e.g. Murphy et al. 1996, Borne et al. 2000, Veilleux et al. 2002, Dasyra et al. 2006). LIRGs are, on the other hand, mostly normal spirals where some are involved in interactions (Arribas et al. 2004, Haan et al. 2011).

In recent years, optical integral field spectroscopy of representative samples of local LIRGs (Arribas et al. 2008, Alonso-Herrero et al. 2009) and ULIRGs (García-Marín et al., 2009b)

have been performed with the goal of investigating the nature of the ionisation sources (Monreal-Ibero et al., 2010), the structure of the star-forming regions (Rodriguez-Zaurín et al. 2011, Arribas et al. 2012), the 2D internal dust/extinction distribution (García-Marín et al., 2009a), and the gas kinematics (Colina et al. 2005, Alonso-Herrero et al. 2009). In parallel, a considerable effort has been made to investigate the nature of star-forming galaxies at redshifts between 1 and 3 (e.g. Förster Schreiber et al. 2006, 2009, 2011a, Law et al. 2009, Wright et al. 2009, Wisnioski et al. 2011, Epinat et al. 2012, Vergani et al. 2012). The advent of IFS has allowed spatially and spectrally resolved studies of optically/UV selected galaxies at early stages in their evolution. Such studies map the morphologies and kinematics of the gas and stars and have demonstrated that massive star-forming galaxies either appear to be large massive rotating disks (Förster Schreiber et al. 2011a, Wisnioski et al. 2011, Epinat et al. 2012) or are found in highly disturbed mergers (Förster Schreiber et al. 2006, Epinat et al. 2012).

The local population of LIRGs and ULIRGs therefore represents the closest examples of the two modes of formation of massive star-forming galaxies at high redshifts, during the peak of star formation in the history of the Universe. Their distances offer the possibility of investigating their physical processes, taking advantage of the high spatial resolution and S/N achieved. The detailed study of these mechanisms on physical scales of a few hundred parsecs can then be applied in more distant galaxies, where such a level of detail is extremely challenging, or not even possible. This is the first paper in a series presenting new H- and K-band SINFONI seeing-limited observations of a sample of local LIRGs and ULIRGs ($z < 0.1$), for which previous optical IFS is already available (see references above). The aim of this paper is to describe the general 2D properties of the whole sample and to lay the foundations for further detailed studies. These studies, to be addressed in forthcoming publications, will focus on the structure and excitation mechanisms of the ionised, partially-ionised and warm molecular gas, the distribution of the different stellar populations, and the stellar and multi-phase gas kinematics.

The Chapter is organised as follows. Section 4.2 gives details about the sample. Section 4.3 contains the description of the observations and techniques that have been used to reduce and calibrate the data, and the procedures applied to obtain the maps of the emission lines. Section 4.4 includes a general overview of the data and the physical processes of the line emitting gas and stellar populations. In Section 4.5, we discuss the 2D properties as inferred

from the SINFONI spectral maps, focussing on the general aspects of the morphology and kinematics of the gas emission. Finally, Section 4.6 includes a brief summary of the Chapter.

4.2. The sample

The sample is part of a larger survey (Arribas et al., 2008) of local LIRGs and ULIRGs observed with different optical IFS facilities including INTEGRAL+WYFFOS (Arribas et al., 1998) at the 4.2 m William Herschel Telescope (WHT), VLT-VIMOS (*VIsible MultiObject Spectrograph*, LeFèvre et al. 2003), and PMAS (*Potsdam MultiAperture Spectrophotometer*, Roth et al. 2005). It covers the whole range of LIRG and ULIRG infrared luminosities and the different morphologies observed in this class of objects, by sampling galaxies in both hemispheres.

The present SINFONI sample comprises a set of ten LIRGs and seven ULIRGs covering a range in luminosity of $\log(L_{IR}/L_{\odot}) = 11.10 - 12.43$ (see Table 4.1). The objects were selected to cover a representative sample of the different morphological types of LIRGs and ULIRGs, although this is not complete in either flux or distance. All the LIRGs of the sample were selected from the volume-limited sample of Alonso-Herrero et al. (2006), whereas all the ULIRGs with the exception of IRAS 06206-6315 and IRAS 21130-4446 come from the *IRAS Bright Galaxy Survey* (Soifer et al. 1989, Sanders et al. 1995). Our sample contains objects with intense star formation, AGN activity, isolated galaxies, strongly interacting systems, and mergers. The mean redshift of the LIRGs and ULIRGs subsamples is $z_{\rm LIRGs} = 0.014$ and $z_{\rm ULIRGs} = 0.072$, and the mean luminosities are $\log(L_{IR}/L_{\odot}) = 11.33$ and $\log(L_{IR}/L_{\odot}) = 12.29$, respectively.

4.3. Observations, data reduction, and analysis

4.3.1. SINFONI observations

The observations were obtained in service mode using the near-infrared spectrometer SINFONI of the VLT, during the periods 77B, 78B, and 81B (from April 2006 to July 2008). All the galaxies in the sample were observed in the K band (1.95–2.45 μm) with a plate scale of $0\farcs250 \times 0\farcs125$ pixel^{-1} yielding an FoV of 8"x8" in a 2D 64x64 spaxel frame[1]. The

[1]A detailed description of the correspondence between the pixels in the focal plane of the instrument and the reconstructed cube can be found in the user manual of the instrument. http://www.eso.org/sci/facilities/paranal/instruments/sinfoni/doc/

ID1	ID2	α	δ	z	D	Scale	log L_{IR}	Classification	References
Common	IRAS	(J2000)	(J2000)		(Mpc)	(pc/arcsec)	($L_\odot$)		
(1)	(2)	(3)	(4)	(5)	(6)	(7)	(8)	(9)	(10)
IRAS 06206-6315	IRAS 06206-6315	06h21m01.21s	-63°17'23.″5	0.092441	425	1726	12.31	Sy2	1,2,3
NGC 2369	IRAS 07160-6215	07h16m37.73s	-62°20'37.″4	0.010807	48.6	230	11.17	Composite	4
NGC 3110	IRAS 10015-0614	10h04m02.11s	-06°28'29.″2	0.016858	78.4	367	11.34	Composite	4
NGC 3256	IRAS 10257-4338	10h27m51.27s	-43°54'13.″8	0.009354	44.6	212	11.74	HII, Starburst	1,5
ESO 320-G030	IRAS 11506-3851	11h53m11.72s	-39°07'48.″9	0.010781	51.1	242	11.35	HII	4
IRAS 12112+0305	IRAS 12112+0305	12h13m46.00s	+02°48'38.″0	0.073317	337	1416	12.38	LINER	1,2
IRASF 12115-4656	IRAS 12115-4657	12h14m12.84s	-47°13'43.″2	0.018489	84.4	394	11.10	HII	1
NGC 5135	IRAS 13229-2934	13h25m44.06s	-29°50'01.″2	0.013693	63.5	299	11.33	HII, Sy2	1,6
IRAS 14348-1447	IRAS 14348-1447	14h37m38.40s	-15°00'20.″0	0.083000	382	1575	12.41	LINER	1,2
IRASF 17138-1017	IRAS 17138-1017	17h16m35.79s	-10°20'39.″4	0.017335	75.3	353	11.42	HII	1
IRAS 17208-0014	IRAS 17208-0014	17h23m21.95s	-00°17'00.″9	0.042810	189	844	12.43	LINER	1,6
IC 4687	IRAS 18093-5744	18h13m39.63s	-57°43'31.″3	0.017345	75.1	352	11.44	HII	1, 6
IRAS 21130-4446	IRAS 21130-4446	21h16m18.52s	-44°33'38.″0	0.092554	421	1712	12.22	HII	7
NGC 7130	IRAS 21453-3511	21h48m19.50s	-34°57'04.″7	0.016151	66.3	312	11.34	HII, Sy2, LINER	1,6
IC 5179	IRAS 22132-3705	22h16m09.10s	-36°50'37.″4	0.011415	45.6	216	11.12	HII	4
IRAS 22491-1808	IRAS 22491-1808	22h51m49.26s	-17°52'23.″5	0.077760	347	1453	12.23	HII	1,2
IRAS 23128-5919	IRAS 23128-5919	23h15m46.78s	-59°03'15.″6	0.044601	195	869	12.04	Sy2, LINER	1,3,6

Table 4.1: Cols. (3) and (4): right ascension and declination from the NASA Extragalactic Database (NED). Col. (5): redshift from NED. Cols. (6) and (7): Luminosity distance and scale from Ned Wright's Cosmology Calculator (Wright, 2006) given $h_0 = 0.70$, $\Omega_M = 0.7$, $\Omega_M = 0.3$. Col. (8): L_{IR}[8–1000μm] calculated from the IRAS flux densities f_{12}, f_{25}, f_{60} and f_{100} (Sanders et al., 2003), using the expression in Sanders & Mirabel (1996) Col. (9): Spectroscopic classification based on the nuclear optical spectra from the literature. Galaxies classified as composite are likely to be a combination of AGN activity and star formation. 1:Sanders et al. (2003), 2: Lutz et al. (1999), 3:Duc et al. (1997), 4:Pereira-Santaella et al. (2011), 5:Wamsteker et al. (1985), 6:Véron-Cetty & Véron (2006), 7:Farrah et al. (2003)

subsample of LIRGs was also observed in the H band (1.45–1.85 μm) with the same scale, so the [FeII] line at 1.64 μm rest frame could be observed. The spectral resolution for this configuration is R$\sim$3000 for H-band and R$\sim$4000 for K-band, and the FWHM as measured from the OH sky lines is 6.6 ± 0.5 Å for the H band and6.4 ± 0.6 Å for the K band with a dispersion of 1.95 Å/pix and 2.45 Å/pix, respectively.

Given the limited field of view (FoV) of 8"x8" in the 250 mas configuration provided by SINFONI , we are sampling the central regions of the objects. However, owing to the jittering process and the different pointings used in some objects, the final FoV of the observations extends beyond that value, typically from $\lesssim$9"$\times$9" up to $\lesssim$12"$\times$12" or more. That is translated to an average coverage of the central regions of $\sim 3 \times 3$ kpc for the LIRGs and of $\sim 12 \times 12$ kpc for the ULIRG subsample. Due to this constraint, some of the more extended galaxies or those with multiple nuclei were observed in different pointings, each located in regions of interest. Our seeing-limited observations have an average resolution of $\sim$0.63 arcsec (FWHM) that corresponds to $\sim$0.2 kpc and $\sim$0.9 kpc.

Owing to the strong and quick variation of the IR sky emission, the observations were split into short exposures of 150 s each, following a jittering OSSO pattern for sky and on-source frames. The detailed information about the observed bands and integration time for each object is shown in Table 4.2. Besides the objects of the sample, a set of spectrophotometric standard stars and their respective sky frames were observed to correct for the instrument response and to flux-calibrate the data. As shown in Table 4.2, NGC 3256 was observed in different pointings for the different bands because of an error during the implementation of the Phase 2 template.

4.3.2. Data reduction

The calibration process was performed using the standard ESO pipeline EsoRex (version 2.0.5). The usual corrections of dark subtraction, flat fielding, detector linearity, geometrical distortion, and wavelength calibration were applied to each object and sky frame, prior to the sky subtraction from each object frame. The method used to remove the background sky emission is outlined in Davies (2007). We used our own IDL routines to perform the flux calibration on every single cube and to reconstruct a final data cube for each pointing, while taking the relative shifts in the jittering pattern into account. For those objects with different pointings, the final data cubes were combined to build a final mosaic.

Object / Pointing (1)	Observed Bands (2)	t_{exp}(s) per band (3)
IRAS 06206-6315	K	2550
NGC 2369	H, K	2250, 2250
NGC 3110	H, K	2250, 1200
NGC 3256-N	H	2250
NGC 3256-S	K	1950
NGC 3256-W	H, K	750, 950
ESO 320-G030	H, K	2700, 1650
IRAS 12112+0305-N	K	2550
IRAS 12112+0305-S	K	2550
IRASF 12115-4656-E	K	2400
IRASF 12115-4656-W	K	2400
NGC 5135	H, K	2400, 1500
IRAS 14348-1447-N	K	2550
IRAS 14348-1447-S	K	1050
IRASF 17138-1017	H, K	5550, 2850
IRAS 17208-0014	K	3450
IC 4687	H, K	3000, 2400
IRAS 21130-4446	K	3000
NGC 7130-N	H, K	2400, 2550
NGC 7130-S	H, K	2400, 2400
IC 5179-E	H, K	2400, 2400
IC 5179-W	H, K	2400, 2400
IRAS 22491-1808	K	4350
IRAS 23128-5919-N	K	2700
IRAS 23128-5919-S	K	2700

Table 4.2: Col. (3): Total integration time on-target for each band in seconds.

The flux calibration was performed in two steps. Firstly, to obtain the atmospheric transmission curves, we extracted the spectra of the standard stars with an aperture of 5σ of the best 2D Gaussian fit of a collapsed image. The spectra were then normalised by a black body profile at the T_{eff} listed in the Tycho-2 Spectral Type Catalog (Wright et al., 2003), taking the more relevant absorption spectral features of the stars into account. As discussed in Bedregal et al. (2009), in most cases the only spectral features in absorption are the Brackett series so we modelled them using a Lorentzian profile. The result is a 'sensitivity function' that accounts for the atmospheric transmission.

Secondly, the spectra of the star was converted from counts to physical units. We made use of the response curves of 2MASS filters (Cohen et al., 2003) to obtain the magnitude in counts of the standard stars and the H and K magnitudes from the 2MASS catalogue (Skrutskie et al., 2006) to translate these values to physical units. Every individual cube was then divided by the 'sensitivity function' and multiplied by the conversion factor to obtain a full-calibrated data cube. The typical relative uncertainty for the conversion factor is $\sim$5% for both bands.

Object	Paα 1.876 μm	Brγ 2.166 μm	H_2 1-0S(1) 2.122 μm	HeI 2.059 μm	[FeII] 1.644 μm	H-band FoV (kpc^2)	K-band FoV (kpc^2)
IRAS 06206-6315	15	···	12	···	···	···	186.1
NGC 2369	···	13	15	10	15	2.8	3.0
NGC 3110	···	15	15	10	10	8.3	7.4
NGC 3256	···	25	20	15	30	4.9	4.6
ESO 320-G030	···	25	10	15	30	3.2	3.1
IRAS 12112+0305	20	···	12	10	···	···	101.3
IRASF 12115-4656	···	15	13	10	···	···	14.4
NGC 5135	···	20	15	15	25	5.4	4.7
IRAS 14348-1447	20	···	13	10	···	···	169.7
IRASF 17138-1017	···	17	20	15	20	6.3	6.1
IRAS 17208-0014	25	···	13	10	···	···	32.3
IC 4687	···	25	20	20	25	7.7	6.9
IRAS 21130-4446	25	···	8	10	···	···	38.3
NGC 7130	···	15	13	12	12	10.0	9.5
IC 5179	···	20	15	13	15	5.2	5.2
IRAS 22491-1808	20	···	9	10	···	···	82.5
IRAS 23128-5919	20	···	15	15	···	···	34.3

Table 4.3: The last two columns give the total area of the FoV used to derive the integrated fluxes for the emission lines and the stacked spectra for the H- and K-bands, respectively.

4.3.3. Line fitting

The maps of the brightest emission lines were constructed by fitting a Gaussian profile on a spaxel-by-spaxel basis. We made use of the IDL routine MPFIT (Markwardt, 2009) and developed our own routines to perform the fitting of the cubes in an automated fashion. For each object and every line, we obtained the integrated flux, equivalent width, radial velocity, and velocity dispersion maps. To account for the instrumental broadening, we made use of OH sky lines for each band at 1.690 μm and 2.190 μm.

4.3.4. Voronoi binning

Before extracting the kinematics, the data were binned using the Voronoi method by Cappellari & Copin (2003) to achieve a minimum S/N over the entire FoV. This technique employs bins of approximately circular shape to divide the FoV, which is described in terms of a set of points called *generators*. Every spaxel of the field is accreted to the bin described by the closest generator, until the S/N threshold is reached. This set of generators is refined to satisfy different topological and morphological criteria and to ensure that the scatter of the S/N of each bin is reduced to a minimum. This method ensures that the spatial resolution of

the regions with high S/N is preserved, since these bins are reduced to a single spaxel.

The maps from different lines are binned independently since the spatial distribution of the emission is different and the S/N is line dependent (see Fig. B.1 and B.2). Every S/N threshold has been chosen to achieve roughly the same number of bins in each map of every object and are listed in Table 4.3.

4.3.5. Spectral maps and aperture normalised spectra

As mentioned above, the maps of the emission lines were constructed by fitting a single Gaussian profile to the spectra. Figure B.1 shows, for the subsample of 10 LIRGs, the Brγ and H_2 1-0S(1) emission and equivalent width maps, together with the velocity dispersion and radial velocity ones. The figures also include emission maps of the HeI at 2.059 μm and, for those objects observed in the H band, [FeII] line emission maps at 1.644 μm. We have also constructed a K band map from the SINFONI data by integrating the flux along the response curve of the 2MASS K-band filter, to compare with archival HST images when available. Figure B.2 shows the maps of the subsample of 7 ULIRGs but with the Paα emission line instead of Brγ. All the line emission maps are shown in arbitrary units on a logarithmic scale to maximise the contrast between the bright and diffuse regions and are oriented following the standard criterium that situates the north up and the east to the left[1].

The radial velocity maps are scaled to the velocity measured at the brightest spaxel in the K band image. This spaxel is marked with a cross in all the maps and usually coincides with the nucleus of the galaxy or with one of them for the interacting systems. The measured systemic radial velocities are similar to the NED published values within less than $\sim$1%. Although the main nucleus of NGC 3256 was observed in the H band, the reference spaxel corresponds to its southern nucleus, which is highly extinguished (Kotilainen et al. 1996, Alonso-Herrero et al. 2006, Díaz-Santos et al. 2008), since the main one was not observed in the K band (see Fig. B.1c). The values of the reference radial velocities are shown in Table 4.4.

Besides the spectral maps, Figs. B.1 and B.2 show, for illustrative purposes, the integrated spectra in the K band of two regions of the FoV. The apertures used to extract the spectra are drawn on the maps and are labelled with the letters "A" and "B". Aperture "A" is centred on the brightest spaxel of the K band image, which usually corresponds to the nucleus of the

[1]The only exception to this criterium is IC 5179 (Fig. B.1j) where we have adopted the original orientation of the data to maximise the size of the maps. The axes' orientation is plotted for reference.

Object	cz ($\mathrm{km\,s^{-1}}$)
IRAS 06206-6315	27625 ± 15
NGC 2369	3465 ± 5
NGC 3110	5151 ± 4
NGC 3256	2780 ± 2
ESO 320-G030	3132 ± 24
IRAS 12112+0305	21973 ± 3
IRASF 12115-4656	5519 ± 52
NGC 5135	4115 ± 6
IRAS 14348-1447	24799 ± 4
IRASF 17138-1017	5184 ± 1
IRAS 17208-0014	12805 ± 6
IC 4687	5226 ± 3
IRAS 21130-4446	28016 ± 17
NGC 7130	4895 ± 2
IC 5179	3384 ± 1
IRAS 22491-1808	23287 ± 5
IRAS 23128-5919	13437 ± 2

Table 4.4: Velocities derived for the sample of galaxies using the Brγ line at the spaxel with the brightest K-band flux. The spaxels are marked with a cross in Figs. B.1 and B.2. The differences between these and NED published values are typically less than $\sim$1%.

galaxy. On the other hand, aperture "B" is centred in regions of interest that differ from object to object. In the LIRG subsample, it covers the brightest region in the Brγ equivalent width map. The same criterion is used for the ULIRG subsample, except in those objects with two distinct nuclei, where aperture "B" covers the secondary nucleus.

The spectra are normalised to the continuum, measured between 2.080 μm and 2.115 μm and between 2.172 μm and 2.204 μm. We also stacked the spectra of one of our sky cubes into a single spectrum and plotted it to illustrate the typical sky emission. This is useful for identifying the residuals from sky lines that are the result of the sky subtraction during the data reduction. Besides the OH sky lines, some of the K-band spectra show the residuals from the atmospheric absorption of water vapour. These features are easily traced along the wavelength ranges [1.991–2.035] μm and [2.045–2.080] μm, and are marked in grey in Figs. B.1 and B.2.

4.3.6. Generation of the stacked spectra for the LIRG and ULIRG subsamples

Figure 4.1 shows the stacked spectra of three different subsets of the sample defined according to the L_{IR} range. As discussed in Rosales-Ortega et al. (2012), there are different techniques for optimising the S/N within IFS data. We have adopted a flux-based criterium to exclude those spaxels with low surface brightness that may contribute to increase the noise of the resulting spectra. For each object, we considered the continuum images for each band and ordered the spaxels by decreasing flux. We then selected a set of spectra from those spaxels that contain at least the $\gtrsim$90% of the total continuum flux. By assuming this criterium, we assure that typically between the $\sim 85-95\%$ of the flux in the lines is also taken into account.

Before the stacking, every individual spectrum is *de-rotated*, i.e. shifted to the same rest frame. This procedure decorrelates the noise due to imperfect sky subtraction, since the residuals are no longer aligned in the spectral axis, and prevents the smearing of the lines due to the stacking along wide apertures. To derotate the spectra, we focussed on the [FeII] line for the H band and on Brγ (Paα for the ULIRG subset) and the H_2 1-0S(1) line for the K band, since the relative shifts in the spectral axis could be different for each phase of the gas. For the ULIRG subset, we have only considered the Paα line, since the H_2 1-0S(1) line is not bright enough in all the spaxels where the spectra are extracted. For the K band spectra of the LIRG subsample, we measured the difference between the relative shifts obtained for the Brγ and H_2 lines, to assure that no artificial broadening is introduced if only one phase is considered as reference for the whole spectra. Given that only less than $\sim$10% of the spaxels have more than one spectral pixel of difference between the relative shifts measured with both emission lines, we considered that the effect in the width of the lines is negligible so we have adopted the Brγ line as reference for the whole LIRG subset.

After the *derotation* procedure, every spectrum of each object is normalised to a linear fit of the continuum, measured within the intervals [1.600, 1.610] μm and [1.690, 1.700] μm for the H-band and [2.080, 2.115] μm and [2.172, 2.204] μm for the K-band, and stacked in one single spectrum per object. Finally, the spectra of each galaxy in each luminosity bin are rebinned, stacked, and convolved to a resolution of 10Å (FWHM) to achieve a homogeneous resolution. The spectra of the different luminosity bins are available as online material.

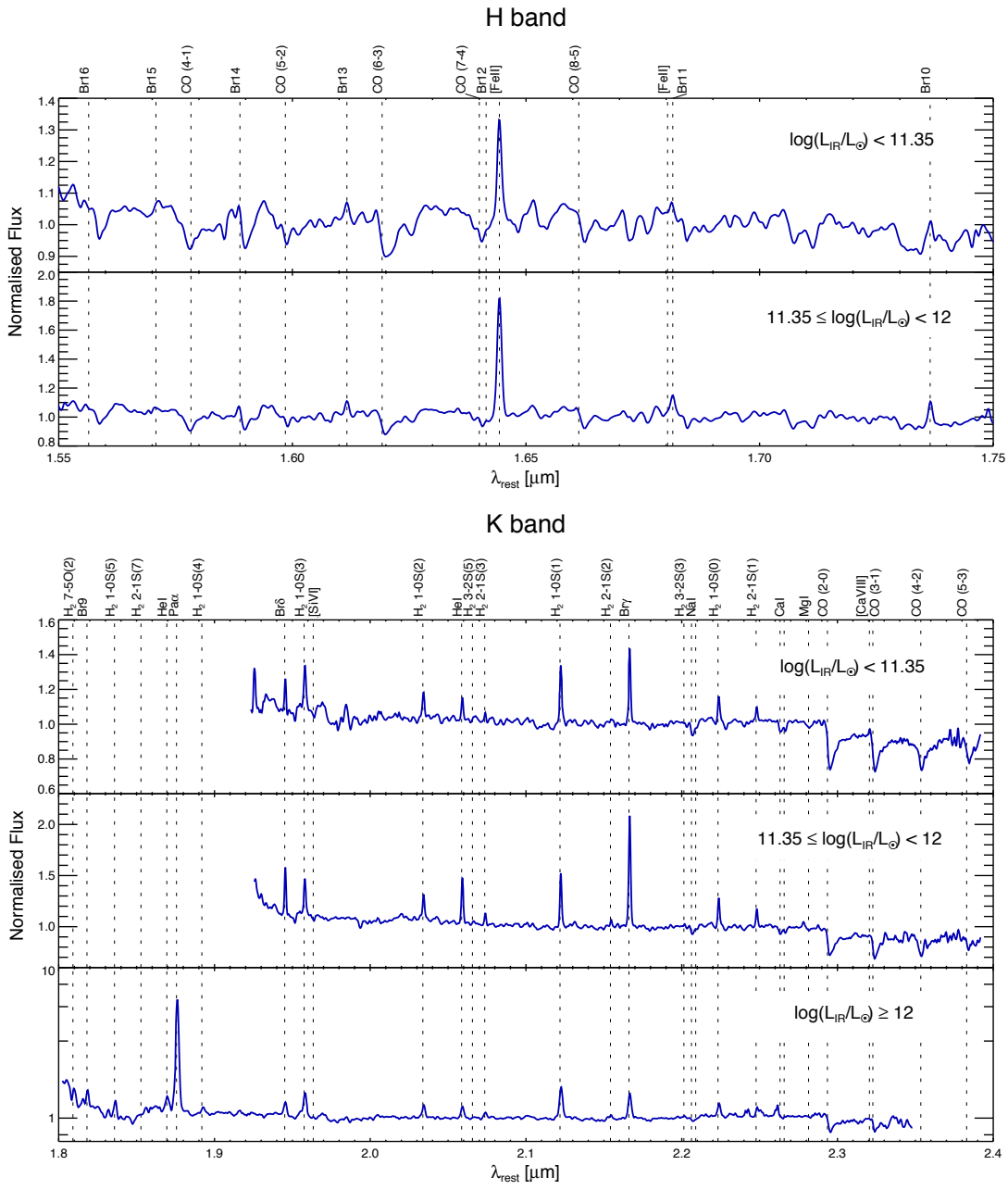

Figure 4.1: H- and K-band stacked spectra of the SINFONI sample - H- and K-band stacked spectra of the sample, divided into three subsets with $\log(L_{IR}/L_{\odot}) < 11.35$, $11.35 \leq \log(L_{IR}/L_{\odot}) < 12$, and $\log(L_{IR}/L_{\odot}) \geq 12$. The spectra are normalised to a linear fit of the continuum measured within the intervals [1.600, 1.610] μm and [1.690, 1.700] μm for the H band and [2.080, 2.115] μm and [2.172, 2.204] μm for the K band. From top to bottom, H-band and K-band spectra of the different subsets by increasing L_{IR}. The spectra are available in electronic form at the CDS via anonymous ftp to ftp://cdsarc.u-strasbg.fr (130.79.128.5) or via http://cdsweb.u-strasbg.fr/cgi-bin/qcat?J/A+A/.

4.3.7. Gas emission and line fluxes

We extracted the spectra of different regions of interest for all the galaxies of the sample, which comprise the nucleus (identified as the K-band continuum peak), the integrated spectrum over the FoV, and the peak of emission of Brγ (Paα for the ULIRGs subsample), H_2 1-0S(1), and [FeII]. For every region, we integrated the spectra within apertures of 400×400 pc for the LIRGs and 2×2 kpc for ULIRGs, and measured the flux of the Brγ, H_2 1-0S(1), and [FeII] lines for all the LIRGs of the sample and the Paα and H_2 1-0S(1) line flux for the ULIRGs subsample. Although the study of the ionised gas is focussed on the Paα line in the ULIRG subset, we have also made measurements of the Brγ line to directly compare with the results obtained for the LIRGs.

To obtain the line fluxes over the FoV, we only took the brightest spaxels in the H and K-band images (for the [FeII] and Brγ Paα and H_2 1-0S(1) respectively) into account, to include $\gtrsim$90% of the total flux in each image. This ensures that only those spaxels with the highest S/N are included in the spectra, and removes all those with a low surface brightness that contributes significantly to increasing the noise and the sky residuals in the spectra.

The line fitting is performed following the same procedure as in the spectral maps, by fitting a single Gaussian model to the line profile. To estimate the errors of the line fluxes, we implemented a Monte Carlo method. We measured the noise of the spectra as the *rms* of the residuals after subtracting the Gaussian profile. Taking this value of the noise into account, we constructed a total of $N = 1000$ simulated spectra whose lines are again fitted. The error of the measurements is obtained as the standard deviation of the fluxes of each line. The advantage of this kind of method is that the errors calculated not only consider the photon noise but also the uncertainties due to an improper line fitting or continuum level estimation.

The values of the line fluxes for the different regions in the sample of galaxies are shown in Table 4.5. Besides the gas emission, we also measured the equivalent width of the CO (2–0) band at 2.293 μm (W_{CO}) using the definition of Förster Schreiber 2000. This stellar feature is detected in all the galaxies of the LIRG subsample and in two ULIRGs (IRAS 17208-0014 and IRAS 23128-5919), since it lays out of our spectral coverage for the rest of the ULIRGs.

4.3.8. Stellar absorption features

Although the study of the stellar populations and of their kinematics, derived from the CO absorption lines, will be addressed in a forthcoming paper, we have included measurements of the equivalent width of the first CO absorption band (see Table 4.5) obtained using the

pPXF software (Cappellari & Emsellem, 2004) to fit a library of stellar templates to our data. We made use of the Near-IR Library of Spectral templates of the Gemini Observatory (Winge et al., 2009), which covers the wavelength range of 2.15 μm – 2.43 μm with a spectral resolution of 1 Å pixel^{-1}. The library contains a total of 23 late-type stars, from F7III to M3III, and was previously convolved to our SINFONI resolution.

4.4. Overview of the data

The wide spectral coverage of the SINFONI data allows us to study in detail a large number of spectral features that trace different phases of the interstellar medium and the stellar population (Bedregal et al., 2009). In this work we focus on the gas emission in LIRGs and ULIRGs by studying the brightest lines in the H and K bands, i.e. [FeII] at 1.644 μm, Paα at 1.876 μm, HeI at 2.059 μm, H_2 1-0S(1) at 2.122 μm and Brγ at 2.166 μm. The maps of these spectral features together with the K-band spectra of the nucleus (identified as the K-band peak), and of the brightest Brγ (or Paα for ULIRGs) region are shown in Figs. B.1 and B.2 for the sample of LIRGs and ULIRGs, respectively.

In the present section, we briefly describe the different physical mechanisms and processes that create the emission lines and stellar features observed in our data. The detailed study of these mechanisms are beyond the scope of the present work, but some of them will be addressed in the forthcoming papers of these series.

4.4.1. Hydrogen lines and 2D extinction maps

The overall structure of the ionised gas, mostly associated with recent star formation, is traced by the hydrogen recombination lines Paα for ULIRGs and Brγ for LIRGs. Although Brγ is also observed in the ULIRGs subsample, for this group we focus the study of the ionised gas on the Paα emission, since its brightness allows better measurements. The Brδ line at 1.945 μm is also observed in all the galaxies of the sample; however, for the LIRG subsample, it lies in a spectral region where the atmospheric transmission is not optimal and, for the ULIRG subset, it is too weak to be mapped.

It is well known that the bulk of luminosity produced in local (U)LIRGs is due to the large amount of dust that hides a large fraction of their star formation and nuclear activity (see Alonso-Herrero et al. 2006, García-Marín et al. 2009a and references therein). This dust is responsible for the absorption of UV photons that are then re-emitted at FIR and

NGC 2369				
Region	Brγ Flux	H_2 1-0S(1) Flux	[Fe II] Flux	W_{CO}
Nuclear	14.71 ± 0.59	10.68 ± 0.57	9.40 ± 0.58	12.3 ± 2.1
Integrated	78.46 ± 12.5	75.51 ± 8.54	91.13 ± 14.8	···
Brγ max†	15.27 ± 0.63	10.92 ± 0.57	10.21 ± 0.61	11.9 ± 1.8
H_2 1-0S(1)†	14.66 ± 0.59	10.58 ± 0.56	9.85 ± 0.59	12.0 ± 1.7
[FeII] max	11.16 ± 0.58	9.15 ± 0.45	9.72 ± 0.81	11.5 ± 1.3

NGC 3256‡				
Region	Brγ Flux	H_2 1-0S(1) Flux	[Fe II] Flux	W_{CO}
Nuclear	22.21 ± 0.33	19.13 ± 0.21	4.36 ± 0.47	11.3 ± 0.7
Integrated	± 4.45	± 3.40	± 6.39	···
	213.92	206.98	132.85	
Brγ max†	22.40 ± 0.36	18.85 ± 0.24	···	11.6 ± 0.5
H_2 1-0S(1)	4.17 ± 0.21	26.98 ± 0.75	···	10.3 ± 0.8
[FeII] max	···	···	4.02 ± 0.46	···

IRASF 12115-4656				
Region	Brγ Flux	H_2 1-0S(1) Flux	[Fe II] Flux	W_{CO}
Nuclear	0.85 ± 0.09	1.89 ± 0.18	···	8.9 ± 0.7
Integrated	69.71 ± 6.95	59.83 ± 6.20	···	···
Brγ max	0.80 ± 0.03	0.37 ± 0.03	···	9.5 ± 0.7
H_2 1-0S(1)†	0.87 ± 0.08	1.90 ± 0.18	···	8.9 ± 0.7
[FeII] max	···	···	···	···

IRASF 17138-1017				
Region	Brγ Flux	H_2 1-0S(1) Flux	[Fe II] Flux	W_{CO}
Nuclear	6.35 ± 0.11	3.06 ± 0.09	5.05 ± 0.14	11.1 ± 1.0
Integrated	89.48 ± 2.69	42.29 ± 1.97	61.55 ± 2.75	···
Brγ max	12.14 ± 0.13	1.75 ± 0.06	5.49 ± 0.11	8.8 ± 0.9
H_2 1-0S(1)†	6.35 ± 0.11	3.06 ± 0.09	5.05 ± 0.14	11.1 ± 1.0
[FeII] max	7.74 ± 0.10	1.90 ± 0.04	4.13 ± 0.08	8.7 ± 0.6

NGC 7130				
Region	Brγ Flux	H_2 1-0S(1) Flux	[Fe II] Flux	W_{CO}
Nuclear	17.32 ± 0.36	25.39 ± 0.44	49.26 ± 1.84	11.4 ± 0.7
Integrated	30.62 ± 1.43	51.12 ± 2.33	32.95 ± 2.40	···
Brγ max†	17.32 ± 0.36	25.39 ± 0.44	49.26 ± 1.84	11.4 ± 0.7
H_2 1-0S(1)†	16.84 ± 0.35	25.17 ± 0.44	49.02 ± 1.84	11.6 ± 0.9
[FeII] max†	17.32 ± 0.36	25.39 ± 0.44	49.26 ± 1.84	11.4 ± 0.7

NGC 3110				
Region	Brγ Flux	H_2 1-0S(1) Flux	[Fe II] Flux	W_{CO}
Nuclear	3.05 ± 0.08	2.98 ± 0.15	1.82 ± 0.22	10.5 ± 0.9
Integrated	45.92 ± 1.48	52.45 ± 2.77	22.66 ± 8.20	···
Brγ max	1.66 ± 0.03	1.08 ± 0.03	0.68 ± 0.06	8.2 ± 0.9
H_2 1-0S(1)†	3.05 ± 0.08	2.98 ± 0.15	1.82 ± 0.22	10.5 ± 0.9
[FeII] max†	2.70 ± 0.06	2.50 ± 0.12	1.59 ± 0.19	10.5 ± 1.1

ESO 320-G030				
Region	Brγ Flux	H_2 1-0S(1) Flux	[Fe II] Flux	W_{CO}
Nuclear	2.35 ± 0.29	16.62 ± 0.50	2.30 ± 0.77	11.4 ± 1.2
Integrated	82.80 ± 7.59	78.57 ± 6.83	49.03 ± 7.65	···
Brγ max	4.15 ± 0.13	2.06 ± 0.13	2.72 ± 0.21	11.1 ± 0.9
H_2 1-0S(1)†	2.07 ± 0.29	16.14 ± 0.49	2.12 ± 0.79	11.6 ± 1.1
[FeII] max†	2.67 ± 0.28	13.27 ± 0.43	2.41 ± 0.71	11.6 ± 1.1

NGC 5135				
Region	Brγ Flux	H_2 1-0S(1) Flux	[Fe II] Flux	W_{CO}
Nuclear	6.45 ± 0.20	9.65 ± 0.22	5.17 ± 0.25	7.1 ± 0.7
Integrated	49.39 ± 2.54	69.23 ± 4.13	42.71 ± 3.69	···
Brγ max	6.87 ± 0.11	4.40 ± 0.17	4.31 ± 0.17	11.4 ± 1.0
H_2 1-0S(1)†	6.45 ± 0.20	9.65 ± 0.22	5.17 ± 0.25	7.1 ± 0.7
[FeII] max	5.23 ± 0.16	10.64 ± 0.38	46.26 ± 1.29	13.4 ± 1.3

IC 4687				
Region	Brγ Flux	H_2 1-0S(1) Flux	[Fe II] Flux	W_{CO}
Nuclear	5.31 ± 0.11	3.27 ± 0.11	3.75 ± 0.23	12.3 ± 1.1
Integrated	± 3.77	59.31 ± 2.91	78.03 ± 7.14	···
	146.64			
Brγ max	7.28 ± 0.10	0.97 ± 0.03	2.64 ± 0.11	8.3 ± 1.0
H_2 1-0S(1)†	4.46 ± 0.09	2.86 ± 0.10	3.34 ± 0.23	11.9 ± 1.3
[FeII] max	7.05 ± 0.09	0.99 ± 0.03	2.86 ± 0.12	9.2 ± 1.0

IC 5179				
Region	Brγ Flux	H_2 1-0S(1) Flux	[Fe II] Flux	W_{CO}
Nuclear	13.70 ± 0.19	8.69 ± 0.32	8.48 ± 0.54	12.2 ± 1.2
Integrated	98.24 ± 6.98	61.19 ± 5.00	45.45 ± 6.25	···
Brγ max†	13.50 ± 0.17	8.06 ± 0.32	8.16 ± 0.52	12.2 ± 1.2
H_2 1-0S(1)†	13.42 ± 0.17	8.34 ± 0.32	8.39 ± 0.52	12.2 ± 1.2
[FeII] max†	13.12 ± 0.16	7.60 ± 0.31	7.98 ± 0.50	12.2 ± 1.1

Table 4.5a: Brγ, H_2 1-0S(1), and [FeII] integrated observed fluxes in units of [$\times 10^{-16}$ erg s^{-1}cm^{-2}], and CO (2-0) equivalent widths (in [Å]) of the LIRG subsample. Spectra are integrated within a 400×400 pc aperture, covering the nuclear region defined as the brightest spaxel in the K-band; the integrated emission of the FoV, defined as the integrated flux of those spaxels that contain at least the $\gtrsim$90% of the total continuum flux in each band; and the peaks of the Brγ, H_2 1-0S(1) and [FeII] emission, centred on the brightest spaxel in each of the respective maps. The errors are obtained by a Monte Carlo method of N = 1000 simulations of each spectra. † Regions that are coincident with the nucleus of the object. The spectra are extracted and the lines are fitted independently.‡The Brγ peak of emission does not coincide with the stellar nucleus of the object but with the region we have adopted as the 'nucleus' (see the main text for a further explanation).

IRAS 06206-6315			
Region	Paα Flux	H_2 1-0S(1) Flux	W_{CO}
Nuclear	32.91 ± 0.90	6.06 ± 0.12	···
Integrated	42.47 ± 6.54	25.13 ± 1.42	···
Paα max†	32.34 ± 0.90	5.85 ± 0.12	···
H_2 1-0S(1)†	32.91 ± 0.90	6.06 ± 0.12	···

IRAS 14348-1447			
Region	Paα Flux	H_2 1-0S(1) Flux	W_{CO}
Nuclear	45.51 ± 0.36	10.21 ± 0.19	···
Integrated	144.90 ± 2.94	39.39 ± 0.81	···
Paα max†	45.51 ± 0.36	10.21 ± 0.19	···
H_2 1-0S(1)†	45.33 ± 0.38	10.25 ± 0.20	···

IRAS 21130-4446			
Region	Paα Flux	H_2 1-0S(1) Flux	W_{CO}
Nuclear	26.98 ± 0.98	3.10 ± 0.11	···
Integrated	107.65 ± 2.62	6.00 ± 0.25	···
Paα max	20.76 ± 0.19	0.57 ± 0.04	···
H_2 1-0S(1)†	27.75 ± 0.98	2.96 ± 0.10	···

IRAS 23128-5919			
Region	Paα Flux	H_2 1-0S(1) Flux	W_{CO}
Nuclear	336.35 ± 6.04	11.76 ± 0.35	8.1 ± 0.7
Integrated	578.33 ± 8.60	26.42 ± 1.54	9.0 ± 1.2
Paα max†	335.42 ± 6.01	11.80 ± 0.35	8.2 ± 0.8
H_2 1-0S(1)†	335.42 ± 6.01	11.80 ± 0.35	8.2 ± 0.8

IRAS 12112+0305			
Region	Paα Flux	H_2 1-0S(1) Flux	W_{CO}
Nuclear	45.48 ± 0.56	3.62 ± 0.10	···
Integrated	190.87 ± 6.61	32.44 ± 1.59	···
Paα max†	45.20 ± 0.56	3.59 ± 0.10	···
H_2 1-0S(1)	42.67 ± 0.42	10.39 ± 0.13	···

IRAS 17208-0014			
Region	Paα Flux	H_2 1-0S(1) Flux	W_{CO}
Nuclear	437.13 ± 14.26	60.50 ± 1.31	11.8 ± 1.1
Integrated	519.96 ± 16.00	96.47 ± 9.99	···
Paα max†	437.13 ± 14.26	60.50 ± 1.31	11.8 ± 1.1
H_2 1-0S(1)†	435.91 ± 14.68	60.70 ± 1.35	11.8 ± 1.3

IRAS 22491-1808			
Region	Paα Flux	H_2 1-0S(1) Flux	W_{CO}
Nuclear	11.68 ± 0.18	0.75 ± 0.05	···
Integrated	54.85 ± 1.18	10.22 ± 0.62	···
Paα max	27.17 ± 0.43	8.64 ± 0.16	···
H_2 1-0S(1)	27.45 ± 0.42	8.65 ± 0.17	···

Table 4.5b: Paα and H_2 1-0S(1) integrated observed fluxes in units of [$\times 10^{-16}$ erg s^{-1}cm^{-2}], and CO (2-0) equivalent widths (in [Å]) of the ULIRGs subsample. Spectra are integrated within a 2×2 kpc aperture, covering the nuclear region defined as the brightest spaxel in the K-band; the integrated emission of the FoV, defined as the integrated flux of those spaxels that contain at least the $\gtrsim$90% of the total continuum flux in each band; and the peaks of the Paα and H_2 1-0S(1) emission, centred on the brightest spaxel in each of the respective maps. The errors are obtained by a Monte Carlo method of N = 1000 simulations of each spectra. † Regions that are coincident with the nucleus of the object. The spectra are extracted and the lines are fitted independently.

NGC 2369			
Region	Brγ σ	H_2 1-0S(1) σ	[Fe II] σ
Nuclear	119 ± 5	113 ± 6	113 ± 8
Integrated	166 ± 25	133 ± 13	174 ± 31
Brγ max†	124 ± 5	116 ± 6	120 ± 8
H_2 1-0S(1)†	121 ± 5	113 ± 6	116 ± 8
[FeII] max	136 ± 7	111 ± 6	125 ± 13

NGC 3110			
Region	Brγ σ	H_2 1-0S(1) σ	[Fe II] σ
Nuclear	78 ± 2	98 ± 6	69 ± 13
Integrated	124 ± 4	145 ± 8	91 ± 29
Brγ max	50 ± 1	48 ± 2	30 ± 11
H_2 1-0S(1)†	78 ± 2	98 ± 6	69 ± 13
[FeII] max†	72 ± 2	89 ± 5	62 ± 14

NGC 3256			
Region	Brγ σ	H_2 1-0S(1) σ	[Fe II] σ
Nuclear	110 ± 1	86 ± 1	57 ± 12
Integrated	82 ± 2	83 ± 1	84 ± 6
Brγ max†	113 ± 2	87 ± 1	...
H_2 1-0S(1)	103 ± 7	130 ± 4	...
[FeII] max	...	...	56 ± 13

ESO 320-G030			
Region	Brγ σ	H_2 1-0S(1) σ	[Fe II] σ
Nuclear	91 ± 13	113 ± 4	72 ± 23
Integrated	137 ± 10	135 ± 10	119 ± 18
Brγ max	48 ± 2	51 ± 5	52 ± 9
H_2 1-0S(1)†	87 ± 15	112 ± 4	71 ± 27
[FeII] max†	89 ± 11	109 ± 4	71 ± 26

IRASF 12115-4656			
Region	Brγ σ	H_2 1-0S(1) σ	[Fe II] σ
Nuclear	82 ± 12	96 ± 11	...
Integrated	155 ± 15	151 ± 13	...
Brγ max	38 ± 4	29 ± 8	...
H_2 1-0S(1)†	82 ± 12	97 ± 11	...
[FeII] max	...	...	...

NGC 5135			
Region	Brγ σ	H_2 1-0S(1) σ	[Fe II] σ
Nuclear	84 ± 3	67 ± 2	61 ± 5
Integrated	75 ± 6	78 ± 7	58 ± 11
Brγ max	65 ± 1	66 ± 3	50 ± 4
H_2 1-0S(1)†	84 ± 3	67 ± 2	61 ± 5
[FeII] max	67 ± 3	90 ± 4	205 ± 7

IRASF 17138-1017			
Region	Brγ σ	H_2 1-0S(1) σ	[Fe II] σ
Nuclear	74 ± 1	67 ± 2	65 ± 3
Integrated	106 ± 4	100 ± 5	97 ± 5
Brγ max	73 ± 1	56 ± 3	66 ± 2
H_2 1-0S(1)†	74 ± 1	67 ± 2	65 ± 3
[FeII] max	62 ± 1	52 ± 1	59 ± 2

IC 4687			
Region	Brγ σ	H_2 1-0S(1) σ	[Fe II] σ
Nuclear	77 ± 2	75 ± 3	67 ± 6
Integrated	117 ± 3	112 ± 5	93 ± 9
Brγ max	49 ± 1	43 ± 3	45 ± 4
H_2 1-0S(1)†	80 ± 2	70 ± 3	69 ± 6
[FeII] max	50 ± 1	43 ± 3	46 ± 4

NGC 7130			
Region	Brγ σ	H_2 1-0S(1) σ	[Fe II] σ
Nuclear	93 ± 2	96 ± 2	143 ± 8
Integrated	64 ± 4	78 ± 5	57 ± 9
Brγ max†	93 ± 2	96 ± 2	143 ± 8
H_2 1-0S(1)†	93 ± 2	96 ± 2	143 ± 8
[FeII] max†	93 ± 2	96 ± 2	143 ± 8

IC 5179			
Region	Brγ σ	H_2 1-0S(1) σ	[Fe II] σ
Nuclear	77 ± 1	96 ± 4	84 ± 7
Integrated	130 ± 9	117 ± 9	123 ± 13
Brγ max†	74 ± 1	91 ± 4	80 ± 7
H_2 1-0S(1)†	74 ± 1	93 ± 4	82 ± 7
[FeII] max†	72 ± 1	89 ± 4	79 ± 7

Table 4.6a: Brγ, H_2 1-0S(1), and [FeII] velocity dispersion values in units of [km s^{-1}] of the LIRGs subsample. The method of extracting the spectra and the selection criteria for the regions are the same as for Table 4.5a.

IRAS 06206-6315		
Region	Paα σ	H_2 1-0S(1) σ
Nuclear	177 ± 4	139 ± 2
Integrated	148 ± 93	117 ± 7
Paα max†	177 ± 4	139 ± 3
H_2 1-0S(1)†	177 ± 4	139 ± 2

IRAS 12112+0305		
Region	Paα σ	H_2 1-0S(1) σ
Nuclear	134 ± 1	118 ± 3
Integrated	153 ± 5	160 ± 8
Paα max†	134 ± 1	119 ± 3
H_2 1-0S(1)	121 ± 1	150 ± 2

IRAS 14348-1447		
Region	Paα σ	H_2 1-0S(1) σ
Nuclear	109 ± 1	111 ± 2
Integrated	124 ± 3	127 ± 3
Paα max†	109 ± 1	111 ± 2
H_2 1-0S(1)†	108 ± 1	111 ± 2

IRAS 17208-0014		
Region	Paα σ	H_2 1-0S(1) σ
Nuclear	219 ± 6	187 ± 3
Integrated	201 ± 5	200 ± 18
Paα max†	219 ± 6	187 ± 3
H_2 1-0S(1)†	222 ± 6	189 ± 3

IRAS 21130-4446		
Region	Paα σ	H_2 1-0S(1) σ
Nuclear	132 ± 6	131 ± 4
Integrated	119 ± 3	113 ± 5
Paα max	75 ± 0	74 ± 6
H_2 1-0S(1)†	137 ± 6	127 ± 4

IRAS 22491-1808		
Region	Paα σ	H_2 1-0S(1) σ
Nuclear	66 ± 1	83 ± 6
Integrated	76 ± 2	102 ± 8
Paα max	105 ± 2	125 ± 2
H_2 1-0S(1)	105 ± 1	125 ± 2

IRAS 23128-5919		
Region	Paα σ	H_2 1-0S(1) σ
Nuclear	116 ± 2	81 ± 3
Integrated	104 ± 2	87 ± 6
Paα max†	116 ± 2	82 ± 3
H_2 1-0S(1)†	116 ± 2	82 ± 3

Table 4.6b: Paα and H_2 1-0S(1) velocity dispersion values in units of [km s^{-1}] of the ULIRGs subsample. The method for extracting the spectra and the selection criteria for the regions are the same as for Table 4.5b.

submillimetre wavelengths. A detailed 2D quantitative study of the internal extinction could be performed by using the Brδ/Brγ ratios in LIRGs and Brγ/Paα in ULIRGs. This study of the objects in the sample will be presented in the next paper of this series (Piqueras López et al. 2013, Chapter 5).

The detailed characterisation of the extinction is essential to achieve accurate measurements of the SFR in these dusty environments. This treatment of the extinction allows us to obtain maps of the SFR surface density that are corrected for extinction on a spaxel-by-spaxel basis. The analysis of the SFR in the objects of the sample, based on the Brγ and Paα maps presented in this work, will be addressed in Piqueras-López et al 2014 (in preparation, Chapter 6).

4.4.2. Emission lines and star formation

The hydrogen recombination lines have been widely used as a primary indicator of recent star-formation activity, where UV photons from massive OB stars keep the gas in an ionised state. The measurements of the Brγ equivalent width, in combination with the stellar population synthesis models, such as STARBURST99 (Leitherer et al., 1999) or Claudia Maraston's models (Maraston 1998, 2005), could be used to constrain the age of the youngest stellar population. The HeI emission is also usually associated to star-forming regions, and used as a tracer of the youngest OB stars, given its high ionisation potential of 24.6 eV. This emission may depend on different factors, such us density, temperature, dust content, and He/H relative abundance and ionisation fractions.

The [FeII] emission is usually associated with regions where the gas is partially ionised by X-rays or shocks (Mouri et al., 2000). Shocks from supernovae cause efficient grain destruction that releases the iron atoms contained in the dust. The atoms are then singly ionised by the interstellar radiation field and excited in the extended post-shock region by free electron collision on timescales of $\sim 10^4$ yr. The [FeII] lines at 1.257 μm and 1.644 μm are widely used to estimate the supernova rate in starbursts (Colina 1993, Alonso-Herrero et al. 2003, Labrie & Pritchet 2006, Rosenberg et al. 2012 and references therein), whereas the $EW_{[FeII]}$ could also be used, in combination with the $EW_{Br\gamma}$, to constrain the age of the stellar populations in the synthesis models.

4.4.3. H_2 lines and excitation mechanisms

The H_2 1-0S(1) line is used to trace the warm molecular gas, since it is the brightest H_2 emission line in the K band and it is well detected in all the objects with sufficient S/N. Furthermore, the presence of several roto-vibrational transitions of the molecular hydrogen within the K band allows studying the excitation mechanisms of the H_2: fluorescence due to the excitation by UV photons from AGB (Asymptotic Giant Branch) stars in PDRs, thermal processes like collisional excitation by SN fast shocks, or X-rays (van der Werf 2000, Davies et al. 2003, 2005). The determination of the H_2 excitation mechanisms in general requires measurements of several lines, usually weak lines, since the different processes mentioned may rise to similar intense and thermalised 1-0 emissions.

Based on the relative fluxes of the transitions to the brightest H_2 1-0S(1) line, we could obtain population diagrams of the emitting regions. In these diagrams, the population of each level in an ideal thermalized PDR could be determined as a function of the excitation temperature. The presence of non-thermal processes like UV fluorescence is translated to an overpopulation of the upper levels and a deviation from the ideal thermalised model. However, the way these levels are overpopulated due to non-thermal processes is complex, and might depend on several parameters like density or the intensity of the illuminating UV field (Davies et al. 2003, 2005, Ferland et al. 2008 and references therein). The detailed study of the excitation mechanisms of the molecular hydrogen will be addressed in a future paper of this series.

4.4.4. Coronal lines as AGN tracers

The [SiVI] at 1.963 μm and [CaVIII] at 2.321 μm coronal lines are the main AGN tracers within the K-band. However, the [CaVIII] line is too faint (typically $\times$4 fainter than [SiVI], Rodríguez-Ardila et al. 2011) and to close to CO (3-1) to be measured easily. Given the high ionisation potential of 167 eV for [SiVI] and 128 eV for [CaVIII], the outskirts of the broad-line region and extended narrow-line regions have been proposed as possible locations for the formation of these lines in AGNs. Although which mechanism is responsible for the emission remains unclear, there are two main processes proposed: photoionisation due to the central source and shocks due to high-velocity clouds and the NLR (Narrow Line Region) gas (see Rodríguez-Ardila et al. 2011 and references therein).

4.4.5. Line ratios

The interpretation of the H_2 1-0S(1)/Brγ ratio is sometimes not straightforward since H_2 could be excited by both thermal and radiative processes, in contrast to the [FeII] emission that is predominantly powered by thermal mechanisms. This ratio is in principle not biased by extinction, and starburst galaxies and HII regions empirically exhibit lower H_2/Brγ ratios, whereas Seyfert galaxies and LINERs (Low-Ionization Nuclear Emission-line Regions) show higher values ($0.6 \lesssim H_2$ 1-0S(1)/Br$\gamma \lesssim 2.0$, Dale et al. 2004, Rodríguez-Ardila et al. 2005, Riffel et al. 2010, Valencia-S et al. 2012).

In combination with the Brγ emission that traces the photoionised regions, the [FeII]/Brγ ratio allows us to distinguish regions where the gas is ionised by star formation activity where the [FeII] is expected to be weak (Mouri et al., 2000), from zones where the gas is partially ionised by shocks (Alonso-Herrero et al., 1997). Since [FeII] is not expected in HII regions where iron would be in higher ionisation states, we could trace different ionisation mechanisms and efficiencies by using the [FeII]/Brγ ratio, and probe the excitation mechanisms that produce the [FeII] line in those regions where the emission has stellar origin. In addition, the [FeII]/Brγ ratio depends on the grain depletion, and a high depletion of iron would reduce the number of atoms available in the interstellar medium, hence reduce the line ratio (Alonso-Herrero et al., 1997).

Although the HeI line could be used as a primary indicator of stellar effective temperature, interpreting the emission and the HeI/Brγ ratio without a detailed photoionisation model is still controversial (Doherty et al. 1995, Lumsden et al. 2001, 2003). In addition, the HeI transition is also influenced by collisional excitation, and a full photoionisation treatment is not enough to predict the line emission (Shields, 1993).

4.4.6. Absorption lines and stellar populations

Besides the emission lines, there are different absorption features that lie within the K band, such as the NaI doublet at 2.206 μm and 2.209 μm, the CaI doublet at 2.263 μm, and 2.266 μm and the CO absorption bands CO (2–0) at 2.293 μm, CO (3–1) at 2.323 μm or CO (4-2) at 2.354 μm. The absorption features, such as the CO bands and the NaI doublet, are typical of K and later stellar types, and they also trace red giant and supergiant populations. Given the limited S/N of the NaI doublet, it is not possible to map the absorption with the present data, but it could be suitable for integrated analysis. On the other hand, the CO (2–0) band can be used to spatially sample the stellar component of all the LIRGs of the

sample and in two of the ULIRGs. Both EW_{CO} and EW_{NaI} could be used in combination with the stellar population synthesis models to constrain the age of the stellar populations (see Bedregal et al. 2009).

4.5. Results and discussion

Most of the LIRGs of the sample are spiral galaxies with some different levels of interaction, ranging from isolated galaxies as ESO 320-G030 to close interacting systems as IC 4687+IC 4686 or mergers like NGC 3256 (Lípari et al., 2000), and to objects that show long tidal tails several kiloparsecs away from its nucleus (e. g. NGC 7130, Fig. B.1i). The emission from ionised and molecular hydrogen has different morphologies in many galaxies of the LIRGs subsample. The ULIRG subsample contains mainly interacting systems in an ongoing merging process with two well-differentiated nuclei. The Paα emission extends over several kiloparsecs with bright condensations not observed in the continuum maps. The molecular hydrogen emission, on the other hand, is rather compact ($\lesssim 2-3$ kpc) and is associated with the nuclei of the systems. An individual description of the more relevant features of the gas emission morphology for each galaxy can be found in Appendix A. We will now discuss each gas phase and the stellar component separately.

4.5.1. Ionised gas

The dynamical structures as spiral arms are clearly delineated on the ionised gas maps traced by the Brγ (LIRGs) and Paα (ULIRGs) lines. The observed ionised gas emission in LIRGs is dominated by high surface brightness clumps associated with extranuclear star-forming regions located in circumnuclear rings or spiral arms at radial distances of several hundred parsecs. The nuclei are also detected as bright Brγ sources in several galaxies but represent the maximum emission peak in only a small fraction ($\sim$33%) of LIRGs. These results are in excellent agreement with those derived from the Paα emission in Alonso-Herrero et al. (2006) using HST NICMOS images for all the objects of our LIRG sample, with the exception of IRASF 12115-4656, which was not included in their sample. On the other hand, the main nucleus is the brightest Paα emission peak in the majority ($\sim$71%) of ULIRGs, also showing emission peaks along the tidal tails, secondary nucleus, or in extranuclear regions at distances of 2–4 kpc from their centre. However, since ULIRGs in our sample are about four to five times more distant than our LIRGs, the typical angular resolution of our SINFONI

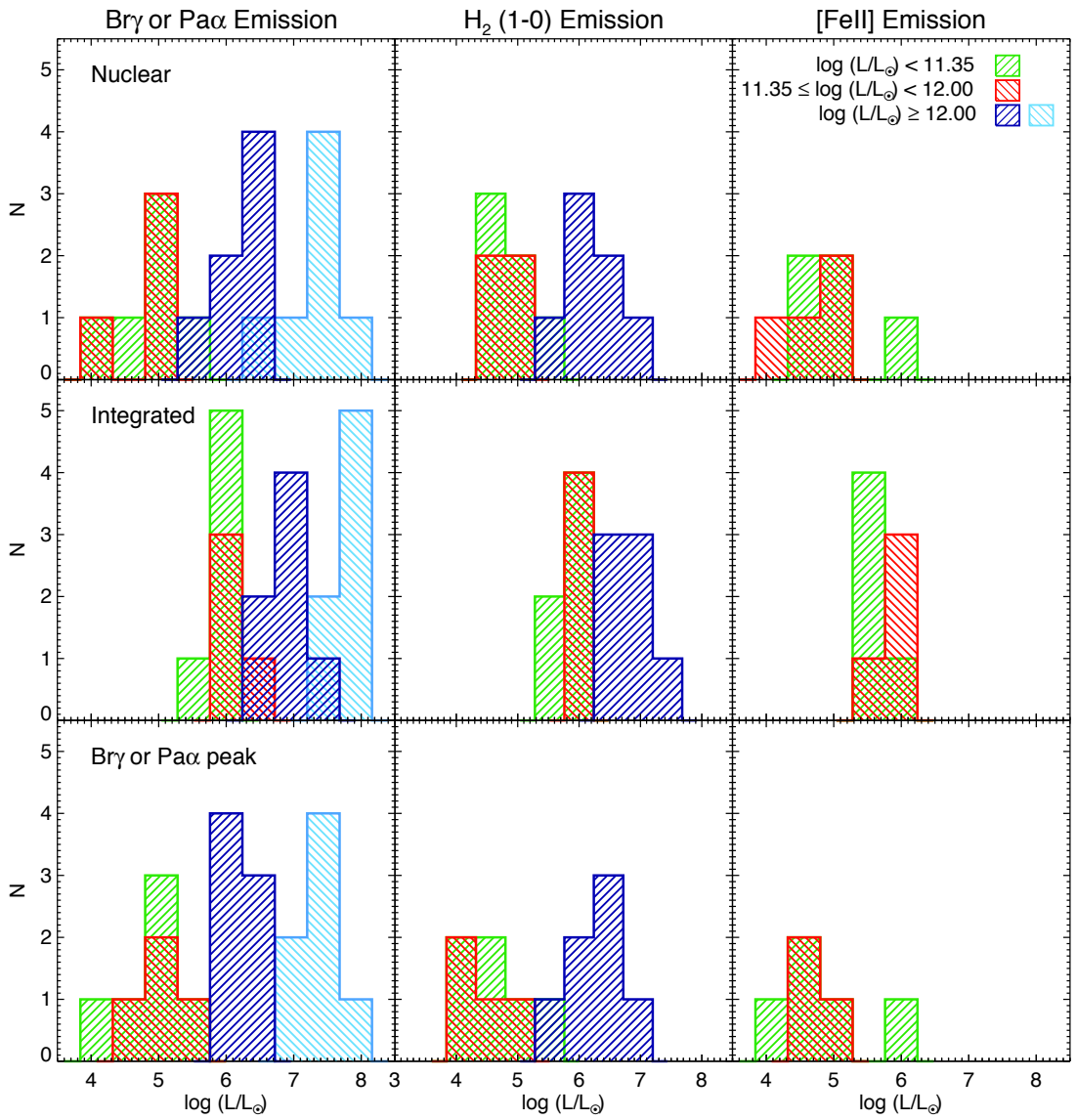

Figure 4.2: Luminosity distributions. - Luminosity distribution of the Brγ, H_2 1-0S(1), and [FeII] emission. From top to bottom, the histograms show the distribution of the total luminosity in solar units of the lines measured in the nucleus (defined by aperture "A" in Figs. B.1 and B.2), the integrated FoV, and the peak of the Brγ (Paα) emission. For the distributions of the ionised gas (first column), we have also included the Paα emission in light blue for the ULIRGs. Note: Brγ (Paα) peak coincides with the nucleus in $\sim$ 33% of the LIRGs and in the $\sim$71% of the ULIRGs.

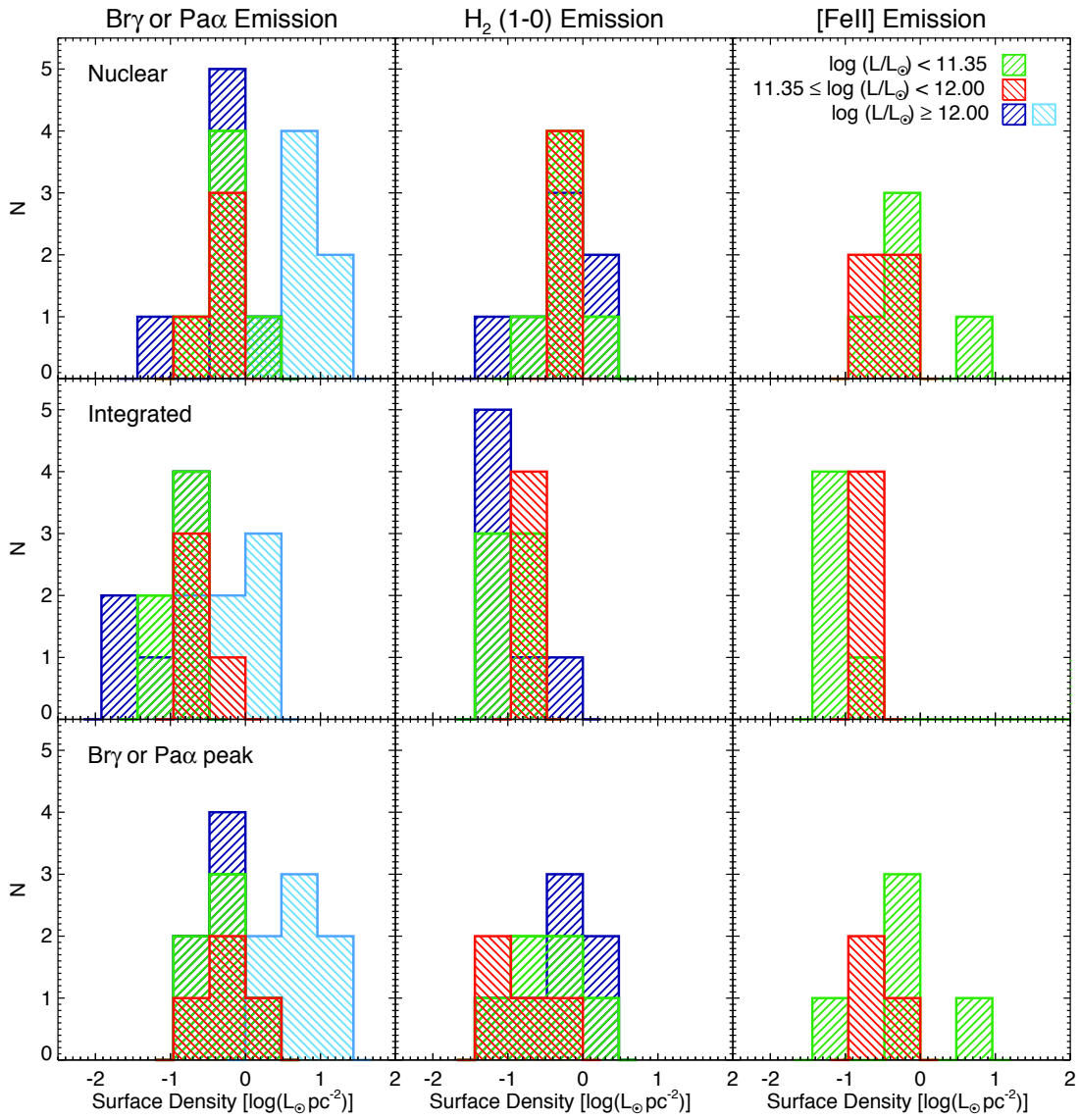

Figure 4.3: Surface density distributions. - Surface density distribution of the Brγ, H_2 1-0S(1), and [FeII] emission. From top to bottom, the histograms show the distribution of the surface density in solar units per unit of area (pc^2) of the lines measured in the nucleus (defined by aperture "A" in Figs. B.1 and B.2), the integrated FoV, and the peak of the Brγ (Paα) emission. For the distributions of the ionised gas (first column), we have also included the Paα emission in light blue for the ULIRGs. The Brγ (Paα) peak coincides with the nucleus in $\sim$ 33% of the LIRGs and in the $\sim$71% of the ULIRGs.

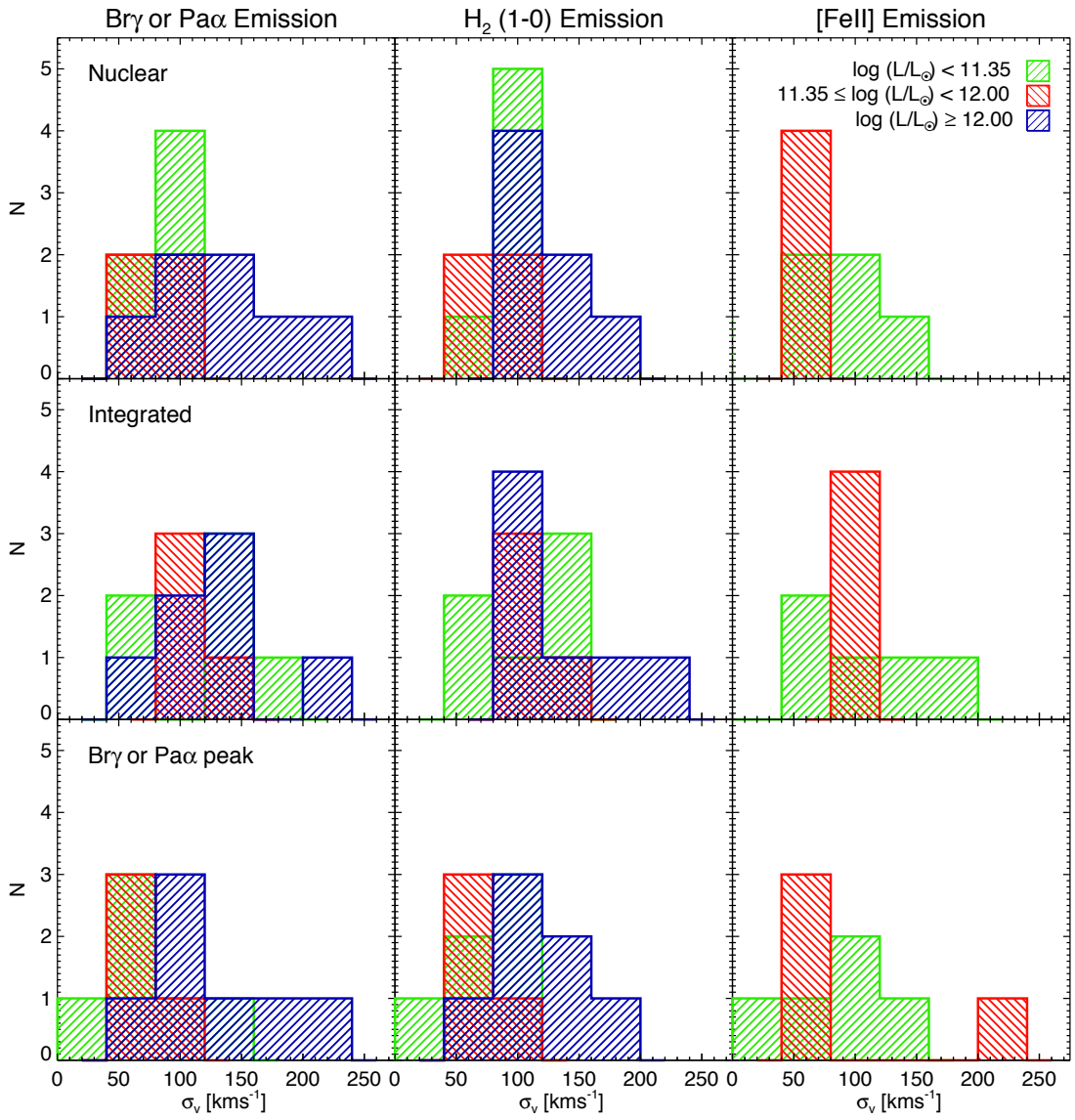

Figure 4.4: Velocity dispersion distributions. - Distributions of the velocity dispersion of the ionised gas (Brγ for LIRGs Paα for ULIRGs), H_2 1-0S(1), and [FeII] emission. From top to bottom, the histograms show the distributions of the velocity dispersion measured in the nucleus (defined by aperture "A" in Figs. B.1 and B.2), the integrated FoV, and the peak of the Brγ (Paα) emission. The Brγ (Paα) peak coincides with the nucleus in $\sim$ 33% of the LIRGs and in the $\sim$71% of the ULIRGs.

maps for ULIRGs covers sizes of about 1.5 kpc, and therefore the Paα peak emission detected in the nuclei could still be due to circumnuclear star-forming regions, as in LIRGs.

The surface density and total luminosity distributions of the Brγ (and Paα for the ULIRG subsample) are presented in Figs. 4.2 and 4.3. On average, the observed (i.e. uncorrected for internal extinction) luminosities of the Brγ brightest emitting region are $\sim 1.2 \times 10^5\,L_\odot$ for LIRGs and $\sim 2.3 \times 10^6\,L_\odot$ for ULIRGs, accounting for about $\sim 10\%$ and $\sim 43\%$ of the integrated Brγ luminosity, respectively. There is a factor $\sim$20 difference in luminosity between LIRGs and ULIRGs. Although the ULIRGs are intrinsically more luminous, this difference is also due to a distance effect since the angular aperture used to obtain the luminosities covers for ULIRGs an area 25 times larger than for LIRGs. For the ULIRG subset, we have also measured peak Paα luminosities of the order of $4.5 \times 10^7\,L_\odot$, in agreement with the expected value derived from Brγ luminosities assuming case B recombination ratios and no extinction.

The observed Brγ surface luminosity densities of the Brγ (and Paα) brightest emitting regions are $\sim 0.7\,L_\odot\,pc^{-2}$ and $\sim 0.6\,L_\odot\,pc^{-2}$, on average, for LIRGs and ULIRGs, respectively, whereas the Paα surface density for the ULIRG subset is $\sim 6\,L_\odot\,pc^{-2}$. Figure 4.3 shows that the distributions of the Brγ surface luminosity density for the different luminosity bins are very similar for the Brγ (and Paα) peak and the nucleus of the objects, and range between $\sim 0.1\,L_\odot\,pc^{-2}$ and $\sim 3\,L_\odot\,pc^{-2}$.

As shown in Fig. 4.2, the luminosity of Brγ ranges from $\sim 1.7 \times 10^4\,L_\odot$ to $\sim 5.1 \times 10^6\,L_\odot$ in the nuclear regions of LIRGs, and the Paα emission reaches up to $\sim 5.0 \times 10^7\,L_\odot$ in ULIRGs. Assuming the standard star formation rate to Hα luminosity ratio given by the expression (Kennicutt, 1998),

$$SFR(M_\odot yr^{-1}) = 7.9 \times 10^{-42} \times L(H\alpha)(erg\,s^{-1}),$$

an estimate of the SFR surface densities, uncorrected for internal reddening, can be directly obtained from the previous expression if the Hα to Paα and Brγ recombination factors are taken into account:

$$\begin{aligned} SFR(M_\odot yr^{-1}) &= 6.8 \times 10^{-41} \times L(P\alpha)(erg\,s^{-1}) \\ &= 8.2 \times 10^{-40} \times L(Br\gamma)(erg\,s^{-1}). \end{aligned}$$

For LIRGs, the mean SFR surface densities integrated over areas of several kpc^2, range between 0.4 and 0.9 $M_\odot$ yr^{-1} kpc^{-2} with peaks of about 2−2.5 $M_\odot$ yr^{-1} kpc^{-2} in smaller regions (0.16 kpc^2) associated with the nucleus or the brightest Brγ region. For ULIRGs, the corresponding values are similar, ∼0.4 for the integrated emission and ∼ 2 $M_\odot$ yr^{-1} kpc^{-2} for peak emission. However, since ULIRGs are at distances further away than LIRGs, the sizes of the overall ionised regions and brightest emission peaks covered by the SINFONI data are greater than those in LIRGs, and they correspond to 100−200 kpc^2 and 4 kpc^2, respectively. A detailed study of the star formation is presented in Chapter 6.

We estimated the extinction effects by comparing the observed Brγ/Brδ and Brγ/Paα ratios (for LIRGs and ULIRGs, respectively) with the theoretical ones derived from a case B recombination. We measured A_V values that range from ∼2–3 mag up to ∼10–12 mag in the nuclei of the objects (Chapter 5). This is translated to extinction values from ∼ 0.3 mag to ∼ 1.0 mag at Brγ wavelengths, and from ∼ 0.4 mag to ∼ 1.6 mag at Paα, and indicates that the internal extinction in these objects still plays a role at these wavelengths. These values are similar to those obtained by Alonso-Herrero et al. (2006) from the nuclear emission in LIRGs. From the detailed 2D study of the internal extinction that will be presented in Chapter 5, we estimated the median visual extinction for each luminosity subsamples of LIRGs and ULIRGs. These values are $A_{V,LIRGs} = 5.27$ mag and $A_{V,ULIRGs} = 6.48$ mag, that correspond to $A_{Br\gamma} = 0.5$ mag and $A_{Pa\alpha} = 0.9$ mag respectively.

Considering the median extinction values presented above, the Brγ and Paα luminosities, hence the SFR surface densities, are underestimated approximately by a factor ×1.7 in LIRGs and ×2.5 in ULIRGs. However, on scales of a few kpc or less, the distribution of dust in LIRGs and ULIRGs is not uniform, and it shows a patchy structure that includes almost transparent regions and very obscured ones (see García-Marín et al. 2009a and Chapter 5). This non-uniform distribution of the dust implies that the correction from the extinction depends on the sampling scale, so that the correction to the SFR would depend on the scales where the Brγ (Paα) is sampled. For further discussion of the extinction and the implications of the sampling scale in its measurements, please see Chapter 5.

A detailed analysis of SFR surface densities based on the Brγ, Paα, and Hα emission lines will be presented elsewhere (Piqueras López et al. 2014, in preparation, Chapter 6).

4.5.2. Warm molecular gas

The H_2 emission is associated with the nuclear regions of the objects, either to the main nucleus or to the secondary in the interacting systems. In some cases, its maximum does not coincide with the Brγ peak, although in all the LIRGs and $\sim 71\%$ of the ULIRGs it coincides with the main nucleus, identified as the brightest region in the K-band image. The typical H_2 1-0S(1) luminosity of the nuclei ranges from $\sim 1.3 \times 10^5\,L_\odot$ for the LIRG subsample up to $\sim 4.6 \times 10^6\,L_\odot$ for the ULIRGs, and accounts for $\sim 13\%$ and $\sim 41\%$ of the total luminosity measured in the entire FoV. The H_2 luminosity observed in the nucleus and in the Brγ (Paα) peak in both LIRGs and ULIRGs is very similar to the Brγ luminosity. The range of observed luminosity in the nuclei spans from $\sim 4.2 \times 10^4\,L_\odot$ to $\sim 6.8 \times 10^6\,L_\odot$, and is also very similar to the distribution observed for the Brγ emission. Since the H_2 $(1-0)$/Brγ ratio is close to one (range of 0.4 to 1.4, see Fig. 4.7), the surface brightness values derived for the H_2 emission are similar to those obtained for Brγ (see Figure 4.3).

4.5.3. Partially ionised gas

The [FeII] maps reveal that the emission roughly traces the same structures as the Brγ line, although the emission peaks are not spatially coincident in some of the objects, and the [FeII] seems to be more extended and diffuse. In $\sim 55\%$ of the LIRGs, the peak of the [FeII] emission is measured in the nucleus, with typical luminosities of $\sim 1.2 \times 10^5\,L_\odot$ on scales of $\sim 0.16\,\mathrm{kpc}^2$. The nuclear emission accounts on average for $\sim 16\%$ of the total observed luminosity. The differences in the morphology between the ionised and partially ionised gas could be understood in terms of the local distribution of the different stellar populations: although both lines trace young star-forming regions, the Brγ emission is enhanced by the youngest population of OB stars of $\lesssim 6\,\mathrm{Myr}$, whereas the [FeII] is mainly associated with the supernova explosions of more evolved stellar populations of $\sim 7.5\,\mathrm{Myr}$ (see STARBURST99 models, Leitherer et al. 1999).

4.5.4. Coronal line emission

The [SiVI] coronal line at $1.963\,\mu$m (see Fig. 4.5) is detected in two LIRGs (NGC 5135 and IRASF 12115-4656) and in one ULIRG (IRAS 23128-5919), with a tentative detection in another LIRG (NGC 7130). The [SiVI] line has a high ionisation potential (167 eV) and it is associated with Seyfert activity where the gas is ionised outside the broad line region of the AGN (Bedregal et al., 2009). The [SiVI] emission is usually rather compact, concentrated

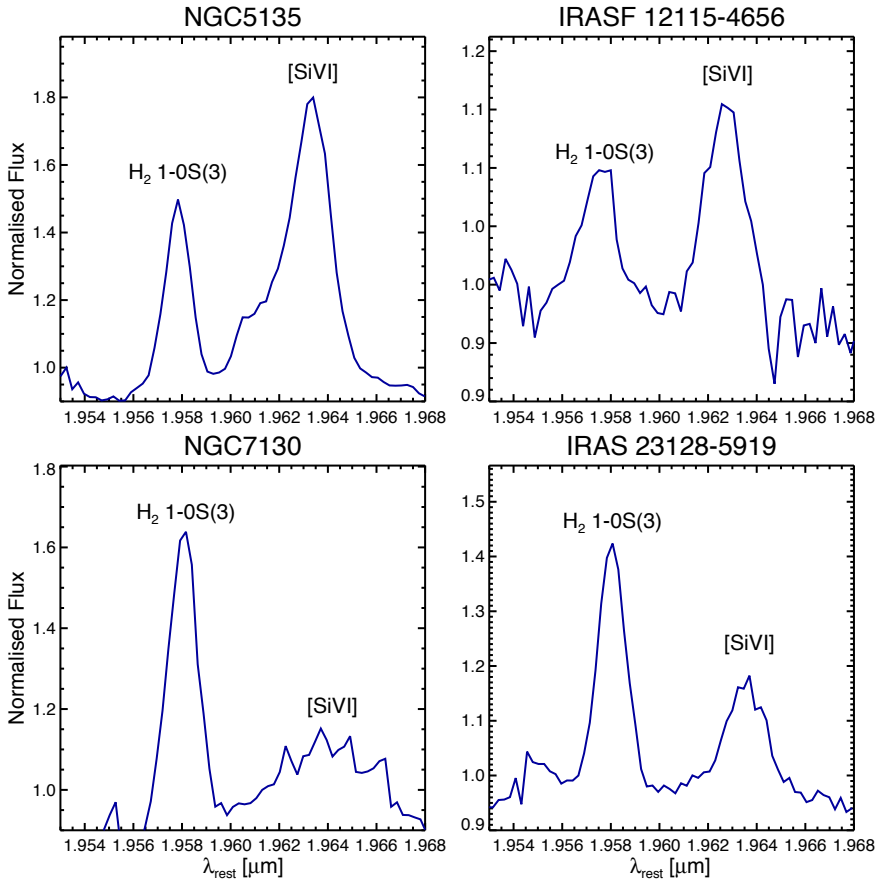

Figure 4.5: H_2 1–0S(3) and coronal line profiles. - H_2 1–0S(3) and [SiVI] normalised flux profiles of the brightest spaxel in [SiVI] for the four objects where the coronal line is detected.

around the unresolved nucleus and extending up to a few tens or a few hundred parsecs in some Seyferts (Prieto et al. 2005, Rodríguez-Ardila et al. 2006). While in galaxies like IRASF 12115-4656 and IRAS 23128-5919 the emission is unresolved (i.e. sizes less than ~ 150 pc and ~ 550 pc, respectively), a relevant exception is NGC 5135, which presents a cone of emission centred on the AGN and extending $\sim$600 pc (~ 2 arcsec) from the nucleus, as discussed in Bedregal et al. (2009). The line profiles for the four galaxies are given in Fig. 4.5.

As shown in Fig 4.6, the [CaVIII] coronal line at 2.321 μm is also detected in three of these objects, NGC 5135, IRASF 12115-4656 and tentatively in NGC 7130. Although the [CaVIII] line lays also within the rest-frame spectral coverage of IRAS 23128-5919, the S/N in this region of the spectra is very low, so was not included in the figure.

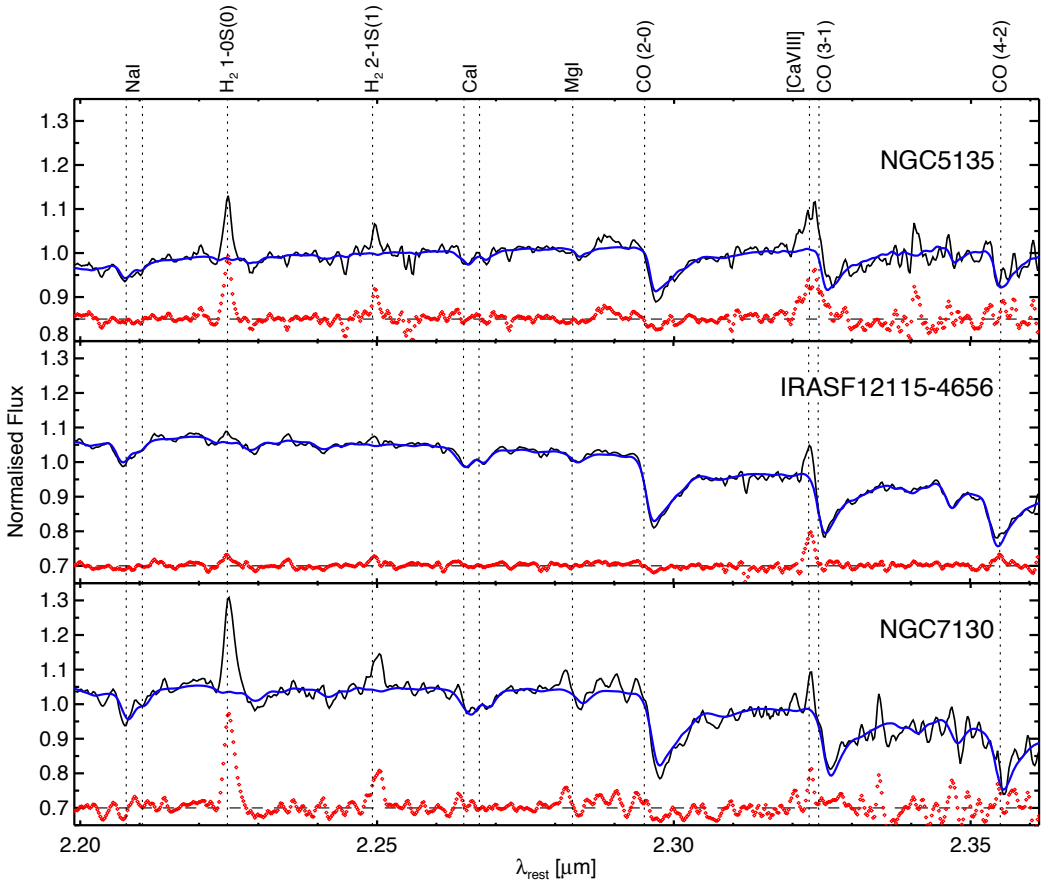

Figure 4.6: Detail on the stellar absorption features and the coronal emission. - Zoom around the region containing the stellar absorption features and the coronal line [CaVIII] at 2.321 μm for three of the objects where coronal emission is detected. Spectra correspond to the brightest spaxel in [SiVI] (see Fig. 4.5). The pPXF fitting of the stellar absorptions is plotted in blue, and the residuals from the fitting are shown as a red dotted line.

4.5.5. Characteristics of the near-IR stacked spectra of LIRGs and ULIRGs

To obtain representative spectra of LIRGs and ULIRGs, we divided the sample into three subsamples according to their total infrared luminosity (see Section 4.3.6), i.e. low luminosity bin, $\log(L_{IR}/L_{\odot}) < 11.35$; intermediate, $11.35 \leq \log(L_{IR}/L_{\odot}) < 12$; and high, the ULIRGs subsample, $\log(L_{IR}/L_{\odot}) \geq 12$. The average luminosities for each bin are $\log(L_{IR}/L_{\odot}) = 11.23$, $\log(L_{IR}/L_{\odot}) = 11.48$, and $\log(L_{IR}/L_{\odot}) = 12.29$. Each luminosity bin contains a similar number of objects in each subsample, six, four, and seven, respectively. The stacked spectra for each luminosity bin are presented in Fig. 4.1

The H-band spectrum of LIRGs is dominated by the stellar continuum, with pronounced absorption features from water vapour and CO. The main emission feature is the [FeII] line at

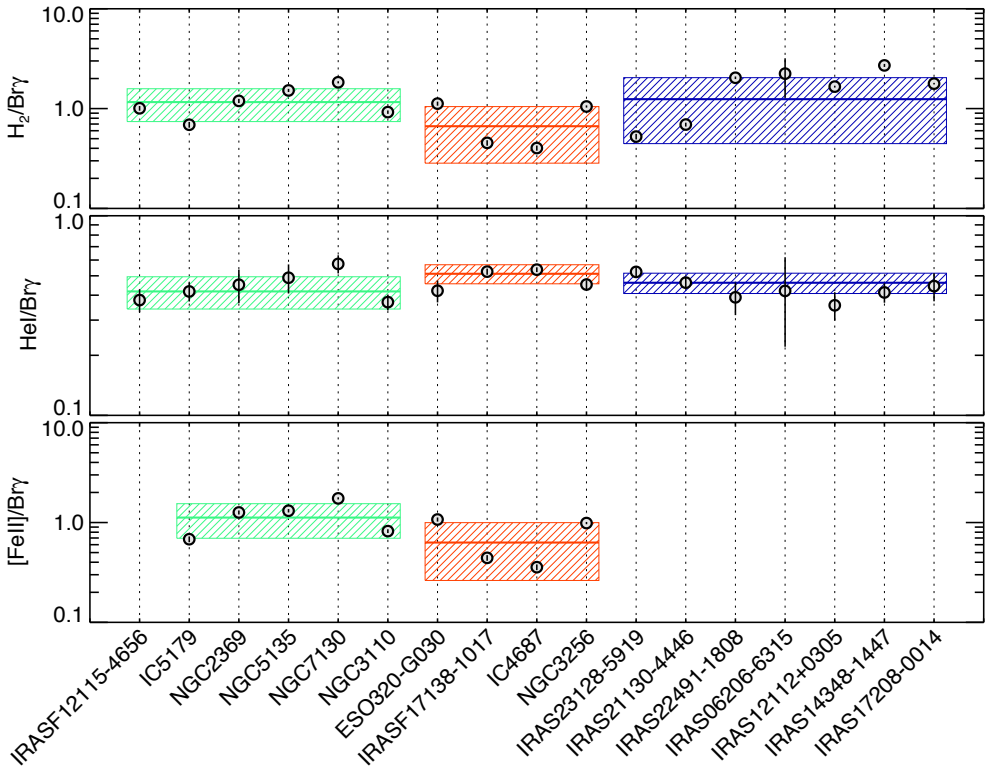

Figure 4.7: Line ratios. - $H_2/Br\gamma$ (top), HeI/Brγ (centre), and [FeII]/Brγ (bottom) line ratios of the galaxies of the sample, ordered by increasing L_{IR}. The values are measured in the integrated spectra. The weighted mean of each luminosity bin (low, $\log(L_{IR}/L_\odot) < 11.35$; intermediate, $11.35 \leq \log(L_{IR}/L_\odot) < 12$ and high, $\log(L_{IR}/L_\odot) \geq 12$) is plotted as a thick line, whereas the box represents the standard deviation of the values. Since all the ULIRGs and one LIRG were not observed in the H-band, [FeII]/Brγ data are presented for only nine LIRGs.

1.644 μm, while the faint high-order hydrogen Brackett lines (Br10 to Br14) are also present. The K-band spectra show various stellar absorption features like the faint NaI, CaI, MgI, lines and the strong CO bands. The emission line spectra contain the hydrogen (Brγ and Brδ) and He recombination lines, as well as a series of the H_2 lines covering different transitions. While the [SiVI] coronal line is detected in some LIRGs and ULIRGs, it is a weak line and thus not visible in the stacked spectra at any luminosity. The average luminosity and surface brightness of the Brγ and Paα emission for each bin is shown in Table 4.7.

Considering only the brightest emission lines that trace different phases of the gas and/or excitation conditions, there appears to be some small differences ($\sim 1\,\sigma$) in their ratios with the L_{IR} (see Fig 4.7 for the H_2 1-0S(1)/Brγ, HeI/Brγ, and [FeII]/Brγ line ratios measured for the different luminosity bins). The HeI/Brγ ratio is slightly higher ($\times$1.3) in intermediate and high luminosity galaxies than in low luminosity objects. A plausible interpretation could

be that young and massive stars in low luminosity LIRGs represent a lower fraction than in more luminous infrared galaxies. Whether this could be caused by age effects or by lower IMF upper mass limits remains to be investigated in more detail. Some differences are also identified in the H_2 1-0S(1)/Brγ line ratio. While this ratio is close to unity for low luminosity LIRGs, it drops to about 0.6 for intermediate luminosity LIRGs, and increases up to about 1.3 for the most luminous galaxies. However, given the large dispersion of the values for the individual objects, and the low number of galaxies in each bin, we could not draw any significant conclusion about these differences. While low H_2 1-0S(1)/Brγ values appear to be characteristic of starbursts (H_2 1-0S(1)/Br$\gamma \lesssim 0.6$), classical Seyfert 1 and 2 galaxies also display a range of values (Rodríguez-Ardila et al. 2004, 2005, Riffel et al. 2010) that are compatible with those measured in our sample.

The [FeII]/Brγ ratio also shows values compatible with those observed in starbursts, although higher values would have been expected for Seyfert galaxies, such as NGC 5135 and NGC 7130 (Rodríguez-Ardila et al. 2004, Riffel et al. 2010, Valencia-S et al. 2012). These galaxies show the highest values of the [FeII]/Brγ ratio of the whole sample, close to ~ 2.0, and are similar to values reported for other Seyfert 2 galaxies (Blietz et al., 1994). These differences could be related to the different apertures used to extract the integrated values of the ratios. Even more, the reported ratios are observed values (not corrected for extinction). Although the H_2 1-0S(1)/Brγ ratio is almost unaffected by extinction, the [FeII]/Brγ ratio could be affected by obscuration, so that an accurate study of the extinction is needed to confirm or dismiss these discrepancies between both ratios.

Based on our current survey, no evidence of relevant differences in the emission line spectra of LIRGs and ULIRGs appear as a function of L_{IR}. A larger sample would be required to confirm the differences in the emission line ratios presented here, since they are still compatible within the uncertainties. The full two-dimensional study of the line ratios and the ionisation and excitation mechanisms of the gas will be addressed in a future paper of the series, since its detailed analysis is beyond the scope of the present work.

4.5.6. Stellar component

In Table 4.5, we have included the EW of the first absorption band of the CO at 2.293 μm. In most of the objects, the values correspond to the Brγ (Paα) peak and nucleus, which are the regions with enough S/N in the continuum to detect the band. The nuclear values of the LIRGs are 7.1 Å $\leq EW_{CO} \leq$ 12.3 Å, with typical uncertainties of $\sim$ 10% and an average of

Region	Brγ and Paα Emission							
	Low		Intermediate		High			
	$L_{Br\gamma}(\times10^5 L_\odot)$	$S_{Br\gamma}(L_\odot\,pc^{-2})$	$L_{Br\gamma}(\times10^5 L_\odot)$	$S_{Br\gamma}(L_\odot\,pc^{-2})$	$L_{Br\gamma}(\times10^5 L_\odot)$	$S_{Br\gamma}(L_\odot\,pc^{-2})$	$L_{Pa\alpha}(\times10^5 L_\odot)$	$S_{Pa\alpha}(L_\odot\,pc^{-2})$
HII max	0.958 (0.785)	0.599 (0.490)	1.292 (0.744)	0.807 (0.465)	22.92 (15.12)	0.573 (0.378)	236.5 (148.3)	5.912 (3.708)
H_2 max	0.977 (0.722)	0.611 (0.451)	0.585 (0.452)	0.366 (0.282)	...		241.1 (143.8)	6.026 (3.596)
[FeII] max	0.873 (0.801)	0.546 (0.501)	0.709 (0.700)	0.443 (0.438)	...		...	
Integrated	7.829 (0.405)	0.120 (0.048)	15.450 (7.931)	0.286 (0.067)	97.76 (116.8)	0.119 (0.072)	521.5 (207.9)	0.972 (0.792)
Nuclear	0.991 (0.746)	0.620 (0.467)	0.909 (0.512)	0.568 (0.320)	23.14 (15.44)	0.578 (0.386)	233.8 (154.8)	5.846 (3.869)

Table 4.7: Brγ (and Paα) average luminosities and surface brightness for the U/LIRGs according to their L_{IR}. The low-luminosity bin is defined as $\log(L_{IR}/L_\odot) < 11.35$, the intermediate is defined as $11.35 \leq \log(L_{IR}/L_\odot) < 12$, and the high-luminosity bin corresponds to the ULIRGs subsample, $\log(L_{IR}/L_\odot) \geq 12$. The standard deviation of the values within each bin is shown in brackets. The number of objects is six, four, and seven for the low, intermediate, and high luminosity bins, respectively.

10.6 Å whereas the values measured at the Brγ (Paα) peak cover the range 8.3 Å $\leq$ EW$_{CO}$ $\leq$ 12.2 Å, with the same uncertainties and a mean value of 10.7 Å. According to the stellar population synthesis models like STARBURST99 (Leitherer et al., 1999), these values of the EW correspond to stellar populations older than log T(yr) $\sim$ 6.8 and up to log T(yr) $\sim$ 8.2 or more, depending on whether we consider a instantaneous burst or a continuum star-formation activity. The detailed study of the 2D distribution of the stellar populations using the CO stellar absorption, the H, and He emission lines will be addressed in forthcoming papers.

4.5.7. Kinematics of the gas

Besides the general morphology and luminosities of the different emission lines, their 2D kinematics (velocity field and velocity dispersion maps) are also presented (Figs. B.1 and B.2). We obtained the velocity dispersion of the different regions of interest described above, i.e. nucleus, the emission peaks of the Brγ (Paα), H_2 1-0S(1) and [FeII] lines, and the entire FoV. The values of the velocity dispersion, corrected for the instrumental broadening, are shown in Table 4.6. The errors are obtained following the same Monte Carlo method implemented to estimate the flux error. Figure 4.4 shows the distributions of the velocity dispersion obtained from the values of Table 4.6. The distributions show that there is no clear relationship between the L_{IR} of the objects and the velocity dispersion of the different regions, although the highest values of velocity dispersion tend to come from high-luminosity objects where measurements come from scales $\times$4–5 larger, so could be affected by beam smearing.

The average velocity dispersion of the Brγ and H_2 1-0S(1) lines in the LIRGs is $\sim$ 90 km s^{-1}, whereas the measured average values for the ULIRG subsample are $\sim$ 140 km s^{-1} and $\sim$ 120 km s^{-1}, respectively. The higher velocity dispersion measured in the ULIRG subset can be explained mainly as a distance effect: the contribution from the unresolved velocity field to the width of the line is larger since the physical scales are also larger. We estimated this effect by extracting several spectra over apertures of increasing radius and measuring the width of the Brγ and H_2 1-0S(1) lines in one of the objects of the LIRG subset. We used NGC 3110 since the Brγ and H_2 emitting gas is extended and well sampled in almost the entire FoV, and their velocity fields show a well defined rotation pattern. The velocity dispersion of the unresolved nuclear Brγ emission is $\sigma_v \sim 75$ km s^{-1} at a distance of 78.4 Mpc. We then simulated the observed spectra of the object at increasing distances up to 500 Mpc and found that, at the average distance of the ULIRG subsample of $\sim$ 328 Mpc, the measured velocity dispersion of the Brγ line rises up to $\sigma_v \sim 105$ km s^{-1}, yielding an increase of

$\sim 30\,\mathrm{km\,s^{-1}}$. The results obtained with the H_2 1-0S(1) line are equivalent and yield a difference of $\sim 28\,\mathrm{km\,s^{-1}}$, since the amplitude of the velocity fields of both phases of the gas are almost identical. Based on these estimates, the difference in velocity dispersion observed between LIRGs and ULIRGs appears to mainly be due to distance effects. However, galaxies with steeper velocity gradients, radial gas flows, turbulence, or massive regions with intrinsically high velocity dispersion would produced an additional increase in the value of the dispersion.

The velocity fields of the gas observed in the rotating LIRGs have the typical spider pattern characteristic of a thin disk, with a well identified kinematic centre that coincides in most cases with the K-band photometric centre, and with a major kinematic axis close to the major photometric axis. These results are similar to those derived from the Hα emission in the central regions of LIRGs (Alonso-Herrero et al., 2009) and from the mid-infrared [NeII] and H_2 emission (Pereira-Santaella et al., 2010) for larger FoVs. These characteristics indicate that the velocity fields of both the ionised and the warm molecular gas are dominated by the rotation of a disk around the centre of the galaxy, as expected given that almost all of the objects of the subsample are spiral galaxies with different levels of inclination. Local deviations and irregularities from rotation, as well as regions of higher velocity dispersion, are present in most/all the LIRGs, suggesting the presence of additional radial flows and/or regions of higher turbulence or outflows outside and close to the nucleus (e.g. NGC 3256, NGC 5135). Besides these local deviations, the ionised and molecular gas of the LIRGs show the same velocity field on almost all scales, from regions of a few hundred parsecs to scales of several kpc.

In the ULIRG subsample, since all the objects but one are mergers in a pre-coalescence phase, the kinematics of the gas show a more complex structure, with signs of strong velocity gradients associated with the different progenitors of the systems, and asymmetric line profiles that indicate there are outflows of gas associated with AGN or starburst activity. It is interesting to note that, as in LIRGs, the ionised and warm molecular gas in ULIRGs show the same overall kinematics on scales of a few to several kpc. Whether the kinematics in (U)LIRGs are dominated by rotation, radial starbursts/AGN flows, tidal-induced flows, or a combination of these, the ionised and molecular gas share the same kinematics on physical scales ranging from a few hundred parsecs (LIRGs) to several kpc (ULIRGs). A detailed study of the gas kinematics of the sample is beyond the aim of this work and will be addressed in a

forthcoming paper; however, a brief individual description of the most relevant features of the gas kinematics is included in Appendix A.

4.6. Summary

- We have obtained K-band SINFONI seeing limited observations of a sample of local LIRGs and ULIRGs ($z < 0.1$), together with H-band SINFONI spectroscopy for the LIRG subsample. The luminosity range covered by the observations is $\log(L_{IR}/L_{\odot})= 11.1 - 12.4$, with an average redshift of $z_{LIRGs} = 0.014$ and $z_{ULIRGs} = 0.072$ ($\sim$63 Mpc and $\sim$328 Mpc) for LIRGs and ULIRGs, respectively. The IFS maps cover the central $\sim 3 \times 3$ kpc of the LIRGs and the central $\sim 12 \times 12$ kpc of the ULIRGs with a scale of 0.″125 per spaxel. We present the 2D distribution of the emitting line gas of the whole sample and some general results of the morphology, luminosities, and kinematics of the line-emitting gas as traced by different emission lines. The detailed studies of the excitation mechanisms, extinction, stellar populations, and stellar and gas kinematics of the entire sample will be presented in forthcoming papers.

- In a third of LIRGs, the peaks of the ionised and molecular gas coincide with the stellar nucleus of the galaxy (distances of less than 0.″25), and the Brγ line typically shows luminosities of $\sim 1.2 \times 10^5\, L_{\odot}$. However, in galaxies with star-forming rings or giant HII regions in the spiral arms, the emission of ionised gas is dominated by such structures. The warm molecular gas shows very similar luminosities to the Brγ emission and is highly concentrated in the nucleus, where it reaches its maximum in all the objects of our sample. The Brγ and [FeII] emission traces the same structures, although their emission peaks are not spatially coincident in some of the objects, and the [FeII] seems to be more extended and diffuse.

- The ULIRG subsample is at greater distances ($\sim$4–5 times) and mainly contains pre-coalescence interacting systems. Although the peaks of the molecular gas emission and the main nucleus of the objects coincide in $\sim$ 71% of the galaxies, we also detect regions with intense Paα emission up to $\sim 1.1 \times 10^8\, L_{\odot}$ which trace luminous star-forming regions located at distances of 2–4 kpc away from the nucleus.

- LIRGs have mean observed (i.e. uncorrected for internal extinction) SFR surface densities of about 0.4 to 0.9 $M_{\odot}$ yr^{-1} kpc^{-2} over extended areas of 4$-$9 kpc^2 with

peaks of about 2−2.5 $M_\odot$ yr^{-1} kpc^{-2} in compact regions (0.16 kpc^2) associated with the nucleus of the galaxy or the brightest Brγ region. ULIRGs do have similar values ($\sim$0.4 and $\sim$ 2 $M_\odot$ yr^{-1} kpc^{-2}) over much larger areas, 100−200 kpc^2 and 4 kpc^2 for the integrated and peak emission, respectively. To correct the above values from extinction, we applied a median A_V value of $\sim$ 5.3 mag for LIRGs and $\sim$ 6.5 mag for ULIRGs, and found that the SFR measurements should increase by a factor $\sim$ 1.7 in LIRGs and $\sim$ 2.5 in ULIRGs, when dereddened luminosities are considered.

- The observed gas kinematics in LIRGs is primarily due to rotational motions around the centre of the galaxy, although local deviations associated with radial flows and/or regions of higher velocity dispersions are present. The ionised and molecular gas share the same kinematics (velocity field and velocity dispersion), showing in some cases slight differences in the velocity amplitudes (peak-to-peak). Given the interacting nature of the objects of the subsample, the kinematics of the ULIRG show complex velocity fields with different gradients associated with the progenitors of the system and tidal tails.

5

Characterisation of the visual extinction and dust clumpiness

Spaxel-by-spaxel 2D A_V distributions and distance effects

"Non est ad astra mollis e terris via."
[There is no easy way from the earth to the stars.]
— Seneca

We present a 2D study of the internal extinction on (sub)kiloparsec scales of a sample of local ($z < 0.1$) LIRGs (10) and ULIRGs (7), based on near-infrared Paα, Brδ, and Brγ line ratios, obtained with VLT-SINFONI integral-field spectroscopy (IFS). The 2D extinction (A_V) distributions of the objects, map regions of $\sim 3 \times 3$ kpc (LIRGs) and $\sim 12 \times 12$ kpc (ULIRGs), with average angular resolutions (FWHM) of $\sim$0.2 kpc and $\sim$0.9 kpc, respectively. The individual A_V galaxy distributions indicate a very clumpy dust structure already on sub-kiloparsec scales, with values (per spaxel) ranging from $A_V \sim 1$ to 20 mag in LIRGs, and from $A_V \sim 2$ to 15 mag in ULIRGs. As a class, the median values of the distributions are $A_V = 5.3$ mag and $A_V = 6.5$ mag for the LIRG and ULIRG subsamples, respectively. In $\sim$70% of the objects, the extinction peaks at the nucleus with values ranging from $A_V \sim 3$ to 17 mag. Within each galaxy, the A_V radial profile shows a mild decrement in LIRGs within the inner 2 kpc radius, while the same radial variation is not detected in ULIRGs, likely because of the lower linear scale resolution of the observations at the distance of ULIRGs. We evaluated the effects of the galaxy distance in the measurements of the extinction as a function of the linear scale (in kpc) of the spaxel (i.e. due to the limited angular resolution of the observations). If

the distribution of the gas/dust and star-forming regions in local LIRGs (63 Mpc, 40 pc/spaxel on average) is the same for galaxies at greater distances, the observed median A_V values based on emission line ratios would be a factor $\sim$ 0.8 lower at the average distance of our ULIRG sample (328 Mpc, 0.2 kpc/spaxel), and a factor $\sim$0.67 for galaxies located at distances of more than 800 Mpc (0.4 kpc/spaxel). This distance effect would have implications for deriving the intrinsic extinction in high-z star-forming galaxies and for subsequent properties such as star formation rate, star formation surface density, and KS-law, based on Hα line fluxes. If local LIRGs are analogues of the main-sequence (MS) star-forming galaxies at cosmological distances, the extinction values (A_V) derived from the observed emission lines in these high-z sources would need to be increased by a factor 1.4 on average.

5.1. Introduction

Since the first results obtained by the *Infrared Astronomical Satellite* (*IRAS*) (Soifer et al., 1984), there has been strong effort to study the physical processes that power the luminous and ultraluminous infrared galaxy population (Sanders & Mirabel 1996, Lonsdale et al. 2006). The origin of the mid- and far-infrared emission (L_{IR}[8-1000 μm]) that dominates their bolometric luminosity is established as mainly due to massive starbursts with a small AGN contribution for LIRGs and with an increasing contribution in ULIRGs (e.g. Goldader et al. 1995, Veilleux et al. 2009, Nardini et al. 2010, Alonso-Herrero et al. 2012 and references therein). The radiation that originates in the starburst and/or the active galactic nucleus is then reprocessed by a surrounding dust component, and then re-emitted at long wavelengths in the form of a huge infrared emission.

One of the main difficulties in understanding the underlying power source of LIRGs and ULIRGs is the high opacity of their nuclear regions. Previous optical (García-Marín et al., 2009a) and near-infrared studies in LIRGs and ULIRGs (Genzel et al. 1998, Scoville et al. 2000, Alonso-Herrero et al. 2006) reveal that the distribution of the dust in these object is not uniform and that, though the dust tends to concentrate in the inner kiloparsecs with average visual extinction of $A_V\sim$3-5 mag in LIRGs and even higher in ULIRGs, the global distribution shows a patchy structure on kiloparsec and sub-kiloparsec scales (Colina et al. 2000, García-Marín et al. 2006, Bedregal et al. 2009).

Besides the importance of knowing the 2D structure of the dust to understand the environment where the power source of the LIRGs and ULIRGs is embedded, dust plays a

key role in the derivation of other physical and structural parameters of these objects, such as the derived star formation rate (García-Marín et al., 2009a), the effective radius (Arribas et al., 2012), and as a consequence, the dynamical masses.

Understanding the distribution and effect of dust in star-forming galaxies is also important for correctly interpreting or comparing different tracers of star formation during the history of the Universe. This is in turn relevant when comparing local and high-z star-forming galaxy populations, which are often observed using different tracers and/or resolutions. The distribution of dust can in principle be studied in detail in local (U)LIRGs with the advantage of the relatively high linear resolution and S/N. These studies can, therefore, help us interpret observations of analogous high-z star-forming galaxies, for which such a level of resolution, and S/N is not attainable with current instruments.

The present work is part of a series presenting new H- and K-band SINFONI seeing-limited observations of a sample of local LIRGs and ULIRGs. Piqueras López et al. (2012a) (Chapter 4) presented the atlas of the sample, the data reduction, and a brief analysis and discussion of the morphology of the gas emission and kinematics. In this chapter, we focus on the study of the 2D distribution of the dust derived using the Brγ/Brδ and Paα/Brγ ratios for LIRGs and ULIRGs, respectively, whereas in Piqueras López et al. 2014 (in preparation, Chapter 6), we will apply the results for the 2D dust structure to study both the overall star formation rate (SFR) and the kpc structure of the SFR surface density (Σ_{SFR}) of the galaxies of the sample.

The description of the sample, observations, and data reduction process are detailed in Chapter 4. The procedures for obtaining the emission and A_V maps are described in Section 5.2, and the results and analysis of the A_V maps and distributions are presented in Section 5.3. Finally, Section 5.4 includes a brief summary of the chapter.

5.2. Data analysis

The 2D extinction / dust structure was derived using the Brγ/Brδ and Paα/Brγ line ratios for LIRGs and ULIRGs respectively. Although the Brδ line is detected in most of the ULIRGs, its S/N is not high enough to map the emission and, in most of the cases, it is not sufficient to perform an integrated analysis of the emission.

As mentioned before, the maps of the different lines were constructed by fitting a single Gaussian profile on a spaxel-by-spaxel basis (see Fig. C.1 and C.2). Based on the

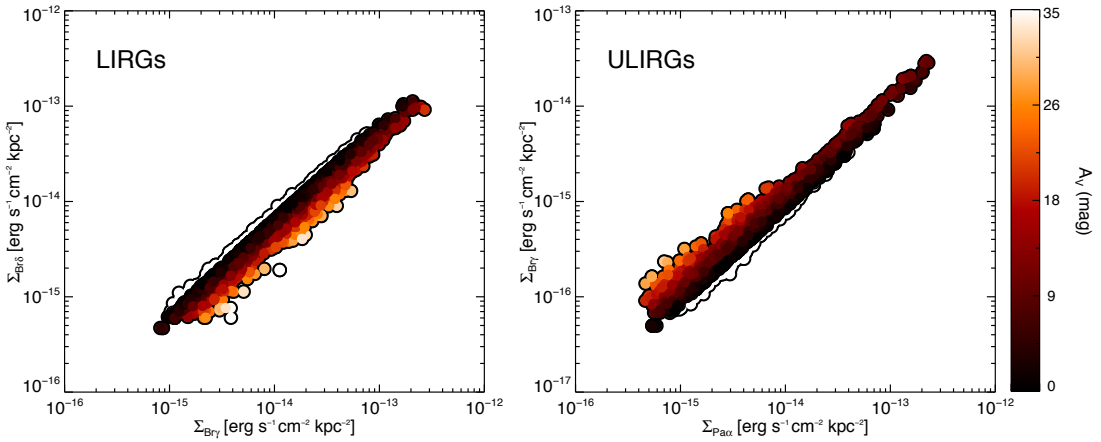

Figure 5.1: Surface brightness distributions of individual spaxels - Surface brightness distributions of the individual spaxels of LIRGs and ULIRGs. For clarity, we only plot a random distribution of the 20% and 50% of the points for LIRGs and ULIRGs, respectively. The colour code indicates the A_V value of each spaxel, whereas the points with $A_V < 0$ are outlined with a black contour line. The increase in the extinction towards low surface brightness values is mainly due to the high uncertainties of the flux measurements, in particular in ULIRGs, where the highest A_V values correspond to the spaxels with the lower Brγ surface brightness.

emission maps, we obtained the extinction in magnitudes (A_V) following the procedure outlined in Bedregal et al. (2009). We compared the theoretical ratio between the two lines (Brγ/Brδ= 1.52 and Paα/Brγ= 12.07 at T= 10,000 K and $n_e = 10^4\,cm^{-3}$, case B; Osterbrock 1989) with the measurements for each spaxel. The extinction in magnitudes could be expressed in the form

$$A_{\lambda_1} - A_{\lambda_2} = -2.5 \cdot \log\left[\frac{(F_{\lambda_1}/F_{\lambda_2})_O}{(F_{\lambda_1}/F_{\lambda_2})_T}\right], \tag{5.1}$$

where $F_{\lambda_i,O}$ and $F_{\lambda_i,T}$ are the observed and theoretical fluxes for a line centred at λ_i. We made use of the extinction law described in Calzetti et al. (2000) to express Equation 5.1 in terms of the visual extinction A_V ($A_{Br\gamma} = 0.096\,A_V$, $A_{Br\delta} = 0.132\,A_V$ and $A_{Pa\alpha} = 0.145\,A_V$).

Since the individual values of A_V are sensitive to the S/N of the weakest line (Brδ and Brγ for LIRGs and ULIRGs respectively), we have only considered those spaxels where the weakest line has been detected above an S/N threshold of four to obtain reliable A_V. This effect is very significative in the case of the Brγ/Brδ ratio since the Brδ line lies close to the blue limit of the SINFONI K-band. As discussed in Chapter 4, this wavelength region is strongly affected by noise due to the sky emission, and the atmospheric transmission also decreases. This translates into a more complex local continuum determination, making the line fitting more uncertain. An excess in the continuum level estimation would decrease the

line flux and, therefore, increase the extinction (see expression above). Although the Paα line also lies in this region of the spectra, this effect is not so relevant, given the strength of the line ($\times$12 the Brγ emission), and it is in the numerator of Equation 5.1.

The 1σ uncertainties of the individual A_V values vary typically from 10–20% in central regions with high S/N, up to 70–80% in external areas of low surface brightness ($\Sigma \lesssim 10^{-16}\,\mathrm{erg\,s^{-1}\,cm^{-2}\,kpc^{-2}}$), with a median value of 30-35%. Owing to the larger individual errors in the low surface brightness areas, we observed an artificial increase in the A_V measurements, especially in the ULIRGs. This systematic effect is observed in Fig. 5.1, where the highest extinction values are measured in those spaxels with the lower Brγ surface brightness. The A_V uncertainties are obtained from the corresponding errors in the fluxes of the two lines, which as described in Chapter 4, are estimated using Monte Carlo simulations. The advantage of this kind of error estimation is that uncertainties are directly measured from the spectra, so they not only include the effect from photon noise but also take uncertainties due to an improper continuum determination or line fitting into account.

5.3. Results and discussion

5.3.1. Two-dimensional extinction structure in LIRGs and ULIRGs

Our 2D extinction maps cover areas from $\sim$2 kpc to $\sim$12 kpc for LIRGs and ULIRGs, respectively (see Figs. C.1 and C.2). The seeing-limited observations provide a linear resolution equivalent to a physical scale resolution of $\sim$0.2 kpc and $\sim$0.9 kpc for each subsample. On these scales, the extinction maps show that dust is not uniformly distributed, revealing a clumpy structure with almost transparent areas ($A_V \lesssim 1$ mag) and regions where the visual extinction is higher than ten magnitudes.

In LIRGs, the extinction maps show a very irregular and clumpy structure on scales of $\sim$200-300 pc, already observed from near-IR continuum maps (Scoville et al., 2000). The higher A_V values are usually associated with the nuclear regions of the objects, although obscured extranuclear regions are also common. The star-forming regions with high Brγ surface brightness, found along the dynamical structures like arms of rings, are typically low-extinction regions.

As shown in the radial profiles of NGC 3110 or IRASF 12115-4656 (Figs. C.1b and C.1e), the extinction increases inwards up to $A_V\sim$15–25 mag. This behaviour is also observed in ESO 320-G030 (Fig. C.1d), where the emission is concentrated on a star-forming ring of

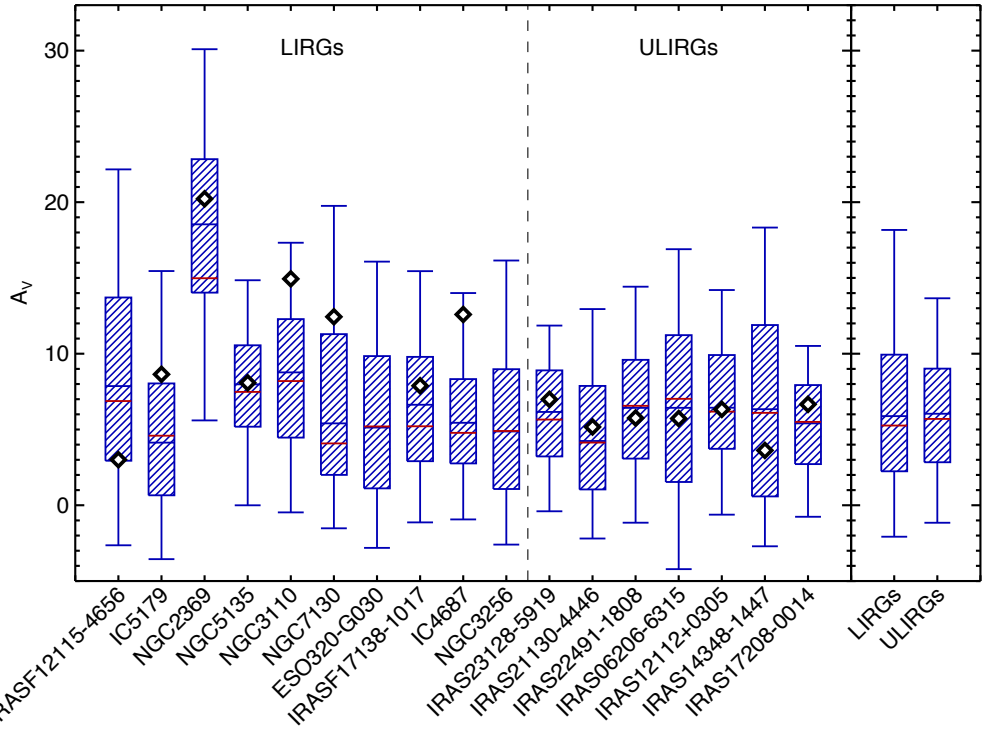

Figure 5.2: Spaxel-by-spaxel individual A_V distributions - Individual A_V distributions of the galaxies of the sample ordered by increasing L_{IR}. The extremes of the distributions are the 5th and 95th percentiles (P_5 and P_{95}). The boxes illustrate the interquartile range, whereas the horizontal blue and red lines correspond to the median and the weighted mean of the distribution, respectively. The measurements of the nuclear extinction are plotted as black diamonds. The total A_V distributions for LIRGs and ULIRGs are shown on the right-hand side of the plot.

$\sim$500–600 pc radius. Although the nucleus might also be obscured, the radial profile of this object is not as steep as in NGC 3110 or IRASF 12115-4656 and indicates that the lack of emission could also be due to the intrinsic distribution of the star-forming regions around the ring.

The morphology of the A_V maps in the ULIRG subsample suggest a patchy, non-uniform distribution of the dust, typically on physical scales of $\gtrsim$1 kpc that correspond to our resolution limit. Owing to the higher linear resolution (i.e. kpc/spaxel) of the ULIRG subsample, the comparison with the LIRGs is not straightforward. As shown in Fig. 5.3, although our data samples similar areas of $\sim$1-2 R_{eff}, the dust structure is probed with significantly different spatial resolutions, owing to the factor $\times$5 in distance between both subsamples. This difference precludes us from resolving sub-kiloparsec structures in ULIRGs, such as the ones observed in the LIRG A_V maps, limiting our physical resolution to $\sim$1 kpc. As discussed in Sec. 5.3.4, these differences in the linear resolution between both subsamples not only shape

the observed dust morphology in the more distant galaxies, but also might determine global measurements of the extinction, such as the median of the A_V distributions. In Sec. 5.3.5 we discuss how this distance effect would have direct implications for the study of high-z galaxies.

5.3.2. A_V distributions and radial profiles

Figures C.1 and C.2 show the A_V distributions for each galaxy. Although it is clear that most of the spaxels with $A_V<0$ have no physical meaning individually, we have kept them in the distributions since they do have statistical relevance. If we remove them from the distributions, we introduce a bias toward the high A_V values, displacing the mean and median of the distributions artificially. On the other hand, due to the S/N threshold adopted, we assure that most of those spaxels with $A_V<0$ are compatible with $A_V\sim0$ within the uncertainties.

The histograms show a wide variety of distributions, from narrow, peaked distributions, such as NGC 5135 or IC 4687 (Fig. C.1f and C.1h), concentrated towards low A_V values, to wide distributions such as NGC 3110 or IRAS 14348-1447 (Figs. C.1b and C.2c) that extend up to $\sim$30-35 mag. The median and weighted mean A_V values, together with the 5th and 95th percentiles of the distributions, are listed in Table 5.1. Figure 5.2 also compares the individual distributions of each galaxy of the sample, ordered by increasing L_{IR}. As shown in the figure, most of the individual values, within the interquartile ranges, are concentrated between $A_V\sim1$ and $A_V\sim20$ mag, and there is no clear evidence of any dependence with L_{IR}.

In LIRGs, the visual extinction ranges between $A_V\sim 1-20$ mag, whereas in ULIRGs, the A_V values range between $A_V\sim 2-15$ mag. In LIRGs, these values of the visual extinction are very similar although slightly lower than previous results in the mid-infrared from Spitzer, $A_V \lesssim 1-30$ mag with a mean value of $\sim$11 mag (Pereira-Santaella et al. 2010, Alonso-Herrero et al. 2012). On the other hand, ULIRGs show slightly higher values than previous measurements in the optical, from $A_V \lesssim 0.2$ mag to ~ 9 mag (García-Marín et al., 2009a), and significantly lower than mid-infrared measurements based on the silicate absorption feature at 9.7 μm, from $A_V\sim6$ mag up to $A_V \gtrsim 40$ mag (Imanishi et al., 2007).

These A_V values have to be considered as lower limits of the dust extinction, since the theoretical values of the ratios are based on the assumption that the gas is optically thin. However, it is well known that the central regions of these objects are dusty environments and that the observed recombination lines might have been originated at different depths

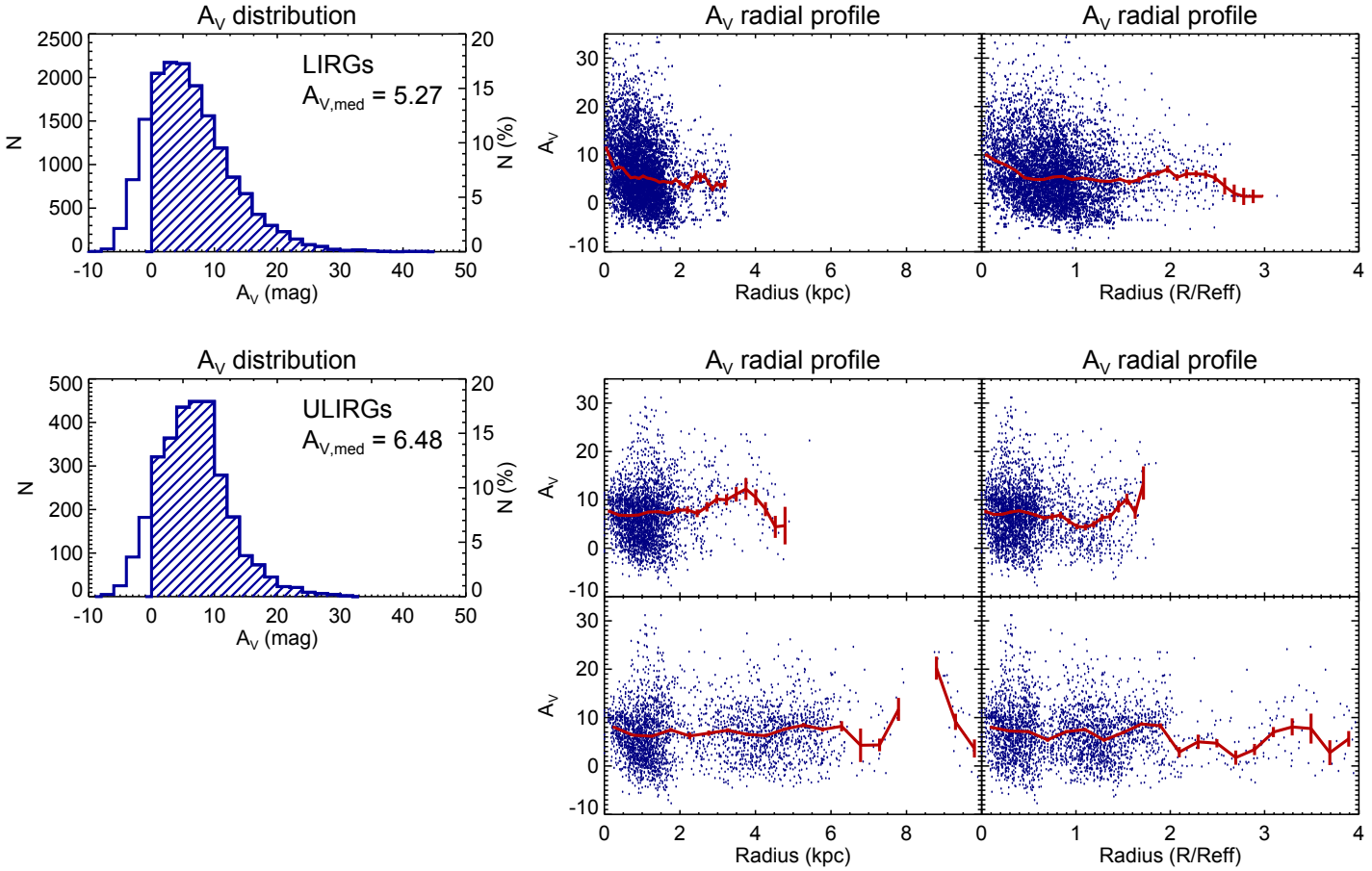

Figure 5.3: A_V distributions and radial profiles of LIRGs and ULIRGs - A_V distributions and radial profiles of the LIRGs (top) and ULIRGs (bottom) subsamples on a spaxel-by-spaxel basis. The median A_V values of each distribution are shown in the left panels. In the central and right panels, the radial profiles are plotted in terms of the radius in kpc (centre) and in units of the Hα effective radius (R_{eff}, right panel) extracted from Arribas et al. (2012). The red line represents the weighted mean of A_V and its error for different radial bins in steps of 1/30 of the total radial coverage. For the ULIRG subsample, we plotted the radial profile of the sample by considering each component of the systems separately (top) and the profile extracted by taking the brightest nucleus in the K-band continuum as the centre of the systems (bottom).

Object	$A_{V,nuclear}$	$A_{V,nuclear}$	$A_{V,R_{eff}}$	$A_{V,FoV}$	$A_{V,median}$	$A_{V,mean}$	A_V (P_5)	A_V (P_{95})	N_{spaxel}
(1)	(2)	(3)	(5)	(6)	(7)	(8)	(9)	(10)	(11)
IRASF12115-4656	···	···	7.7 ± 0.1	5.2 ± 0.1	4.9	6.3 ± 8.1	-3.65	21.5	1533
IC5179	10.4 ± 0.4	···	4.2 ± 0.1‡	4.2 ± 0.1	4.4	5.2 ± 6.3	-3.00	17.3	2099
NGC2369	16.8 ± 0.2	···	17.3 ± 0.1	15.0 ± 0.1	15.5	13.5 ± 6.6	3.75	26.0	603
NGC5135	2.8 ± 0.2	···	3.8 ± 0.1	3.7 ± 0.1	4.2	4.7 ± 4.5	-1.72	11.7	1100
NGC3110	···	···	7.4 ± 0.1‡	7.4 ± 0.1	7.9	7.9 ± 5.8	-3.02	16.6	400
NGC7130	12.3 ± 0.3	···	11.8 ± 0.2	8.7 ± 0.1	6.2	5.9 ± 6.5	-2.45	18.6	687
ESO320-G030	···	···	7.8 ± 0.1	7.0 ± 0.1	7.8	8.0 ± 7.1	-2.82	20.1	1383
IRASF17138-1017	15.2 ± 0.4	···	11.1 ± 0.1	7.0 ± 0.1	7.6	6.1 ± 5.6	-0.91	17.2	806
IC4687	10.6 ± 0.1	···	3.9 ± 0.1	3.7 ± 0.1	4.2	4.5 ± 5.1	-1.74	13.1	3401
NGC3256†	···	12.2 ± 0.2	5.0 ± 0.1	4.1 ± 0.1	5.0	6.6 ± 6.1	-2.73	16.8	4522
IRAS23128-5919	8.7 ± 0.3	6.7 ± 0.2	7.1 ± 0.1	6.8 ± 0.1	6.2	7.0 ± 4.7	-1.60	13.4	1182
IRAS21130-4446	4.3 ± 0.4	3.2 ± 0.2	4.7 ± 0.3	4.4 ± 0.1	5.4	5.0 ± 5.9	-1.80	15.5	214
IRAS22491-1808	4.1 ± 0.3	4.5 ± 0.2	5.5 ± 0.1	5.3 ± 0.1	6.4	6.5 ± 5.1	-1.79	16.0	299
IRAS06206-6315	7.5 ± 0.3	11.3 ± 0.4	7.6 ± 0.2	8.5 ± 0.2	10.7	9.5 ± 7.7	-3.05	22.7	114
IRAS12112+0305	8.9 ± 0.3	8.4 ± 0.2	9.2 ± 0.2	8.5 ± 0.1	8.2	9.0 ± 6.2	-0.52	20.9	466
IRAS14348-1447	5.5 ± 0.2	8.1 ± 0.3	6.2 ± 0.2	7.1 ± 0.1	8.6	7.9 ± 6.9	-1.04	20.6	301
IRAS17208-0014	8.0 ± 0.2	···	6.8 ± 0.1	5.8 ± 0.1	4.8	6.3 ± 4.0	-1.61	10.8	485

Table 5.1: Integrated properties and statistics of the A_V distributions. Cols. (2) and (3): Nuclear extinction measured at the main (2) and secondary (3) nucleus within an aperture radius of 0.″63. Cols. (4) and (5): Measurements of the A_V within the Hα effective radius from Arribas et al. (2012), and the integrated measurement over the whole FoV, respectively. Cols. (6) to (9): Median, weighted mean, and 5th and 95th percentiles of the A_V distributions. Col. (10): Number of valid spaxels in the A_V maps and distributions. † Since the main nucleus of NGC 3256 was not observed, we centred the aperture for $A_{V,R_{eff}}$ on the centre of the FoV, so the measurement might be inaccurate. ‡Due to the limited FoV of the observations, in these objects the Hα effective radius is greater than our FoV, and the $A_{V,R_{eff}}$ measurements are equivalent to $A_{V,FoV}$.

within the star-forming regions. That also means that we would infer different extinction values from different emission line ratios, since the lines are probing different optical depths.

To compare the A_V distributions of LIRGs and ULIRGs, we combined all the available spaxels of each luminosity bin to obtain a typical A_V distribution. These distributions are shown in Fig. 5.2 and, in more detail, in Fig. 5.3. The median values of A_V for each subsample are similar, $A_{V\,med} = 5.3$ mag and $A_{V\,med} = 6.5$ mag, and the number of individual spaxels is ∼16000 for the LIRG distribution and ∼3000 for the ULIRG one. The shape of the distributions are, however, slightly different. Whereas the LIRG distribution seems to have more than 50% of the points concentrated within the range $A_V \simeq 1 - 10$ mag, the ULIRGs extend over a somewhat narrower range of $A_V \simeq 3 - 10$ mag and tend to reach higher A_V values on individual spaxels. On the other hand, the modes of the distributions are also different; whereas the LIRG distribution peaks at $\sim 3 - 4$ mag, the mode of the ULIRG distribution reaches up to $\sim 7 - 8$ mag. Although some of these differences might be intrinsic, we discuss in Section 5.3.4 that the physical sampling of the maps plays an important role in the study of the extinction, owing to the patchy structure of the dust.

We obtained the radial profiles of the extinction for every individual object of the sample and characteristic profiles for both LIRG and ULIRG subsamples. For this purpose, we adopted the same criterion as in Chapter 4 to identify the central spaxel of each object with the brightest spaxel of the FoV in the K-band image (see Figs.C.1 and C.2). The only exception is NGC 3256, since the nucleus of this galaxy was not observed in the K-band (see Chapter 4 for further details). For this object, we used the H-band continuum image of the nucleus to identify the central spaxel. For those systems with multiple nuclei (i.e. all the ULIRGs with the exception of IRAS 17208-0014), we also extracted the radial profiles of each component separately.

As shown in Figs. C.1 and C.2, the profiles typically sample the inner ~ 2 kpc for the LIRGs and $\lesssim 6$ kpc for the ULIRGs, and most of them have an almost flat or negative slope. LIRGs show steeper negative slopes than ULIRGs, especially in the central 0.5–1 kpc. In LIRGs, these slopes are typically of ~ -2.4 mag kpc^{-1} on average, versus ~ -0.3 mag kpc^{-1} in ULIRGs. This could be explained by the different sampling scales of both subsamples, since we cannot resolve the innermost regions of the ULIRGs with the resolution achieved for the LIRG subset. In those pre-coalescent systems with multiple nuclei, we found no systematic differences between the radial profiles of both components. These profiles typically sample the

innermost $\sim 2-3$ kpc of each component of the system, and show no clear radial dependence of the extinction on these scales.

We extracted the radial profiles of the total A_V distributions of LIRGs and ULIRGs separately. Since each object has been observed with different sampling and physical scales, we also obtained the profiles in units of the effective radius R_{eff}, using the values from Arribas et al. (2012) obtained from Hα maps. As shown in Fig. 5.3, the LIRG profile is almost flat beyond r$\sim$1 kpc or $\sim$0.5 R_{eff}, with an average value of $A_V\sim$5.3 mag. Within the central kiloparsec, the extinction increases up to $\sim$10 mag. The ULIRG subsample shows a very uniform profile, with a median value of $A_V\sim$6.0 mag and only local deviations due to the presence of double nuclei in some of the systems, or due to strong complexes of star formation at distances beyond 2-3 kpc radius (see Fig.C.2a and C.2b for some examples). The radial profile shows small differences when extracted from each component separately, with an almost flat slope over the inner 2-3 kpc radius ($\sim R_{eff}$). The measurements beyond $r \sim$6 kpc or $r \sim 2\, R_{eff}$ are very uncertain, owing to the lack of available spaxels and to the low surface brightness of the Brγ emission in these regions. As mentioned before, the extinction in ULIRGs derived using Eq. 5.1 is highly affected by noise fluctuations of the Brγ line.

5.3.3. Nuclear and integrated A_V measurements

We obtained integrated A_V measurements for different regions of interest in each object (Table 5.1). The uncertainties of the parameters are obtained by a Monte Carlo method of N = 1000 simulations, and do not take the 1σ uncertainties of $\sim$5% into account in the absolute flux calibration (see Piqueras López et al. 2012a). We found that, in $\sim$70% of the objects, its nucleus corresponds to a peak in the extinction, ranging from $A_V\sim$3 mag up to $A_V\sim$17 mag. These values of the nuclear extinction are higher than each median and mean A_V values in $\sim$ 57% of the objects. However, there are some galaxies, such as NGC 3110 or IC 4687 (Figs. C.1b and C.1h), where the nucleus is completely obscured, and no measurements of the extinction are available. That the nucleus of the objects coincides with a peak of the extinction agrees with other studies in LIRGs and ULIRGs (see Alonso-Herrero et al. 2006 and García-Marín et al. 2009a) based on Hα/Hβ and Paα/Brγ ratios, and with mid-infrared studies with Spitzer, based on the silicate absorption feature at 9.7 μm (Imanishi et al. 2007, Pereira-Santaella et al. 2010). These authors found that either the highest extinctions coincide with the nucleus of the objects or the nuclear regions are local maxima in the A_V maps.

For those objects with a double nucleus, we also presented integrated measurements of the extinction for the secondary one. Although almost all of the interacting systems in our sample are ULIRGs, NGC 3256 presents a well known, highly obscured nucleus ~ 5 arcsec to the south of the main one. Our measurements of the extinction of the southern nucleus of this object shows that it is one of the most extinguished regions in our sample, with $A_V \simeq 12.2$ mag, in good agreement with previous works (Kotilainen et al. 1996, Alonso-Herrero et al. 2006, Díaz-Santos et al. 2008, Rich et al. 2011).

5.3.4. Dust clumpiness and the effect of the linear resolution.

As mentioned in Section 5.3.1, the A_V maps reveal a patchy, clumpy structure of the dust at sub-kiloparsec and kiloparsec scales in LIRGs and ULIRGs, respectively. Given this non-uniform distribution, the measurements of the extinction at different distances might be affected by the physical scale of the observations. To probe how the pixel scale might bias the A_V measurements, we have obtained the A_V distribution of our LIRG sample simulating different scales, hence different distances. This distance effect because of the linear resolution might be even more relevant for high-z objects, where the structure is sampled on even larger scales of $\sim$1-2 kpc.

To simulate the distribution at further distances, we degraded the individual Brγ and Brδ maps to different scales, and obtained maps of poorer spatial resolution. In this process, we only considered the same valid spaxels as in the original maps. Once the maps were degraded, we obtained the A_V distributions of each individual object as described in Section 5.2, which were finally combined in one single distribution.

Since the FoV of our SINFONI observation is limited to $\sim 8'' \times 8''$, we could only sample the innermost $\sim 3 \times 3$ kpc of the LIRGs (typically $\sim R_{eff}$). If we translate these scales to a distance that is ten times larger, these ~ 3 kpc are equivalent to an angular distance of $\sim$1", i.e. 1/8 of the FoV or ~ 8 spaxels. The lack of data from the external regions of the local objects keeps the extrapolation to larger distances from beeing straight-forward.

Figure 5.4 shows the relation of the median of the individual A_V simulated distributions to the sampling scale/distance, for each galaxy in the LIRG subsample. Although each curve shows a different behaviour that depends on the particular gas and dust distribution, there is a general trend towards lower A_V values as distance increases. This decrement of the median value of the visual extinction is also observed when we consider the distribution of LIRGs as a class, adding all the individual spaxels of the LIRG subsample in a single distribution, as

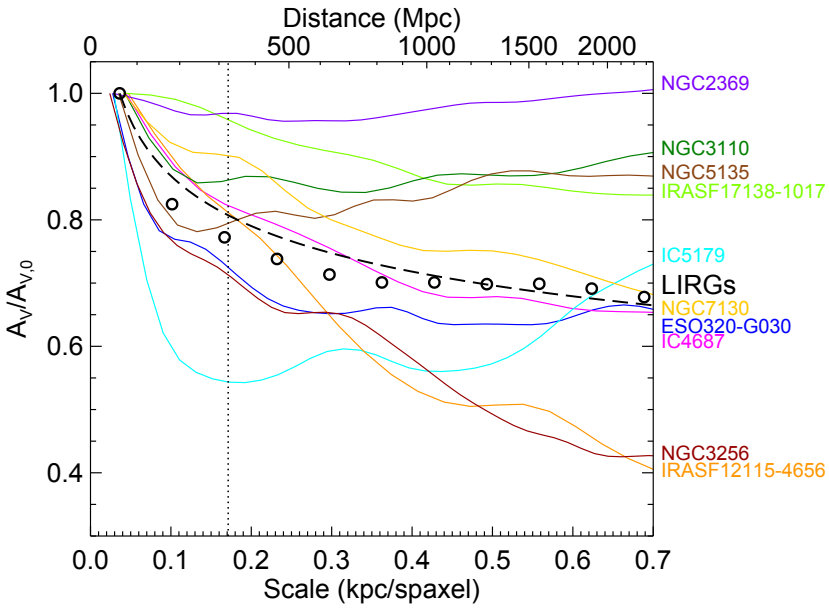

Figure 5.4: Evolution of the median A_V as a function of scale/distance - Evolution of the computed median A_V of the individual distributions of the LIRG subsample as a function of scale/distance. The A_V values are normalised to the rest-framed distribution. The value that corresponds to the A_V distribution of the whole LIRG subsample is plotted as black circles and a power-law fit to the data as a dashed black line. The mean distance of the ULIRG subsample (328 Mpc) is plotted as a vertical dotted line for reference.

shown in the figure. To parametrize this observed decrement of the median A_V of the LIRG distribution with the sampling scale/distance, we fitted the data points to a simple power-law model, and found that the best-fit model corresponds to

$$A_V/A_{V0} \simeq (D/D_0)^{-0.13} \simeq (S/S_0)^{-0.14}, \tag{5.2}$$

where A_V and S are the median values of the A_V distribution and the physical scale at a distance D, respectively, and $A_{V0} = 5.27$ mag and $S_0 = 290\,\mathrm{pc\,arcsec^{-1}}$ are the median values of the rest-frame A_V distribution and median physical scale at the mean distance of the LIRGs subset, $D_0 = 63.3$ Mpc, respectively.

In figure 5.5, we show in detail the observed A_V distribution of the LIRG subsample and the simulated distributions for increasing distances. The different panels reveal that not only the median value of the distribution decreases when the galaxies are sampled on a larger physical scale, but also that the shape of the distribution is slightly different, becoming narrower than the rest-framed distribution, and more compact. The mode of the simulated distribution also changes with respect to the ULIRG observed distribution, and becomes lower

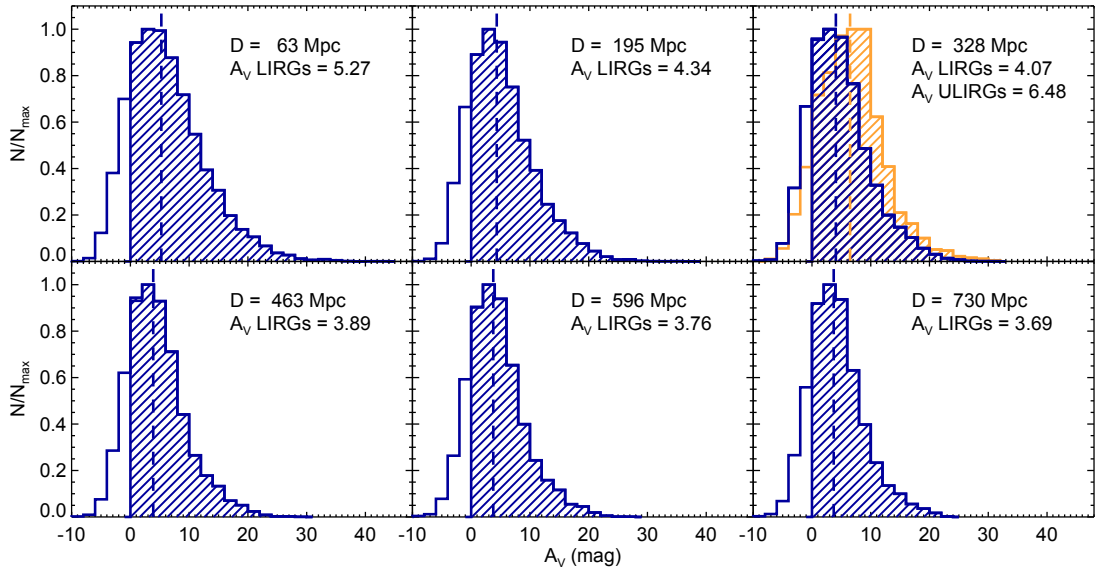

Figure 5.5: Simulated A_V distributions of the LIRG subsample - Different simulations of the LIRGs A_V distribution for increasing distance (from top to bottom and left to right). The median of each distribution is highlighted with a vertical dashed line. The distance and the median A_V of the simulated distribution is annotated in each panel. The top left panel corresponds to the average distance of the ULIRG subsample, and shows the observed A_V distribution of the ULIRGs and its median, in yellow.

than the median. As shown in Fig. 5.4, the difference between the rest-frame extinction, A_{V0}, and the simulated A_V increases rapidly within the first D$\sim$700 Mpc, and seems to reach an asymptotic value of A_V/A_{V0} $\sim$0.65 beyond that distance.

The non-uniform distribution of the dust, even on small scales, makes that, at a given resolution unit, we map both obscured regions and areas where the interstellar medium is more transparent. This average is biased towards the brightest regions, which are those were the emission is less absorbed. The result is that, on average, the dust distribution is smoothed, becomes narrower, and the A_V values that we measure are biased towards the lowest values.

As mentioned in Section 5.3.2, we measured a median extinction of $A_{V,\mathrm{LIRGs}} = 5.3$ and $A_{V,\mathrm{ULIRGs}} = 6.5$ magnitudes for our LIRG and ULIRG subsamples, respectively. Since the average distance of each subsample is $\sim$ 63 Mpc and $\sim$ 328 Mpc (see Chapter 4), this factor $\sim$5 in distance and sampling scale (from $\sim$0.2 kpc to $\sim$0.9 kpc on average, respectively) translates to a decrease in the measured A_V of $\sim$1.2 mag, as shown in Fig. 5.5 (top right panel). If we assume that LIRGs and ULIRGs have similar structures and apply the same correction to the ULIRGs subsample, we find that the average A_V in the ULIRGs, corrected from distance effects, reaches $A_V\sim$8.0 mag, i.e. $\sim$2.8 mag higher than in LIRGs.

Besides this resolution/distance effect, the difference between the observed A_V distribution

in LIRGs and ULIRGs could also be interpreted in terms of intrinsic differences in the morphology between both classes. Although there seems to be a general trend for LIRGs as a class that suggest that the observed A_V decreases with the distance/resolution, Fig.5.4 also shows that the behaviour of each individual galaxy is very different, and depends strongly on the particular morphology of the dust distribution. These differences among the objects of the LIRGs subset suggest that the correction to the observed A_V could not be accurate for individual galaxies, and would only reflect a general trend for LIRGs as a class.

5.3.5. Implication for extinction-corrected properties in high-z galaxies

There are different observational proofs that suggest that SMGs could be the high-z analogous of local (U)LIRG. The sub-millimetre and radio fluxes of this population of galaxies indicate that their bolometric luminosities are comparable to local ULIRGs, whereas their mid-IR emission seems to be similar to the observed in local LIRGs (Kovács et al. 2006, Takata et al. 2006, Menéndez-Delmestre et al. 2009). Besides this, recent IFS-based observations of SMGs reveal that they present evidence of clumpy star formation on kiloparsec scales and similar star-formation rate surface densities (Σ_{SFR}) to the local counterparts (Nesvadba et al. 2007, Harrison et al. 2012, Alaghband-Zadeh et al. 2012, Menéndez-Delmestre et al. 2013). It is well known that these high-z galaxies may be highly obscured and that a combination of intense dust-obscured star formation and dust-enshrouded AGN activity would be responsible for the high infrared luminosities of these objects (Blain et al., 2002). HST-NICMOS and ACS observations reflect structured dust obscuration in these objects (Swinbank et al., 2010). In particular, Takata et al. (2006) find that the internal extinction in these objects are similar to the extinction in local ULIRGs, and measured a median extinction of $A_V = 2.9 \pm 0.5$ mag in a sample of SMGs at z$\sim$1.0–3.5 using the H_α/H_β flux ratio.

Clumpy and dusty star-forming structures have also been identified at high redshifts in more common star forming galaxies (i.e. the so called 'main sequence', MS, of star forming galaxies). These galaxies have (sub)kpc star-forming clumps mostly spread over galactocentric distances of few to several kpc (Förster Schreiber et al. 2011a, 2011b, Genzel et al. 2011), and with internal nebular extinctions of 2 to 4 magnitudes, assuming $A_{v,H_\alpha} = A_{v,stellar}/0.44$ (Förster Schreiber et al. 2009, Wuyts et al. 2011).

In the previous subsection we showed that the distance/linear scale may play an important role in deriving the internal extinction properties of LIRGs and ULIRGs, by comparing both populations of galaxies locally, albeit with a difference of a factor $\times$5 in distance between

both subsamples. According to the simulations, the median extinction measured in a given galaxy decreases when placed at increasing distances. This effect is due to the fixed angular resolution of the IFS data that translates into a larger physical scale per spatial resolution element (spaxel) as the distance to the galaxy increases, and is particularly important when the physical scales sampled by the spaxel are much larger than that of the intrinsic clumpy structure of the dust distribution and star-forming regions.

It is clear that if the intrinsic star-forming structure of high-z galaxies is in general similar to that of our local LIRGs (i.e. mostly disks) and ULIRGs (i.e. mostly interacting), the smearing effect mentioned above would have a direct impact in the derivation of their 2D internal extinction values, and of all relevant subsequent extinction corrected properties such as star formation surface densities, KS-laws, and overall star formation rates. This would certainly be the case not only with seeing-limited near-IR IFS, heavily undersampling the galaxies at redshifts of 1 to 3, with each spaxel corresponding to about 1.5-2 kpc, but even when using AO assisted IFS where the spaxel (50 to 100 mas) translates to about 0.4 to 0.8 kpc. Thus, if the results given by Eq. 5.2 (see also Fig. 5.4) are applied to high-z galaxies, the extinction values derived directly from the observed optical emission line ratios would require to be increased by a factor 1.4 on average. This correction would correspond to an additional increase in the H_α flux by a factor $\sim$3 and hence, in the extinction-corrected SFR and Σ_{SFR}.

Finally, it is worth noticing that this distance effect could also have a minor wavelength dependency. The method presented here to derive the A_V values is based on specific emission line ratios in the near-infrared. Since these lines originate in regions of higher optical depths than the optical emission lines, and the stellar continuum measured at optical wavelengths, differences in the amount and/or distance dependency could appear. It would be worth exploring these effects with a suitable set of data, in particular if, as in many high-z studies, the A_V corrections applied to the observed Hα flux is obtained indirectly using the standard Calzetti recipe $A_{H\alpha} = 7.4\,E(B–V)$, where $E(B–V)_{gas} = 0.44\,E(B–V)_{stars}$ (Calzetti et al. 2000, 2001)

5.4. Summary

- In this chapter, we presented a detailed 2D study of the extinction structure of a representative local sample of 10 LIRGs and 7 ULIRGs, based on VLT-SINFONI IFS K-band observations. We sample the central $\sim 3 \times 3$ kpc for LIRGs and the

$\sim 12 \times 12$ kpc for ULIRGs, with average linear resolutions (FWHM) of $\sim$0.2 kpc and $\sim$0.9 kpc, respectively. The extinction maps are based on measurements of the Brγ/Brδ line ratio for LIRGs and of the Paα/Brγ line ratio for ULIRGs.

- In agreement with previous studies, we found that the distribution of the dust in these galaxies presents a patchy structure on sub-kiloparsec scales, with regions almost transparent with $A_V \sim 0$ to heavily obscured areas with A_V values up to $\sim 20 - 30$ mag. In most of the objects in the sample ($\sim$70%), the nucleus of the galaxy coincides with the peak in the extinction maps, with values that range from $A_V \sim 3$ mag up to $A_V \sim 17$ mag.

- We obtained the A_V distribution of the individual galaxies on a spaxel-by-spaxel basis (see Fig. 5.2). The individual A_V distributions show a wide range of values with most of them spread between $A_V \sim 1$ and $A_V \sim 20$ mag, with no clear evidence of any dependence with L_{IR}. However, as a class (see Fig. 5.3), ULIRGs show A_V values (median of 6.5 mag, mode of $\sim$7-8 mag) higher than those for LIRGs (median of 5.3 mag, mode of $\sim$3-4 mag). The A_V distribution in LIRGs shows a mild decrease as a function of galactocentric distances of up to 1 kpc and a flattening at larger distances (2-3 kpc). No similar behaviour is detected in ULIRGs, most likely owing to the lower linear resolution of the observations.

- To study the effect of the spatial sampling in the derived extinction values at increasing galaxy distances, the individual Brγ and Brδ maps of our subsample of local LIRGs (at an average distance of 63 Mpc) have been artificially smeared. These simulations have shown that the spatial resolution plays an important role in shaping the A_V distributions. The median value of the visual extinction measured on the LIRG subsample decreases as a function of the linear resolution/distance by a factor $\sim$ 0.8 at the average distance (328 Mpc, 0.2 kpc/spaxel) of our ULIRG sample, and up to $\sim$0.67 for distances above 800 Mpc (0.4 kpc/spaxel). This distance effect would have implications in the derivation of the intrinsic extinction, and subsequent properties, such as SFR, Σ_{SFR}, and the KS-law, in high-z star-forming galaxies, even in AO-based spectroscopy. If local LIRGs are analogues of the main-sequence star-forming galaxies at cosmological distances, the extinction values (A_V) derived from the observed emission lines in these high-z sources would need to be increased by a factor 1.4 on average.

6

Sub-kpc study of the star formation in local LIRGs and ULIRGs

Analysis of the global Σ_{SFR} structure and characterisation of individual star-forming clumps

"E quindi uscimmo a riveder le stelle."
[And we came forth to contemplate the stars.]
— Dante Alighieri, *Purgatorio*

6.1. Introduction

In this Chapter, we present a detailed 2D study of the global star formation rate (SFR) and the sub-kpc structure of the star-formation rate surface density (Σ_{SFR}) in our local sample of LIRGs and ULIRGs. Besides the spaxel-by-spaxel approach, we also analyse in detail the properties of individual star-forming clumps, in terms of their size, Σ_{SFR} and velocity dispersion, and compare the results with local and high-z clumps from other samples. Finally, we briefly discuss the effect of the spatial sampling on the Σ_{SFR} measurements.

The Chapter is organised as follows: Section 6.2 contains a summary of the SFR tracers and calibrations used, and details the procedures for obtaining the Σ_{SFR} maps and characterising the star-forming clumps. The results and analysis of the Σ_{SFR} maps and distributions, as well as the individual regions, are presented in Sec. 6.3, whereas Sec. 6.4 includes a brief summary of the main results.

6.2. Data analysis

6.2.1. Star-formation measurements. Optical and infrared tracers

One of the key issues regarding the measurement of the star-formation rate is the calibration of the SFR indicators. The UV/optical/near-IR range indicators probe the star-formation by measuring directly the stellar light. The young and most massive stars produce considerable amount of ionising photons that ionise the surrounding gas that, due to recombination processes, creates line emission cascades including the Balmer, Paschen and Brackett series. The conversion from the flux of light into SFR is performed under the assumption of a particular stellar IMF, that has to be fully sampled (i.e. stars are formed in every mass bin), and the star-formation has to be roughly constant over the time scale probed by the specific emission used. In the present work, we focus on the hydrogen recombination tracers that relate the intensity of a particular emission line with the SFR through the ionising photon rate. In particular, for the Hα line, we have the well-known calibration from Kennicutt (1998):

$$\mathrm{SFR}\,[\mathrm{M_\odot yr^{-1}}] = 7.9 \times 10^{-42} \times \mathrm{L_{H\alpha}}\,[\mathrm{erg\,s^{-1}}], \tag{6.1}$$

that assumes a Salpeter IMF from 0.1 to 100 $\mathrm{M_\odot}$ (Salpeter, 1955) and solar abundances, and the star formation has to have remained constant over ~ 6 Myr for the expression to be applicable. The variations of the calibration constant are $\sim 15\%$ due to variations of the electron temperature within $\mathrm{T_e} = 5000 - 20000$ K and almost negligible for electron density variations within the range $\mathrm{n_e} = 10^2 - 10^6\,\mathrm{cm^{-3}}$ (Osterbrock & Ferland, 2006). The calibration constant for other emission lines at longer wavelengths, like Brγ and Paα, can be derived from this using the recombination factors from Osterbrock & Ferland (2006). Although these lines have the advantage of being less sensitive to dust attenuation, they are also progressively fainter and more sensitive to the physical conditions of the gas (Calzetti, 2012). In particular, Brγ is $\sim$100 times fainter than Hα, on average, and its luminosity changes $\sim 35\%$ within $\mathrm{T_e} = 5000 - 20000$ K, whereas Paα is ~ 7.5 times fainter than Hα and its luminosity varies $\sim 25\%$ within the same temperature range. The dependence on the density is, in both cases, less than a $\sim 3\%$ (Osterbrock & Ferland, 2006).

The indicators based on ionisation of hydrogen are also highly sensitive to the effects of dust by the attenuation of the line itself or by the direct absorption of Lyman continuum (Lyc) photons by dust. The effect of the dust attenuation on the line decreases at increasing

wavelength, and could be handled if measurements of the extinction are available, e.g. in terms of line ratios, as it is the case of this work. On the other hand, the absorption of Lyc photons by dust is a more difficult effect to treat from an empirical point of view, since the photons are directly removed from the beam and no emission results. In particular, this effect could be significant in typical local (U)LIRGs, where large ionisation parameters (ionizing photons per atom) and dust-to-gas ratios (metallicities) are expected, and could exceed the 20% of absorbed Lyc photons (Inoue 2001, Dopita et al. 2003).

Another plausible effect that might bias the SFR measurements based on recombination lines is the leakage of Lyc photons. It is well known that a fraction of the ionising photons created could escape the regions of star formation without been absorbed by the neutral atomic gas (e.g. Relaño et al. 2002, Eldridge & Relaño 2010). Under these circumstances, the case B recombination does not fully apply since not all the ionising radiation is absorbed. Although leakage might be negligible when considering galaxies as a whole, star-forming regions tend, on the other hand, to lose about $\sim 25-40\%$ of ionising photons (Crocker et al. 2012, Pellegrini et al. 2012, Relaño et al. 2012), and the local SFR measurements from recombination lines might be biased downwards by a factor 1/3 (Calzetti, 2012).

Besides the mentioned effects, that are either consequence of the transition probabilities or might occur in a wide range of scales, an incomplete sampling of the stellar IMF could become particularly problematic when creating spatially-resolved SFR maps, specially for ionised-gas tracers that are most sensitive to the uppermost part of the IMF. Regardless of whether the IMF is universal, stochastic sampling of the IMF, i.e. the stellar IMF is randomly, not fully sampled, will yield large fluctuations in the line luminosity for a fixed SFR, since only stars more massive than $\sim 20\,M_\odot$ produce a measurable ionising photon flux. For star-forming disk galaxies, this typically occurs on spatial scales of $\sim 0.1-1\,$kpc, and SFR of $\sim 0.001-0.01\,M_\odot\,yr^{-1}$ (Kennicutt & Evans, 2012). This effect implies a practical limitation of $SFR \gtrsim 0.001\,M_\odot\,yr^{-1}$ for the use of SFR tracers based on ionised gas for a $\sim 20\%$ or less uncertainty (Cerviño et al. 2002, Lee et al. 2009). However, this limit is far from the typical SFR observed in LIRGs and ULIRG of $\gtrsim$1-20 $M_\odot\,yr^{-1}$

Although hydrogen recombination lines and UV emission represents the most traditional SFR tracers (Kennicutt, 1998), indicators based on dust-processed stellar light have been widely used since the advent of high-sensitive IR space telescopes like *Spitzer* or *Herschel*. Among all the available IR-continuum tracers, we focused on the L_{IR} and monochromatic 24 μm indicators to compare with our SFR measurements from the near-IR hydrogen lines.

In particular, we used the total-IR-based (TIR, L_{IR}[8–1000μm]) SFR calibration derived by Kennicutt (1998):

$$SFR\,[M_{\odot}yr^{-1}] = 4.5 \times 10^{-44} \times L_{IR}\,[erg\,s^{-1}], \tag{6.2}$$

that assumes a continuous burst of star formation of age 10-100 Myr, with a completely dust-enshrouded stellar population and dust heating fully dominated by young stars. The main disadvantage of this indicator is the need to obtain multiple measurements along the IR spectral energy distribution (SED) and/or perform extrapolations.

In that sense, the monochromatic SFR indicators, like the 24μm continuum, have the advantage of only requiring a single measurement. This tracer, as all the indicators in the mid-IR range, is based on the continuum emission dominated by a warm ($T \geq 50\,K$) dust component in thermal equilibrium, and small-grain dust heated by the absorption of individual starlight photons (Draine, 2003). Among the multiple calibrations available in the literature, we used the calibration from Alonso-Herrero et al. (2006):

$$SFR\,[M_{\odot}yr^{-1}] = 1.5 \times 10^{-8} L_{24\mu m}\,[L_{\odot}]^{0.871}. \tag{6.3}$$

Unlike the previous optical and TIR tracers, several calibrators of the SFR use a non-linear relation between the luminosity at 24 μm and the SFR. These models predict that the 24 μm luminosity increases proportionally faster than the SFR, due to the increasing mean dust temperature. For a detailed description of the 24μm calibrations, see Calzetti et al. (2010) and references therein.

As other SFR indicators, dust emission is subject of important systematics effects that depend on the particular dust distribution and metallicity (Hirashita et al., 2001). The TIR-based indicator assumes that dust completely absorbs the starlight from the recent star formation. However, as occurred with the Lyc photons, some radiation might escape without heating the dust, so the IR emission will systematically underestimate the SFR, if we assume no AGN emission. The fraction of the not absorbed radiation varies as a function of the dust content of the galaxies, from almost negligible in dusty starburst galaxies to nearly 100% in dust-poor objects or metal poor regions (Kennicutt & Evans, 2012). Another systematic effect of the IR-continuum based SFR tracer is the contribution of evolved stars ($\sim 100 - 200$ Myr) to the L_{IR} that overestimate the SFR. Although in individual star-forming regions almost all

the dust heating comes from young stars, the fraction of evolved stars that contributes to the heating of the dust could be significative in galaxies with low specific SFR (Cortese et al. 2008, Kennicutt & Evans 2012).

6.2.2. Spatially-resolved star-formation rate at sub-kpc scales

Object	Σ_{obs}^{median}	Σ_{corr}^{median}	Σ_{obs}^{mean}	Σ_{corr}^{mean}	$\Sigma_{obs}(P_5)$	$\Sigma_{obs}(P_{95})$	$\Sigma_{corr}(P_5)$	$\Sigma_{corr}(P_{95})$	$A_{V,median}$
(1)	(2)	(3)	(4)	(5)	(6)	(7)	(8)	(9)	(10)
IRASF12115-4656	0.7	1.0	1.6 ± 0.6	2.9 ± 3.3	0.4	2.1	0.5	7.5	7.9
IC5179	0.7	0.7	5.2 ± 1.7	2.8 ± 5.3	0.3	3.0	0.3	6.1	4.1
NGC2369	1.4	3.9	5.0 ± 2.5	13.8 ± 21.5	0.3	7.8	0.6	60.7	18.5
NGC5135	1.5	2.3	6.2 ± 2.6	8.6 ± 6.8	0.3	7.7	0.4	19.7	8.0
NGC3110	1.0	1.6	2.2 ± 0.8	2.6 ± 2.6	0.3	3.0	0.5	7.6	8.8
NGC7130	0.6	0.8	4.9 ± 3.5	4.9 ± 13.4	0.3	5.3	0.3	17.4	5.4
ESO320-G030	1.4	1.8	3.0 ± 1.1	3.6 ± 3.3	0.4	3.8	0.5	8.7	5.1
IRASF17138-1017	1.5	2.8	9.4 ± 4.3	12.6 ± 8.3	0.4	12.5	0.5	23.3	6.6
IC4687	1.9	3.3	5.7 ± 2.8	8.7 ± 5.4	0.4	7.9	0.5	16.0	5.4
NGC3256[†]	2.4	3.4	6.6 ± 3.1	10.6 ± 8.1	0.5	9.0	0.5	18.6	4.9
IRAS23128-5919	0.2	0.2	4.0 ± 3.0	4.6 ± 9.8	0.0	3.5	0.1	8.1	6.2
IRAS21130-4446	0.2	0.3	2.4 ± 1.0	1.7 ± 2.7	0.0	3.0	0.0	6.1	4.2
IRAS22491-1808	0.1	0.2	1.1 ± 0.6	1.2 ± 1.7	0.0	1.6	0.1	4.6	6.4
IRAS06206-6315	0.1	0.2	1.2 ± 0.6	1.5 ± 2.3	0.1	1.5	0.1	4.5	6.4
IRAS12112+0305	0.2	0.3	1.8 ± 1.0	2.8 ± 3.4	0.1	2.2	0.1	6.4	6.4
IRAS14348-1447	0.1	0.2	1.9 ± 0.9	3.2 ± 3.2	0.0	1.6	0.1	4.8	6.3
IRAS17208-0014	0.2	0.3	2.9 ± 2.0	4.3 ± 6.4	0.1	5.1	0.1	12.6	5.4
LIRGs	1.2	1.7	2.1 ± 2.6	4.5 ± 8.8	0.3	6.8	0.4	17.0	5.3
ULIRGs	0.2	0.2	0.7 ± 2.0	1.6 ± 6.6	0.0	2.8	0.1	6.8	6.5

Table 6.1: Statistics of the star formation rate density, Σ_{SFR}, distributions. Cols. (2) and (3): Median Σ_{SFR} values of the observed (2) and extinction-corrected (3) spaxel-by-spaxel distributions. Cols. (4) and (5): Weighted mean Σ_{SFR} values of the observed (4) and extinction-corrected (5) distributions. Cols. (6) to (9): 5th and 95th percentiles of the distributions. Col. (10): Median A_V from the spaxel-by-spaxel extinction distributions (Piqueras López et al., 2013). All the quantities are expressed in [$M_\odot\,yr^{-1}\,kpc^{-2}$], except A_V that is expressed in magnitudes.

The SFR and Σ_{SFR} values were derived using the Brγ and Paα emission lines for LIRGs and ULIRGs, respectively, and assuming the standard star formation rate to Hα luminosity ratio given by the expression from Kennicutt (1998) (Eq. 6.1) that assumes solar abundances, and a Salpeter IMF from 0.1 to 100 $M_\odot$. It is well known that this expression yields higher values of the SFR than those based on other IMF like Kroupa (Kroupa, 2001) or Chabrier (Chabrier, 2003). The conversion factor from these IMF to Salpeter are 1.44 and 1.59 respectively (Kennicutt et al. 2009, Calzetti et al. 2007). From this expression, taking into account the recombination factors Hα to Paα and Brγ (T$= 10,000$ K and $n_e = 10^4\,cm^{-3}$, case B; Osterbrock & Ferland 2006), we can directly obtain equivalent relations in terms of the Brγ and Paα luminosities:

$$\mathrm{SFR}\,[\mathrm{M_\odot yr^{-1}}] = 8.2 \times 10^{-40} \times \mathrm{L_{Br\gamma}}\,[\mathrm{erg\,s^{-1}}] \quad (6.4)$$

$$\mathrm{SFR}\,[\mathrm{M_\odot yr^{-1}}] = 6.8 \times 10^{-41} \times \mathrm{L_{Pa\alpha}}\,[\mathrm{erg\,s^{-1}}]. \quad (6.5)$$

To obtain the extinction-corrected values of the SFR and Σ_{SFR} for the maps and spaxel-by-spaxel distributions, we have applied the A_V correction presented in Piqueras López et al. (2013) (Chapter 5), based on the Brγ/Brδ and Paα/Brγ line ratios for LIRGs and ULIRGs, respectively. As outlined in Chapter 5, this correction is made on a spaxel-by-spaxel basis on those spaxels where the weakest line (Brδ and Brγ in LIRGs and ULIRGs, respectively) has been detected above a S/N threshold of 4. In those spaxels where this point-to-point correction is not available, we have used a flux-weighted median value of A_V.

The individual SFR uncertainties are obtained directly from the 1σ errors in the flux and in the extinction measurements. As described in Chapter 5, the A_V uncertainties are derived from the error in the line fluxes using Monte Carlo simulations, with the main advantage that uncertainties take into account both the photon noise, and the errors from the line fitting or from an inaccurate continuum determination. Since the A_V measurements are highly sensitive to the S/N of the weakest line of the ratio, we observed an artificial increase of the corrected SFR in those regions with low surface brightness, specially in the ULIRGs. In those regions, that are typically the external regions of the sources, the uncertainties in the A_V measurements reach up to 70-80%, and are directly propagated to the SFR measurements.

Figures D.1 and D.2 show the two-dimensional structure of the extinction-corrected Σ_{SFR}, together with the A_V map, and Brγ and Paα emission maps for LIRGs and ULIRGs, respectively. We marked the main nucleus of the objects, defined as the brightest spaxel of the SINFONI K band image (Chapter 4), and the Brγ (Paα) peak, that corresponds to the brightest spaxel of the corresponding emission map. The statistics of the spaxel-by-spaxel distributions (i.e. median and percentiles) are shown in Table 6.1.

Although the detection limit of the emission maps varies from object to object, we found an average sensitivity limit of $10^{-18}\,\mathrm{erg\,s^{-1}\,cm^{-2}}$ per spaxel on the Brγ and Paα maps in LIRGs and ULIRGs, respectively. Considering the most favourable case, i.e. the closest LIRG and ULIRG, this flux threshold yields to Σ_{SFR} values of $\sim$0.3 $\mathrm{M_\odot\,yr^{-1}\,kpc^{-2}}$ and $\sim$0.03 $\mathrm{M_\odot\,yr^{-1}\,kpc^{-2}}$ per spaxel in LIRGs and ULIRGs, respectively, that are different due to the use of different tracers. Therefore, we hereafter assume these values as our detection limits in the Σ_{SFR} maps and spaxel-by-spaxel distributions.

6.2.3. Integrated measurements of the star-formation rate

Object	R_{eff}	$F^{obs}_{Pa\alpha}$	$F^{corr}_{Pa\alpha}$	Σ^{obs}_{SFR}	Σ^{corr}_{SFR}	σ	A_V
(1)	(2)	(3)	(4)	(5)	(6)	(7)	(8)
IRASF12115-4656	1.3	9.4 ± 0.2	25.5 ± 0.6	0.9 ± 0.1	2.4 ± 0.1	46 ± 2	11.3 ± 0.2
IC5179†	1.6	22.3 ± 0.6	42 ± 1	0.7 ± 0.1	1.2 ± 0.1	50 ± 2	7.2 ± 0.2
NGC2369	0.5	10.6 ± 0.3	72 ± 2	2.0 ± 0.1	13.9 ± 0.4	108 ± 3	21.7 ± 0.3
NGC5135	0.5	12.2 ± 0.2	27.9 ± 0.6	4.1 ± 0.1	9.4 ± 0.2	69 ± 2	9.3 ± 0.1
NGC3110†	1.9	14.3 ± 0.2	30.1 ± 0.5	0.9 ± 0.1	2.0 ± 0.1	53 ± 1	8.4 ± 0.1
NGC7130	1.0	10.6 ± 0.3	35.2 ± 0.9	1.2 ± 0.1	4.1 ± 0.1	83 ± 2	13.6 ± 0.3
ESO320-G030	0.7	13.7 ± 0.4	23.4 ± 0.7	1.7 ± 0.1	2.8 ± 0.1	43 ± 2	6.1 ± 0.1
IRASF17138-1017	0.6	9.7 ± 0.1	18.9 ± 0.3	4.5 ± 0.1	8.9 ± 0.1	62 ± 1	7.6 ± 0.1
IC4687	1.1	25.0 ± 0.4	47.1 ± 0.8	3.1 ± 0.1	5.8 ± 0.1	51 ± 1	7.2 ± 0.1
NGC3256‡	1.0	73 ± 1	131 ± 2	3.0 ± 0.1	5.4 ± 0.1	56 ± 1	6.6 ± 0.1
IRAS23128-5919	2.0	9.5 ± 0.2	24.9 ± 0.5	2.4 ± 0.1	6.3 ± 0.1	116 ± 2	7.2 ± 0.1
IRAS21130-4446	1.6	0.7 ± 0.1	1.5 ± 0.1	1.2 ± 0.1	2.6 ± 0.1	127 ± 3	5.7 ± 0.4
IRAS22491-1808	1.7	0.6 ± 0.1	1.4 ± 0.1	0.6 ± 0.1	1.6 ± 0.1	73 ± 1	6.6 ± 0.3
IRAS06206-6315	2.5	0.7 ± 0.1	2.0 ± 0.1	0.5 ± 0.1	1.4 ± 0.1	174 ± 3	7.4 ± 0.3
IRAS12112+0305	2.6	1.1 ± 0.1	3.2 ± 0.1	0.5 ± 0.1	1.4 ± 0.1	138 ± 1	8.0 ± 0.2
IRAS14348-1447	3.8	1.7 ± 0.1	4.2 ± 0.1	0.4 ± 0.1	1.1 ± 0.1	109 ± 1	6.5 ± 0.2
IRAS17208-0014	0.9	4.4 ± 0.1	11.8 ± 0.1	5.1 ± 0.1	13.7 ± 0.2	144 ± 1	7.3 ± 0.1

Table 6.2: Star-forming properties of the sample. Col. (2): Hα effective radius in [kpc] from Arribas et al. (2012). Cols (3) and (4): Observed (3) and extinction-corrected (4) Paα fluxes measured within R_{eff}, expressed in $[\times 10^{14} \mathrm{erg\,s^{-1}\,cm^{-2}}]$. The Pa$\alpha$ fluxes for the LIRGs are obtained from the Brγ fluxes using the case B recombination factor at $T = 10,000$ K and $n_e = 10^4\,\mathrm{cm^{-3}}$ (Osterbrock & Ferland, 2006). Cols. (5) and (6): Observed (5) and extinction-corrected (6) Σ_{SFR} in $[M_\odot\,\mathrm{yr^{-1}\,kpc^{-2}}]$. Col. (7): Intrinsic velocity dispersion in $[\mathrm{km\,s^{-1}}]$ of the Brγ and Paα lines for LIRGs and ULIRGs respectively. Col. (8): A_V in magnitudes. All the uncertainties are calculated by a *bootstrap* method of N = 300 simulations. †Due to the limited FoV of the observations, in these objects the Hα effective radius is greater than our FoV, and the fluxes should be considered lower limits. ‡ Since the main nucleus of NGC 3256 was not observed, we centred the aperture for in the centre of the FoV, so the measurements might be inaccurate.

Besides the statistical analysis of the spaxel-by-spaxel distributions, we obtained integrated measurements of the SFR and Σ_{SFR} by stacking the spectra of the individual spaxels within the Hα effective radius from Arribas et al. (2012). The spectra of each individual spaxel were previously *derotated*, i.e. corrected from the intrinsic velocity field, to prevent from beam smearing effects and improve the S/N of the lines. The lines were then fitted to a gaussian profile, accounting for the instrumental broadening using the OH sky line at 2.190 μm (see Piqueras López et al. 2012a, Chapter 4, for details). Although the extinction of each region could be estimated directly from the stacked spectra, we argued in Piqueras López et al. (2013), Chapter 5, that the A_V measurements could be affected by aperture effects when measured over large apertures. To prevent this effect and to take advantage of the more detailed A_V maps, we calculated the extinction on an spaxel-by-spaxel basis by performing

synthetic photometry over the observed and extinction corrected Brγ and Paα emission maps, and derived the visual extinction using the formula:

$$A_V = -2.5\alpha_\lambda^{-1} \log\left[\frac{F_{obs}}{F_{corr}}\right],$$

where F_{obs} and F_{corr} are the observed and corrected fluxes within the aperture measured on the observed and extinction-corrected emission maps, respectively, and α_λ is defined as $A_\lambda = \alpha_\lambda A_V$ and is given by the extinction law described in Calzetti et al. (2000) ($\alpha_{Br\gamma} = 0.096$ and $\alpha_{Pa\alpha} = 0.145$, see Piqueras López et al. 2013). We used this latter value of the extinction to correct the luminosity of each region, extracted from the line fitting of the stacked spectrum. The measurements of the Σ_{SFR}, velocity dispersion and A_V for each object are listed in Table 6.2.

6.2.4. Characterisation of the star-forming clumps

We have identified a total of 95 individual star-forming clumps / complexes by a visual inspection of the Brγ and Paα emission maps. To characterise the size of an individual star-forming clump is a key issue to accurately measure important properties of the region such as its luminosity, velocity dispersion or Σ_{SFR}. There are two parameters that have been widely employed to characterise the size of an emitting region, i.e. the effective radius or half-light radius, r_{eff} (Kennicutt, 1979), and the 'core' radius, r_{core} (Sandage & Tammann, 1974).

The r_{eff} is traditionally defined as the radius that encloses half of the total flux of the emitting region assuming circular symmetry, although it could be generalised in terms of an isophotal region with arbitrary shape that encloses a total flux greater than a defined fraction of light. Depending on the flux threshold, the intrinsic flux distribution of the region and the sensitivity of the observations, this radius can represent either the core of the region or also include the surrounding diffuse inter-clump emission. The presence of tails, halos or smeared background emission when two regions are close together increase r_{eff} and therefore bias the measurements. This could be particularly important when comparing low- and high-redshift samples, since the contribution of the surrounding background could be significantly higher locally than at higher redshift.

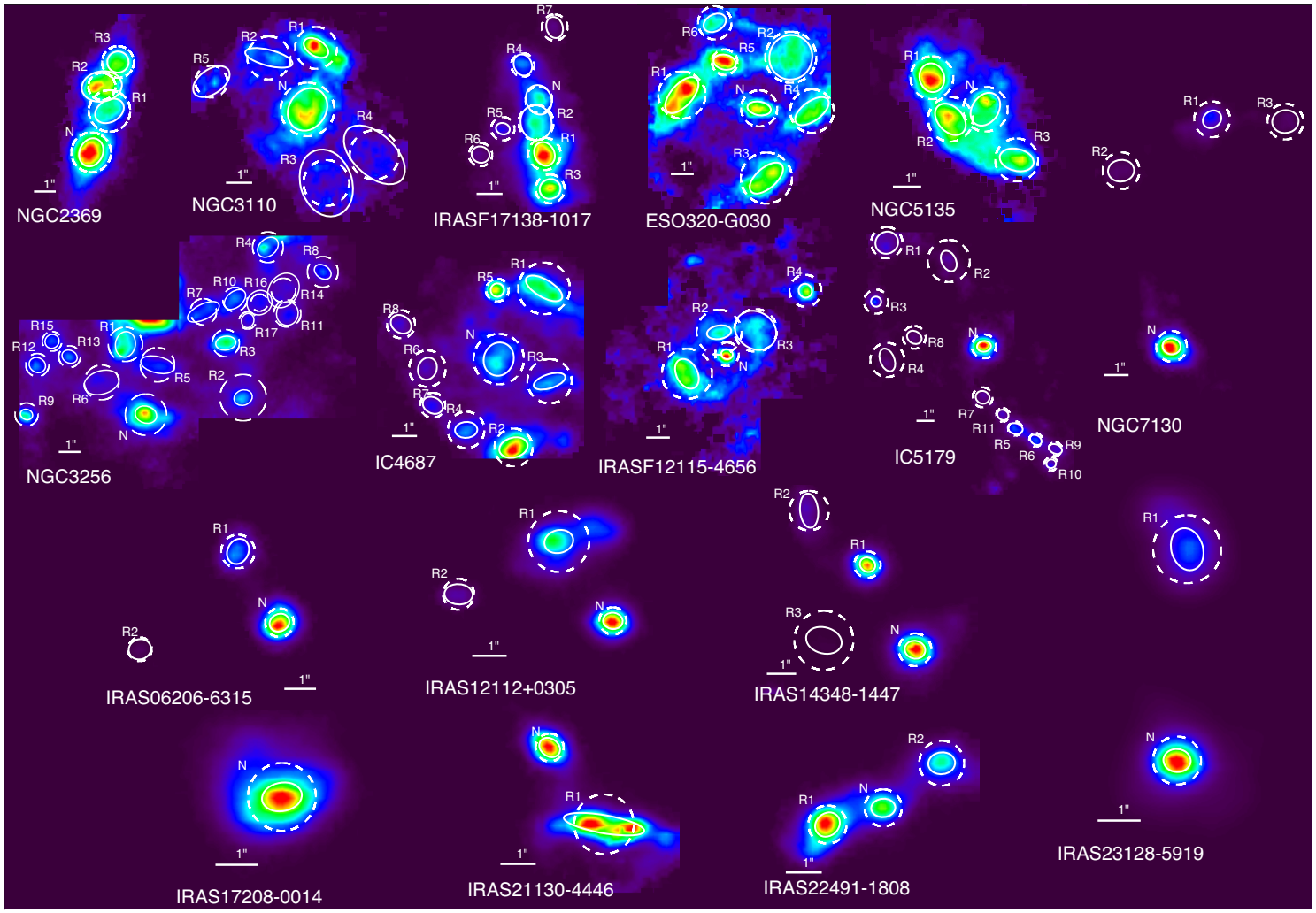

Figure 6.1: Locations of the individual star-forming clumps - Maps of the observed Brγ (LIRGs) and Paα (ULIRGs) emission. The angular scale of each object is indicated by a white horizontal bar that marks 1 arcsec. The nucleus of each object (see definition in the text) is labeled as 'N', whereas the remaining regions are tagged as 'R#' by decreasing total observed flux (see Table 6.3). The white ellipses over each individual region are the 1σ fitting to the 2D gaussian profile, whereas the white dashed circles have r_{eff} radius. The color scheme is linear and autoscaled.

The 'core' method consists on fitting the light profile of the region using a particular analytic function, typically a 2D Gaussian function. One of the advantages of this method is that it does not depend on any particular flux or surface brightness threshold, and it is less sensitive to the local background. This method is widely used in high-redshift data where the regions are almost unresolved, and seems suitable for a direct comparison between low- and high-redshift observations. However, the main limitation of the method is that it assumes a light profile, typically Gaussian, that might not reproduce accurately the intrinsic profile of resolved clumps, particularly in local samples where the spatial resolution of the observations is of parsec scales. For a further discussion on both methods see Wisnioski et al. (2012).

Figure 6.1 shows the Brγ (LIRGs) and Paα (ULIRGs) maps of the objects of the sample where the individual regions have been overplotted. To obtain the r_{eff} of the individual clumps, we considered a flux threshold of $10^{-18}\,erg\,s^{-1}\,cm^{-2}$ to calculate the total flux of each region. This flux limit corresponds typically to a S/N ratio of ~ 2 in the Brγ and Paα lines per spaxel for LIRGs and ULIRGs, respectively. For this isophotal regions, we estimate the r_{eff} using the 'A/2' method described in Arribas et al. (2012), i.e., the r_{eff} is obtained as $r_{eff} = \sqrt{A/\pi}$ where 'A' is the area covered by the minimum set of spaxels that accounts for half of the total flux of the region.

We show a comparison between the area of the isophotal region (A_{iso}) and the circular area derived from the r_{eff} (A_{eff}) in Fig. 6.2. This relationship would give us an idea of how compact or extended each individual region is, since one would expect that compact regions would present a higher ratio than more uniform regions. In that sense, we also plotted the expected ratio of both areas for an ideal region with an uniform flux distribution, that represents the extreme case of an extended region with diffuse background emission, and a mock region with a symmetric 2D gaussian light profile, that represents a typical unresolved, compact star-forming clump. The region with a constant flux distribution represents the lower limit for the ratio, since $A_{iso} \sim 2 \times A_{eff}$. On the other hand, the relationship between both areas for the mock region would depend on the total flux of the clump, the FWHM of the 2D gaussian profile and our limiting flux threshold. We considered an unresolved clump with a total flux of $10^{13}\,erg\,s^{-1}\,cm^{-2}$ that corresponds to the total flux of a typical star-forming clump of our sample, with a FWHM of $\sim$0.63 arcsec and a detection limit of $10^{-18}\,erg\,s^{-1}\,cm^{-2}$. Most of the clumps from the LIRG subsample lay close to the lower limit of $A_{iso} \sim 2 \times A_{eff}$, whereas the regions observed in the ULIRG subsample present higher ratios, similar to those of more compact distributions. Although it could be argued that this

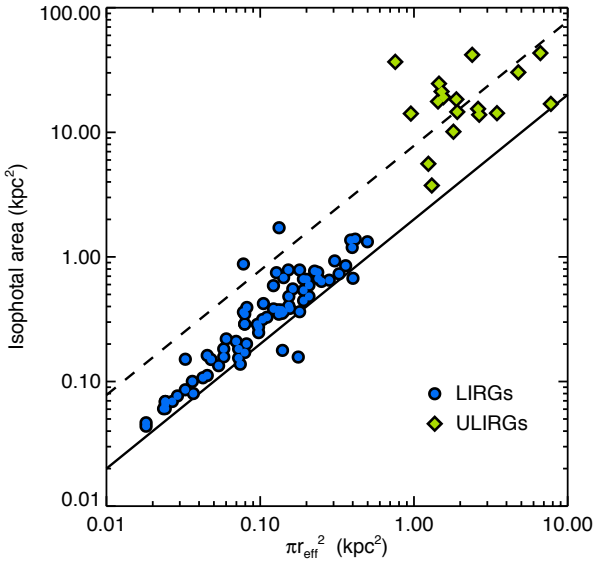

Figure 6.2: Comparison between the isophotal area and the circular area of star-forming regions - Comparison between the isophotal area (region enclosed by an isophote of $10^{-18}\,\mathrm{erg\,s^{-1}\,cm^{-2}}$) and the circular area obtained from the r_{eff} of the individual star-forming regions in LIRGs (circles) and ULIRGs (diamonds). The thick black line represents the ratio between both quantities for a region with an uniform flux distribution, whereas the dashed line represents the same ratio for a region with a symmetric 2D gaussian light profile and a total flux of $10^{13}\,\mathrm{erg\,s^{-1}\,cm^{-2}}$.

might respond to intrinsic differences between the structure of star-forming clumps in LIRGs and ULIRGs, the differences in the spatial resolution and FoV of our observations between both LIRG and ULIRG subsamples make this conclusion not straight forward, and could be a direct implication of the distinct diffuse background contribution in both subsamples.

To calculate r_{core}, we fitted each individual region to a general 2D Gaussian profile that included the local background level as a free parameter. The final value of the radius is obtained as a quadratic mean of the widths of the Gaussian function, $\sigma_{x'}$ and $\sigma_{y'}$, where x' and y' are the canonical axes of the ellipse.

6.2.5. Star-forming clump luminosity, velocity dispersion and extinction correction

Once the region is delimited by one of the two methods, we measured the luminosity, velocity dispersion and visual extinction of the clump from the stacked spectra of the individual spaxels within the circular area defined by r_{eff} and by the ellipse given by $\sigma_{x'}$ and $\sigma_{y'}$. The measurements are performed using the same procedure as for the whole objects, we fitted a Gaussian profile to the *derotated* stacked spectrum of each region, accounting for the

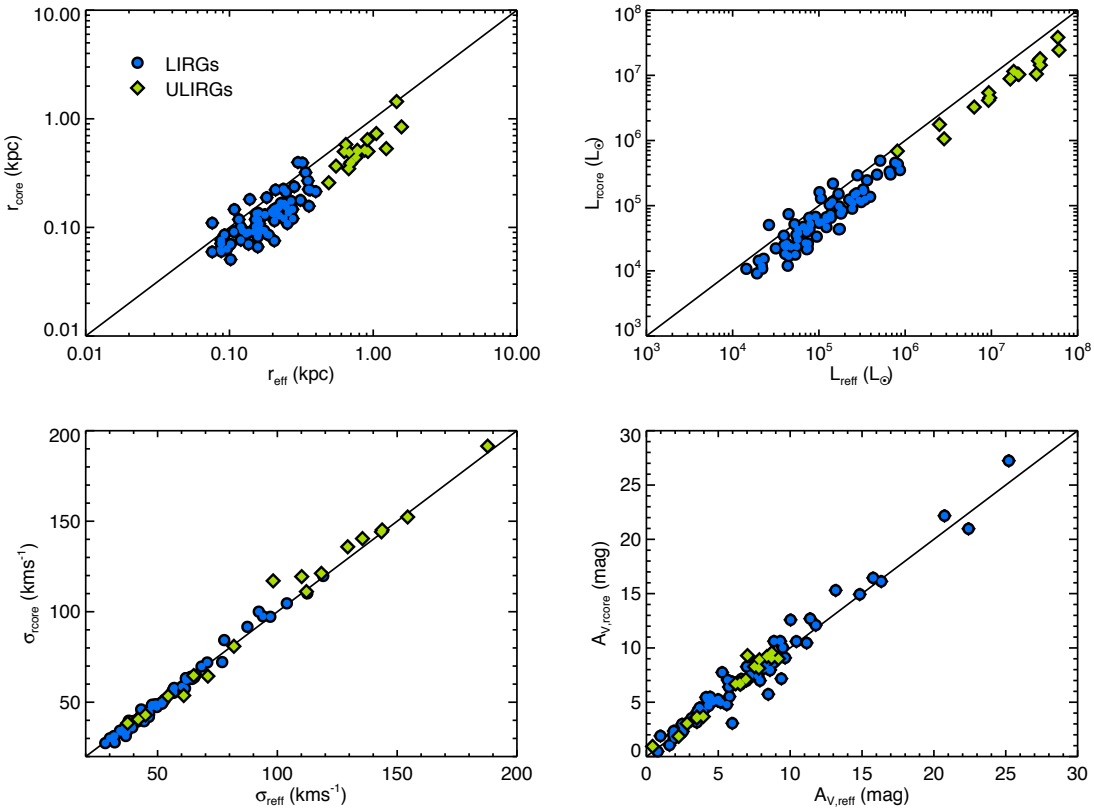

Figure 6.3: Comparison between the scaling properties of individual clumps measured using the effective radius and core radius methods - Comparison between the Brγ (LIRGs) and Paα (ULIRGs) radius (top left), luminosity (top right), velocity dispersion (bottom left) and visual extinction (bottom right) of individual clumps measured using the effective radius and core radius methods. The black lines represent a one-to-one ratio in all the panels.

instrumental broadening and used an spaxel-by-spaxel correction to account for the extinction. The resulting values are shown in Table 6.3.

The measurements of the SFR and Σ_{SFR} could also be performed directly over the emission maps. We checked whether the method, i.e. fitting the stacked spectrum or synthetic aperture photometry of the emission map, could bias the measurements. We found that the values of the luminosity obtained directly from the maps are slightly larger than those obtained from the line fitting, although the differences are less than $\sim 10\%$. There is also a small dependence with the luminosity/size of the region, those regions with small sizes/less number of spaxels show the largest differences ($\lesssim 10\%$) whereas the more extended regions present differences between both measurements of less than $\sim 5\%$ due to the larger number of spaxels within the region.

Figure 6.3 shows a comparison between the luminosity, radius, velocity dispersion and

visual extinction of the clumps measured using the r_{eff} and r_{core} methods. We found that the sizes of the clumps measured using r_{eff} are typically larger than those obtained by the core method, with differences of $\sim$ 30% on average, and hence, the luminosities extracted using the effective radius method yield values larger than the corresponding to the r_{core} measurements. The differences in the area of the region obtained by both methods are typically of the 50-60% or less, and are translated to differences in luminosity of $\sim$ 50% on average. We observed that the velocity dispersion and the A_V values are less sensitive to the method for characterising the size of the clumps, and found a close one-to-one correlation between the values measured using the effective radius and the core method, with differences lower than $\sim$ 5% in the velocity dispersion, and lower than $\sim$ 20% in A_V.

6.3. Results and discussion

6.3.1. Two-dimensional Σ_{SFR} structure and spaxel-by-spaxel Σ_{SFR} distributions

The Σ_{SFR} maps show a very similar structure than the Brγ and Paα emission maps, with some differences at sub-kiloparsec scales due to the clumpy morphology of the extinction structure. We observed that approximately half of the sources ($\sim$47%) present the maximum of both the observed and extinction-corrected Σ_{SFR} at their main nucleus. In those sources with multiple nuclei (NGC 3256 and all the ULIRGs with the exception of IRAS 17208-0014), the Σ_{SFR} peaks either at the main or secondary nucleus. When the observed maps are considered, the fraction of systems with the maximum of the Σ_{SFR} at the main nucleus reaches up to $\sim$71%, and decreases significantly to $\sim$57% when the maps are corrected from extinction.

Figs. D.1 and D.2 also shown the histograms of the spaxel-by-spaxel individual distributions of the observed and corrected Σ_{SFR}. The histograms of the LIRG subsample show a wide variety of morphologies, from concentrated distributions with extended tails towards high Σ_{SFR} values like IRASF 12115-4656 or IC 5179, to wide distributions like NGC 3110, NGC 3256 or IRASF 17138-1017. In ULIRGs, the histograms are typically narrower due to the large amount of spaxels with low surface brightness. The extinction correction typically increases the median and weighted mean of the distributions by $\sim$50% (see Table 6.1), although differences between the observed and the corrected distributions can reach up to $\sim$75%. Besides the median and mean values, the shape of the distributions does not significantly

Table 6.3: Properties of individual star-forming clumps

Object	Region	r_{eff}	$F^{obs}_{Pa\alpha}$	$F^{corr}_{Pa\alpha}$	Σ^{obs}_{SFR}	Σ^{corr}_{SFR}	σ	A_V	r_{core}	$F^{obs}_{Pa\alpha}$	$F^{corr}_{Pa\alpha}$	Σ^{obs}_{SFR}	Σ^{corr}_{SFR}	σ	A_V
(1)	(2)	(3)	(4)	(5)	(6)	(7)	(8)	(9)	(10)	(11)	(12)	(13)	(14)	(15)	(16)
IRASF12115-4656	Nucleus	187	2.6 ± 0.2	6.0 ± 0.6	1.2 ± 0.1	2.7 ± 0.3	97 ± 11	9.4 ± 1.2	85	0.7 ± 0.1	1.4 ± 0.2	1.6 ± 0.2	2.9 ± 0.5	97 ± 16	7.2 ± 2.5
	R1	398	18.5 ± 0.4	39.2 ± 1.0	1.9 ± 0.1	4.1 ± 0.1	46 ± 1	8.5 ± 0.3	213	6.8 ± 0.1	11.3 ± 0.3	2.7 ± 0.1	4.5 ± 0.1	41 ± 1	5.7 ± 0.3
	R2	357	10.5 ± 0.2	65.4 ± 1.3	1.4 ± 0.1	8.6 ± 0.2	46 ± 1	20.7 ± 0.5	157	2.6 ± 0.1	18.6 ± 0.4	2.0 ± 0.1	13.9 ± 0.3	44 ± 1	22.2 ± 1.0
	R3	338	10.1 ± 0.3	21.6 ± 0.6	1.5 ± 0.1	3.1 ± 0.1	41 ± 2	8.6 ± 0.3	320	9.1 ± 0.2	18.4 ± 0.5	1.5 ± 0.1	3.0 ± 0.1	39 ± 2	8.0 ± 0.3
	R4	252	5.7 ± 0.2	8.9 ± 0.4	1.4 ± 0.1	2.3 ± 0.1	37 ± 2	5.2 ± 0.4	108	2.0 ± 0.1	3.1 ± 0.1	2.6 ± 0.1	4.1 ± 0.2	39 ± 2	5.0 ± 0.6
IC5179	Nucleus	157	46.4 ± 0.5	124 ± 1	11.7 ± 0.1	31.3 ± 0.5	65 ± 1	11.1 ± 0.4	81	19.1 ± 0.2	48.3 ± 1.0	18.5 ± 0.2	46.6 ± 1.0	63 ± 1	10.5 ± 0.5
	R1	204	12.6 ± 0.3	15.7 ± 0.6	1.9 ± 0.1	2.3 ± 0.1	36 ± 2	2.5 ± 0.4	146	8.4 ± 0.2	11.0 ± 0.5	2.4 ± 0.1	3.1 ± 0.1	34 ± 2	3.0 ± 0.5
	R2	275	11.8 ± 0.5	12.8 ± 0.7	1.0 ± 0.1	1.1 ± 0.1	32 ± 4	1.0 ± 0.3	120	3.5 ± 0.2	4.1 ± 0.3	1.7 ± 0.1	2.0 ± 0.1	27 ± 4	1.9 ± 0.6
	R3	157	8.4 ± 0.3	12.3 ± 0.5	2.1 ± 0.1	3.0 ± 0.1	43 ± 2	4.2 ± 0.4	66	2.8 ± 0.1	4.5 ± 0.2	4.1 ± 0.1	6.5 ± 0.3	46 ± 1	5.3 ± 0.8
	R4	222	7.1 ± 0.3	10.5 ± 0.6	0.9 ± 0.1	1.3 ± 0.1	45 ± 4	4.4 ± 0.5	128	2.7 ± 0.1	4.3 ± 0.3	1.2 ± 0.1	1.9 ± 0.1	42 ± 3	5.5 ± 0.8
	R5	92	6.2 ± 0.1	12.3 ± 0.3	4.4 ± 0.1	8.7 ± 0.2	44 ± 1	7.7 ± 0.4	85	5.5 ± 0.1	10.6 ± 0.3	4.7 ± 0.1	9.1 ± 0.2	44 ± 1	7.4 ± 0.4
	R6	87	5.0 ± 0.1	9.0 ± 0.3	4.0 ± 0.1	7.2 ± 0.2	34 ± 1	6.6 ± 0.4	71	3.5 ± 0.1	6.6 ± 0.2	4.3 ± 0.1	8.0 ± 0.2	33 ± 1	7.1 ± 0.4
	R7	130	3.5 ± 0.2	11.1 ± 0.6	1.3 ± 0.1	4.3 ± 0.2	32 ± 4	13.2 ± 0.8	87	1.9 ± 0.1	7.3 ± 0.4	1.7 ± 0.1	6.5 ± 0.3	31 ± 4	15.3 ± 1.0
	R8	148	3.5 ± 0.1	5.3 ± 0.3	1.0 ± 0.1	1.5 ± 0.1	35 ± 2	4.6 ± 0.6	91	1.7 ± 0.1	2.7 ± 0.2	1.3 ± 0.1	2.0 ± 0.1	33 ± 3	5.1 ± 0.9
	R9	87	3.2 ± 0.1	3.8 ± 0.2	2.5 ± 0.1	3.0 ± 0.1	28 ± 2	1.9 ± 0.4	76	2.3 ± 0.1	2.6 ± 0.1	2.8 ± 0.1	3.2 ± 0.1	27 ± 2	1.7 ± 0.4
	R10	87	3.0 ± 0.1	3.8 ± 0.2	2.6 ± 0.1	3.2 ± 0.1	42 ± 1	2.4 ± 0.5	60	1.5 ± 0.1	1.8 ± 0.1	2.8 ± 0.1	3.4 ± 0.2	40 ± 1	2.1 ± 0.6
	R11	87	2.3 ± 0.1	2.9 ± 0.1	2.0 ± 0.1	2.6 ± 0.1	31 ± 2	2.6 ± 0.6	70	1.7 ± 0.1	2.2 ± 0.1	2.2 ± 0.1	2.8 ± 0.1	31 ± 2	2.7 ± 0.6
NGC2369	Nucleus	201	48.6 ± 1.5	352 ± 11	6.6 ± 0.2	47.9 ± 1.5	119 ± 3	22.4 ± 0.5	133	27.5 ± 1.1	175 ± 7	8.6 ± 0.4	54.8 ± 2.3	119 ± 5	21.0 ± 0.6
	R1	210	33.2 ± 0.9	308 ± 9	4.2 ± 0.1	38.8 ± 1.1	112 ± 3	25.2 ± 0.6	135	14.9 ± 0.6	166 ± 6	4.7 ± 0.2	52.5 ± 2.1	110 ± 5	27.2 ± 0.9
	R2	138	25.8 ± 1.0	104 ± 4	7.7 ± 0.3	31.2 ± 1.3	103 ± 5	15.8 ± 0.7	181	38.6 ± 1.0	165 ± 4	6.9 ± 0.2	29.4 ± 0.9	104 ± 3	16.4 ± 0.6
	R3	161	24.2 ± 0.7	102 ± 3	5.3 ± 0.1	22.4 ± 0.7	76 ± 3	16.3 ± 0.5	108	12.9 ± 0.3	53.7 ± 1.6	6.2 ± 0.2	25.8 ± 0.8	72 ± 2	16.1 ± 0.7
NGC5135	Nucleus	221	28.5 ± 0.7	59.6 ± 1.6	5.3 ± 0.1	11.1 ± 0.3	77 ± 2	8.4 ± 0.3	155	16.1 ± 0.4	35.8 ± 1.1	6.1 ± 0.2	13.5 ± 0.4	84 ± 2	9.0 ± 0.4
	R1	212	36.0 ± 0.5	68.2 ± 1.1	7.2 ± 0.1	13.6 ± 0.2	60 ± 1	7.2 ± 0.2	133	18.2 ± 0.2	35.4 ± 0.6	9.3 ± 0.1	18.0 ± 0.3	58 ± 1	7.5 ± 0.3
	R2	221	35.8 ± 0.9	82.8 ± 2.2	6.7 ± 0.2	15.6 ± 0.4	64 ± 2	9.5 ± 0.3	153	19.5 ± 0.5	47.3 ± 1.3	8.0 ± 0.2	19.4 ± 0.5	62 ± 2	10.0 ± 0.3
	R3	212	24.7 ± 0.6	58.0 ± 1.5	4.9 ± 0.1	11.6 ± 0.3	68 ± 2	9.7 ± 0.3	143	13.6 ± 0.3	30.4 ± 0.8	6.5 ± 0.1	14.5 ± 0.4	69 ± 2	9.1 ± 0.4
NGC3110	Nucleus	351	26.1 ± 0.4	65.7 ± 1.4	2.9 ± 0.1	7.4 ± 0.2	61 ± 1	10.4 ± 0.4	268	17.7 ± 0.3	45.1 ± 1.1	3.5 ± 0.1	8.8 ± 0.2	63 ± 1	10.6 ± 0.5
	R1	274	13.1 ± 0.2	28.6 ± 0.6	2.5 ± 0.1	5.5 ± 0.1	47 ± 1	8.8 ± 0.3	146	5.5 ± 0.1	11.8 ± 0.4	3.8 ± 0.1	8.2 ± 0.2	48 ± 1	8.6 ± 0.5
	R2	282	7.9 ± 0.2	18.0 ± 0.5	1.4 ± 0.1	3.1 ± 0.1	51 ± 1	9.3 ± 0.4	237	4.0 ± 0.1	10.3 ± 0.3	1.6 ± 0.1	4.1 ± 0.1	49 ± 2	10.6 ± 0.6
	R3	299	7.3 ± 0.2	14.8 ± 0.5	1.1 ± 0.1	2.3 ± 0.1	56 ± 2	7.9 ± 0.6	397	11.6 ± 0.2	21.6 ± 0.7	1.1 ± 0.1	2.0 ± 0.1	57 ± 1	7.0 ± 0.5
	R4	322	7.6 ± 0.2	13.6 ± 0.5	1.0 ± 0.1	1.8 ± 0.1	61 ± 1	6.5 ± 0.5	392	9.3 ± 0.2	16.7 ± 0.5	1.0 ± 0.1	1.7 ± 0.1	57 ± 1	6.6 ± 0.4
	R5	209	3.8 ± 0.1	5.8 ± 0.3	1.2 ± 0.1	1.8 ± 0.1	47 ± 2	5.0 ± 0.5	221	3.7 ± 0.1	5.9 ± 0.2	1.2 ± 0.1	1.9 ± 0.1	48 ± 2	5.1 ± 0.5
NGC7130	Nucleus	205	53.3 ± 1.2	197 ± 4	16.1 ± 0.4	59.9 ± 1.5	93 ± 2	14.8 ± 0.5	114	23.7 ± 0.5	88.8 ± 2.5	23.3 ± 0.5	87.3 ± 2.5	97 ± 2	14.9 ± 0.7
	R1	239	14.0 ± 0.3	18.0 ± 0.4	3.0 ± 0.1	3.9 ± 0.1	41 ± 1	2.9 ± 0.1	121	6.0 ± 0.1	7.9 ± 0.2	5.1 ± 0.1	6.7 ± 0.1	40 ± 1	3.1 ± 0.2
	R2	246	5.7 ± 0.1	10.8 ± 0.3	1.2 ± 0.1	2.2 ± 0.1	37 ± 1	7.3 ± 0.4	161	3.1 ± 0.1	6.5 ± 0.2	1.5 ± 0.1	3.2 ± 0.1	38 ± 2	8.3 ± 0.5
	R3	239	4.3 ± 0.2	5.0 ± 0.3	0.9 ± 0.1	1.0 ± 0.1	36 ± 4	1.6 ± 0.4	165	2.8 ± 0.1	3.1 ± 0.2	1.3 ± 0.1	1.5 ± 0.1	34 ± 4	1.1 ± 0.6
ESO320-G030	Nucleus	174	9.8 ± 0.5	14.4 ± 0.9	1.9 ± 0.1	2.7 ± 0.2	87 ± 5	4.3 ± 0.6	93	4.2 ± 0.2	6.3 ± 0.5	3.1 ± 0.1	4.7 ± 0.4	91 ± 5	4.7 ± 1.1
	R1	227	30.4 ± 0.7	62.5 ± 1.7	3.3 ± 0.1	6.7 ± 0.2	38 ± 1	8.1 ± 0.4	167	17.4 ± 0.4	35.6 ± 0.9	4.3 ± 0.1	8.7 ± 0.2	38 ± 1	8.1 ± 0.4
	R2	246	23.7 ± 0.5	34.7 ± 0.9	2.2 ± 0.1	3.2 ± 0.1	30 ± 2	4.3 ± 0.2	211	18.4 ± 0.4	28.0 ± 0.8	2.3 ± 0.1	3.5 ± 0.1	30 ± 2	4.7 ± 0.3
	R3	246	24.5 ± 0.5	40.4 ± 1.2	2.3 ± 0.1	3.8 ± 0.1	38 ± 1	5.7 ± 0.4	155	11.6 ± 0.2	21.7 ± 0.7	3.4 ± 0.1	6.3 ± 0.2	37 ± 1	7.0 ± 0.5
	R4	210	17.9 ± 0.3	39.3 ± 1.0	2.3 ± 0.1	5.0 ± 0.1	43 ± 1	8.9 ± 0.4	149	9.7 ± 0.2	24.7 ± 0.6	3.1 ± 0.1	7.8 ± 0.2	41 ± 1	10.6 ± 0.5
	R5	123	10.3 ± 0.2	22.1 ± 0.7	3.8 ± 0.1	8.1 ± 0.2	42 ± 2	8.6 ± 0.5	92	6.7 ± 0.1	13.6 ± 0.4	4.4 ± 0.1	9.0 ± 0.3	41 ± 1	7.9 ± 0.6
	R6	161	7.2 ± 0.3	11.5 ± 0.6	1.6 ± 0.1	2.5 ± 0.1	36 ± 3	5.3 ± 0.5	99	3.2 ± 0.1	6.4 ± 0.3	2.1 ± 0.1	4.2 ± 0.2	31 ± 3	7.7 ± 0.8
IRASF17138-1017	Nucleus	181	19.1 ± 0.3	42.1 ± 0.9	8.4 ± 0.1	18.5 ± 0.4	62 ± 1	8.9 ± 0.4	188	20.0 ± 0.3	44.5 ± 1.0	8.3 ± 0.1	18.5 ± 0.4	62 ± 1	9.1 ± 0.3
	R1	220	56.2 ± 0.7	93.3 ± 1.4	17.1 ± 0.2	28.3 ± 0.4	70 ± 1	5.7 ± 0.2	151	29.6 ± 0.4	52.1 ± 0.9	20.6 ± 0.3	36.3 ± 0.6	71 ± 1	6.4 ± 0.2
	R2	237	35.1 ± 0.5	64.9 ± 1.1	9.2 ± 0.1	17.1 ± 0.3	64 ± 1	7.0 ± 0.2	225	33.5 ± 0.5	62.0 ± 1.1	9.4 ± 0.1	17.5 ± 0.3	64 ± 1	7.0 ± 0.2
	R3	197	32.2 ± 0.5	63.5 ± 1.1	12.7 ± 0.2	25.1 ± 0.4	61 ± 1	7.7 ± 0.2	138	20.4 ± 0.3	41.9 ± 0.8	15.1 ± 0.2	31.0 ± 0.6	63 ± 1	8.1 ± 0.3
	R4	158	9.8 ± 0.2	18.4 ± 0.5	5.7 ± 0.1	10.6 ± 0.3	56 ± 1	7.2 ± 0.4	135	7.8 ± 0.2	14.7 ± 0.4	6.1 ± 0.1	11.6 ± 0.4	56 ± 1	7.2 ± 0.5
	R5	158	5.1 ± 0.1	9.4 ± 0.3	2.9 ± 0.1	5.5 ± 0.2	56 ± 1	7.0 ± 0.4	86	1.8 ± 0.1	3.7 ± 0.1	3.9 ± 0.1	8.0 ± 0.3	55 ± 1	8.3 ± 0.7
	R6	158	2.9 ± 0.1	6.1 ± 0.2	1.7 ± 0.1	3.5 ± 0.1	56 ± 2	8.5 ± 0.6	117	1.8 ± 0.1	3.9 ± 0.2	1.8 ± 0.1	4.1 ± 0.2	55 ± 2	9.0 ± 0.8
	R7	176	2.7 ± 0.1	7.4 ± 0.2	1.3 ± 0.1	3.6 ± 0.1	47 ± 1	11.4 ± 0.8	129	1.7 ± 0.1	5.2 ± 0.2	1.5 ± 0.1	4.7 ± 0.2	47 ± 1	12.7 ± 1.0

Object (1)	Region (2)	r_{eff} (3)	$F^{obs}_{Pa\alpha}$ (4)	$F^{corr}_{Pa\alpha}$ (5)	Σ^{obs}_{SFR} (6)	Σ^{corr}_{SFR} (7)	σ (8)	A_V (9)	r_{core} (10)	$F^{obs}_{Pa\alpha}$ (11)	$F^{corr}_{Pa\alpha}$ (12)	Σ^{obs}_{SFR} (13)	Σ^{corr}_{SFR} (14)	σ (15)	A_V (16)
IC4687	Nucleus	355	45.0 ± 0.7	127 ± 2	5.2 ± 0.1	14.8 ± 0.2	51 ± 1	11.8 ± 0.3	224	22.7 ± 0.4	66.3 ± 1.2	6.6 ± 0.1	19.2 ± 0.4	49 ± 1	12.1 ± 0.3
	R1	363	59.3 ± 1.1	82.2 ± 1.6	6.6 ± 0.1	9.2 ± 0.2	61 ± 1	3.7 ± 0.1	221	24.0 ± 0.4	35.7 ± 0.7	10.0 ± 0.2	14.8 ± 0.3	62 ± 1	4.5 ± 0.2
	R2	268	52.3 ± 0.8	81.3 ± 1.4	10.7 ± 0.2	16.6 ± 0.3	48 ± 1	5.0 ± 0.1	174	31.1 ± 0.5	49.5 ± 0.9	15.7 ± 0.2	24.9 ± 0.4	48 ± 1	5.3 ± 0.2
	R3	311	26.7 ± 0.4	43.8 ± 0.8	4.1 ± 0.1	6.7 ± 0.1	44 ± 1	5.6 ± 0.2	178	9.3 ± 0.1	14.2 ± 0.3	6.1 ± 0.1	9.4 ± 0.2	43 ± 1	4.8 ± 0.2
	R4	257	16.6 ± 0.3	23.5 ± 0.5	3.7 ± 0.1	5.3 ± 0.1	39 ± 1	4.0 ± 0.2	136	6.1 ± 0.1	8.9 ± 0.2	5.4 ± 0.1	7.8 ± 0.2	36 ± 1	4.2 ± 0.3
	R5	158	16.8 ± 0.3	28.5 ± 0.6	10.0 ± 0.2	16.9 ± 0.3	52 ± 1	6.0 ± 0.2	94	7.5 ± 0.1	13.7 ± 0.3	12.6 ± 0.2	23.2 ± 0.5	49 ± 1	6.9 ± 0.3
	R6	257	8.3 ± 0.2	11.5 ± 0.3	1.9 ± 0.1	2.6 ± 0.1	44 ± 1	3.6 ± 0.3	145	3.2 ± 0.1	4.4 ± 0.1	2.2 ± 0.1	3.0 ± 0.1	39 ± 1	3.5 ± 0.4
	R7	176	5.4 ± 0.1	7.6 ± 0.2	2.6 ± 0.1	3.7 ± 0.1	37 ± 1	3.9 ± 0.3	131	3.5 ± 0.1	5.0 ± 0.2	2.9 ± 0.1	4.3 ± 0.1	33 ± 2	4.2 ± 0.4
	R8	197	5.3 ± 0.1	7.9 ± 0.3	2.0 ± 0.1	2.9 ± 0.1	36 ± 2	4.5 ± 0.3	138	3.0 ± 0.1	4.7 ± 0.2	2.3 ± 0.1	3.6 ± 0.1	34 ± 2	5.2 ± 0.5
NGC3256	Nucleus	182	81.2 ± 1.0	196 ± 2	10.2 ± 0.1	24.9 ± 0.3	92 ± 1	10.0 ± 0.2	86	29.5 ± 0.5	89.9 ± 1.7	17.0 ± 0.3	51.6 ± 1.0	100 ± 1	12.6 ± 0.3
	R1	151	56.0 ± 0.8	115 ± 1	10.3 ± 0.1	21.3 ± 0.3	63 ± 1	8.2 ± 0.2	101	27.7 ± 0.4	59.6 ± 1.1	11.8 ± 0.2	25.4 ± 0.5	63 ± 1	8.7 ± 0.2
	R2	205	40.3 ± 0.9	68.3 ± 1.8	4.0 ± 0.1	6.8 ± 0.2	49 ± 2	6.0 ± 0.2	75	10.3 ± 0.2	13.5 ± 0.4	7.6 ± 0.1	10.0 ± 0.3	47 ± 1	3.1 ± 0.3
	R3	120	29.3 ± 0.6	31.4 ± 0.8	8.3 ± 0.2	8.9 ± 0.2	36 ± 1	0.8 ± 0.2	76	14.5 ± 0.3	15.1 ± 0.4	11.5 ± 0.2	12.0 ± 0.3	35 ± 1	0.5 ± 0.2
	R4	135	28.9 ± 1.1	38.1 ± 1.8	6.7 ± 0.2	8.8 ± 0.4	49 ± 3	3.1 ± 0.4	90	15.7 ± 0.5	21.5 ± 1.1	9.0 ± 0.3	12.3 ± 0.7	48 ± 3	3.5 ± 0.6
	R5	151	23.5 ± 0.5	35.2 ± 0.8	4.4 ± 0.1	6.6 ± 0.2	52 ± 1	4.6 ± 0.2	118	13.4 ± 0.3	21.3 ± 0.6	5.3 ± 0.1	8.4 ± 0.2	51 ± 1	5.2 ± 0.3
	R6	153	21.7 ± 0.2	45.0 ± 0.8	3.8 ± 0.1	8.0 ± 0.1	65 ± 1	8.3 ± 0.4	134	16.0 ± 0.2	33.4 ± 0.7	4.1 ± 0.1	8.5 ± 0.2	65 ± 1	8.3 ± 0.4
	R7	116	18.4 ± 0.4	25.0 ± 0.7	5.7 ± 0.1	7.8 ± 0.2	38 ± 1	3.5 ± 0.3	118	15.4 ± 0.4	20.4 ± 0.6	6.3 ± 0.1	8.4 ± 0.3	37 ± 2	3.2 ± 0.3
	R8	135	16.5 ± 0.3	19.6 ± 0.6	3.7 ± 0.1	4.4 ± 0.1	42 ± 1	1.9 ± 0.3	70	6.3 ± 0.1	7.8 ± 0.3	5.4 ± 0.1	6.6 ± 0.3	41 ± 1	2.4 ± 0.5
	R9	101	17.2 ± 0.3	23.5 ± 1.2	6.9 ± 0.1	9.5 ± 0.5	56 ± 1	3.6 ± 0.7	50	5.1 ± 0.1	7.3 ± 0.7	9.7 ± 0.3	14.1 ± 1.3	57 ± 2	4.1 ± 1.4
	R10	107	15.7 ± 0.3	18.5 ± 0.4	5.9 ± 0.1	7.0 ± 0.2	34 ± 1	1.9 ± 0.2	91	11.2 ± 0.2	13.4 ± 0.3	6.4 ± 0.1	7.7 ± 0.2	34 ± 1	2.0 ± 0.2
	R11	120	13.6 ± 0.3	29.0 ± 0.8	3.9 ± 0.1	8.4 ± 0.2	39 ± 2	8.6 ± 0.4	100	10.2 ± 0.2	22.3 ± 0.7	4.2 ± 0.1	9.1 ± 0.3	39 ± 2	8.8 ± 0.4
	R12	101	13.5 ± 0.2	23.9 ± 0.6	5.5 ± 0.1	9.8 ± 0.2	46 ± 1	6.5 ± 0.3	70	7.2 ± 0.1	13.1 ± 0.4	6.1 ± 0.1	11.1 ± 0.3	43 ± 1	6.8 ± 0.4
	R13	96	11.2 ± 0.2	19.8 ± 0.5	5.0 ± 0.1	8.9 ± 0.2	46 ± 1	6.4 ± 0.3	63	5.5 ± 0.1	10.1 ± 0.3	6.4 ± 0.1	11.6 ± 0.3	43 ± 1	6.8 ± 0.4
	R14	108	10.6 ± 0.2	15.2 ± 0.5	3.7 ± 0.1	5.4 ± 0.2	45 ± 1	4.1 ± 0.4	146	17.6 ± 0.4	28.5 ± 0.8	3.6 ± 0.1	5.8 ± 0.2	43 ± 1	5.5 ± 0.3
	R15	86	9.7 ± 0.1	19.2 ± 0.4	5.5 ± 0.1	10.7 ± 0.2	46 ± 1	7.7 ± 0.4	62	5.5 ± 0.1	11.9 ± 0.3	6.0 ± 0.1	13.0 ± 0.3	44 ± 1	8.7 ± 0.6
	R16	75	6.2 ± 0.1	10.4 ± 0.3	4.6 ± 0.1	7.7 ± 0.3	36 ± 1	5.8 ± 0.5	109	12.0 ± 0.3	19.5 ± 0.6	4.2 ± 0.1	6.8 ± 0.2	35 ± 1	5.5 ± 0.4
	R17	75	5.4 ± 0.1	6.8 ± 0.3	4.2 ± 0.1	5.2 ± 0.2	38 ± 2	2.5 ± 0.5	59	3.6 ± 0.1	4.5 ± 0.2	4.4 ± 0.1	5.4 ± 0.2	37 ± 2	2.3 ± 0.5
IRAS23128-5919	Nucleus	490	49.8 ± 1.0	152 ± 3	20.5 ± 0.4	62.9 ± 1.4	112 ± 3	8.4 ± 0.2	257	20.0 ± 0.4	68.3 ± 1.7	31.0 ± 0.7	105 ± 2	111 ± 3	9.2 ± 0.3
	R1	693	28.8 ± 0.2	72.6 ± 0.7	6.2 ± 0.1	15.7 ± 0.2	81 ± 1	6.9 ± 0.1	385	13.7 ± 0.1	35.4 ± 0.4	9.3 ± 0.1	23.9 ± 0.3	80 ± 1	7.1 ± 0.2
IRAS21130-4446	Nucleus	680	3.2 ± 0.1	8.8 ± 0.4	3.5 ± 0.1	9.6 ± 0.4	143 ± 4	7.5 ± 0.6	490	2.0 ± 0.1	6.2 ± 0.3	4.0 ± 0.1	12.2 ± 0.6	145 ± 5	8.3 ± 0.7
	R1	1454	10.5 ± 0.1	16.8 ± 0.4	2.3 ± 0.1	3.7 ± 0.1	70 ± 1	3.5 ± 0.2	1441	6.8 ± 0.1	11.1 ± 0.2	3.6 ± 0.1	5.8 ± 0.1	64 ± 1	3.6 ± 0.2
IRAS22491-1808	Nucleus	758	2.5 ± 0.1	5.9 ± 0.2	1.4 ± 0.1	3.3 ± 0.1	65 ± 1	6.5 ± 0.4	439	1.2 ± 0.1	2.8 ± 0.1	2.0 ± 0.1	5.0 ± 0.2	64 ± 1	6.7 ± 0.5
	R1	780	4.3 ± 0.1	9.8 ± 0.2	2.2 ± 0.1	5.1 ± 0.1	110 ± 1	6.2 ± 0.3	501	2.3 ± 0.1	5.6 ± 0.1	3.0 ± 0.1	7.2 ± 0.2	119 ± 1	6.7 ± 0.4
	R2	919	2.4 ± 0.1	8.1 ± 0.2	0.9 ± 0.1	3.1 ± 0.1	44 ± 1	9.2 ± 0.3	500	1.1 ± 0.1	3.5 ± 0.1	1.4 ± 0.1	4.6 ± 0.1	42 ± 1	9.0 ± 0.5
IRAS06206-6315	Nucleus	775	3.6 ± 0.1	10.3 ± 0.3	2.8 ± 0.1	7.9 ± 0.3	187 ± 4	7.8 ± 0.5	512	1.9 ± 0.1	5.5 ± 0.2	3.5 ± 0.1	10.3 ± 0.4	191 ± 4	8.1 ± 0.6
	R1	912	1.7 ± 0.1	2.8 ± 0.2	0.9 ± 0.1	1.5 ± 0.1	129 ± 2	4.0 ± 0.8	643	1.0 ± 0.1	1.6 ± 0.1	1.1 ± 0.1	1.8 ± 0.2	135 ± 2	3.7 ± 1.1
	R2	644	0.1 ± 0.1	0.2 ± 0.1	0.2 ± 0.1	0.3 ± 0.1	37 ± 2	3.5 ± 0.7	579	0.1 ± 0.1	0.2 ± 0.1	0.2 ± 0.1	0.3 ± 0.1	38 ± 3	3.5 ± 0.8
IRAS12112+0305	Nucleus	551	4.8 ± 0.1	15.4 ± 0.3	4.4 ± 0.1	14.1 ± 0.3	143 ± 1	8.7 ± 0.3	367	2.6 ± 0.1	8.7 ± 0.2	5.9 ± 0.1	19.6 ± 0.4	144 ± 1	9.1 ± 0.4
	R1	1232	9.7 ± 0.1	24.8 ± 0.3	1.8 ± 0.1	4.7 ± 0.1	98 ± 1	7.0 ± 0.2	531	3.0 ± 0.1	10.5 ± 0.2	3.3 ± 0.1	11.5 ± 0.2	117 ± 1	9.3 ± 0.3
	R2	628	0.7 ± 0.1	1.0 ± 0.1	0.5 ± 0.1	0.7 ± 0.1	41 ± 9	2.2 ± 0.4	498	0.5 ± 0.1	0.7 ± 0.1	0.6 ± 0.1	0.7 ± 0.1	40 ± 16	1.9 ± 0.5
IRAS14348-1447	Nucleus	872	8.2 ± 0.1	19.6 ± 0.3	4.0 ± 0.1	9.6 ± 0.2	118 ± 1	6.5 ± 0.2	515	4.0 ± 0.1	10.0 ± 0.2	5.9 ± 0.1	14.5 ± 0.3	121 ± 1	6.8 ± 0.3
	R1	703	4.7 ± 0.1	15.0 ± 0.3	3.5 ± 0.1	11.1 ± 0.2	135 ± 1	8.7 ± 0.4	399	2.3 ± 0.1	8.3 ± 0.2	5.0 ± 0.1	18.0 ± 0.5	140 ± 2	9.6 ± 0.6
	R2	1050	1.4 ± 0.1	1.5 ± 0.1	0.5 ± 0.1	0.5 ± 0.1	54 ± 1	0.4 ± 0.4	731	0.7 ± 0.1	0.8 ± 0.1	0.6 ± 0.1	0.7 ± 0.1	53 ± 1	0.9 ± 0.5
	R3	1573	0.6 ± 0.1	0.9 ± 0.1	0.1 ± 0.1	0.1 ± 0.1	60 ± 2	2.8 ± 0.3	842	0.2 ± 0.1	0.4 ± 0.1	0.1 ± 0.1	0.2 ± 0.1	53 ± 2	3.0 ± 0.5
IRAS17208-0014	Nucleus	675	32.9 ± 0.3	94.1 ± 1.1	6.6 ± 0.1	19.0 ± 0.2	154 ± 1	7.9 ± 0.2	347	12.8 ± 0.3	42.0 ± 1.0	10.1 ± 0.2	33.4 ± 0.8	152 ± 3	8.9 ± 0.3

Table 6.3: Col. (2): Region label (see Fig. 6.1). Col (3): Effective radius in [pc]. Cols (4) and (5): Observed (4) and extinction-corrected (5) Paα fluxes measured within r_{eff}, expressed in $[\times 10^{-15} \mathrm{erg\,s^{-1}\,cm^{-2}}]$. The Pa$\alpha$ fluxes for the LIRGs are obtained form the Brγ fluxes using the case B recombination factor at T$= 10,000$ K and $n_e = 10^4\,\mathrm{cm^{-3}}$ (Osterbrock & Ferland, 2006). Cols. (6) and (7): Observed (6) and extinction-corrected (7) Σ_{SFR} in $[M_\odot\,\mathrm{yr^{-1}\,kpc^{-2}}]$. Col. (8): Intrinsic velocity dispersion in $[\mathrm{km\,s^{-1}}]$ of the Brγ and Paα lines for LIRGs and ULIRGs respectively. Col. (9): A_V in magnitudes. Col. (10): Core radius in [pc] (see text for definition). Cols. (11) to (16): Same as Cols. (4) to (9) but measured within r_{core}. All the uncertainties are calculated by a *bootstrap* method of N = 300 simulations.

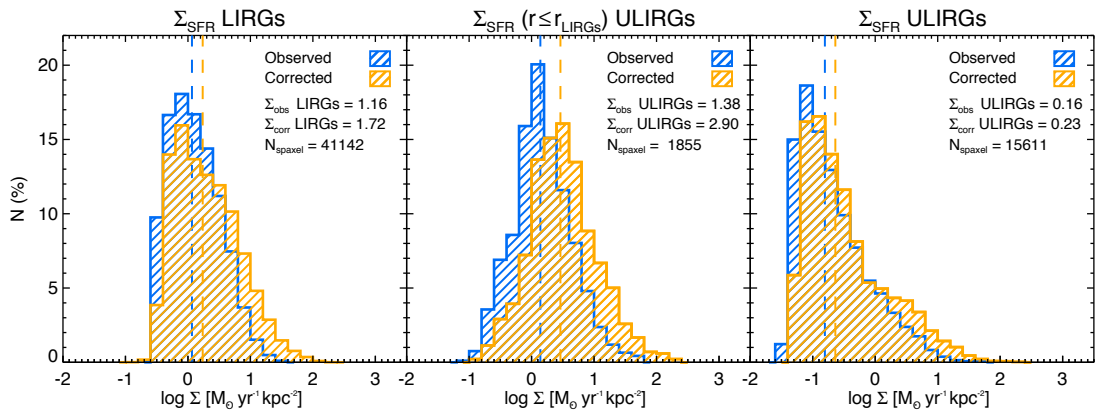

Figure 6.4: Observed and extinction-corrected spaxel-by-spaxel Σ_{SFR} distributions of LIRGs and ULIRGs - Observed and extinction-corrected spaxel-by-spaxel Σ_{SFR} distributions of the LIRGs subsample (left), of the inner spaxels ($r \leq r_{LIRGs}$, see text for details) of the ULIRGs subsample (centre) and the complete ULIRG distributions (right). The median Σ_{SFR} values and the total number of spaxels in each distribution are shown in the panels in units of $[M_\odot\,yr^{-1}\,kpc^{-2}]$, and plotted as dashed vertical lines.

change when comparing the observed and extinction corrected values. However, due to the apparent correlation between Σ_{SFR} and A_V, we observed an increase of the number of spaxels at the high Σ_{SFR} end of the corrected distributions.

We also combined all the spaxels of each luminosity class to obtain a characteristic distribution of the Σ_{SFR} for LIRGs and ULIRGs. The observed and extinction-corrected Σ_{SFR} distributions are shown in Fig. 6.4, and their respective median, weighted mean, and percentiles can be found in Table 6.1. As shown in the figure, the differences between the observed and corrected Σ_{SFR} distributions are similar to those observed when we consider each object separately. In LIRGs, the median of the observed distribution is $\Sigma^{obs}_{LIRGs} = 1.16\,M_\odot\,yr^{-1}\,kpc^{-2}$, and increases up to a $\sim$32% in the extinction-corrected distribution, $\Sigma^{corr}_{LIRGs} = 1.72\,M_\odot\,yr^{-1}\,kpc^{-2}$. The corrected distribution also becomes a $\sim$ 50% wider than the observed one. In ULIRGs, the median of the observed and corrected distributions are $\Sigma^{obs}_{ULIRGs} = 0.16\,M_\odot\,yr^{-1}\,kpc^{-2}$ and $\Sigma^{corr}_{ULIRGs} = 0.23\,M_\odot\,yr^{-1}\,kpc^{-2}$, whereas the interquartile range increases $\sim$ 45% from the observed to the corrected distribution.

As discussed in Chapter 5, the difference in distance, and hence in angular resolution, between LIRGs and ULIRGs is a key issue when comparing both subsamples. The $\sim 8'' \times 8''$ FoV of our SINFONI observations limits our analysis of the LIRGs to their innermost ~ 3 kpc. Taking that the average distance of the ULIRGs is typically ten times larger into account, the complete area sampled for the LIRGs is equivalent to $\sim 1/8$ of the ULIRGs FoV ($\sim 12'' \times 12''$), i.e. $\sim$ 8 spaxels. Due to differences in the sampling scale and the lack of data from the

external regions of the LIRGs, the direct comparison between both subsamples is not straightforward. However, although we could not eliminate the effect of the linear resolution, we could limit the comparison to the inner kiloparsecs of the ULIRGs. We estimated an average radius, $r_{LIRGs} = 1.4\,kpc$, that correspond to the spaxel-weighted mean of the LIRG FoVs, and considered only those spaxels from the ULIRG distribution within this physical scales. The resulting observed and extinction-corrected Σ_{SFR} distributions are shown in the central panel of Fig. 6.4. This set of the innermost spaxels of the ULIRG distributions is $\sim 10\%$ of the whole Σ_{SFR} distributions, and corresponds to those spaxels with the largest Σ_{SFR} values. When we consider only these values, the medians of the observed and extinction-corrected distributions reach up to $1.38\,M_\odot\,yr^{-1}\,kpc^{-2}$ and $2.90\,M_\odot\,yr^{-1}\,kpc^{-2}$, respectively, i.e. the median Σ_{SFR} increases by a factor ~ 10 when only the inner regions of the ULIRGs are considered.

6.3.2. The effect of the linear resolution on the Σ_{SFR} measurements. Implications for high-z galaxies

As discussed in Chapter 5, due to the clumpy structure of the dust observed in LIRGs and ULIRGs at sub-kiloparsec and kiloparsec scales, the measurement of the extinction could be affected by the physical scale of the observations at increasing distance. Fig. D.1 shows that the morphology of the ionised gas within the inner $\sim 3\times3\,kpc$ in LIRGs is mainly in the form of nuclear star formation rings, emission associated with the nucleus of the galaxy and bright HII regions with typical sizes of a few hundred parsecs, some of them barely resolved in our observations. Besides, the A_V maps show that dust seems to be not uniformly distributed in a patchy and clumpy structure at the same sub-kiloparsec scales. As shown in Fig. D.2, ULIRGs show a more compact morphology, of both dust and ionised gas phases, with not resolved structures beyond $\lesssim 1\,kpc$, that suggest that the reduced linear resolution of the observations might play a role in shaping the gas and dust distributions.

To probe how the differences in the pixel scale might bias the Σ_{SFR} measurements, we simulated the Brγ and Brδ maps of the LIRGs at increasing distances. We performed two different sets of simulations, the first set considers only the effect of the decreasing spatial sampling of the maps whereas the second set also takes the smearing effect of the seeing into account. In the first set of simulations, we rebinned each individual map as if it was observed at increasing distances with the same instrument set-up. The simulated maps are hence sampled by a decreasing number of spaxels with a constant angular resolution of $0\farcs125$ per

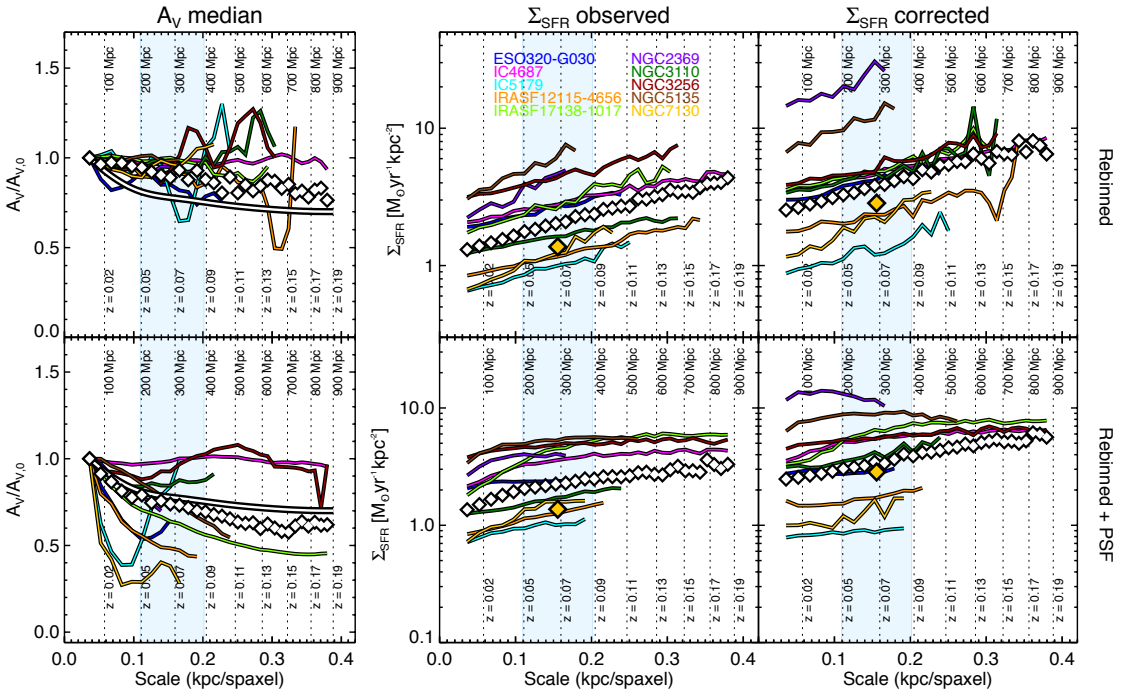

Figure 6.5: Simulated A_V and Σ_{SFR} distributions - Evolution of the computed median A_V and Σ_{SFR} of the spaxel-by-spaxel LIRG distributions, as a function of distance/scale. Colour lines represent the evolution of the median of each individual distribution, whereas white diamonds show the median of the whole LIRG distribution. The median Σ_{SFR} values of the ULIRG distributions within $r_{LIRGs} = 1.4$ kpc are also plotted as yellow diamonds, for reference.

spaxel, as the original maps. The rebinning process is performed using the basic equations of angular diameter distance and luminosity distance, and assuring that the total luminosity within the FoV is conserved. In the second set of simulations, before the rebinning process, we considered the effect of the seeing to obtain more realistic emission maps that could be directly compared with our SINFONI observations of the ULIRG subsample. The resulting maps presents the same spatial sampling and scale as those from the first set of simulations, but with a $\sim$0.63 arcsec (FWHM) seeing as the original observations.

Once the simulated maps are built, we followed the same procedure as described in Sec. 6.2 to obtain a spaxel-by-spaxel A_V correction, and finally a extinction-corrected Σ_{SFR} distribution. As discussed in Chapter 5, we sample typically the innermost $\sim3\times3$ kpc of the LIRGs, i.e. $\sim R_{eff}$. Since the average distance of the ULIRG subsample is $\times10$ larger, the whole FoV of the LIRGs are equivalent to $\sim$1" of the ULIRG FoV, i.e. $\sim$8 spaxels. These limitations and the lack of information about the external regions of the LIRGs makes that the extrapolation to larger distances to be not straight-forward.

The evolution of the median values of the simulated Σ_{SFR} observed and corrected

distributions is shown in Fig. 6.5. We observe a clear increment of the median Σ_{SFR} at increasing distances in both the observed and corrected distributions, up to $\sim$90% at 328 Mpc, the average distance of the ULIRG subsample. We observe that in most of the cases the predicted median of the LIRG distribution is slightly higher than the median of the ULIRG distribution. However, there is a good agreement between both quantities when the extinction correction is applied, and the PSF effects are taken into account. Although the simulations are a first-order approximation, this result suggests that the Σ_{SFR} measurements of the ULIRGs might be very much affected by such distance effects.

6.3.3. Optical vs near-IR star-formation measurements.

As mentioned before, the current SINFONI sample is part of a parent sample of local LIRGs and ULIRGs described in Arribas et al. (2008), that has been observed with other optical IFS facilities like INTEGRAL+WYFFOS at the WHT, VLT-VIMOS or PMAS. In this subsection, we compare our Brγ and Paα SFR measurements with those derived from Hα measurements from García-Marín et al. (2009a) and Rodriguez-Zaurín et al. (2011). As we did in the previous subsection, although for our LIRG subsample the SFR values were derived from the Brγ luminosity, we will generalise and refer to the $SFR_{Pa\alpha}$, assuming that the LIRGs Brγ measurements are translated to the Paα ones using the corresponding case B recombination factor.

García-Marín et al. (2009a) presented optical IFS observations from INTEGRAL of 22 local ULIRG systems, and provides with not only observed Hα fluxes of three of our ULIRGs (IRAS 12112+0305, IRAS 14348-1447 and IRAS 17208-0014), but also spaxel-by-spaxel extinction-corrected measurements based on the Hα/Hβ ratio, with an angular resolution of $\sim$ 1″per spaxel. For our LIRG subsample and the rest of the ULIRGs, we used the Hα fluxes and A_V corrections from Rodriguez-Zaurín et al. (2011), based on optical IFS observations from VIMOS. The A_V corrections for these objects are derived from the Hα/Hβ values that were available in the literature, mainly based on nuclear long-slit spectroscopic observations. To account for the extinction effects, authors used the nuclear reddening spectroscopic measurements to correct the fraction of Hα emission within a typical slit width ($\sim$ 2 arcsec), and considered the remaining fraction of flux not affected by extinction. As authors discussed in this current work, although extinction effects are particularly important in the nuclear regions, this approach will tend to underestimate the extinction corrected

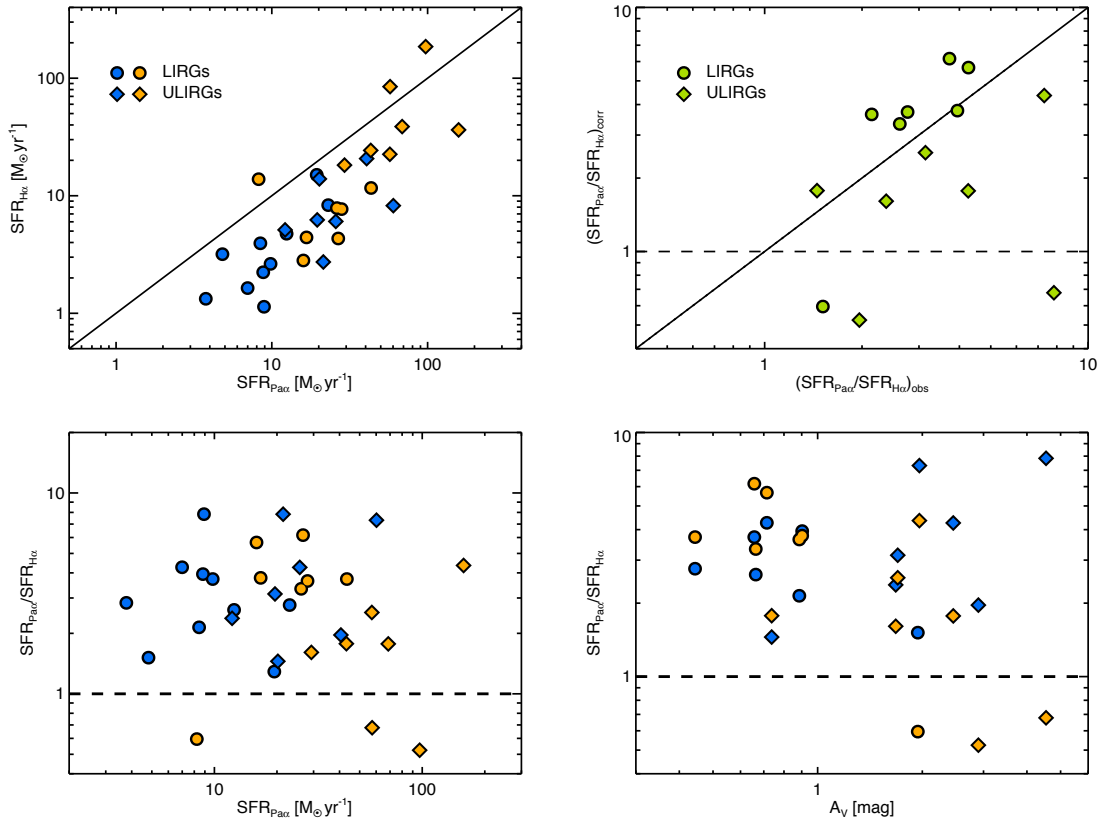

Figure 6.6: Optical vs near-IR based SFR - *Top left*: Comparison between the star-formation rate derived from Hα and Paα observed (blue) and extinction-corrected (yellow) luminosities for LIRGs (circles) and ULIRGs (diamonds). *Top right*: Comparison of the observed and extinction-corrected SFR$_{Pa\alpha}$/SFR$_{H\alpha}$ ratios. *Bottom left*: Ratio of the star-formation rate derived from the Hα and Paα luminosities as a function of the star-formation rate derived from the Paα line. *Bottom right*: SFR$_{Pa\alpha}$/SFR$_{H\alpha}$ ratio as a function of the visual extinction, A$_V$, derived from near-IR lines. In all panels, the solid black line represents a one-to-one ratio whereas the dashed line represents a constant ratio of SFR$_{Pa\alpha}$/SFR$_{H\alpha}$ = 1. The Hα luminosities are extracted from García-Marín et al. (2009a) and Rodriguez-Zaurín et al. (2011).

SFR$_{H\alpha}$ measurements, since, as shown in Figs. D.1 and D.2, it is also frequent to find dusty, highly-obscured extranuclear regions in these objects.

Figure 6.6 shows the comparison between the optical and near-IR-based SFR values, for observed and extinction-corrected measurements. As one would expected, we found a close correlation between the SFR$_{H\alpha}$ and SFR$_{Pa\alpha}$ values, although the infrared measurements tend to yield larger SFR, even for extinction-corrected measurements. For the observed values, we found that infrared measurements are $\sim$ 3.6 times larger than the optical ones, on average, although individual values ranges between $\sim$ 1.2 and $\sim$ 8 times larger. When the extinction corrections are applied, the SFR$_{Pa\alpha}$/SFR$_{H\alpha}$ ratio decreases to $\sim$ 2.9 on average, while the individual factors are constrained between $\sim$ 0.5 and $\sim$ 6.

As mentioned in Chapter 4, we found evidences of nuclear activity in four of the objects of the sample, i.e. IRASF 12115-4656, NGC5135, NGC7130 and IRAS 23128-5919, in terms of detection of [SiVI] coronal emission. Those objects, in particular the three LIRGs, present the highest $SFR_{H\alpha}/SFR_{Pa\alpha}$ ratios, and suggest that the contribution of the AGN to the Hα and Paα luminosities might be larger at longer wavelengths. If these objects are removed from the sample, the average ratios of the $SFR_{H\alpha}/SFR_{Pa\alpha}$ become ~ 3.4 and ~ 2.0 for the observed and extinction-corrected values.

Although the ratio slightly decreases when the extinction corrections are applied, we still found significative differences between both tracers. As it will be discussed later, these differences could probably be the result of an incomplete extinction correction in both Hα and Paα measurements, since the regions where the star-formation occurs are dense, dusty environments. Besides the differences in the ratio, we found an increase in the dispersion of the individual values, consequence of the high uncertainties of the A_V measurements, that could reach up to $\sim$70 % on an spaxel-by-spaxel basis.

As mentioned before, some differences could be expected, though, between the optical and infrared SFR measurements due to the dependence of the transition probabilities with T_e and n_e, since the infrared recombination lines are progressively more sensitive to the conditions of the gas. However, although the luminosity of Brγ could change 35-40% within the ranges $5000-20000$ K and 10^2-10^6 cm^{-3}, it is clear that dust obscuration still plays a central role when comparing optical and infrared SFR measurements. We explored the possibility that some of the differences could be explained by the choice of a different extinction law for the optical and infrared data, respectively. As described in Chapter 5, we used the extinction law from Calzetti et al. (2000) to obtain the A_V measurements from the Brγ/Brδ and Paα/Brγ line ratios, assuming a total effective obscuration at the V-band of $R_V = 4.05$, whereas García-Marín et al. (2009a) and Rodriguez-Zaurín et al. (2011) considered the extinction law from Savage & Mathis (1979), that assumes $R_V = 3.1$ that corresponds to the Galactic diffuse interstellar medium. The differences between both extinction curves, Savage & Mathis (1979) considering a value of 3.1 for R_V, and Calzetti et al. (2000) using $R_V = 4.05$, are less than $\sim 5\%$ at the Hα wavelength, and hence, can not explain the differences observed between the extinction-corrected SFR measurements.

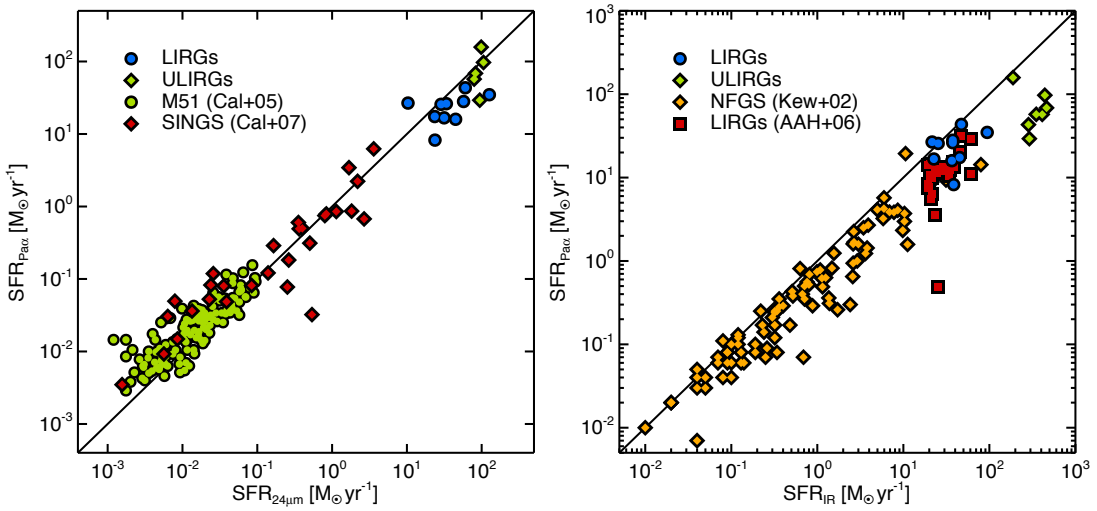

Figure 6.7: Comparison between near-IR based SFR and 24 μm and L_{IR} measurements - *Left:* Comparison of the extinction-corrected $SFR_{Pa\alpha}$ with the monochromatic $SFR_{24\mu m}$. The blue circles and green diamonds correspond to our local LIRGs and ULIRGs, respectively. The green circles are data of M51 individual star-forming regions from Calzetti et al. (2005), and the red diamonds correspond to data from Calzetti et al. (2007) of SINGS galaxies. *Right:* Comparison of extinction-corrected Paα luminosity and L_{IR}. Our LIRG and ULIRG samples are plotted as blue circles and green diamonds, respectively, orange diamonds are data from Kewley et al. (2002) of normal galaxies from the NFGS while red squares correspond to local LIRGs from Alonso-Herrero et al. (2006). In both panels, the black line correspond to a one-to-one ratio.

6.3.4. Near-IR vs mid-IR star-formation rates

We also compared our $SFR_{Pa\alpha}$ values with measurements of $SFR_{24\mu m}$ and SFR_{IR} from Pereira-Santaella et al. (2011) and archive data, respectively. Fig. 6.7 shows the relation of the $SFR_{24\mu m}$ and SFR_{IR} with extinction corrected $SFR_{Pa\alpha}$ for different datasets, that include nearby galaxies and individual star-forming regions of M51.

Calzetti et al. (2005) present *Spitzer* MIPS 24 μm observations of resolved star-forming regions within the central 6 kpc of M51, together with Hα and Paα data from ground-based and HST-NICMOS images, respectively. We derived the extinction corrections from Hα/Paα line ratios using the same recipe as we used in our own dataset. On the other hand, the data from Calzetti et al. (2007) correspond to *Spitzer* MIPS 24 μm and HST-NICMOS narrow-filter Paα observations of a subsample of galaxies from the *Spitzer* Infrared Nearby Galaxies Survey (SINGS, Kennicutt et al. 2003).

We used Eqs. 6.2 and 6.3 to obtain the SFR measurements from the corresponding luminosities. As can be seen in Fig. 6.7 (*left*), both SFR tracers, i.e. Paα and 24 μm, yield very similar values, as one would expected, although with some deviations at both the

low- and high-luminosity ends. These deviations are also observed in previous works, like Alonso-Herrero et al. (2006), Rieke et al. (2009) or Calzetti et al. (2007), using different calibrations and datasets, and respond to the fact that the relation between $L_{24\mu m}$ and the SFR is not longer lineal, since the increasing starlight rises the temperature of larger dust grains and hence the absorbed energy reradiated at 24 μm. Besides this effect, the high-luminosity end (LIRGs and brighter) corresponds to objects where the star formation occurs in dusty environments with increasing density, where standard extinction corrections (e.g. based on hydrogen recombination line ratios) become less effective and lead to an underestimation of the Paα luminosities.

As shown in the right-side panel of Fig. 6.7, although there is a reasonable agreement between the SFR measurements derived from Paα and L_{IR}[8–1000μm], the SFR_{IR} values are systematically higher than $SFR_{Pa\alpha}$. In particular, the differences between the measurements for our LIRG and ULIRG sample are up to a factor $\times$2, and suggest that, as observed when comparing with the 24 μm data, the $SFR_{Pa\alpha}$ measurements are underestimated due to an incomplete extinction correction. Other possible systematic effects, as discussed in Sec. 6.2.1, are that a fraction of the starlight from the star-forming regions may escape without heating the dust, and that the contribution from the more evolved stellar populations to the heating may not be negligible. Both effects work in different directions, i.e. whereas an increase of the escape fraction leads to an underestimation of the SFR, a larger contribution from old stellar populations (or larger time scales of the star formation) yields an overestimation of the SFR measurements. However, since the LIRGs and ULIRGs of our sample are dust-rich objects with multiple evidences of recent episodes of star formation, we consider that the differences between $SFR_{Pa\alpha}$ and SFR_{IR} are better explained in terms of extinction effects.

6.3.5. Scaling relations of star-forming clumps in local LIRGs and ULIRGs. Comparison with high-z giant star-forming regions and SMG

To investigate the scaling relations of star-forming regions, we show in Fig. 6.8 the relations between Σ_{SFR} and luminosity with the size of our sample of clumps. We also plot the integrated values of the individual LIRGs and ULIRGs, together with measurements from local starburst galaxies, high-z clumps and SMGs from several samples. Although most of the data from other samples correspond to Hα measurements, we converted the extinction-corrected Hα luminosities into Paα luminosities using the case B recombination factor at T$=10,000$ K and $n_e = 10^4$ cm^{-3} (Osterbrock & Ferland, 2006) ($L_{H\alpha}/L_{Pa\alpha}=8.582$).

Almost all the local and, specially, the high-z samples are based on Hα measurements of the SFR. As discussed in Sec. 6.3.3, even when the extinction corrections are applied, it is expectable to have a factor $\sim$2–3 between Hα- and Paα-based SFR measurements in dusty environments such as LIRGs and ULIRGs. This effect could be even larger when the correction from extinction is less accurate, such as object-averaged corrections, A_V measurements from different datasets, or SED fitting. Although the uncertainties of the extinction could be intrinsically large, the different methods used would yield additional sources of uncertainties when comparing the different datasets. To account for this effect, we corrected the luminosity and Σ_{SFR} measurements from Hα data by a factor 2.9 to compare them with Paα measurements.

As discussed in Sec. 6.3.2, the spatial resolution of the data also plays a role in shaping the 2D distribution of Σ_{SFR}. Although we explored this effect at low redshifts ($z < 0.2$), our dataset is not well suited to study the effect of distance at higher redshifts, given the limited FoV of our SINFONI observations. Although this effect might be as significative as overestimate the Σ_{SFR} by a factor 2-3 in an spaxel-by-spaxel basis, due to the limitations of the FoV, we cannot quantify accurately the effect, specially at increasing distances.

We will now describe the local and high-z samples used to compare our measurements. Planesas et al. (1997) presented extinction-corrected narrow band Hα measurements of individual star-forming regions from local starburst galaxies, where the correction of the dust extinction is calculated using the Hα/Hβ ratio. We also plotted extinction-corrected HST-NICMOS Paα luminosities of local HII regions from Liu et al. (2013), which applied an average extinction correction of $A_V = 2.2$ mag based on measurements from Calzetti et al. (2007). Besides data from 'normal' spiral galaxies, we include data of young star clusters from the Antennae (NGC 4038/39, Bastian et al. 2006), based on IFS VLT-VIMOS observations.

We also use data from Genzel et al. (2011) of $z \sim 2$ giant star-forming clumps, based on AO-SINFONI Hα measurements. These Hα luminosities are corrected from extinction using stellar E(B–V) values from SED fitting. The extinction of the stars is then re-scaled to the extinction of the gas using the standard recipe $A_{H\alpha} = 7.4\,E(B–V)$, where $E(B–V)_{gas} = 0.44\,E(B–V)_{stars}$ from Calzetti et al. (2000). Data from Swinbank et al. (2012) correspond to extinction-corrected Hα measurements of $z = 0.8 - 2.2$ individual star-forming clumps from disk galaxies. The correction from dust is performed using galaxy-averaged E(B–V) values derived from SED fitting. Finally, we also included data of $z \sim 2.0 - 2.7$ SMGs

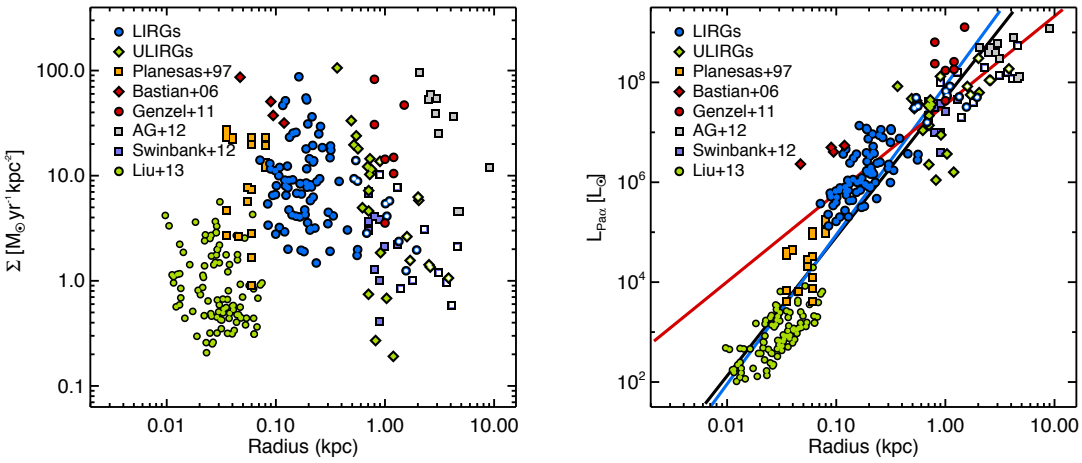

Figure 6.8: Scaling relations of star-forming regions - Dependence of the Σ_{SFR} and $L_{Pa\alpha}$ with the radius of individual star-forming clumps and whole galaxies. The individual regions of LIRGs and ULIRGs are plotted as blue circles and green diamonds, respectively, whereas the integrated measurements of each object of our sample are marked using hollow symbols. We also show data from Planesas et al. (1997) (orange squares), and Liu et al. 2013 (green circles) of individual regions from local starburst and normal galaxies, respectively. Data from Bastian et al. (2006) correspond to young star clusters from the Antennae galaxies, whereas Genzel et al. (2010) points come from giant star-forming clumps of $z \sim 2$ galaxies (red circles); purple squares correspond to star-forming clumps and global measurements (hollow symbols) of high-z ($z = 0.8 - 2.2$) disks from Swinbank et al. (2012), and grey squares are data from Alaghband-Zadeh et al. (2012) of $z \sim 2.0 - 2.7$ SMG. The black line in the right panel corresponds to a power law $L_{Pa\alpha} \sim r^{\eta}$, with $\eta = 2.78$ fit to all the data points, whereas the blue and red lines are the fits to our data from local LIRGs and ULIRGs together with the local samples ($\eta = 2.98$) and high-z points ($\eta = 1.77$), respectively.

from Alaghband-Zadeh et al. (2012) consisting on Hα measurements corrected from dust extinction, using an average $A_V = 2.9$ mag from Takata et al. (2006).

Our local star-forming regions have sizes within ∼60–400 pc and ∼300–1500 pc, whereas their extinction-corrected luminosities range within $\sim 10^5$–$10^7\,L_\odot$ and $\sim 10^6$–$10^8\,L_\odot$, in LIRGs and ULIRGs, respectively. These values yield to Σ_{SFR} values typically of 1–90 $M_\odot\,yr^{-1}\,kpc^{-2}$ and 0.1–100 $M_\odot\,yr^{-1}\,kpc^{-2}$ for LIRG and ULIRG clumps. The intrinsic velocity dispersion (i.e. corrected from instrumental broadening) measured in the individual regions are ∼30-120 km s^{-1} in LIRGs and ∼40-200 km s^{-1} in ULIRGs (see Table 6.3). The lack of regions below $\Sigma_{SFR} \sim 1\,M_\odot\,yr^{-1}\,kpc^{-2}$ and $L_{Pa\alpha} \sim 10^5\,L_\odot$ could be explained in terms of observational biases. The observed regions from the LIRG subset come from the central kiloparsecs of the objects, and, as discussed in 6.2.2, our detection limit for the LIRGs is $\Sigma_{SFR} \sim 0.3\,M_\odot\,yr^{-1}\,kpc^{-2}$ per spaxel. These effects could bias our sample of regions from the LIRGs towards high-luminosity, high-Σ_{SFR} regions.

As shown in Fig. 6.8, if we compare the Σ_{SFR} and $L_{Pa\alpha}$ of our LIRGs regions, we find that

they have higher luminosity densities than clumps in local 'normal' galaxies, although seem to be similar to the regions from the ongoing spiral-spiral merger of the Antennae (Bastian et al., 2006). In the left panel of the figure, we also plot the luminosity-radius relation $L_{Pa\alpha} \sim r^{\eta}$, with $\eta = 2.72$, from Liu et al. (2013), obtained from fitting a local sample of HII regions from nearby galaxies. The regions of our LIRG subsample and those from the Antennae are significantly more luminous than predicted for their radius range, and follow a relation with $\eta \sim 1.7$.

The slope of the L-r relation is usually interpreted in terms of physical properties of the star-forming regions. If we assume that the regions are ionised-bounded, they can be represented by a Strömgren sphere, and their L-r relation is of the form $L_{Pa\alpha} \sim r^{\eta}$, with $\eta = 3$. The deviations from this model could result from a variety of factors, both physical and observational. If the regions are density-bounded, i.e. the hydrogen atoms recombine faster than they are ionised and some ionising photons scape, a shallower slope of the L-r is expected, since regions turns to be less luminous at a given radius (Wisnioski et al., 2012). Beckman et al. (2000) presented a detailed discussion of this transition, and proposed a luminosity threshold of $L_{Pa\alpha} \gtrsim 10^5\, L_{\odot}$beyond which regions turn to be density-bounded. Nevertheless, the exponent of this relation is subject to variations that could be unrelated to intrinsic physical properties of the HII regions, and are likely to be induced by observational biases as region blending, or low S/N ratio of the clumps. In addition, the different spatial resolution of the local and high-z observations might also contribute to change the slope of the L-r relation (Scoville et al. 2001, Liu et al. 2013). Despite this observational bias, the use of either Hα or Paα data to perform the analysis seems to have little impact on η (Liu et al., 2013).

The sample of clumps from the ULIRG subset seems to have similar properties than those observed in high-z star-forming galaxies, like Genzel et al. (2011) and Swinbank et al. (2012), with slightly lower Σ_{SFR} than regions from local LIRGs although over ∼5–10 times larger scales. Although the ULIRG clumps seem to fit better the L-r power law with $\eta = 2.72$ than LIRGs regions, they also show higher luminosities than predicted. However, as mentioned before, the difference in the spatial resolution of the subsamples might introduce an observational bias when comparing regions at increasing distances.

Fig. 6.8 also shows the integrated measurements of the individual LIRGs and ULIRGs of our sample (Table 6.2). The global measurements lie in similar luminosity, Σ_{SFR} and radius ranges than the high-z clumps from Genzel et al. (2011) and Swinbank et al. (2012), and ULIRGs in particular show slightly larger luminosities and Σ_{SFR} than the individual disks from

Swinbank et al. (2012) at the same spatial scales. On the other hand, our most luminous ULIRGs also have similar $L_{Pa\alpha}$ than the SMGs from Alaghband-Zadeh et al. (2012), typically $L_{Pa\alpha}\sim10^8\,L_\odot$, although their Σ_{SFR} is, on average, lower than the Σ_{SFR} observed in the high-z proposed analogs.

6.4. Summary

- We presented a detailed 2D study of the star formation of a representative sample of local LIRGs and ULIRGs, based on VLT-SINFONI IFS K-band observations, that sample the inner$\sim 3\times3$ kpc and $\sim 12\times12$ kpc in LIRGs and ULIRGs, respectively, with an average linear resolution of $\sim$0.2 kpc and $\sim$0.9 kpc (FWHM). The analysis of the SFR and Σ_{SFR} is performed using an spaxel-by-spaxel extinction correction, based on measurements of the Brγ/Brδ and Paα/Brγ line ratios for LIRGs and ULIRGs, respectively (Chapter 5).

- We obtained 2D Σ_{SFR} maps and spaxel-by-spaxel distributions of the individual galaxies (Figs. D.1 and D.2). We found that, in a significant fraction of the objects ($\sim$57 %), the corrected Σ_{SFR} peaks either at the main or secondary nucleus of the systems, and that the extinction correction typically increases the median of the distributions by $\sim$50 %. When all the spaxels of each luminosity class are combined, we found that the distributions of the LIRG subsample have median values of $\Sigma^{obs}_{LIRGs} = 1.16\,M_\odot\,yr^{-1}\,kpc^{-2}$, and $\Sigma^{corr}_{LIRGs} = 1.72\,M_\odot\,yr^{-1}\,kpc^{-2}$ for the extinction-corrected distribution. The median values for the ULIRG distributions are $\Sigma^{obs}_{ULIRGs} = 0.16\,M_\odot\,yr^{-1}\,kpc^{-2}$ and $\Sigma^{corr}_{ULIRGs} = 0.23\,M_\odot\,yr^{-1}\,kpc^{-2}$ for the observed and the extinction-corrected Σ_{SFR} values, respectively. Due to the difference in distance, and hence in angular resolution between LIRGs and ULIRGs, to compare both classes, we also extracted the distributions of the inner regions of the ULIRGs, up to the average FoV of the LIRG subsample. If we consider only those spaxels within $r_{LIRGs} = 1.4$ kpc, the medians of the observed and extinction-corrected distributions increase a factor ~ 10, and reach up to $1.38\,M_\odot\,yr^{-1}\,kpc^{-2}$ and $2.90\,M_\odot\,yr^{-1}\,kpc^{-2}$, respectively.

- As discussed in Chapter 5, the spatial sampling (i.e. physical scale per spaxel) of the observations shapes not only the A_V structure but also the Σ_{SFR} distributions. Our simulations of the Σ_{SFR} maps of the LIRGs at increasing distances show that the predicted median of the Σ_{SFR} distributions is artificially increased by the poorer

sampling of the maps. At the average distance of the ULIRG subsample (328 Mpc), the computed median of the LIRG observed and extinction-corrected distributions is a factor ∼2–3 larger that local measurements.

- We extracted the integrated SFR and Σ_{SFR} of the objects of our sample, using the Hα effective radius from Arribas et al. (2012), and compared the near-IR measurements with optical, mid-IR and L_{IR}-based measurements. We found that the observed $SFR_{H\alpha}$ and $SFR_{Pa\alpha}$ values differ a factor ∼3.6 on average, and that the difference decreases slightly when the extinction correction is applied, up to $SFR_{H\alpha}/SFR_{Pa\alpha}$∼2.9. In agreement with previous studies, we observed a tight correlation between the extinction-corrected $SFR_{Pa\alpha}$ and the 24 μm measurements from *Spitzer*, and a reasonable agreement with SFR values from L_{IR}.

- We identified a total of 95 individual star-forming clumps in the Brγ and Paα emission maps of LIRGs and ULIRGs. These regions present sizes that rage within ∼60–400 pc and ∼300–1500 pc in LIRGs and ULIRGs, with Paα luminosities of $\sim10^5$–10^7 $L_\odot$ and $\sim10^6$–10^8 $L_\odot$, respectively. The Σ_{SFR} of the clumps presents a wide range of values within 1–90 $M_\odot\,yr^{-1}\,kpc^{-2}$ and 0.1–100 $M_\odot\,yr^{-1}\,kpc^{-2}$ for LIRGs and ULIRGs.

- We compared the properties of the local clumps from LIRGs and ULIRGs with other local and high-z samples, and showed that the regions from LIRGs, and specially ULIRGs, are more similar to high-z clumps like Genzel et al. (2011) or Swinbank et al. (2012) than 'normal' local star-forming regions, although at different spatial scales.

7

Conclusions and Future Work

"Da steh ich nun, ich armer Tor!
Und bin so klug als wie zuvor."
[And so I sit, poor silly man
No wiser now than when I began.]
— Faust, *Johann Wolfgang von Goethe*

In this final chapter, we summarise the most relevant conclusions of this thesis project. We also present a brief summary of the on-going research that would be the continuation of the present work, and discuss the future prospects of the study of local LIRGs and ULIRGs.

7.1. Conclusions

The main purpose of this thesis work has been the detailed 2D study of a representative sample of local ($z < 0.1$) LIRGs ($10^{11} L_\odot < L_{IR} < 10^{12} L_\odot$) and ULIRGs ($10^{12} L_\odot < L_{IR} < 10^{13} L_\odot$), observed with the IFS SINFONI at the VLT. Our seeing-limited observations covered a luminosity range of $\log(L_{IR}/L_\odot) = 11.1 - 12.4$, with an average redshift of $z_{LIRGs} = 0.014$ and $z_{ULIRGs} = 0.072$ for LIRGs and ULIRGs, respectively. The IFS observations cover the inner $\sim$3$\times$3 kpc and $\sim$12$\times$12 kpc in LIRGs and ULIRGs, with an average spatial resolution of $\sim$0.2 kpc and $\sim$0.9 kpc, respectively.

In this thesis, we presented the emission and kinematic maps of the Brγ, H_2 1-0S(1) and [FeII] lines of our sample of LIRGs, and the Paα and H_2 1-0S(1) maps for ULIRGs, that correspond to the brightest emission features in the H and K bands. We studied in detail the 2D extinction structure of local LIRGs and ULIRGs, derived from the Brγ/Brδ and Paα/Brγ line ratios, and their spaxel-by-spaxel A_V distributions. Using these corrections, we analysed in detail the extinction-corrected SFR and Σ_{SFR} distributions of the galaxies of the sample, using

the Brγ and Paα emission maps. Together with the spatial and spaxel-by-spaxel distributions of the Σ_{SFR}, we studied the properties of a sample of 95 individual star-forming regions, in terms of their size, luminosity and Σ_{SFR}.

Besides the analysis of the LIRG and ULIRG sample, we also presented the study of the spatially resolved kinematics of the central regions of M83, using AO VLT-SINFONI H+K observations. This galaxy is a nearby face-on grand-design spiral that, albeit widely studied given its proximity, still has some open questions regarding its innermost regions. To address these questions, we presented a detailed study of the gas and stellar kinematics with an unprecedented spatial resolution of ~ 0.2 arcsec, focused on the brightest emission features of the H and K bands (i.e. Brγ, Paα, H_2 1-0S(1) and [FeII] lines), together with the CO stellar bands at 2.293 μm and 2.323 μm.

The main results of this thesis are summarised as follows:

Spatially resolved kinematics of the central regions of M83

- The detailed study of the kinematics of M83 shows that, although the stellar kinematics are compatible with a global velocity field of uniform rotation, the kinematics of the gas seem to be dominated by shocks and inflows at small scales of tenths of parsecs, and totally unrelated to the stellar kinematics. Therefore, the gas kinematics are unsuitable to estimate dynamical properties of the central regions of M83.

- We find numerous evidences of recent supernova events. The strong [FeII] emission along the star-forming arc, together with the high velocity dispersion measured, are suggestive of shocks from supernova remnants. In addition, the study of the H_2 excitation in the arc is also consistent with recent supernovae. These evidences support the hypothesis that the off-nuclear mass concentrations, that had been proposed based on emission gas kinematics, are instead regions with perturbed kinematics due to supernova events.

- We argue that the optical nucleus of M83 is not its 'true' nucleus, but instead a star cluster of $\sim$100 Myr with its own coherent internal kinematics, and a dynamical mass of $M_{dyn} = (1.1 \pm 0.4) \times 10^7 M_\odot$. We suggest that the 'true' nucleus of M83 is located at the photometric and kinematic centre of the galaxy, where we found a modest enhancement of the K-band continuum.

VLT-SINFONI study of local LIRGs and ULIRGs

- The analysis of the emission maps of LIRGs shows that, whereas the more luminous regions in the Brγ line are located typically in star-forming rings or spiral arms (2/3 of the sources), the peak of the H_2 emission coincides with the stellar nucleus in all the sources. In addition, the H_2 emission shows very similar luminosities to the Brγ, although its spatial distribution is, in many cases, different at small scales. On the other hand, the [FeII] emission typically traces the same structures as the Brγ, although their peaks are not spatially coincident in some of the sources. The gas kinematics are primarily due to rotational motions, although we find signatures of radial flows in some of the objects. All the gas phases (i.e. ionised, partially ionised and molecular) appear to share the same large kinematics in terms of their velocity fields.

- Due to the interacting nature of most of the ULIRGs in our sample, and the fact that the average distance of these sources is a factor $\sim$4–5 larger than LIRGs, the gas morphology and kinematics in the more luminous systems are rather different. In ULIRGs, the Paα and H_2 peaks coincide with the main nucleus of the system in $\sim$71 % of the galaxies, and we find off-centre star-forming regions with $L_{Pa\alpha}$ up to $\sim 1 \times 10^8\,L_\odot$. The kinematics in ULIRGs are very complex given that most of the sources are interacting systems, and show features like coherent velocity gradients that can be associated with the progenitors or dynamical structures like tidal tails.

- In agreement with previous studies, the dust distribution in LIRGs and ULIRGs shows a patchy structure on sub-kpc scales, with areas that are almost transparent and regions where the measured extinction reaches up to $\sim$20–30 mag. The analysis of the spaxel-by-spaxel A_V distributions in the individual objects reveals no clear evidence of any dependence with L_{IR}. However, the combined distributions of LIRGs and ULIRGs as separated classes show that, whereas the LIRG distribution has a median value of $A_V = 5.3$ mag, ULIRGs present a slightly higher value of $A_V = 6.5$ mag.

- We find a mild dependence on the A_V radial profile of LIRGs with the galactocentric distance up to $\sim$1 kpc. Most of the individual objects show a decrease of the A_V in an spaxel-by-spaxel basis, and a flattening of the profile at larger distances ($\sim$2–3 kpc). In ULIRGs, such behaviour is not observed, and the A_V profiles are almost constant, most likely owing to the dearth of spatial resolution of the observations.

- We obtained the Σ_{SFR} 2D distribution of the LIRGs and ULIRGs based on their Brγ or Paα maps. The analysis of the maps shows that, in a significative fraction of the objects ($\sim$57 %), the peak of the extinction-corrected Σ_{SFR} is located at the main or secondary nucleus of the systems, and that the A_V correction increases the median of the individual spaxel-by-spaxel distributions by $\sim$50 %.

- We combined the individual distribution in two general LIRG and ULIRG spaxel-by-spaxel distributions. For the LIRG subsample, we obtain median values of $\Sigma^{obs}_{LIRGs} = 1.16\,M_\odot\,yr^{-1}\,kpc^{-2}$, and $\Sigma^{corr}_{LIRGs} = 1.72\,M_\odot\,yr^{-1}\,kpc^{-2}$ for the observed and the extinction-corrected distributions, whereas the median values for the ULIRGs are $\Sigma^{obs}_{ULIRGs} = 0.16\,M_\odot\,yr^{-1}\,kpc^{-2}$ and $\Sigma^{corr}_{ULIRGs} = 0.23\,M_\odot\,yr^{-1}\,kpc^{-2}$, respectively. However, when we compare regions of the same physical extend, the medians of the ULIRG distributions increase a factor $\sim$10, up to $1.38\,M_\odot\,yr^{-1}\,kpc^{-2}$ and $2.90\,M_\odot\,yr^{-1}\,kpc^{-2}$, respectively.

- We find that the spatial sampling, i.e. the physical scale per spaxel, of the maps have direct implications in deriving the A_V and Σ_{SFR}. We probed this distance effect by simulating the emission maps of the LIRGs at increasing distances using maps that are artificially smeared. This first-order approximation yields that, due to the poorer sampling of the maps, the median of the LIRG A_V distribution is decreased by a $\sim$20 % at the average distance of the ULIRG subsample, and can be reduced in a factor $\sim$40 % beyond 800 Mpc. When we consider the effect on the Σ_{SFR} measurements, we observe that the medians of the LIRG Σ_{SFR} distributions (observed and extinction-corrected) are increased by a factor $\sim 2-3$. This would have direct implications in the derivation of these physical quantities in high-z studies.

- We compared our SFR and Σ_{SFR} measurements with optical, mid-IR and far-IR SFR tracers. In agreement with previous studies, we observed a tight correlation between our near-IR measurements and the SFR derived from *Spitzer* 24 μm data, and a reasonable agreement with SFR measurement from L_{IR}. When we compare our $SFR_{Pa\alpha}$ values with optical measurements from Hα emission, we find that the near-IR measurements are a factor $\sim$3 larger than the $SFR_{H\alpha}$, even when the extinction corrections are applied.

- We identified a total of 95 individual star-forming clumps in our sample of (U)LIRGs, with sizes that range within $\sim$60–400 pc and $\sim$300–1500 pc, and Paα luminosities of

$\sim 10^5$–$10^7\,L_\odot$ and $\sim 10^6$–$10^8\,L_\odot$ in LIRGs and ULIRGs, respectively. We find that the local star-forming regions, specially in ULIRGs, are more similar to high-z clumps in terms of luminosity and Σ_{SFR} than local regions from 'normal' galaxies.

7.2. Future work

In the present thesis we have investigated the near-IR properties of a local sample of LIRGs and ULIRGs, based on IFS observations from VLT-SINFONI. We have presented a general analysis of the more prominent emission and absorption features in the H and K bands, and their kinematics. We have also focused our study on the analysis of the hydrogen recombination lines, i.e. Paα, Brγ and Brδ, to investigate in detail the extinction and the star formation in extreme environments such LIRGs and ULIRGs.

However, due to the great amount of information provided by the H- and K-band IFS data, there are other basic topics that require further research. Some of then are already in an advance stage of the analysis whereas others are specific topics that need to be addressed in future works.

7.2.1. Kinematic properties of star-forming clumps in LIRGs and ULIRGs

In Chapter 6 we presented a detail study of individual star-forming regions, in terms of their $L_{Pa\alpha}$ and size. However, to deeply understand how clumps are formed and evolve, it is essential to characterise the kinematic properties of the regions. In Fig. 7.1, we plot the velocity dispersion of the clumps and individual galaxies as a function of the Paα luminosity. We also include three models for the L-σ relation of the form $L_{Pa\alpha} \sim \sigma^n$, with $n = 3.5, 4.18, 5.0$. In particular, for a Strömgren sphere, the expected exponent for the L-σ relation is $n = 6$. However, as discussed in Chapter 6, the model of ionised-bounded region is not an accurate realisation of bright clumps as the ones in LIRGs and ULIRGs, and a shallower relation is expected. The exponent $n = 4.18$ corresponds to the best-fit model from Wisnioski et al. (2012), and seems to be a good approximation to the local clumps from Rozas et al. (2006) and Bastian et al. (2006), and also for the high-z regions from Genzel et al. (2011), although with greater scatter. On the other side, the regions from our LIRG and ULIRG present a shallower relation of $n \sim 3.8$.

If we assume that the clumps are formed following isothermal Jean collapse, it implies a relationship between the mass of collapsing gas and the velocity dispersion within the gas.

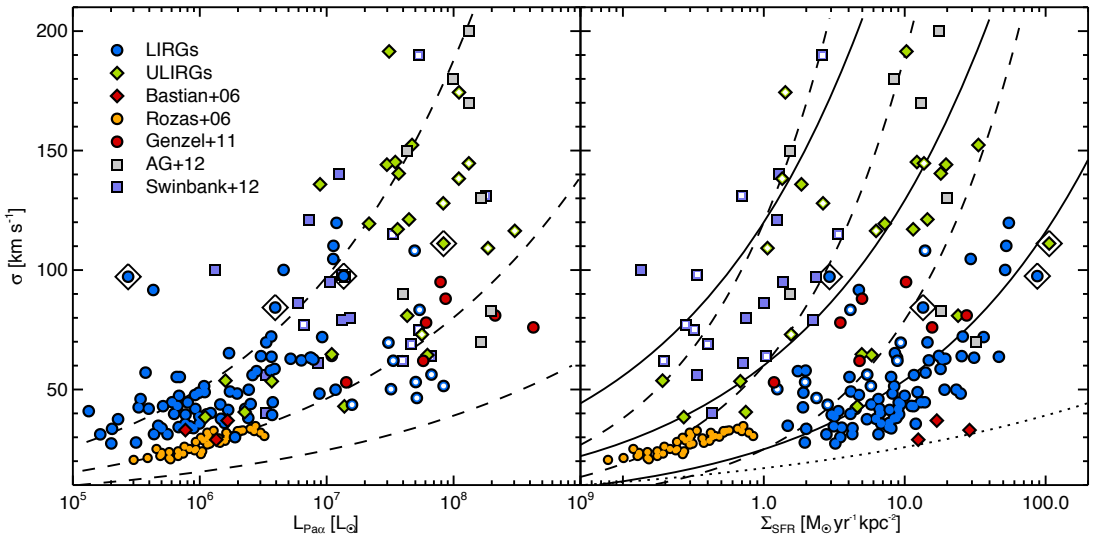

Figure 7.1: Scaling relations of star-forming regions - *Left:* Velocity dispersion vs $L_{Pa\alpha}$ for LIRGs (blue circles) and ULIRGs (green diamonds). Global measurements within R_{eff} are plotted as hollow symbols. Dashed lines correspond to models of the type $L_{Pa\alpha} \sim \sigma^n$, with $n = 3.5, 4.18, 5.0$, from top to bottom, respectively, using the same scaling. The curve $n = 4.18$ correspond to the empirical relation from Wisnioski et al. (2012). *Right:* Velocity dispersion vs Σ_{SFR}. Dashed lines correspond to models of the type $\sigma = \epsilon(\Sigma_{SFR})^{1/2}$ whereas solid lines are $\sigma = \epsilon(\Sigma_{SFR})^{1/3}$, with $\epsilon = 25, 60, 120$, from bottom to top, respectively. The dotted line correspond to the values derived directly from the KS and Jeans relations of a $\sim 10^7\,M_\odot$ clump (see the text for details). In both panels, points encircled by black diamonds represent nuclear regions with possible AGN contamination.

Using the KS relation ($\Sigma_{SFR} = A\Sigma_{gas}^n$) to convert from gas surface density to Σ_{SFR}, the relation between the velocity dispersion of the gas and the Σ_{SFR} is of the form (Lehnert et al., 2009):

$$\sigma_{gas} \sim M_J^{1/4} G^{1/2} \Sigma_{gas}^{1/4} = 0.3 M_J^{1/4} \Sigma_{SFR}^{0.18},$$

where σ_{gas} is the velocity dispersion of the gas, G is the gravitational constant, Σ_{gas} is the gas surface density in $[M_\odot\,pc^{-2}]$, M_J is the Jeans mass in $[M_\odot]$ and Σ_{SFR} is expressed in units of $[M_\odot\,yr^{-1}\,kpc^{-2}]$. Fig. 7.1 shows the above relation for a region of $10^7\,M_\odot$ (right panel, black line), and represent a lower limit for a σ-Σ_{SFR} relation where the velocity dispersion is purely dominated by the internal dispersion of the clumps themselves.

As discussed in Lehnert et al. (2009), if we consider that the energy output from the star formation determines the dynamics of the gas, the velocity dispersion would be proportional to the square root of the energy injection rate due to the stars. The energy injected per unit

area would then be proportional, with a certain coupling efficiency, to the Σ_{SFR}, yielding a function of the form $\sigma = \epsilon(\Sigma_{SFR})^{1/2}$. This hypothesis would be equivalent to consider that the mechanical energy output from the star formation is conserved within the ISM, with some efficiency. On the contrary, if the star formation is responsible for the observed line width by a combination of bulk and turbulent motion, the expected relation would be of the form $\sigma = \epsilon(\Sigma_{SFR})^{1/3}$. The different coupling efficiencies are difficult to constrain, and depend on parameters like the energy injection scales that spawn over wide ranges values. Fig. 7.1 shows different models for the σ-Σ_{SFR} relation. Those models of the form $\sigma = \epsilon(\Sigma_{SFR})^{1/3}$, with $\epsilon = 25, 60, 120$, seem to follow the overall trend of the local clumps, whereas the regions from the ULIRGs subsample and the high-z clumps from Swinbank et al. (2012) and SMG from Alaghband-Zadeh et al. (2012) suggest a steeper slope, closer to what would be expected from a $\sigma \sim \Sigma_{SFR}^{1/2}$ relation. These results suggest that star formation itself could power the turbulence through energetic feedback at kpc scales, and large scale random motions would drive the 'turbulence' at galactic scales. Obviously, these toy models are used as a simple scaling, and a deeper understanding of the underlaying mechanisms would require a thorough study of the scale energy injection, density of the gas, etc, that are out of the scope of the present work.

7.2.2. Outflow and stellar wind signatures from individual star-forming regions

Besides the possible contribution from AGN in the surroundings of the nuclear regions of the objects, large-scale stellar winds are known to increase the velocity dispersion of clumps with intense star formation ($\Sigma_{SFR} > 0.1\,M_\odot\,yr^{-1}\,kpc^{-2}$, Heckman et al. 2000). There are also multiple empirical evidence (e.g. Green et al. 2010, Genzel et al. 2011, Wisnioski et al. 2012) that these winds could represent a large fraction ($\sim$40 %) of the overall line flux, and increase significantly the line width. These broad components are typically blue-shifted $\sim$30–50 $km\,s^{-1}$ and present line FWHM of $\sim$500–1500 $km\,s^{-1}$.

In Fig.7.2 we show the Brγ and H_2 1-0S(1) line profiles of an individual region of ESO320-G030 ('R3', see Fig. 6.1) to illustrate the signatures of these stellar winds in our sample. These signatures of outflowing gas are observed in the majority of the clumps, in both the ionised and the molecular phase of the gas, and are clearly decoupled from the main global kinematics of the galaxy. In addition, the relative offsets of both phases, ionised (blue-shifted) and molecular (red-shifted), would indicate that both phases of the outflow are not only

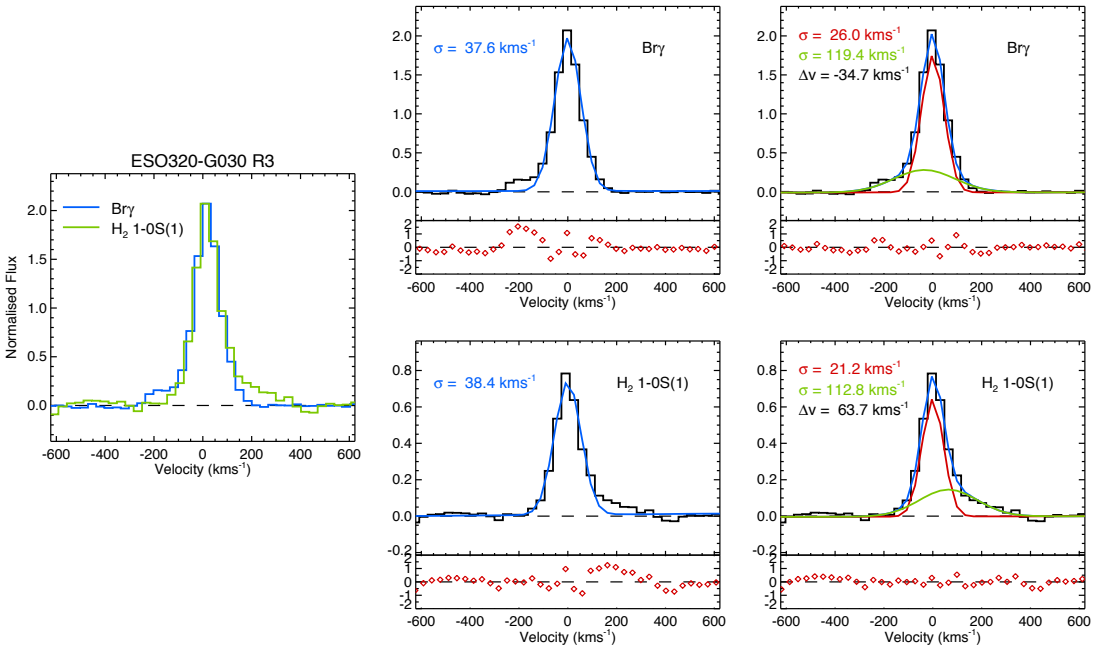

Figure 7.2: Outflow signatures in star-forming regions - *Left:* Brγ (blue) and H_2 1-0S(1) (green) line profiles from the integrated spectrum of the star-forming clump 'R3' of ESO320-G030 (see Fig. 6.1). The line profiles are normalised to the continuum, and the H_2 1-0S(1) profile has been re-scaled to the maximum of the Brγ line. *Centre:* Single-component Gaussian fit to the Brγ (top) and H_2 1-0S(1) (bottom) profiles. *Right:* Double-component Gaussian fit to the Brγ (top) and H_2 1-0S(1) (bottom) profiles. The insets of the centre and right panels show the residuals of the fits in units of the rms. The line widths of the Gaussian profiles, together with the offset between the narrow and broad components, are also shown in each panel.

dynamical but also geometrically decoupled. This analysis of the broad components of the ionised and warm molecular gas in the clumps will allow us to characterise the different phases of the outflowing gas, and study the physical driving mechanisms and feedback from the winds. In addition, since some of the regions host AGN, we would be able to establish the role of AGN-driven outflows in quenching the star-formation.

7.2.3. 2D kinematics of local LIRGs and ULIRGs

The analysis of the kinematics of some of the LIRGs and ULIRGs presented in this thesis has been published in Bellocchi et al. (2013), based on the multi-component analysis of the Hα emission from VLT-VIMOS observations. This detailed 2D analysis of the ionised gas already showed the key role of non-circular motions on shaping the kinematics of these objects, in particular in ULIRGs, due to their interacting nature.

The kinematic analysis of LIRGs and ULIRGs presented in Chapter 4, based on a single-

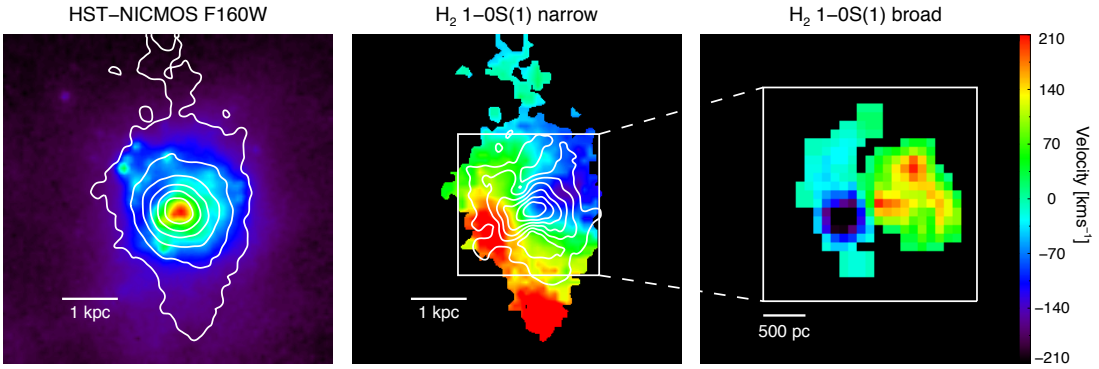

Figure 7.3: Spatially-resolved kinematics of IRAS 17208-0014 - *Left:* HST-NICMOS F160W continuum map of IRAS 17208-0014, with the contours of the H_2 1-0S(1) emission overlaid. *Centre:* H_2 1-0S(1) velocity field of the narrow component. The emission from the H_2 broad component is overplotted as white contours. *Right:* Detail of the inner region of IRAS 17208-0014 showing the velocity field of the H_2 broad component.

component Gaussian fit to the emission lines, also showed that most of the objects exhibit complex kinematics and hence line profiles in most of the gas phases on an spaxel-by-spaxel basis, not only in the ionised gas. The next step on this analysis is to perform a multi-component study of the emission lines, and compare the kinematics of the different phases of the gas with the stellar kinematics from the CO (2-0) band at 2.293 μm.

Figure 7.3 shows some preliminary results on the H_2 1-0S(1) kinematics of the ULIRG IRAS 17208-0014 (Emonts et al. 2014, in preparation). The left panel of the figure shows the velocity field of the H_2 broad component, i.e. not associated with the global (narrow) component that traces the circular motion of the galaxy. This broad component is completely decoupled from the global kinematics of the object, and might indicate not only the presence of outflowing gas, but also circumnuclear discs, warps, infall of gas, or transient structures in ongoing mergers.

This multi-phase 2D analysis will allow us to determine the geometry and kinematic structure of the different phases of the outflowing gas, the total mass outflow rates of each component, analyse the physical driving mechanisms (AGN or starburst), and the energy injection and feedback at sub-kpc scales.

7.2.4. Kennicutt-Schmidt star formation law at sub-kiloparsec scales in LIRGs

In Chapter 6, we presented the analysis of the extinction-corrected Σ_{SFR} on sub-kpc scales of our sample of LIRGs and ULIRGs, based on Paα and Brγ measurements, and showed that the Σ_{SFR} structure in this class of galaxies is very clumpy at scales of a few hundred of

parsecs. The spatially-resolved analysis of the star-formation is crucial to understand whether the KS law breaks-down at these physical scales on the high Σ_{SFR} regime, as it seems to happen in normal spiral galaxies (Onodera et al. 2010, Leroy et al. 2013). In addition, local LIRGs are close analogs, in terms of their Σ_{SFR}, of the high-z star-forming discs observed at cosmological distances. Therefore, they are perfect candidates for filling the gap between local normal spirals and extreme starburst at high-z.

Besides the spatially resolved measurements of the Σ_{SFR}, it is essential to acquire detailed measurements of the surface density of the molecular gas at sub-kpc scales. The sensitivity and the high spatial resolution of the interferometric observations from ALMA will allow, for the first time, to perform this kind of studies in nearby galaxies. Once the first cold molecular gas high-resolution observations from ALMA become available, it would be possible to address and shed some light into these questions.

7.2.5. 2D study of the excitation mechanisms of the H_2

We showed in Chapter 3 that it is feasible to analyse in detail the excitation mechanisms of the H_2, based on K-band spectroscopic data. The amount of different roto-vibrational transitions of the warm molecular hydrogen in the K-band allows to distinguish among the different mechanisms, i.e. radiative or thermal, that produce the different transitions.

Although some of the H_2 transitions are too weak to be mapped in an spaxel-by-spaxel basis, it is possible to obtain integrated measurements of the different H_2 lines over individual regions. We have started some preliminary analysis of the integrated spectra of star-forming regions, using different techniques to increase the S/N of the lines, i.e. 'de-rotate' the spectra from each spaxel before the stacking, and subtract the stellar continuum to improve the continuum determination. This analysis will be extended not only to starburst-dominated regions, but also to clumps identified in terms of their strong H_2 emission.

The multi-component analysis highlighted in Sec. 7.2.2 will allow us to identify possible differences between the excitation mechanisms of both narrow and broad components. Given that some of these secondary components are associated with outflowing gas, we expect to observe H_2 line ratios compatible with shock-induced excitation, whereas the narrow component would trace the emission from PDRs associated to the star-forming regions.

8

Conclusiones

And you will find someday that, after all, it isn't as horrible as it looks.

— Richard P. Feynman,
The Feynman Lectures on Physics Vol III

El objetivo principal del presente proyecto de tesis ha sido el estudio bidimensional detallado de una muestra local ($z < 0{,}1$) de LIRGs ($10^{11}L_\odot < L_{IR} < 10^{12}L_\odot$) y ULIRGs ($10^{12}L_\odot < L_{IR} < 10^{13}L_\odot$), observada con el espectrógrafo de campo integral SINFONI, en el VLT. El rango de luminosidad cubierto por nuestras observaciones es $\log(L_{IR}/L_\odot) = 11{,}1-12{,}4$, mientras que los objetos presentan un desplazamiento al rojo promedio de $z_{LIRGs} = 0{,}014$ y $z_{ULIRGs} = 0{,}072$ en el caso de LIRGs y ULIRGs, respectivamente. Las observaciones de campo integral cubren los $\sim 3\times 3$ kpc y $\sim 12\times 12$ kpc más internos en LIRGs y ULIRGs, con una resolución espacial promedio de ~ 0.2 kpc y ~ 0.9 kpc, respectivamente.

En esta tesis hemos presentado los mapas de emisión y cinemáticos de las líneas Brγ, H_2 1-0S(1) y [FeII], en el caso de las LIRGs, y Paα y H_2 1-0S(1) en las ULIRGs, que corresponden a las líneas espectrales más brillantes en las bandas H y K. Asimismo, hemos estudiado en detalle la estructura 2D de la extinción, obtenida a partir de los cocientes de líneas Brγ/Brδ y Paα/Brγ, así como las distribuciones spaxel a spaxel de la A_V. Aplicando estas correcciones, hemos analizado en detalle las distribuciones de SFR y Σ_{SFR} de las galaxias de la muestra, a partir de los mapas de emisión de las líneas Brγ y Paα. Junto con los mapas y distribuciones spaxel a spaxel de la Σ_{SFR}, hemos estudiado las propiedades de una muestra de 95 regiones individuales de formación estelar, en función de su tamaño, luminosidad y Σ_{SFR}.

Además del estudio de LIRGs y ULIRGs, hemos presentado el análisis detallado de la cinemática de las regiones centrales de M83, basado en observaciones en banda H+K

realizadas con VLT-SINFONI mediante óptica adaptativa. Esta galaxia cercana es una de las llamadas espirales de gran diseño orientada prácticamente de cara y que, pese a haber sido ampliamente estudiada debido a su proximidad, todavía presenta algunas cuestiones que permanecen abiertas en relación a sus regiones más centrales. Para abordar algunas de estas cuestiones, hemos presentado el estudio detallado de la cinemática del gas y de las estrellas con una resolución espacial sin precendentes de $\sim$ 0,2 arcsec, centrado en las líneas de emisión más brillantes en las bandas H y K, como son Brγ, Paα, H_2 1-0S(1) y la línea de [FeII], junto con las bandas estelares de CO a 2.293 μm y 2.323 μm.

Los resultados más importantes de esta tesis se resumen a continuación:

Estudio de la cinemática resuelta espacialmente de las regiones centrales de M83

- El estudio detallado de la cinemática de M83 muestra que, mientras la cinemática estelar parece ser compatible con un campo de velocidades global correspondiente a una rotación uniforme, la cinemática del gas parece estar dominada por ondas de choque y flujos de gas a pequeñas escalas de algunas decenas de pársecs, siendo por tanto independiente de la cinemática estelar. Este hecho demuestra que la cinemática del gas no es apropiada para derivar propiedades dinámicas de la región central de M83.

- Encontramos múltiples evidencias de explosiones recientes de supernova. La fuerte emisión de la línea de [FeII] a lo largo del arco de formación estelar, junto con la alta dispersión de velocidades observada, sugieren la presencia de ondas de choque procedentes de explosiones de supernova. Asimismo, el estudio de los mecanismos de excitación del H_2 en el arco también es consistente con eventos recientes de este tipo. Estas evidencias sustentan la hipótesis de que las concentraciones de masa propuestas en base a la cinemática del gas, son en su lugar regiones en las que la cinemática global del gas se encuentra fuertemente perturbada debido a explosiones de supernova.

- Proponemos que el núcleo óptico de M83 es un cúmulo estelar de $\sim$100 millones de años que presenta su propia cinemática interna, de la que se deriva una masa dinámica de $M_{dyn} = (1{,}1 \pm 0{,}4) \times 10^7 M_\odot$. Por otro lado, consideramos que el núcleo de M83 se encuentra localizado en el centro fotométrico y cinemático de la galaxia, donde observamos un ligero aumento de la emisión en el continuo en banda K.

Estudio de LIRGs y ULIRGs locales mediante VLT-SINFONI

- El análisis de los mapas de las líneas de emisión en el subconjunto de LIRGs muestra que, mientras las regiones más luminosas en la línea de Brγ se encuentran típicamente en los brazos espirales o en anillos circumnucleares de formación estelar (2/3 de las fuentes), el pico de la emisión en H_2 coincide con el núcleo estelar en la totalidad de las fuentes. Asimismo, la emisión del H_2 muestra luminosidades muy similares a la de la línea de Brγ, aunque su distribución espacial es, en muchos casos, diferente a pequeña escala. Por otro lado, la emisión de la línea de [FeII] traza típicamente las mismas estructuras que la línea de Brγ, aunque sus máximos no coinciden espacialmente en algunos de los objetos. La cinemática del gas parece trazar principalmente movimientos de rotación, aunque encontramos evidencias de flujos radiales de gas en algunas de las fuentes. Todas las fases del gas (ionizada, parcialmente ionizada y molecular) muestran la misma cinemática a gran escala, considerando sus campos de velocidades.

- Debido a que la muestra de ULIRGs está formada por sistemas en diversos grados de interación, y a que la distancia promedio de las fuentes es un factor $\sim$4–5 mayor que en el caso de las LIRGs, la morfología y la cinemática del gas es bastante diferente en los objetos más luminosos. En las ULIRGs, los picos de la emisión en Paα y H_2 coinciden con el núcleo principal de los objetos en el $\sim$71 % de los casos, y encontramos regiones extra-nucleares de formación estelar intensa con $L_{Pa\alpha}$ hasta $\sim 1 \times 10^8\,L_\odot$. Asimismo, la cinemática en las ULIRGs es muy compleja debido a que la mayor parte de las fuentes son sistemas en interación, y muestran características como gradientes de velocidad coherentes que pueden ser asociados con los diferentes progenitores o con estructuras dinámicas como colas de marea.

- En concordancia con estudios previos, la distribución del polvo en LIRGs y ULIRGs muestra una estructura irregular a escalas inferiores al kilopársec, con regiones prácticamente trasparentes y zonas donde la extinción visual alcanza valores de hasta $\sim$20–30 mag. El análisis de las distribuciones spaxel a spaxel de la extinción en objetos individuales no sugiere la existencia de ninguna posible dependencia con L_{IR}. No obstante, al considerar las distribuciones globales de LIRGs y ULIRGs como clases de luminosidad, se observa que, mientras que las LIRGs presentan un valor mediano de $A_V = 5{,}3$ mag, en el caso de las ULIRGs se obtiene un valor ligeramente más alto de $A_V = 6{,}5$ mag.

- Encontramos una ligera dependencia con la distancia galactocéntrica de los perfiles radiales de A_V en las LIRGs, hasta $\sim$1 kpc. La mayor parte de los objetos individuales muestran una disminución de la extinción spaxel a spaxel, pasando a un perfil radial aproximadamente constante a partir de distancias de $\sim$2–3 kpc. En las ULIRGs no se observa esta dependencia con la distancia radial, siendo los perfiles de A_V prácticamente constantes, aunque consideramos que dicho comportamiento puede deberse principalmente a la falta de resolución espacial de las observaciones.

- Hemos obtenido las distribuciones bidimensionales de la Σ_{SFR} para las LIRGs y ULIRGs de la muestra, a partir de los mapas de emisión de las líneas de Brγ y Paα. El análisis de dichos mapas muestra que en una fracción significativa de los objetos ($\sim$57 %), el pico de la Σ_{SFR} corregida de extinción se encuentra locaclizado en el núcleo principal o en el secundario de los sistemas. Por otro lado, observamos que la corrección de extinción aumenta la mediana de las distribuciones spaxel a spaxel individuales en $\sim$50 %.

- Siguiendo el mismo método que en caso de la extinción, hemos combinado las distribuciones individuales de la Σ_{SFR} en dos distribuciones globales de LIRG y ULIRG. En el caso de las LIRGs, obtenemos valores medianos para las distribuciones observadas y corregida de extinción de $\Sigma^{obs}_{LIRGs} = 1{,}16\,M_\odot\,yr^{-1}\,kpc^{-2}$, y $\Sigma^{corr}_{LIRGs} = 1{,}72\,M_\odot\,yr^{-1}\,kpc^{-2}$, mientras que para las ULIRGs, encontramos los valores $\Sigma^{obs}_{ULIRGs} = 0{,}16\,M_\odot\,yr^{-1}\,kpc^{-2}$ y $\Sigma^{corr}_{ULIRGs} = 0{,}23\,M_\odot\,yr^{-1}\,kpc^{-2}$, respectivamente. No obstante, al comparar regiones con extensiones físicas equivalentes, las medianas de las distribuciones en el caso de las ULIRGs se ven incrementadas un factor $\sim$10, hasta $1.38\,M_\odot\,yr^{-1}\,kpc^{-2}$ y $2.90\,M_\odot\,yr^{-1}\,kpc^{-2}$, respectivamente.

- Por otro lado, encontramos que la resolución espacial con la que se muestrean los mapas de emisión, y por tanto de Σ_{SFR} (la escala física por spaxel), tiene implicaciones directas en las medidas de magnitudes físicas como A_V y Σ_{SFR}. Hemos estudiado este efecto de distancia mediante simulaciones en las que se disminuye la resolución espacial de los mapas de emisión de las LIRGs, simulando las condiciones observacionales a distancias cada vez mayores. Esta aproximación de primer orden muestra que, debido a la pérdida de resolución espacial, la mediana de las distribuciones spaxel a spaxel de la A_V en el caso de las LIRGs, disminuye en un $\sim$20 % a la distancia promedio de la submuestra de ULIRGs, y que se ve reducida en un factor $\sim$40 % a partir de los 800 Mpc. Cuando consideramos este efecto en las medidas de la Σ_{SFR}, observamos

que la mediana de las distribuciones en el caso de las LIRGs, tanto observadas como corregidas de extinción, se ve incrementada en un factor $\sim 2-3$. Este hecho pude tener implicaciones directas en las medidas de magnitudes físicas, especialmente en estudios de objetos a alto deplazamiento al rojo.

- Hemos comparado nuestras medidas de la SFR y Σ_{SFR} con las obtenidas mediante otros trazadores en el óptico e infrarrojo medio y lejano. En la línea de otros estudios previos, observamos una estrecha correlación entre nuestras medidas en el infrarrojo cercano y las derivadas a partir de observaciones de *Spitzer* en 24 μm, así como un acuerdo razonable con medidas procedentes de L_{IR}. Cuando comparamos los valores de la SFR derivados de la líneas de Paα con medidas en el óptico, basadas en la emisión de Hα, encontramos que las medidas en el infrarrojo cercano son típicamente un factor $\sim$3 mayores que las ópticas, incluso cuando se tienen en cuenta los efectos de la extinción.

- Hemos identificado un total de 95 regiones de formación estelar individuales en nuestra muestra de (U)LIRGs, con tamaños comprendidos entre $\sim$60–400 pc y $\sim$300–1500 pc, y luminosidades de Paα entre $\sim 10^5$–$10^7\,L_\odot$ y $\sim 10^6$–$10^8\,L_\odot$ en LIRGs y ULIRGs, respectivamente. Encontramos que dichas regiones de formación estelar, especialmente en el caso de las ULIRGs, son más similares a regiones observadas en objetos a alto desplazamiento al rojo en términos de luminosidades y Σ_{SFR}, que a aquellas regiones observadas en galaxias locales "normales".

Appendix A

Notes on individual sources

- **IRAS 06206-6315**: This object is a ULIRG classified as a Seyfert 2 galaxy according to its optical spectrum (Duc et al., 1997). The NICMOS F160W image (Bushouse et al., 2002) shows a double nuclei structure with a tidal tail starting at the north and bending towards the south-east, which is not completely covered by our SINFONI data (Fig. B.2a). The projected separation between both nuclei is ~ 4.5 kpc, and the FoV sampled by SINFONI is $\sim 17 \times 17$ kpc. The southern nucleus (labelled as "A" in Fig. B.2a) is the brightest source in the continuum, Paα and H_2 1-0S(1) lines, and it contributes to the $\sim 55\%$ of the total Paα emission within the FoV. A local peak of Paα emission is visible at the end of the tidal tail. The northern nucleus (labelled as "B" in the figure), although similar in Paα brightness to the southern one, is $\sim 75\%$ less bright in the H_2 1-0S(1) emission.

  The kinematics of the ionised gas show the distinct velocity gradients of both progenitors of the interacting system.

- **NGC 2369** (IRAS07160-6215): The SINFONI field of view covers the central $\sim 2 \times 2$ kpc of this almost edge-on spiral LIRG. The NICMOS F160W image (Alonso-Herrero et al., 2006) shows a very complex morphology in the inner regions of the galaxy, with multiple clumps that are not completely resolved in our SINFONI data. One of the brightest sources of Brγ emission is covered by aperture "B" in Fig. B.1a. It is also a bright source in [FeII], but no counterpart is detected in either the continuum image or in the H_2 1-0S(1) map.

  The ionised gas kinematics show a strong velocity gradient between regions "A" and "B", which may indicate the presence of a warp rotating disk.

- **NGC 3110** (IRAS10015-0614): The NICMOS F160W image (Alonso-Herrero et al., 2006) of this almost face-on spiral LIRG shows two well-defined arms that extend for ~ 30 kpc, of which $\sim 3 \times 3$ kpc are covered by our SINFONI data. The arms are outlined by diffuse gas emission that concentrates at the nucleus and in a bright complex to the north of the FoV. The nucleus dominates the emission of both the ionised and molecular gas ($\lesssim 20\%$ of the total flux), although the star-forming region labelled "B" in Fig. B.1b has a comparable brightness in Brγ, and even higher in HeI. The [FeII] emission shows the same structure as the ionised and molecular hydrogen.

  The kinematics of the different phases of the gas are very similar and show the typical pattern of a thin rotating disk.

- **NGC 3256** (IRAS10257-4338): Our SINFONI data cover the central $\sim 2.5 \times 3.2$ kpc of this extreme starburst LIRG. The Brγ map shows a very clumpy morphology, with multiple knots of strong emission spread along the southern spiral arm of the object (see Lípari et al. 2000, Lípari et al. 2004, Alonso-Herrero et al. 2006 and references therein). The H_2 emission also shows a clumpy distribution with a more diffuse component and two bright spots of strong compact emission in the south of the secondary nucleus (aperture "A", Fig. B.1c). These knots are also clearly visible in the velocity dispersion map, with values up to $\sim$180 km s^{-1}, together with a bright spot east of the southern nucleus (aperture "B").

- **ESO 320-G030** (IRAS11506-3851): The NICMOS F160W image (Alonso-Herrero et al., 2006) of this SBA LIRG (Erwin, 2004) reveals an overall spiral structure that extends over $\sim$32 kpc. Our SINFONI data cover the inner $\sim 2 \times 2$ kpc. The Brγ map shows a ring-like structure of star formation not observed in the continuum images, with well-defined bright regions (Fig. B.1d), as observed in Paα by Alonso-Herrero et al. (2006). The maximum of Brγ emission is reached by the easternmost region and accounts for $\sim$40% of the integrated flux. The nucleus is a faint source in Brγ but dominates the emission of the molecular hydrogen, with up to $\sim$45% of the total emission of the H_2 1-0S(1) in the inner $\sim 2 \times 2$ kpc. The molecular hydrogen emission reveals the structure of the nuclear bar, which connects both sides of the star-forming ring. The [FeII] emission has a similar morphology as the Brγ.

  The orientation of the galaxy is almost face-on, and the gas kinematics show a well-defined rotation pattern.

- **IRAS 12112+0305**: This system is a close interacting pair classified as ULIRG and separated ∼4.2 kpc with a bright tidal tail extending 18 kpc to the north (Surace et al., 2000). Our SINFONI data covers the central $\sim 14 \times 14$ kpc of the system (Fig. B.2b). The southern nucleus is the brightest source in the K-band and in Paα ($\sim$ 35% of the integrated flux), although the large Paα EW ($\sim$ 300 Å) measured along the tidal tail suggests a recent burst of star formation in the northern component. Also remarkable is the bright spot of Paα emission in the east of the nuclei, not detected in the continuum, that traces a young massive HII complex that could represent a tidally induced giant extranuclear star-forming region (Colina et al., 2000). The H_2 emission is highly concentrated in the northern nucleus, accounting for $\sim$ 52% of the total flux of the FoV. The southern nucleus is $\sim$ 42% less bright than the northern component, and no significative emission is measured along the tail.

  The kinematics of the gas reveal two different velocity gradients for each progenitor, with a steep gradient along the tidal tail and the northern nucleus of more than $\Delta v \sim 400\,km\,s^{-1}$.

- **IRASF 12115-4656**: This spiral-like LIRG might be interacting with IRAS12112-4659, located at $\sim$ 100 kpc south-west (Arribas et al., 2008). Our data cover the central $\sim 5 \times 5$ kpc and show that a star-forming ring dominates the Brγ emission, clearly outlined in the ionised gas map, whereas the nucleus seems to be highly obscured (see Chapter 5). The emission from the arms is diffuse, with the exception of a very compact source, labelled "B" in Fig. B.1e, where the Brγ emission reaches its maximum. The ring is not so clearly visible on the H_2 1-0S(1) map, where the emission is more diffuse, with a peak at the nucleus of the galaxy. As shown in Figs. 4.5 and 4.6, the [SiVI] line at 1.963 μm and the [CaVIII] line at 2.321 μm are detected in the nucleus of the galaxy and suggest there is an AGN. The gas kinematics show a smooth velocity gradient along the whole FoV, as is typical of a rotating disk.

- **NGC 5135** (IRAS13229-2934): This LIRG is an SBab starburst galaxy classified as Seyfert 2 (Bedregal et al., 2009). Our SINFONI data sample the inner $\sim 3 \times 3$ kpc of the galaxy, and reveal a high excitation ionisation cone centred on the AGN, and extending up to ∼600 pc radius (Bedregal et al., 2009). The brightest source of Brγ emission (aperture "B" in Fig. B.1f) do not coincide with the H_2 and [FeII] maxima, which are located at the nucleus and at the bright region $\sim$ 2 arcsec south-west, respectively.

For a detailed study of the ionisation of the different phases of the gas and the star formation activity of NGC 5135 with these SINFONI data, see Bedregal et al. (2009).

- **IRAS 14348-1447**: Our SINFONI data sample the central $\sim 15 \times 15$ kpc of this ULIRG (see Fig. B.2c). The K-band image shows two bright sources and a diffuse component extending towards the north-east of the FoV, where the Paα map reveals a very bright knot of emission. This region shows high values of Paα EW up to $\sim$400 Å that suggest a young starburst in an inner tidal tail (Colina et al., 2005). The southern nucleus represents the $\sim$ 52% of the integrated Paα and H_2 emission, whereas the northern component accounts for the $\sim$ 33% and the $\sim$ 26% respectively. The molecular emission is highly concentrated at both of the nuclei.

  The kinematics of the diffuse ionised gas shows an overall rotation pattern along the system. The high velocity dispersion measured for the northern component of the system is due to the steep velocity gradient of the gas.

- **IRASF 17138-1017**: The K-band image of this galaxy reveals that its central regions are rather complex. Our SINFONI data cover the central $\sim 3 \times 3$ kpc of this almost edge-on spiral LIRG that extends beyond ~ 9 kpc. We have identified the nucleus of the galaxy with the brightest spaxel of the K-band image (labelled "A" in Fig. B.1g). The Brγ emission show a clumpy morphology, with its maximum ($\sim$ 25% of the total Brγ flux in our FoV) at a bright knot ~ 700 pc south of the nucleus, that also reveals a strong emission in HeI. The H_2 emission is more diffuse, reaching its maximum at the nucleus of the galaxy. The [FeII] emission has a similar morphology to the Brγ and shows different bright sources along the central region of the galaxy, with an underlying diffuse emission. The brightest source is identified with aperture "B" in Fig. B.1g.

  The kinematics of the gas are, to first order, compatible with a thin rotating disk.

- **IRAS 17208-0014**: The Paα map of this starburst ULIRG (Arribas & Colina, 2003), which samples the $\sim 7 \times 7$ kpc of the object, shows that the ionised gas emission is highly concentrated at the nucleus, and it reveals a young burst of star formation to the south-east (aperture "B" in Fig. B.2d), with values of Paα EW $\sim$ 130 Å. The H_2 emission is more compact than the Paα, appears highly concentrated in the nucleus, and extended perpendicularly to the projected plane of the disk.

The kinematics of the gas show a very steep rotation pattern, typical of a disk, and high velocity dispersion values of $\sim 250\,\mathrm{km\,s^{-1}}$ in the nuclear regions.

- **IC 4687** (IRAS18093-5744): This LIRG is part of a system that involves a group of three galaxies in close interaction (West, 1976). The nuclear separations between the northern (IC 4687) and the central galaxies (IC 4686) and between the central and the southern galaxies (IC 4689) are ∼10 kpc and ∼20 kpc, respectively. The FoV of our SINFONI observations covers the central $\sim 3 \times 3$ kpc of IC 4687. This object shows a spiral-like morphology with several knots of enhanced Brγ emission along its arms and nucleus, in close agreement with the Paα emission from Alonso-Herrero et al. (2006). The brightest Brγ region is located south of the FoV (labelled "B" in Fig. B.1h), and accounts for the ∼25% of the total Brγ emission within the inner $\sim 3 \times 3$ kpc. Although this region and the nucleus are equally bright, the EW of the Brγ line is much higher, up to 120 Å, and the intense HeI emission suggests that it is a young star-forming complex. The morphology of the H_2 emission is rather different from the observed in the ionised gas, and the peak of emission is located at the nucleus. The [FeII] emission has a similar morphology to the Brγ and shows different circumnuclear sources. The peak of emission coincides with the brightest Brγ region, located south of the FoV.

  The kinematics of the ionised gas on large scales show a smooth velocity gradient along the FoV, with evident signs of deviations from a rotation pattern.

- **IRAS 21130-4446**: This ULIRG is identified as a double nucleus system with a nuclear separation ~ 5 kpc, however, the complex morphology of the galaxy makes it hard to locate the exact position of the two nuclei (Cui et al., 2001). The WFPC2 F814W image of this source shows different condensations and tails, some of them unresolved in our SINFONI data, which cover $\sim 14 \times 14$ kpc centred in the northern nucleus of the galaxy. The Paα emission is concentrated at the northern nucleus, marked as "A" in Fig. B.2e, and extended along the southern part of the system. It reaches its maximum in these concentrations that extends towards aperture "B", where the Paα EW is up to ~ 900 Å. The emission from warm molecular gas comes, on the other hand, mostly from the northern nucleus, and only a weak diffuse emission from the southern region is detected. The properties of this southern area suggest an extremely young burst of star formation spreading over the region.

- **NGC 7130** (IRAS 21453-3511): Our $\sim 3 \times 5$ kpc SINFONI FoV covers the nucleus and part of the northern spiral arm / tidal tail of NGC 7130. The gas emission is highly concentrated at the nucleus and in a bright star-forming region in the arm (aperture "B" in Fig. B.1i), three times less bright than the nucleus (see also Alonso-Herrero et al. 2006 and Díaz-Santos et al. 2010). We have tentatively detected [SiVI] emission at 1.963 μm and [CaVIII] at 2.321 μm, as shown in Figs. 4.5 and 4.6, in agreement with the LINER and Seyfert-like features observed in the nuclear, optical spectrum of this LIRG (Veilleux et al., 1995).

  The kinematics of the gas reveal a rotation pattern in the nucleus of the galaxy and a steady velocity gradient along the arm / tidal tail.

- **IC 5179** (IRAS 22132-3705): Our SINFONI data sample the central $\sim 4 \times 2$ kpc of this spiral LIRG. The gas emission maps show a very clumpy distribution of compact knots of star formation spread along the spiral arms and a very compact nucleus that dominates the emission (see Fig. B.1j). It accounts for the $\sim 40\%$ of the total Brγ emission, up to the $\sim 30\%$ of the H_2 1-0S(1) and $\sim 45\%$ of the [FeII] emission within our FoV.

  The general kinematics of the gas reveal a smooth velocity field, compatible with the rotation pattern of a thin disk.

- **IRAS 22491-1808**: Cui et al. (2001) propose a multiple merger origin for this ULIRG based on its morphology. The K-band image, which samples the central $\sim 12 \times 12$ kpc, reveals two nuclei, separated by a projected distance of ~ 2.3 kpc, with several knots and condensations in the central regions and along the tidal tails, which extend beyond ~ 5 kpc to the east and north-west of the system (see Fig. B.2f). The Paα map shows three clearly distinguished concentrations extending towards the north-west of the FoV. Two of them coincide with the two nuclei observed in the continuum, whereas the third, located to the north-west, could be associated with the knots of emission that extend along the tail, with values of Paα EW ~ 500 Å. On the other hand, the H_2 emission is very concentrated in the eastern nucleus, accounting for $\sim 85\%$ of the total H_2 1-0S(1) flux. Although the mid-infrared spectrum of this galaxy is consistent with a starburst and an AGN (Farrah et al., 2003), we have not detected [SiVI] emission.

The gas kinematics of the eastern nucleus shows a well differentiated steep gradient of $\Delta v \sim 200\,km\,s^{-1}$ in $\sim 2\,kpc$. Due to beam smearing effects, this gradient enhances the measured values of the velocity dispersion up to $\sim 170\,km\,s^{-1}$.

- **IRAS 23128-5919**: This ULIRG is a strong interacting system, classed as a mixture of starburst, LINER, and Sy2 (Kewley et al. 2001, Bushouse et al. 2002). The projected distance between its double nucleus is $\sim 4\,kpc$, and it presents prominent tidal tails, containing many bright knots of emission, extending to the north and south-east over $\sim 50\,kpc$ (Bushouse et al., 2002). Our SINFONI data cover the central $\sim 7 \times 11\,kpc$ of the system. The double nucleus structure is clearly visible in both the K-band image and the ionised gas map (Fig. B.2g). The southern nucleus, which coincides with the AGN, is the brightest Paα source, and it accounts for $\sim 58\%$ of the integrated Paα flux. In contrast, the Paα emission from the northern nucleus seems to be dominated by star-forming activity, with Paα EW up to $\sim 600\,$Å. The presence of an AGN in the southern nucleus is supported by the strong compact [SiVI] emission detected (Fig. 4.5). The H_2 morphology shows a very peaked and concentrated emission in the southern nucleus ($\sim 45\%$ of the total H_2 1-0S(1) flux), whereas the northern nucleus accounts for half the flux of the southern nucleus.

  The gas kinematics of the northern nucleus show a velocity gradient of $\Delta v \sim 140\,km\,s^{-1}$ in the north-south direction, whereas the southern nucleus kinematics seem to be dominated by the AGN. The gas kinematics show extremely high velocities ($\sim 1000\,km\,s^{-1}$) in the ionised gas at radial distances of $\sim 2\,kpc$ from the southern nucleus, and the presence of molecular gas outflows in the same regions. The high velocity dispersion and the blue/red wings in the Paα and H_2 1-0S(1) line profiles suggest a cone-like structure, centred on the AGN, and extending $\sim$3–4 kpc to the north-east and south-west (Fig. B.2g).

A. NOTES ON INDIVIDUAL SOURCES

Appendix B

Emission and kinematic maps

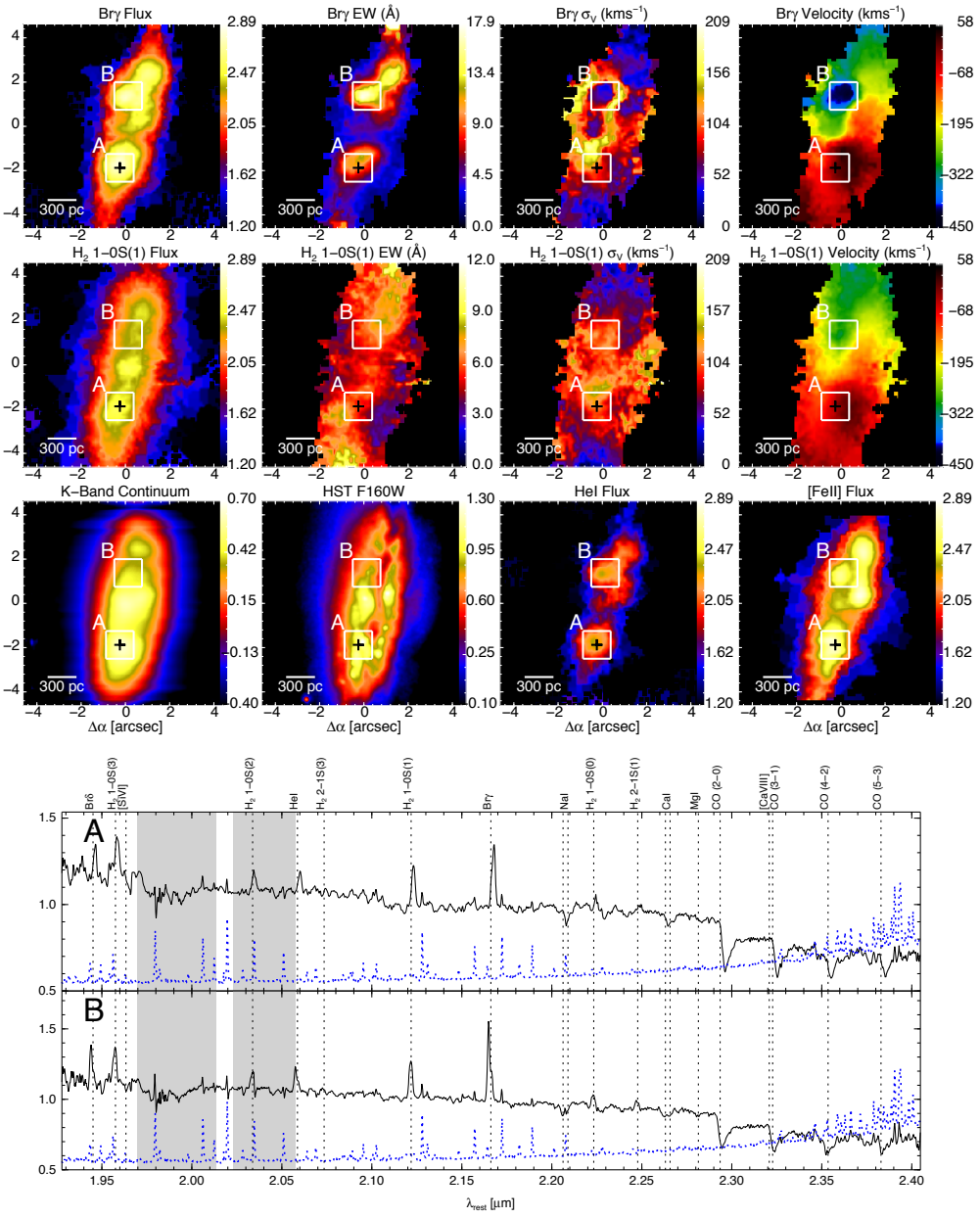

Figure B.1a: NGC 2369 - Top and middle panels are SINFONI observed maps (not corrected from extinction) of the lines Brγ λ2.166μm, and H_2 1-0S(1)λ2.122μm. From left to right: flux, equivalent width, velocity dispersion and velocity. Lower panel shows, from left to right, the K band emission from our SINFONI data, HST/NICMOS F160W continuum image from the archive, HeIλ2.06μm, and [FeII]λ1.64μm emission maps. The brightest spaxel of the SINFONI K band is marked with a cross. The apertures used to extract the spectra at the bottom of the figure are drawn as white squares and labelled accordingly. At the bottom, the two rest-frame spectra extracted from apertures "A" and "B" are in black. The most relevant spectral features are labelled at the top and marked with a dotted line. The sky spectrum is overplotted as a dashed blue line, and the wavelength ranges of the water vapour atmospheric absorptions are marked in light grey.

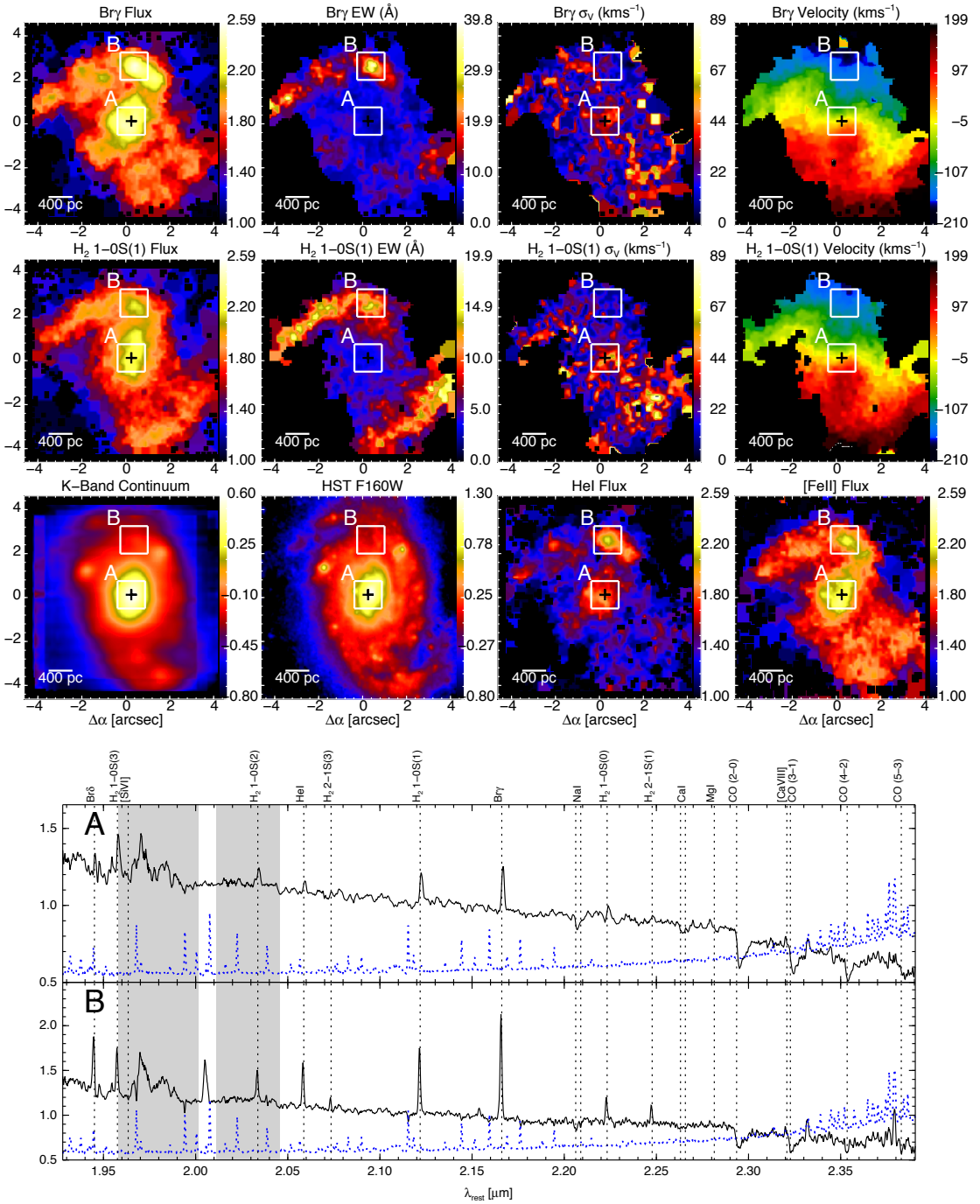

Figure B.1b: NGC 3110 - As Fig. B.1a but for NGC 3110.

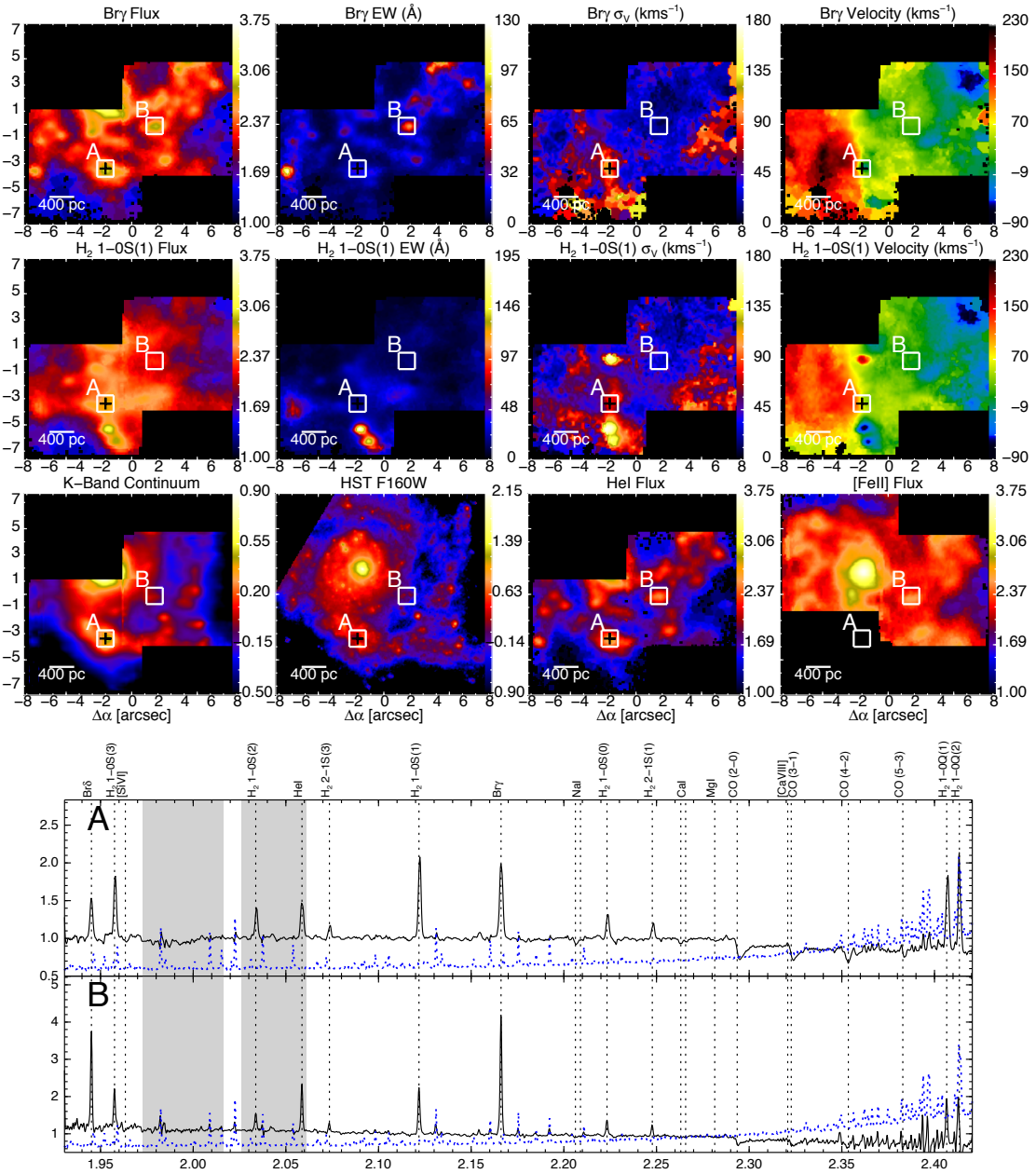

Figure B.1c: NGC 3256 - As Fig. B.1a but for NGC 3256.

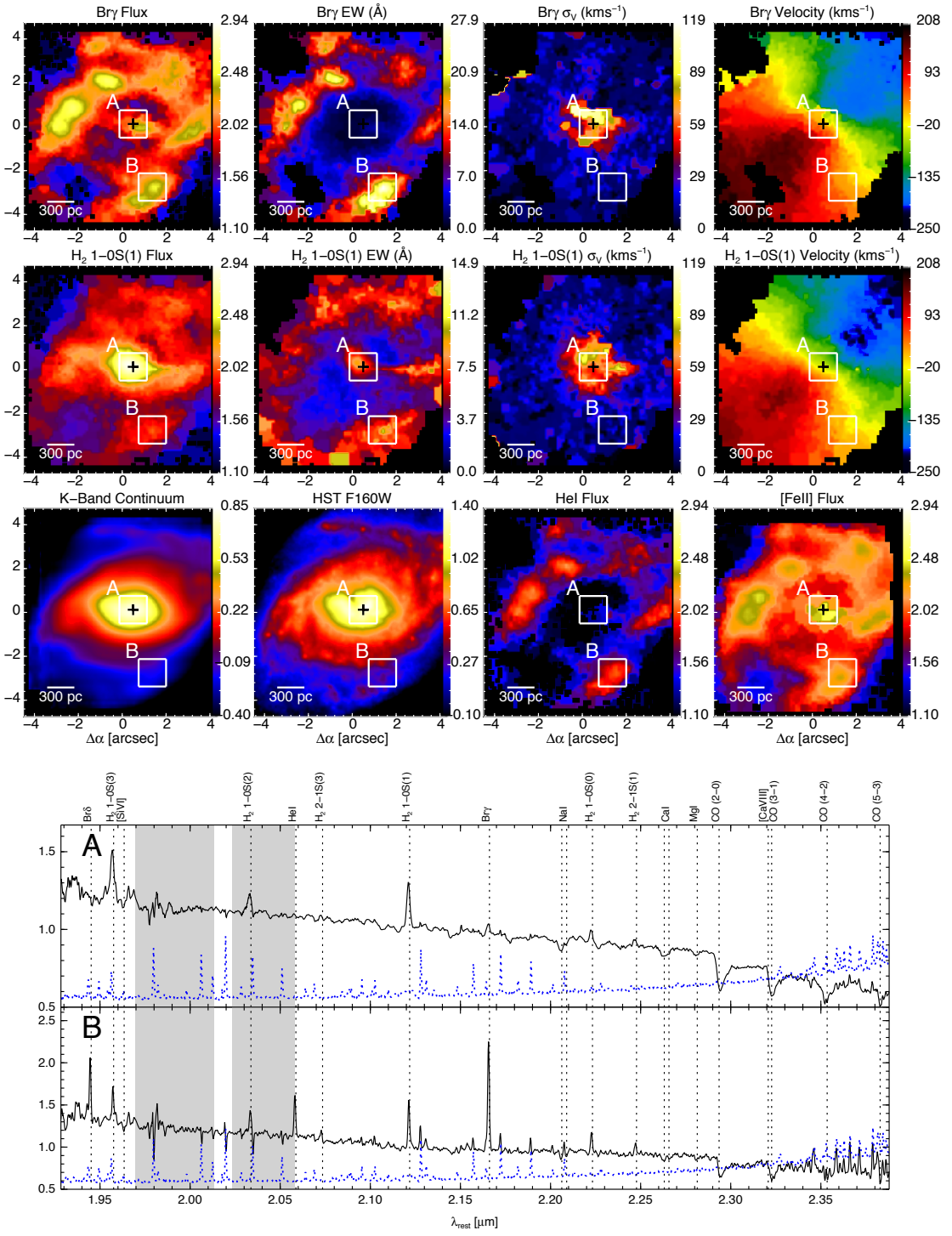

Figure B.1d: ESO 320-G030 - As Fig. B.1a but for ESO 320-G030.

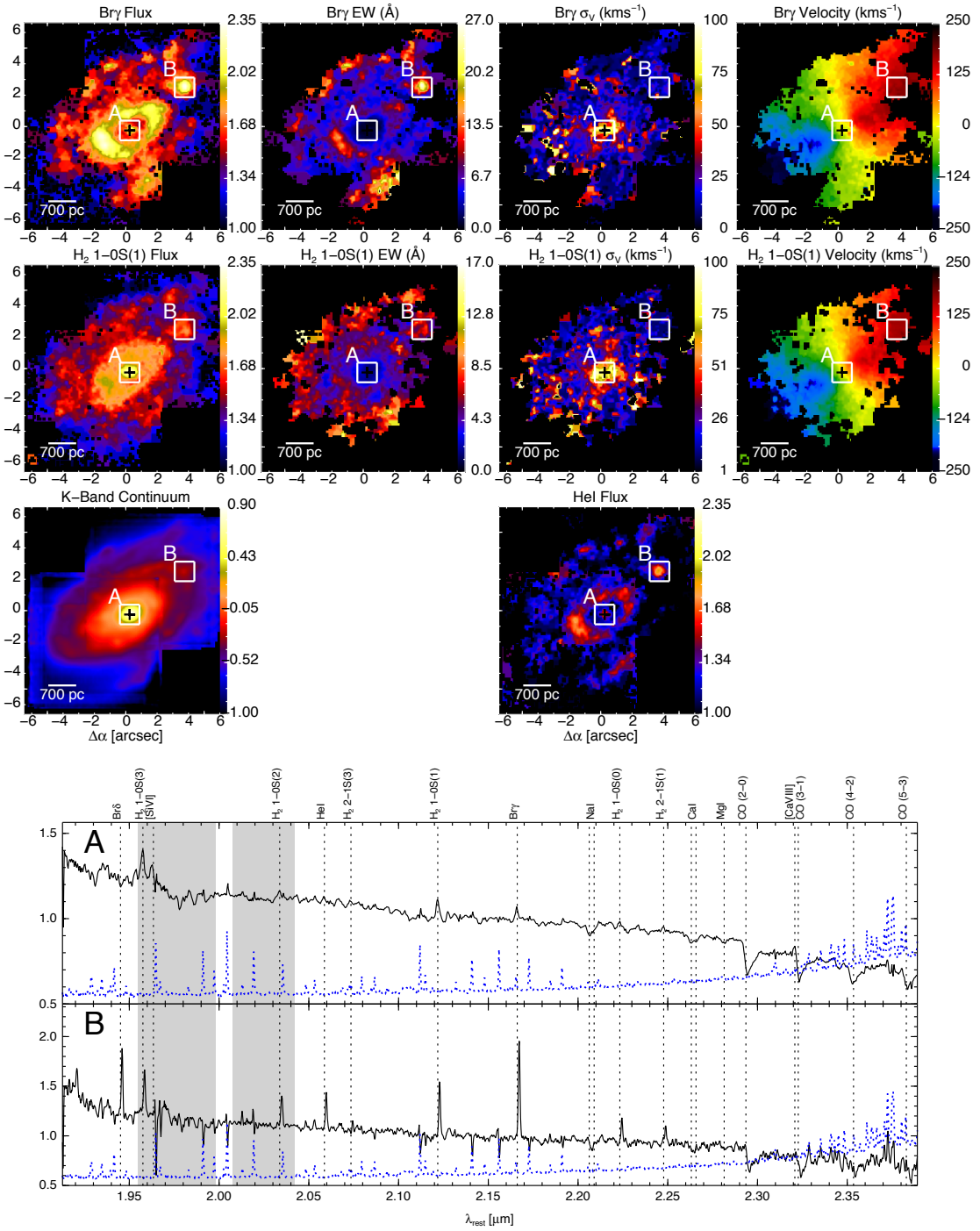

Figure B.1e: IRASF 12115-4656 - As Fig. B.1a but for IRASF 12115-4656.

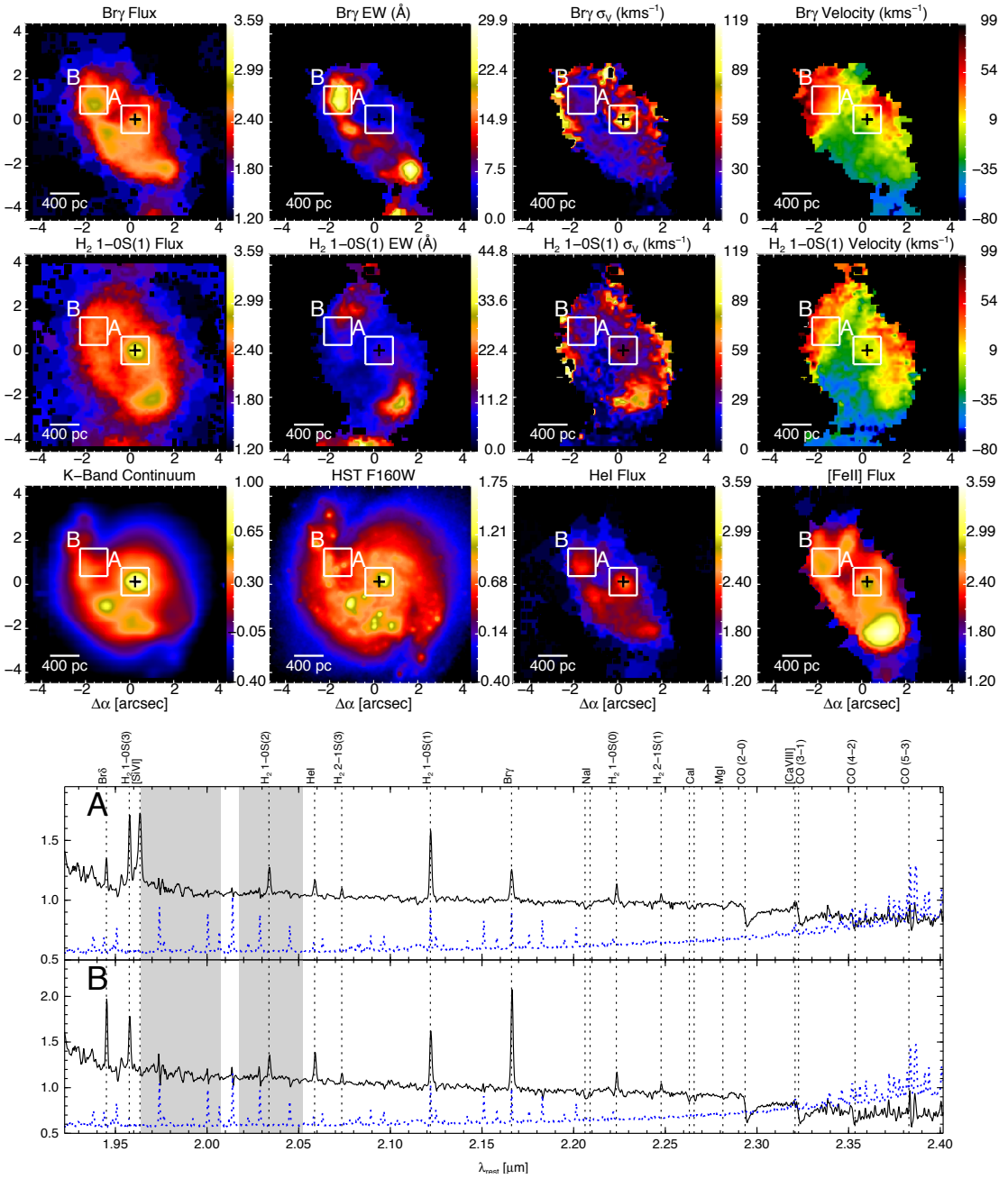

Figure B.1f: NGC 5135 - As Fig. B.1a but for NGC 5135.

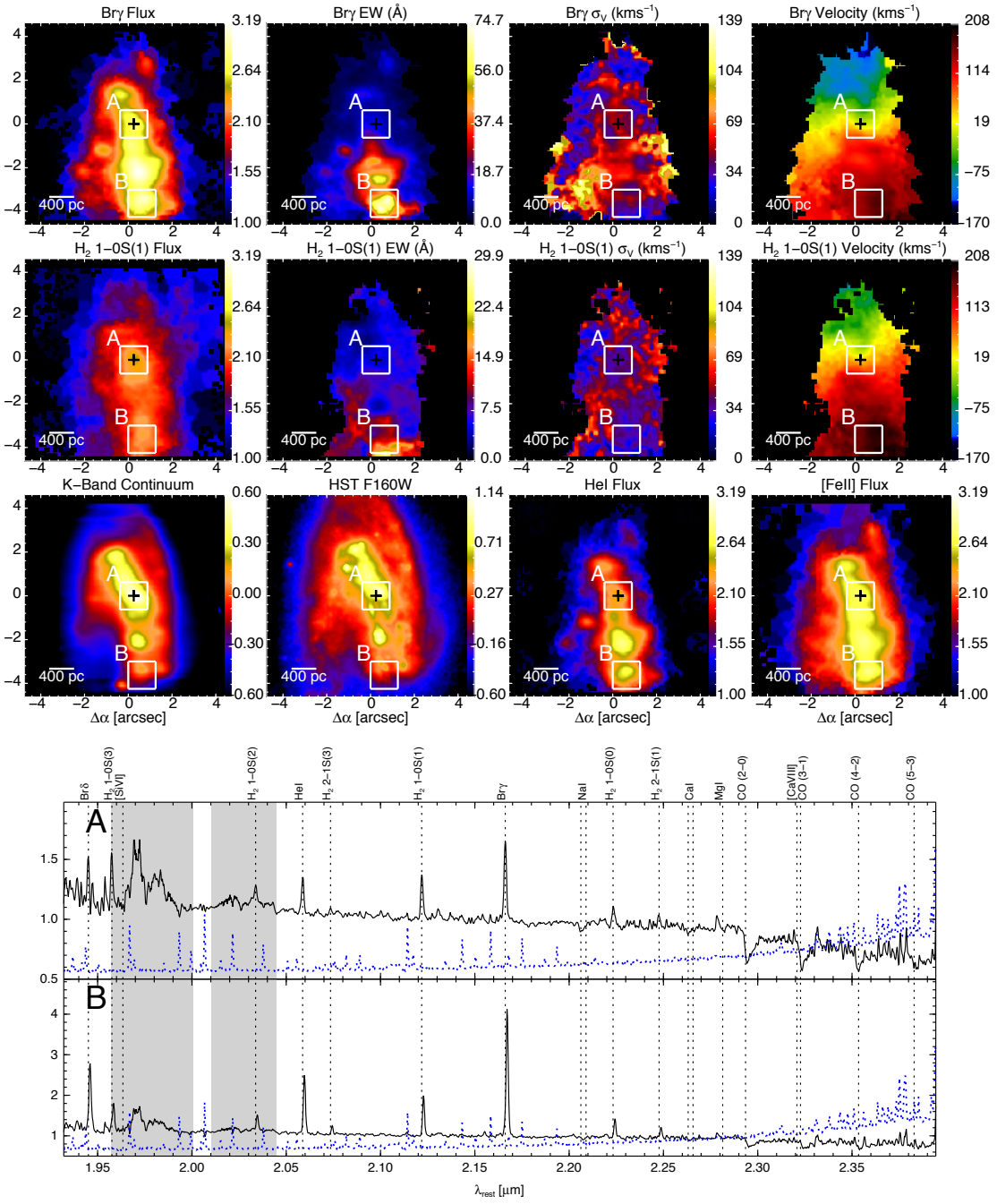

Figure B.1g: IRASF 17138-1017 - As Fig. B.1a but for IRASF 17138-1017.

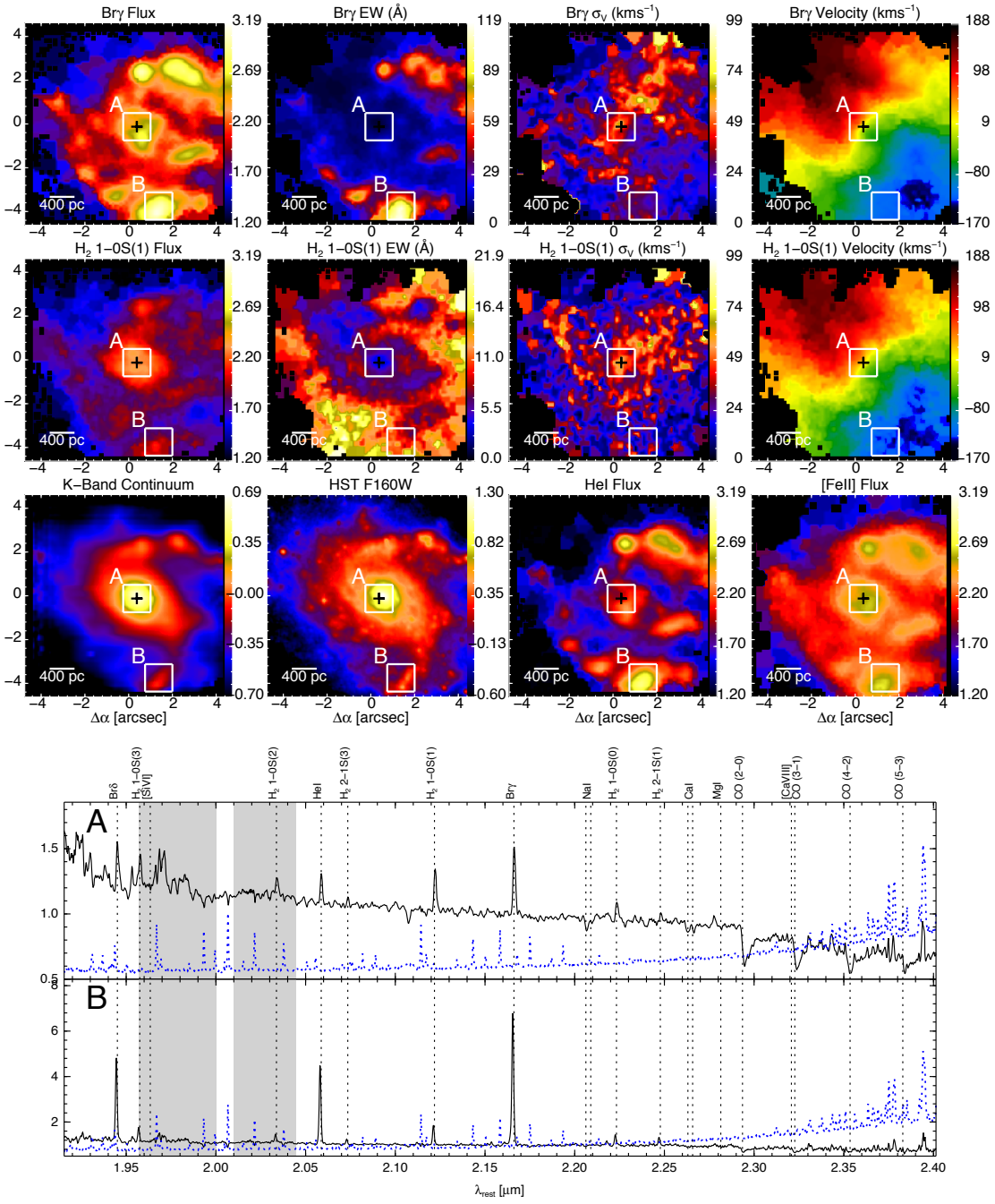

Figure B.1h: IC 4687 - As Fig. B.1a but for IC 4687.

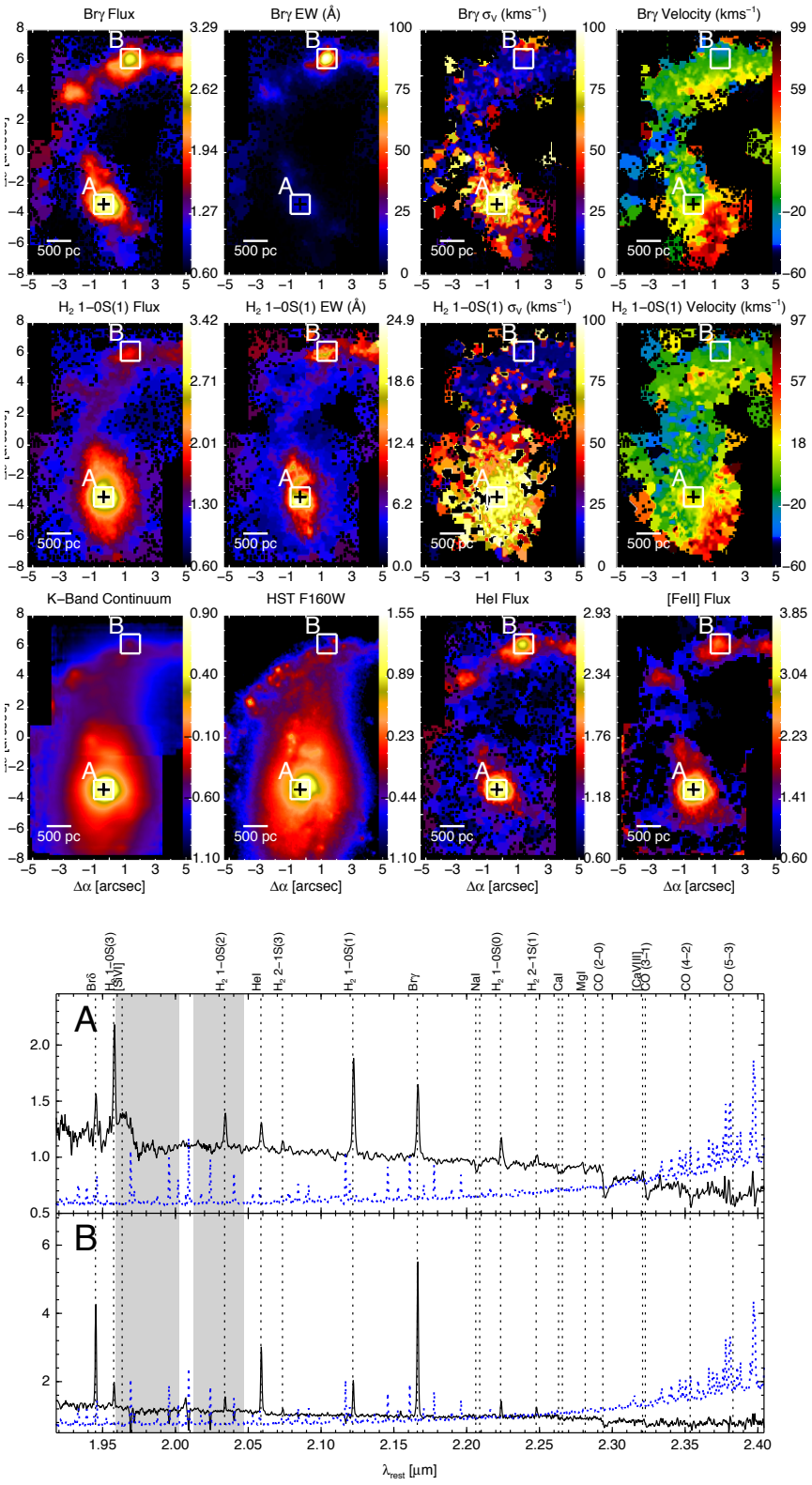

Figure B.1i: NGC 7130 - As Fig. B.1a but for NGC 7130.

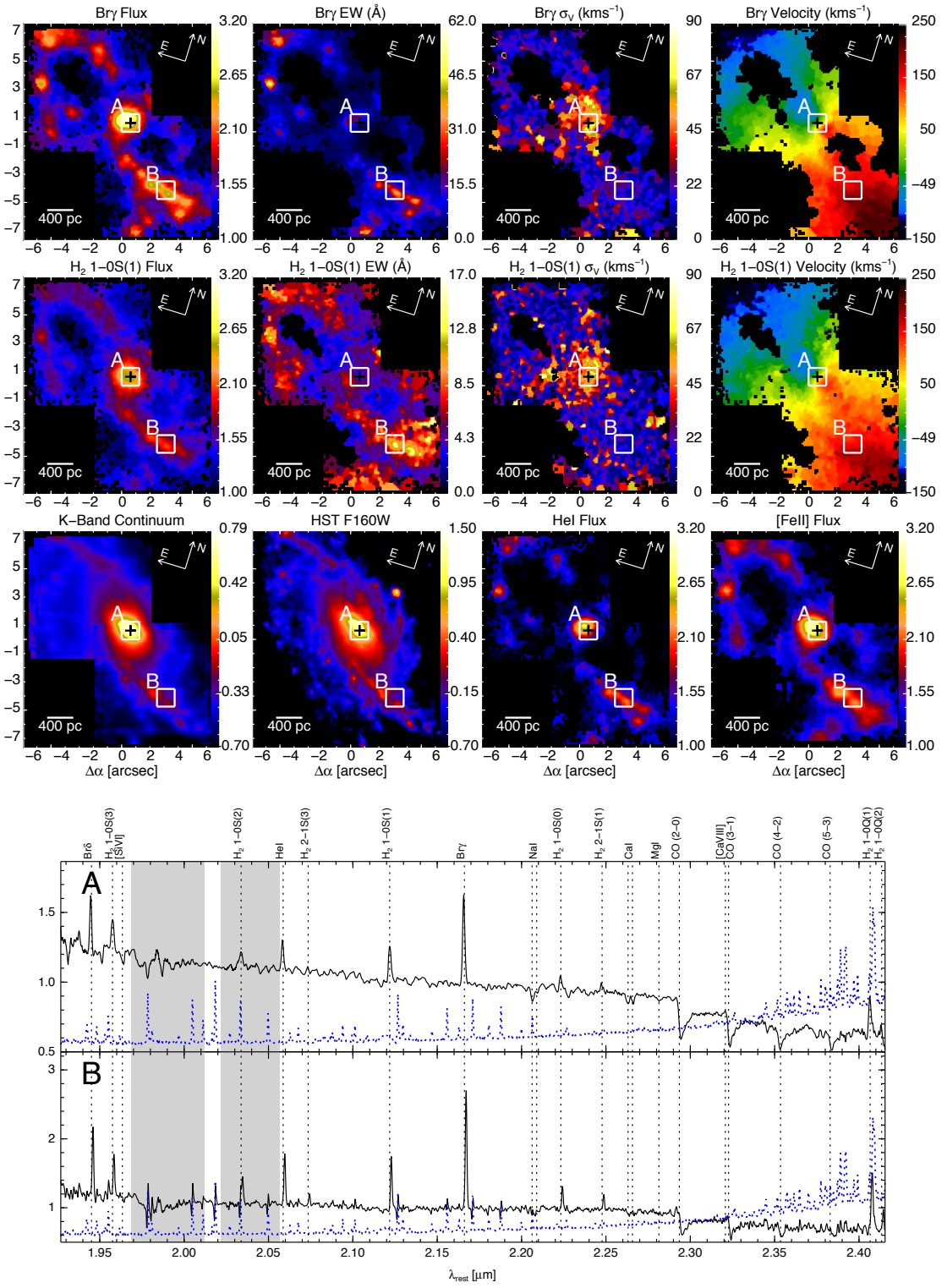

Figure B.1j: IC 5179 - As Fig. B.1a but for IC 5179.

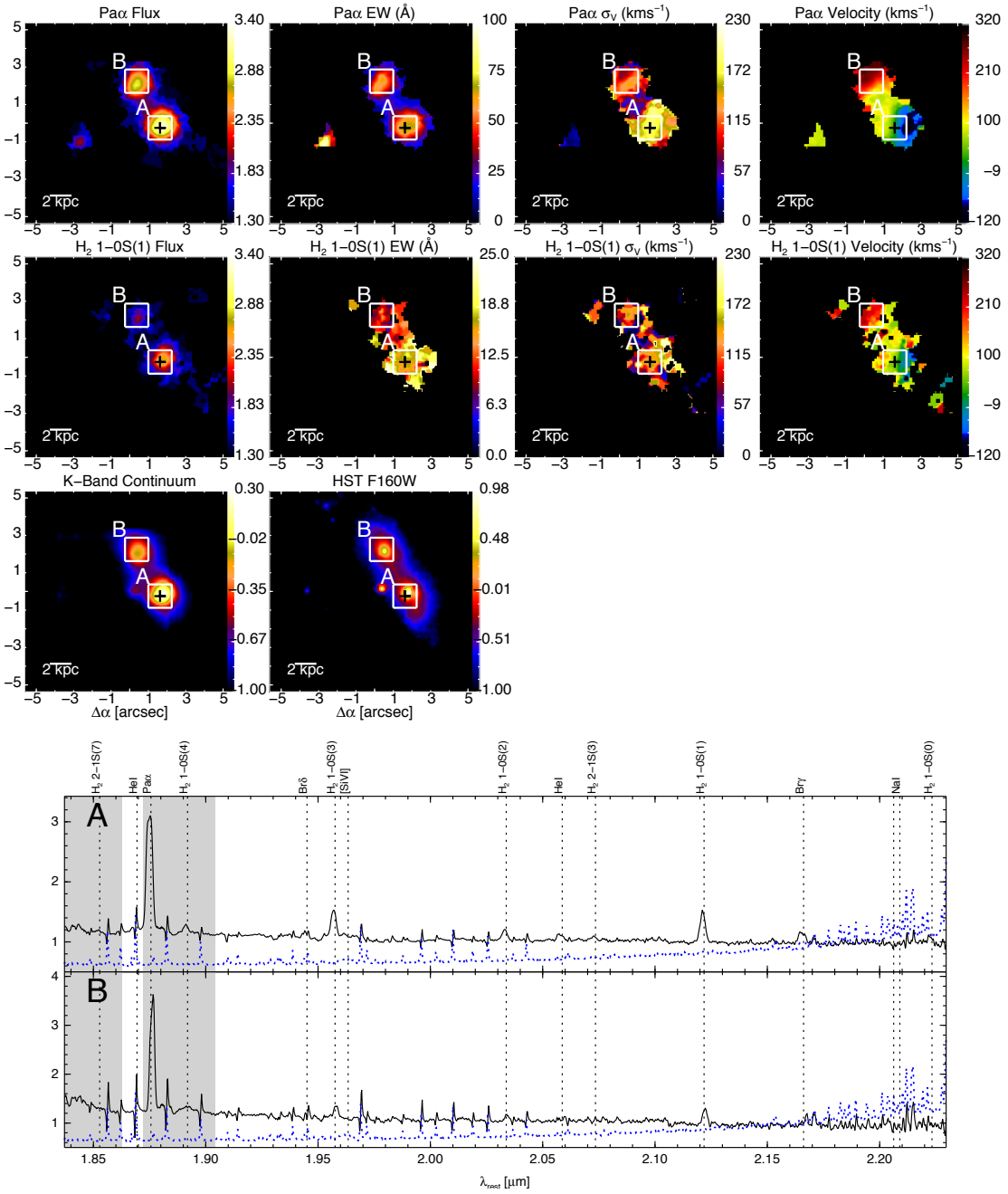

Figure B.2a: IRAS 06206-6315 - Top and middle panels are SINFONI observed maps (not corrected from extinction) of the lines Paα λ1.876μm, and H_2 1-0S(1)λ2.122μm. From left to right: flux, equivalent width, velocity dispersion, and velocity. Lower panel shows, from left to right, the K band emission from our SINFONI data, HST continuum image from the archive, and HeIλ2.06μm (when available). The brightest spaxel of the SINFONI K band is marked with a cross. The apertures used to extract the spectra at the bottom of the figure are drawn as white squares and labelled accordingly. At the bottom, the two rest-frame spectra extracted from apertures "A" and "B" in black. The most relevant spectral features are labelled at the top and marked with a dotted line. The sky spectrum is overplotted as a dashed blue line, and the wavelength ranges of the water vapour atmospheric absorptions are marked in light grey.

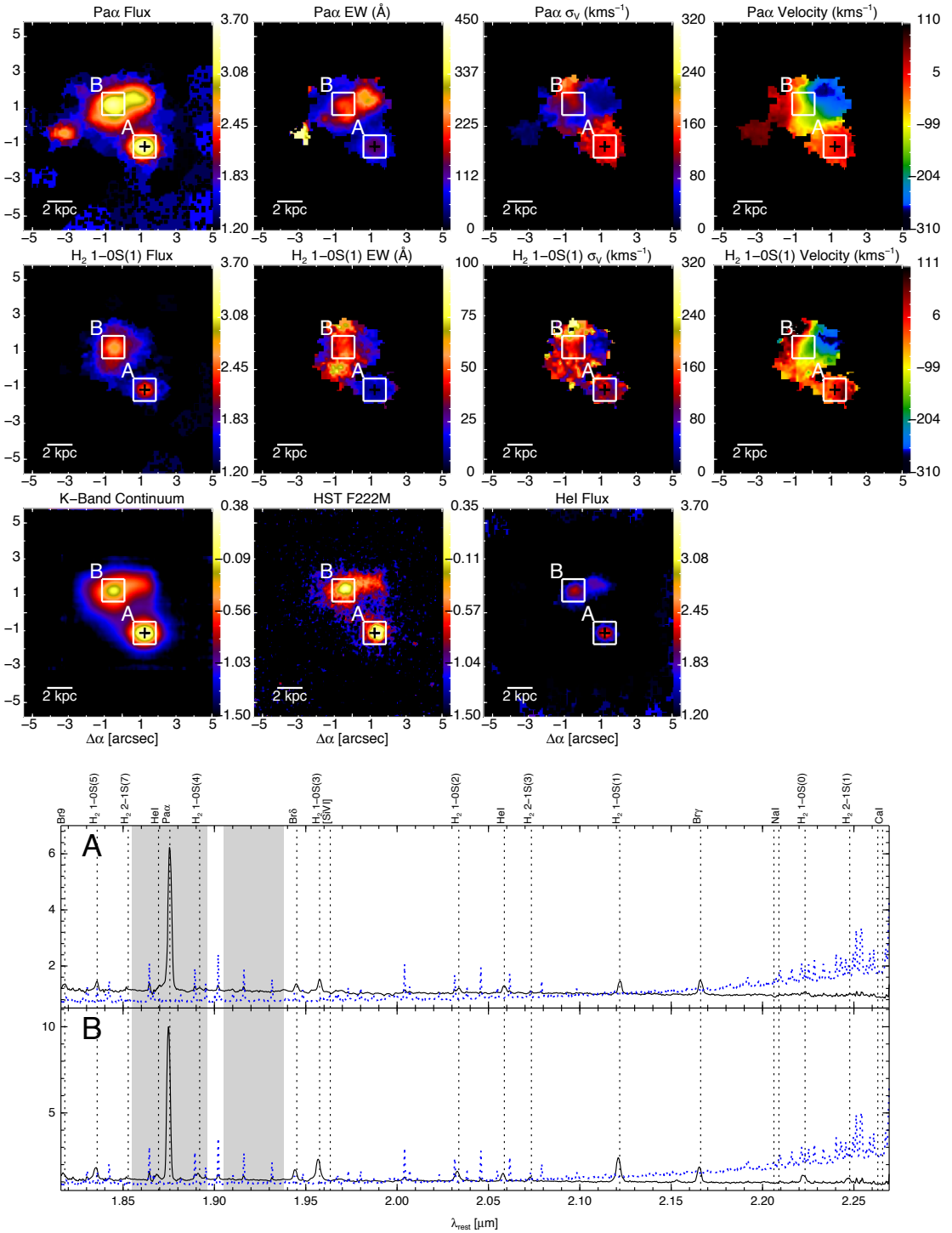

Figure B.2b: IRAS 12112+0305 - As Fig. B.2a but for IRAS 12112+0305.

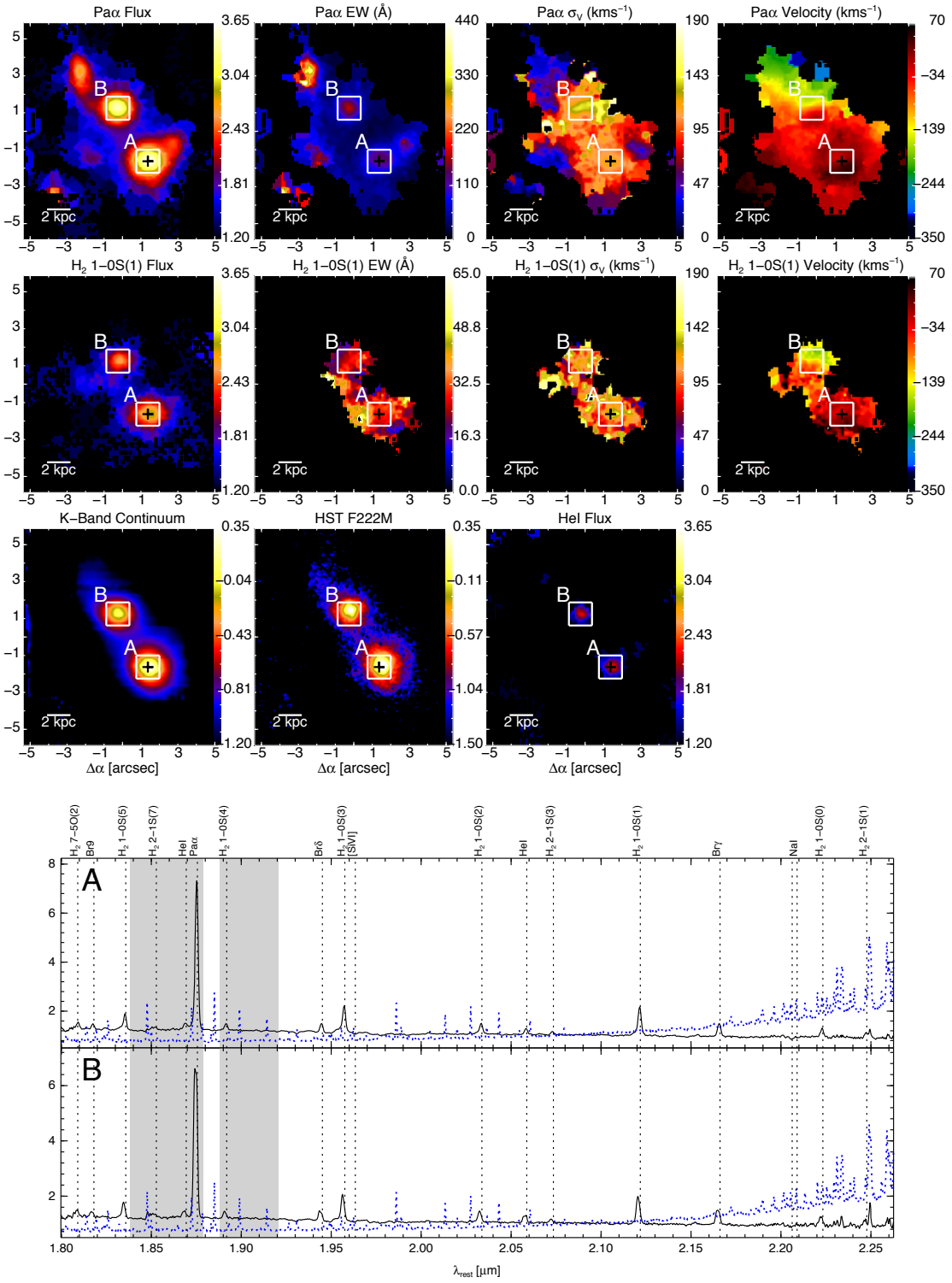

Figure B.2c: IRAS 14348-1447 - As Fig. B.2a but for IRAS 14348-1447.

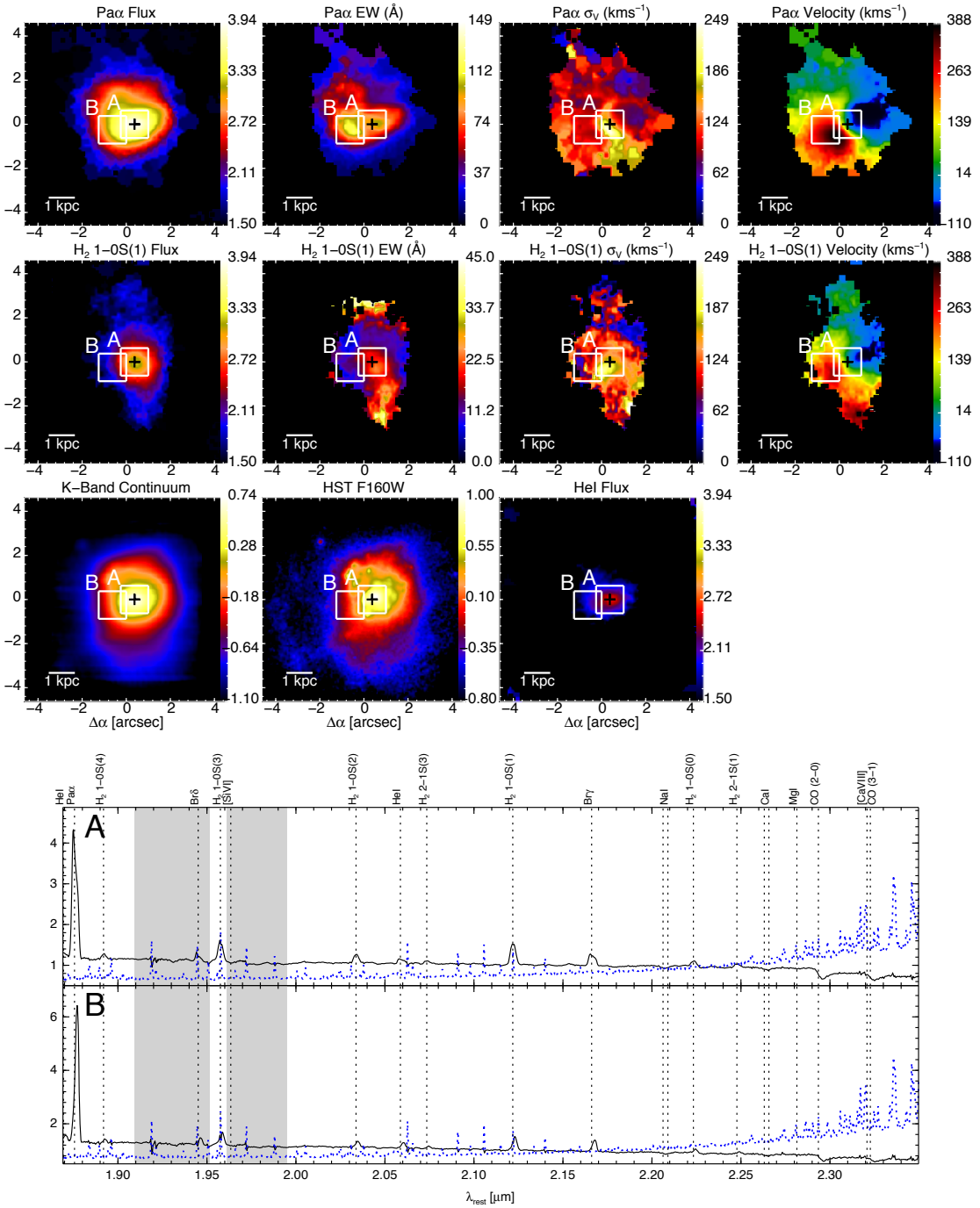

Figure B.2d: IRAS 17208-0014 - As Fig. B.2a but for IRAS 17208-0014.

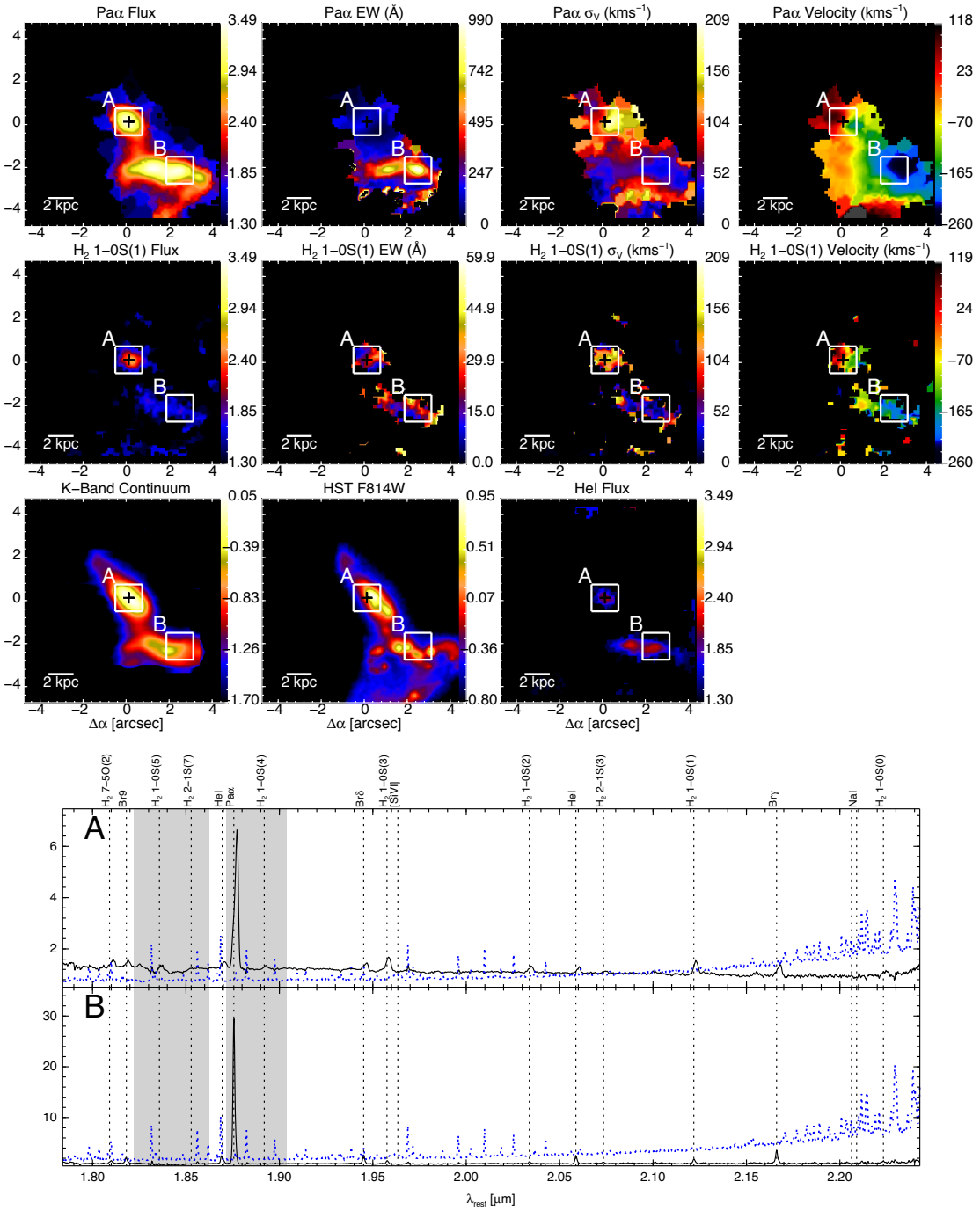

Figure B.2e: IRAS 21130-4446 - As Fig. B.2a but for IRAS 21130-4446.

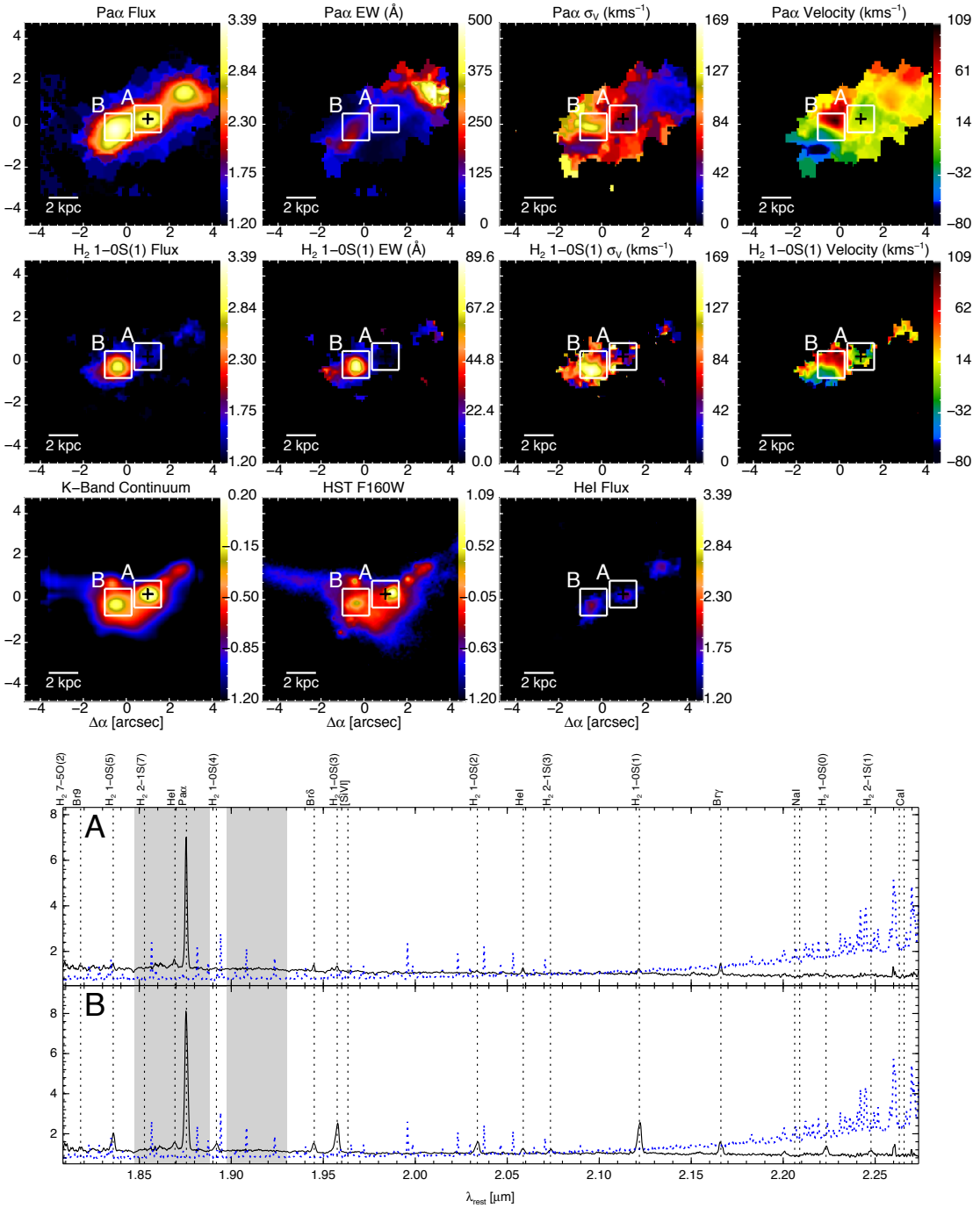

Figure B.2f: IRAS 22491-1808 - As Fig. B.2a but for IRAS 22491-1808.

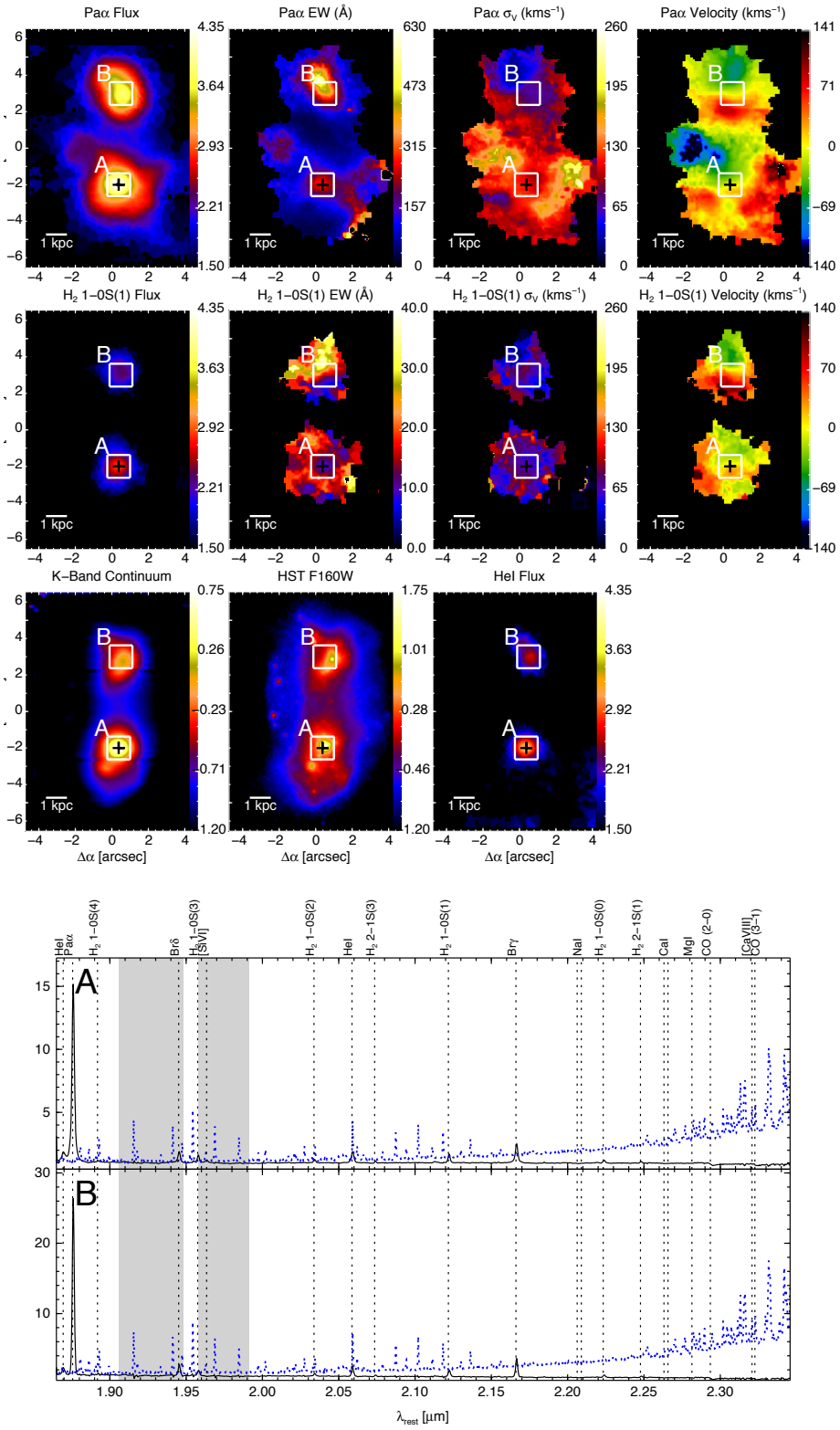

Figure B.2g: IRAS 23128-5919 - As Fig. B.2a but for IRAS 23128-5919.

Appendix C

A_V maps and distributions

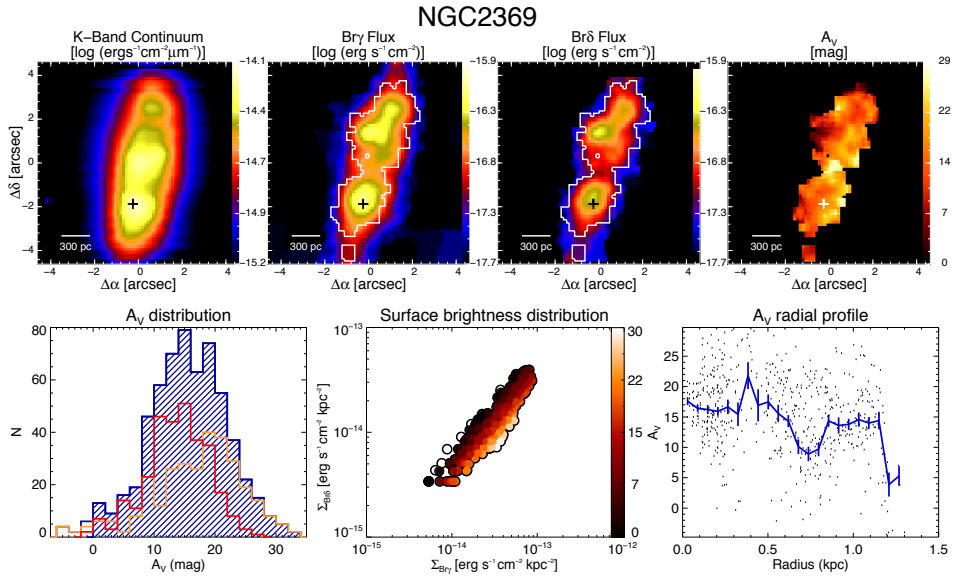

Figure C.1a: NGC 2369 - Top panels show the SINFONI K band continuum emission, the observed maps (not corrected from extinction) of the lines Brγ λ2.166μm and Brδ λ1.945μm, together with the A_V map. The white contour englobes those spaxels above S/N = 4 considered to build the A_V map and distribution. The brightest spaxel of the K band continuum is marked with a plus symbol (+), and has been used as reference to obtain the radial profile in the bottom right panel. The secondary nucleus, if present, is marked with a cross ($\times$). Bottom left panel shows the the Av distribution of all valid spaxels (blue histogram) and the distributions of the those spaxels above (red) and below (yellow) the median value of the Brδ S/N distribution. The relationship between the surface brightness of the lines and the A_V is shown in the central panel, where the points with $A_V<0$ are outlined with a black contour. Finally, the radial distribution of the extinction is shown in the bottom right panel, where the blue line represents the mean value of A_V for different radial bins and its error. The bins are obtained as the 1/30 of the total radial coverage of the map.

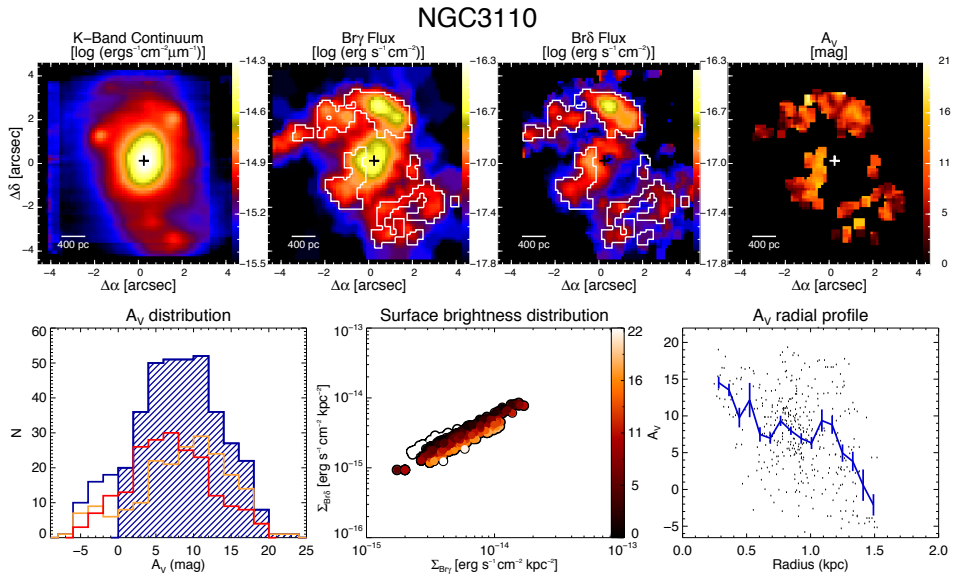

Figure C.1b: NGC 3110 - Same as Fig. C.1a but for NGC 3110.

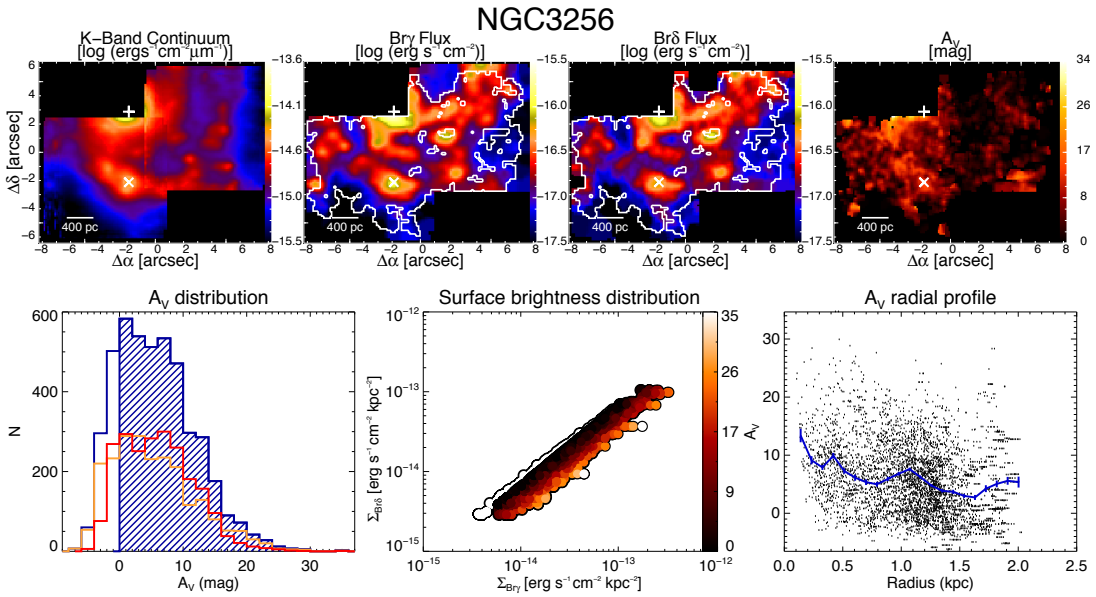

Figure C.1c: NGC 3256 - Same as Fig. C.1a but for NGC 3256. Please note that the central spaxel lays outside the FoV since the nucleus was not observed in K-band. See text and Chapter 4 for further details.

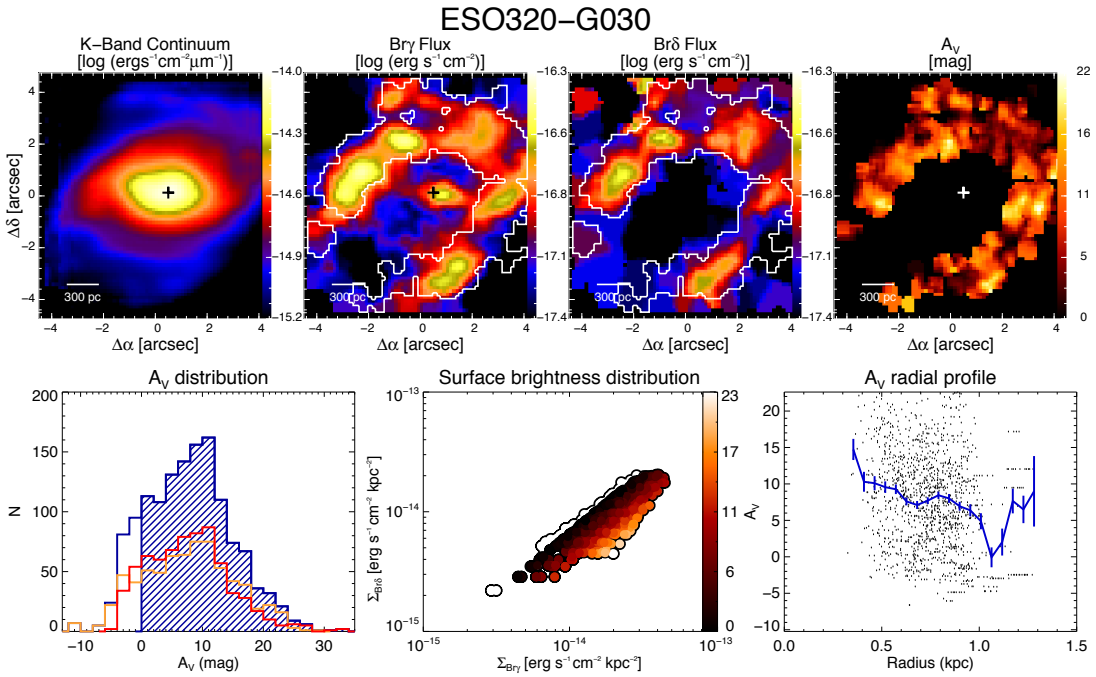

Figure C.1d: ESO 320-G030 - Same as Fig. C.1a but for ESO 320-G030.

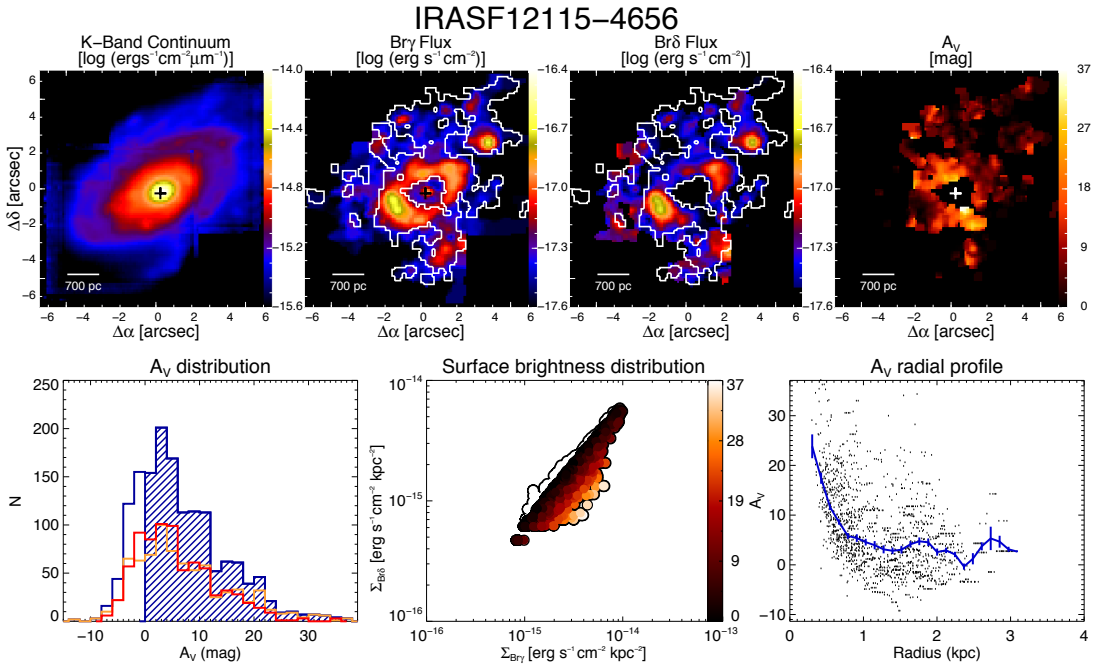

Figure C.1e: IRASF 12115-4656 - Same as Fig. C.1a but for IRASF 12115-4656.

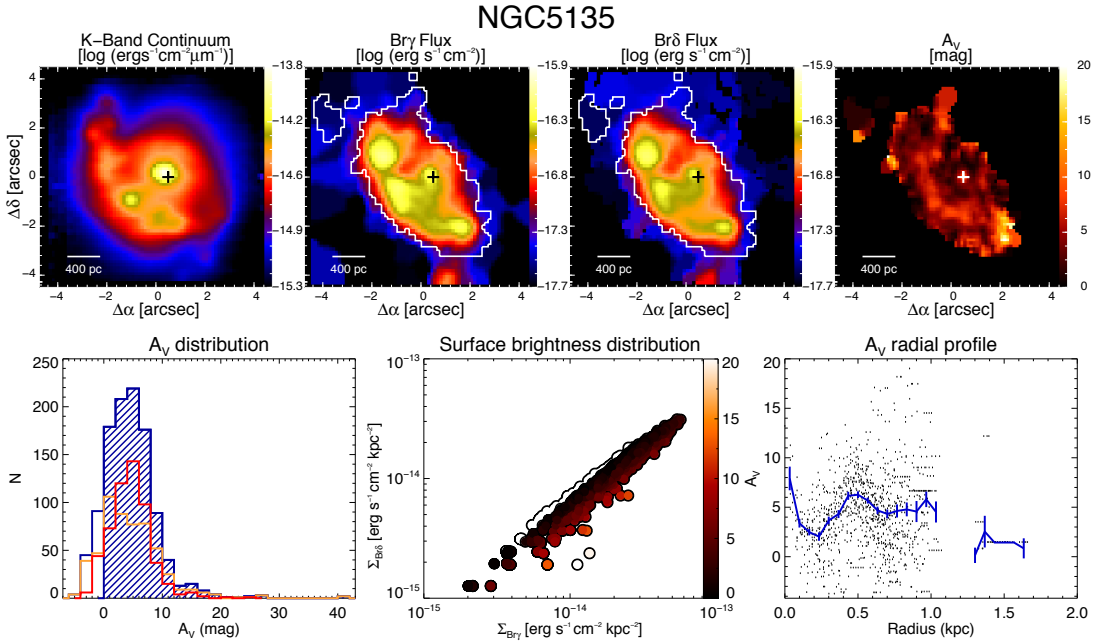

Figure C.1f: NGC 5135 - Same as Fig. C.1a but for NGC 5135.

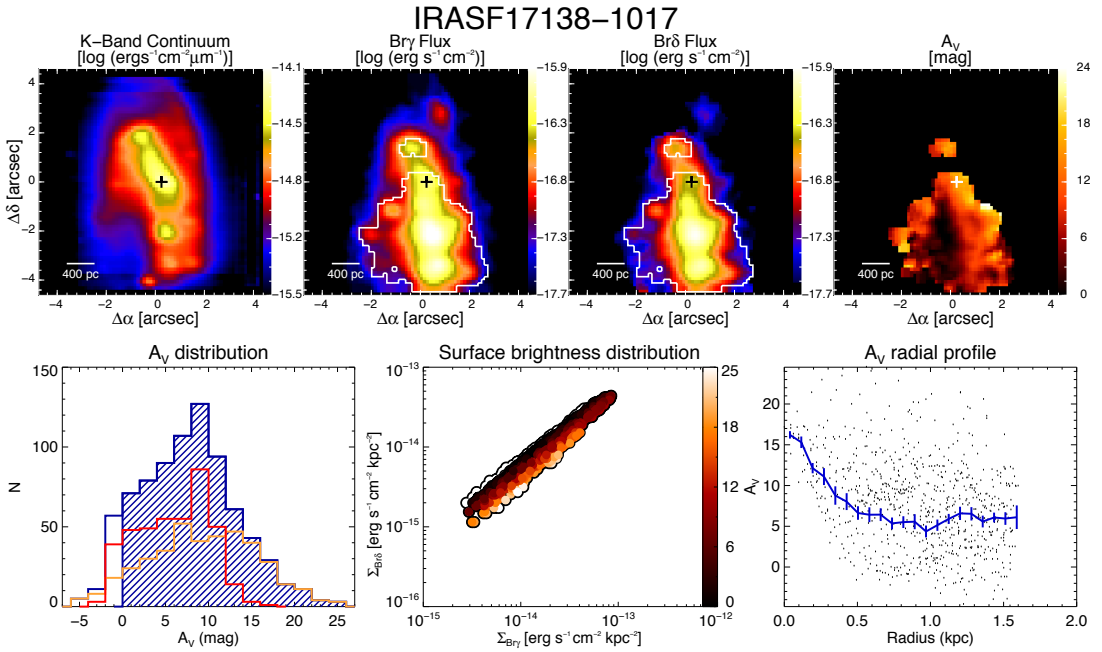

Figure C.1g: IRASF 17138-1017 - Same as Fig. C.1a but for IRASF 17138-1017.

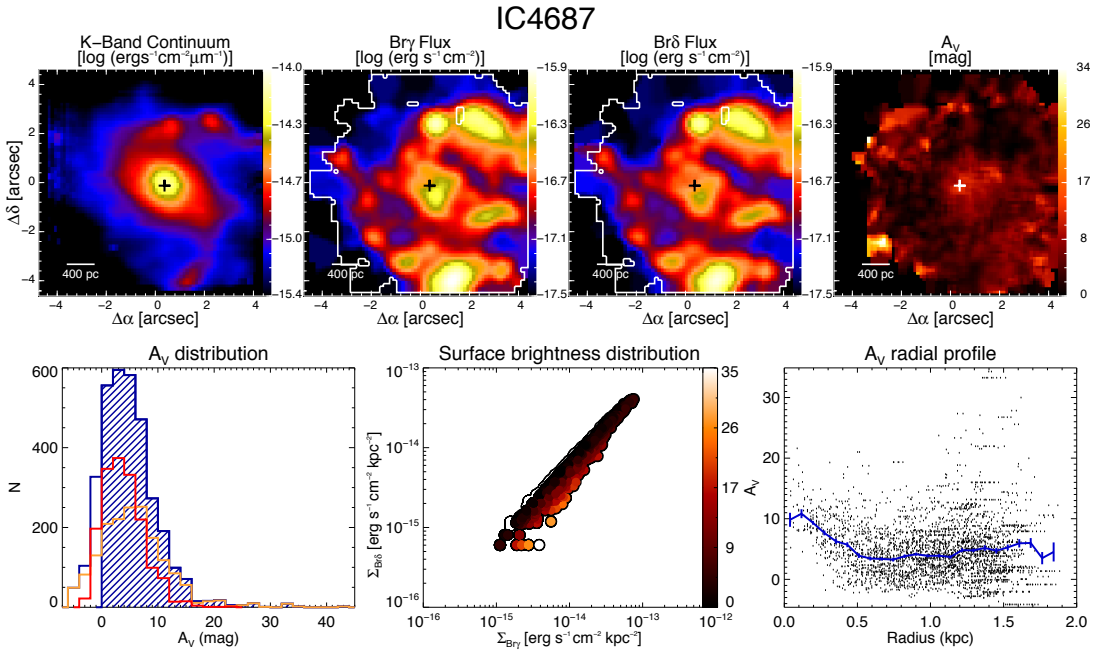

Figure C.1h: IC 4687 - Same as Fig. C.1a but for IC 4687.

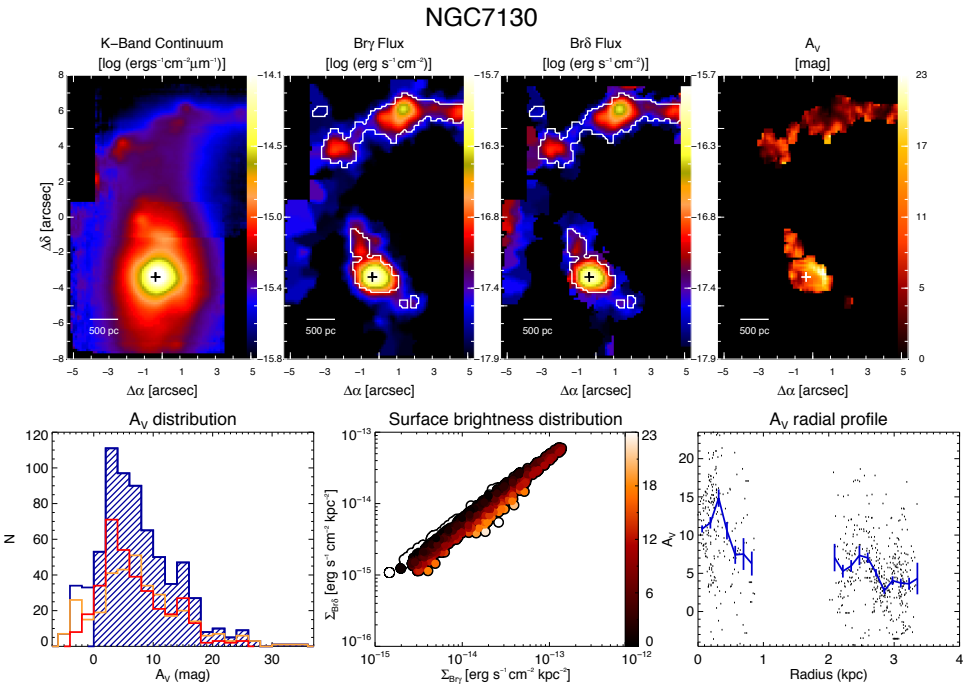

Figure C.1i: NGC 7130 - Same as Fig. C.1a but for NGC 7130.

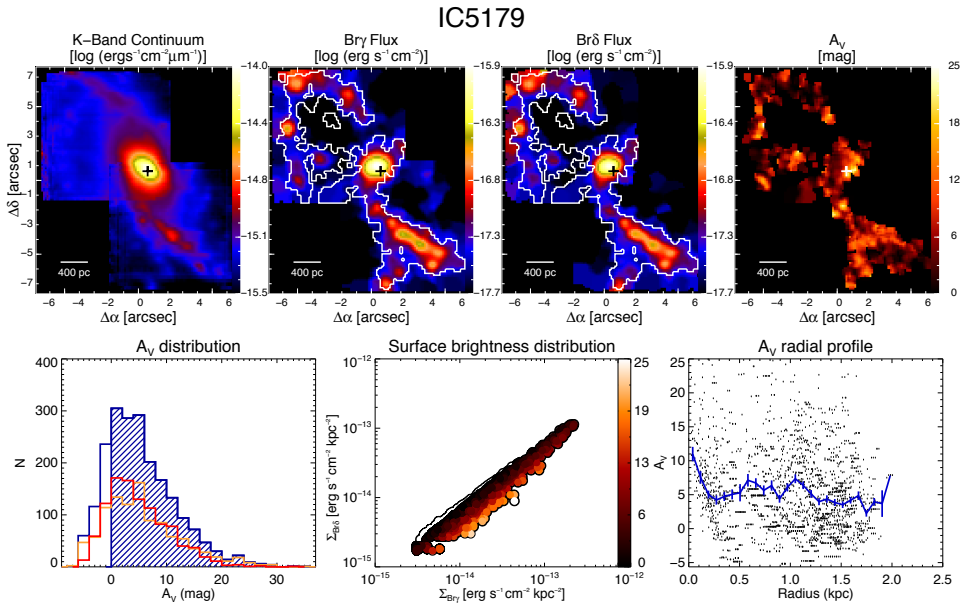

Figure C.1j: IC 5179 - Same as Fig. C.1a but for IC 5179.

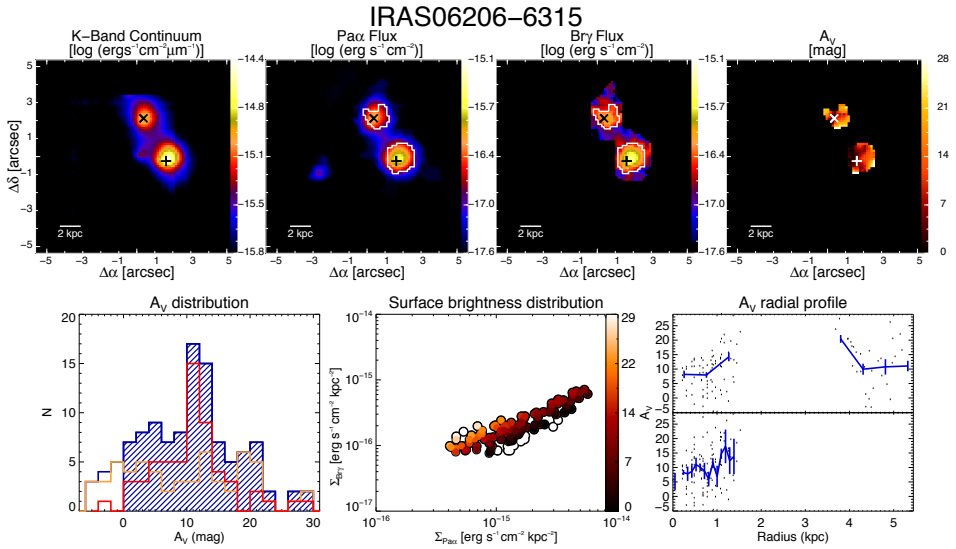

Figure C.2a: IRAS 06206-6315 - Top panels show the SINFONI K band continuum emission, the observed maps (not corrected from extinction) of the lines Paα λ1.876μm and Brγ λ2.166μm, together with the A_V map. The white contour englobes those spaxels above S/N = 4 considered to build the A_V map and distribution. The brightest spaxel of the K band continuum is marked with a plus symbol (+), and has been used as reference to obtain the radial profile in the bottom right panel. The secondary nucleus, if present, is marked with a cross (×). Bottom left panel shows the Av distribution of all valid spaxels (blue histogram) and the distributions of the those spaxels above (red) and below (yellow) the median value of the Brγ S/N distribution. The relationship between the surface brightness of the lines and the A_V is shown in the central panel, where the points with A_V<0 are outlined with a black contour. Finally, the radial distribution of the extinction is shown in the bottom right panel, where the blue line represents the mean value of A_V for different radial bins and its error. The bins are obtained as the 1/30 of the total radial coverage of the map. For those objects with multiple components, the top inset shows the A_V radial profile of the system taking the main nucleus as the centre, whereas the bottom subpanel shows the radial profile obtained by extracting the profiles of each component separately and plotting them in the same reference frame.

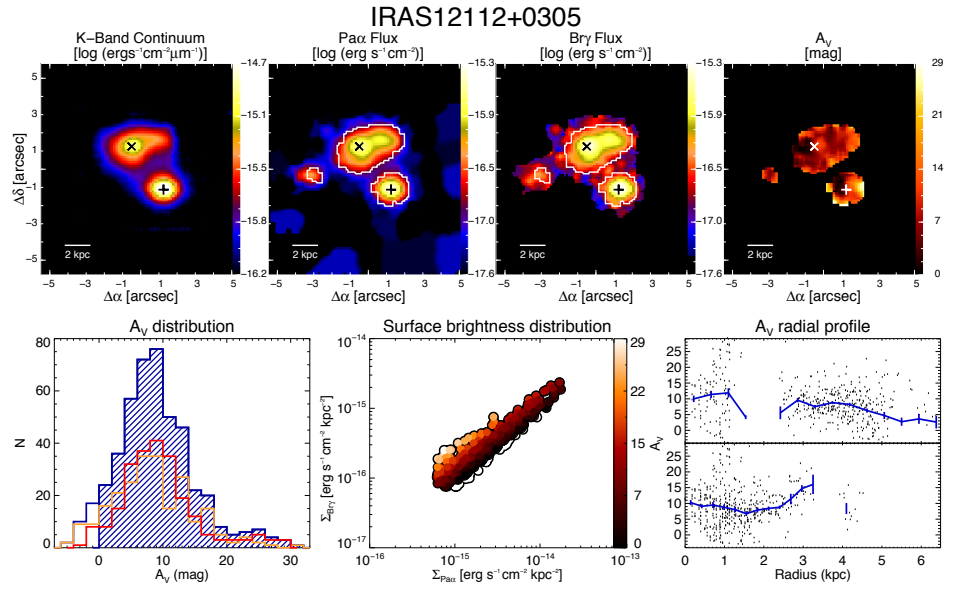

Figure C.2b: IRAS 12112+0305 - Same as Fig. C.2a but for IRAS 12112+0305.

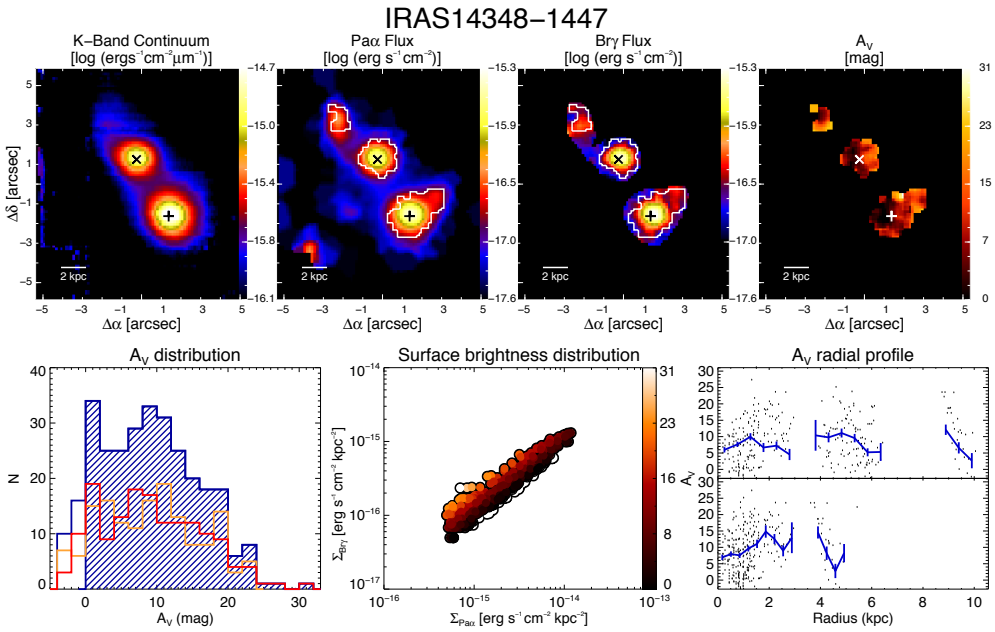

Figure C.2c: IRAS 14348-1447 - Same as Fig. C.2a but for IRAS 14348-1447.

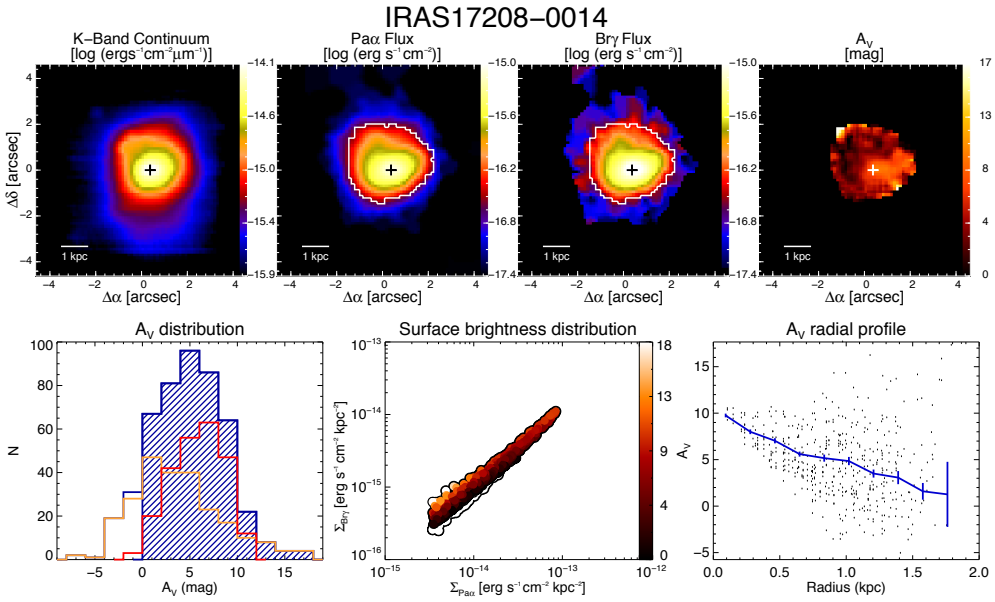

Figure C.2d: IRAS 17208-0014 - Same as Fig. C.2a but for IRAS 17208-0014.

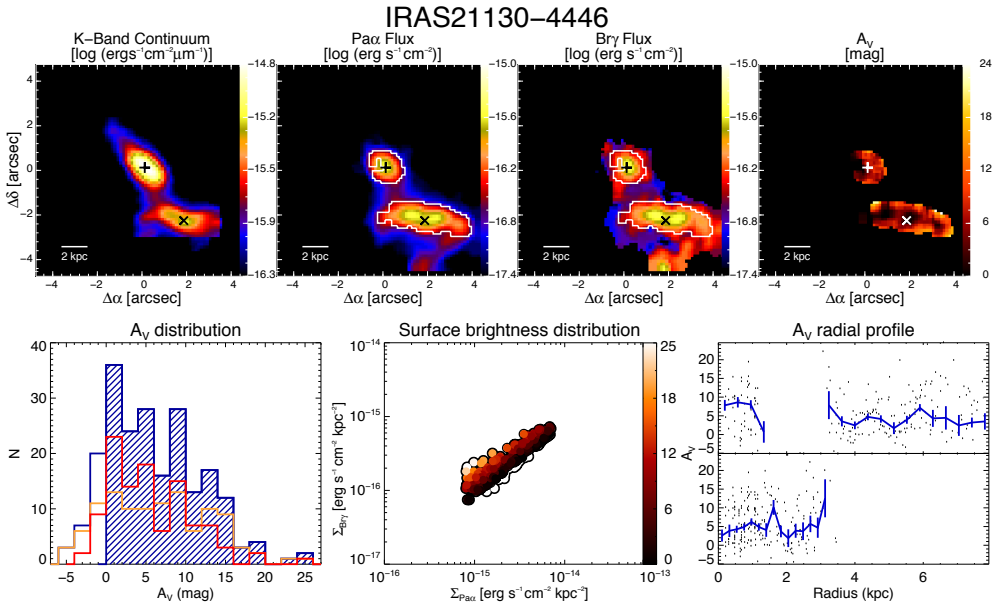

Figure C.2e: IRAS 21130-4446 - Same as Fig. C.2a but for IRAS 21130-4446.

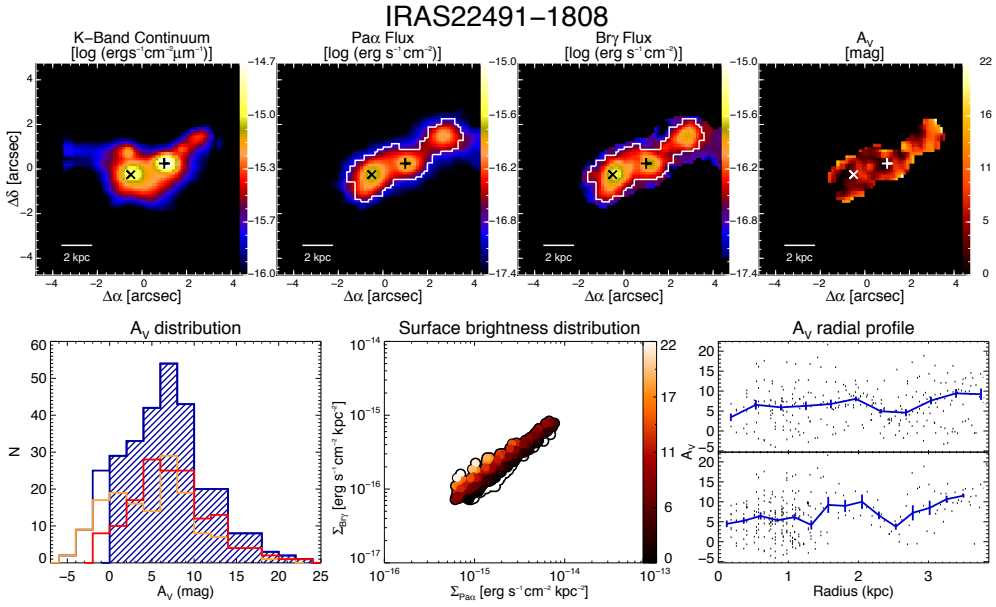

Figure C.2f: IRAS 22491-1808 - Same as Fig. C.2a but for IRAS 22491-1808.

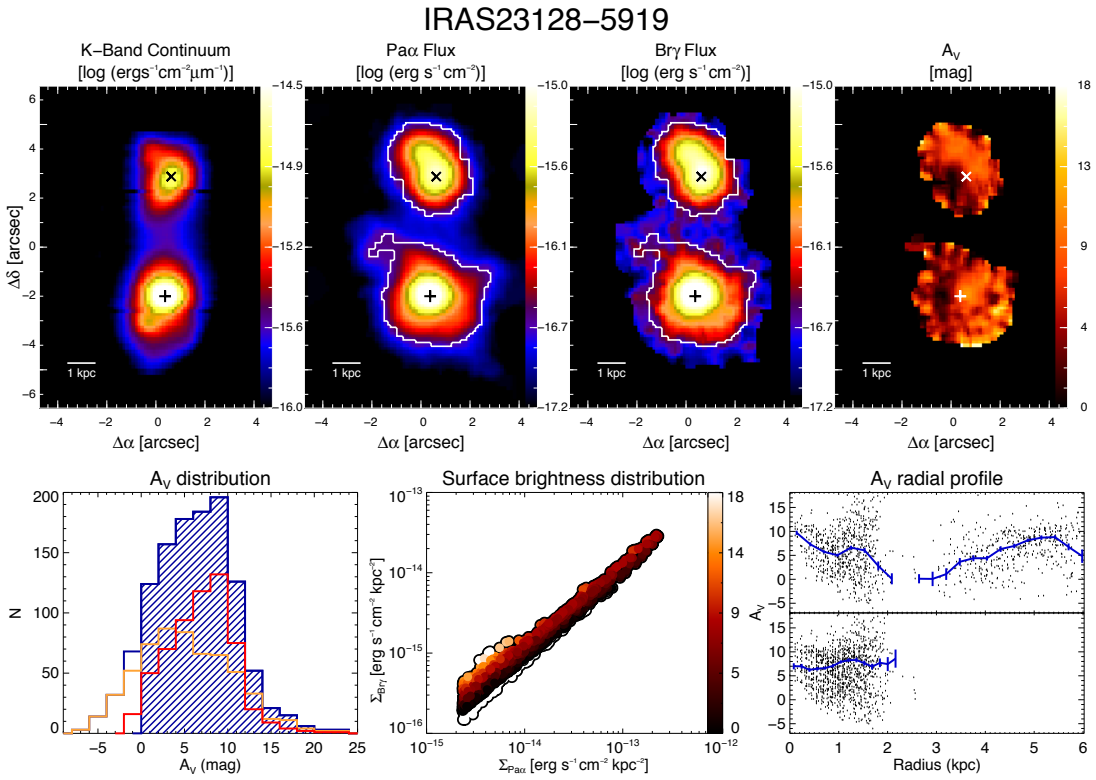

Figure C.2g: IRAS 23128-5919 - Same as Fig. C.2a but for IRAS 23128-5919.

Appendix D

Σ_{SFR} maps and distributions

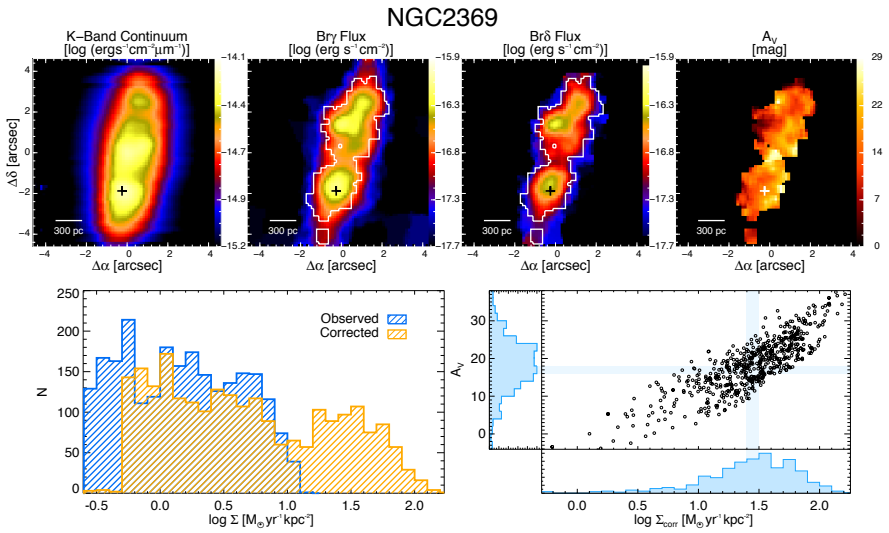

Figure D.1a: NGC 2369 - Top panels show the A_V map derived from the Brγ λ2.166μm and Brδ λ1.945μm line ratio, the observed maps of the Brγ emission, together with the star-formation rate surface density (Σ_{SFR}) map, corrected from extinction. The nucleus and Brγ peak (see Chapter 6) are marked with a plus symbol (+) and a diamond ($\Diamond$), respectively. Bottom left panel shows the observed (blue histogram) and corrected from extinction (yellow histogram) Σ_{SFR} spaxel-by-spaxel distributions. The relationship between the corrected Σ_{SFR} values and the A_V is shown in the bottom right panel only for those points with a spaxel-by-spaxel correction of the extinction. The blue histograms show the projected distribution onto each axis, and are arbitrarily normalised, whereas the blue lines are the median of each distribution.

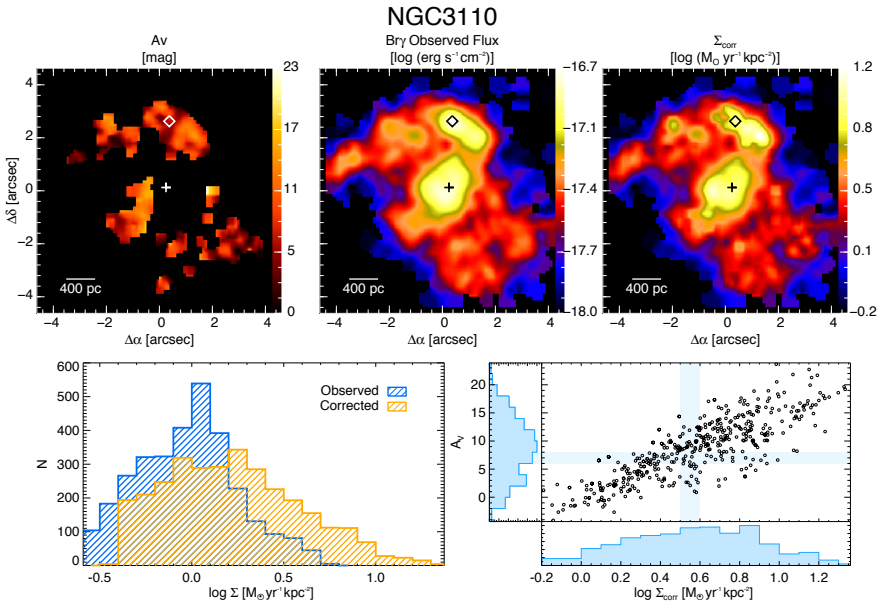

Figure D.1b: NGC 3110 - Same as Fig. D.1a but for NGC 3110.

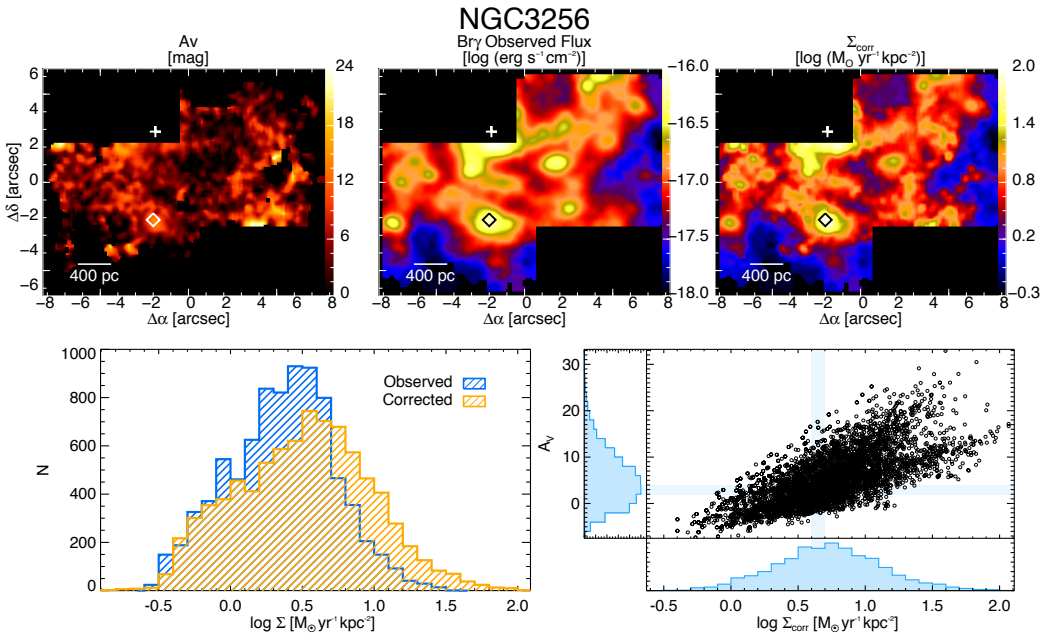

Figure D.1c: NGC 3256 - Same as Fig. D.1a but for NGC 3256. Please note that the central spaxel lays outside the FoV since the nucleus was not observed in K-band. See Chapter 4 for further details.

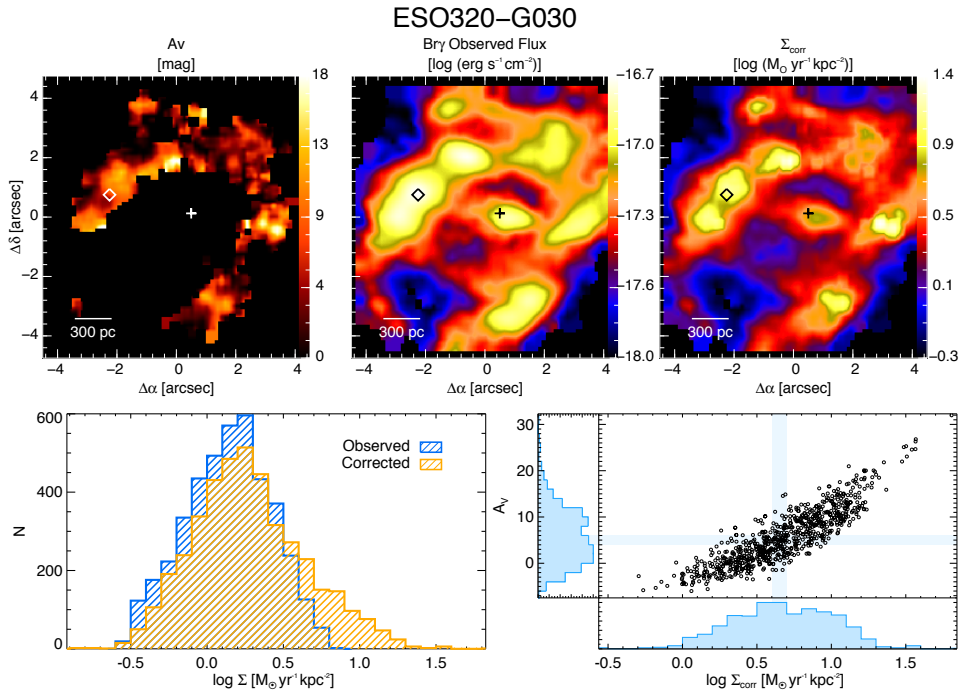

Figure D.1d: ESO 320-G030 - Same as Fig. D.1a but for ESO 320-G030.

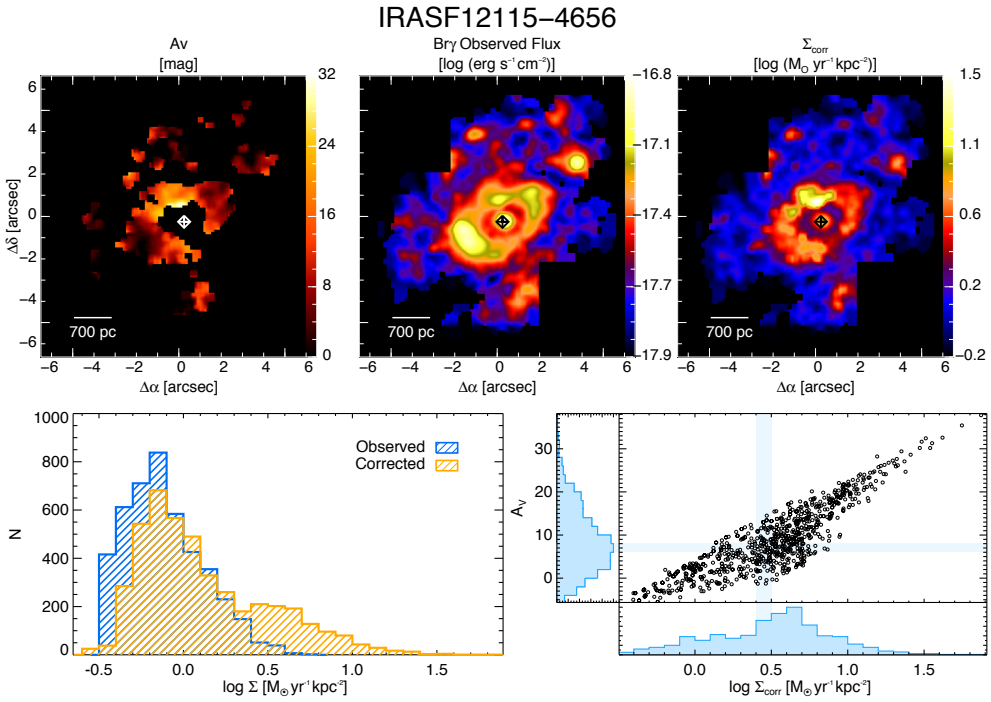

Figure D.1e: IRASF 12115-4656 - Same as Fig. D.1a but for IRASF 12115-4656.

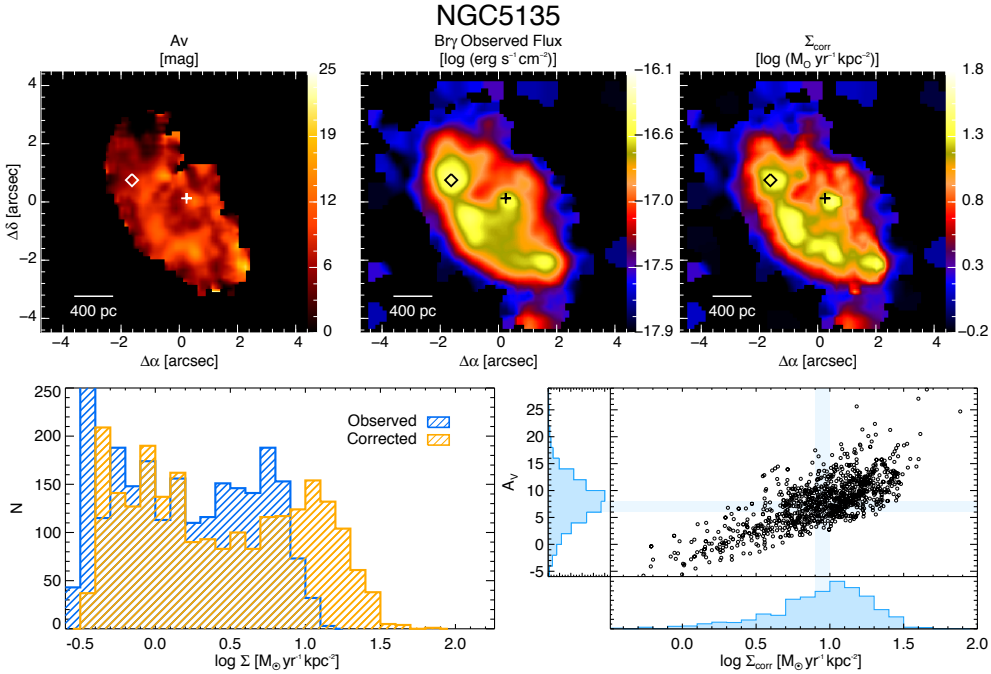

Figure D.1f: NGC 5135 - Same as Fig. D.1a but for NGC 5135.

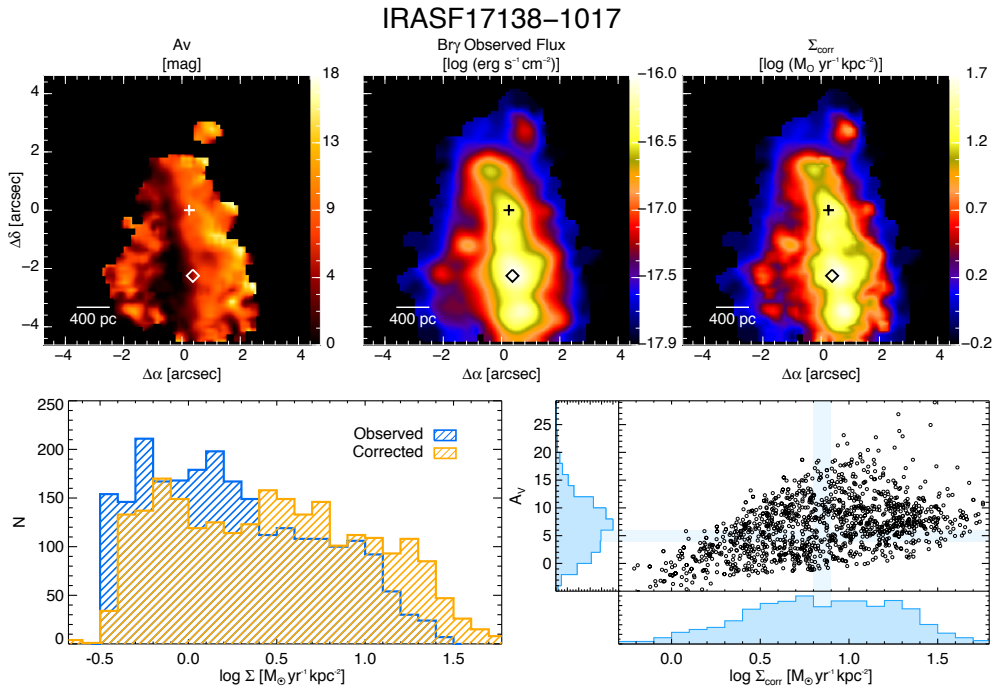

Figure D.1g: IRASF 17138-1017 - Same as Fig. D.1a but for IRASF 17138-1017.

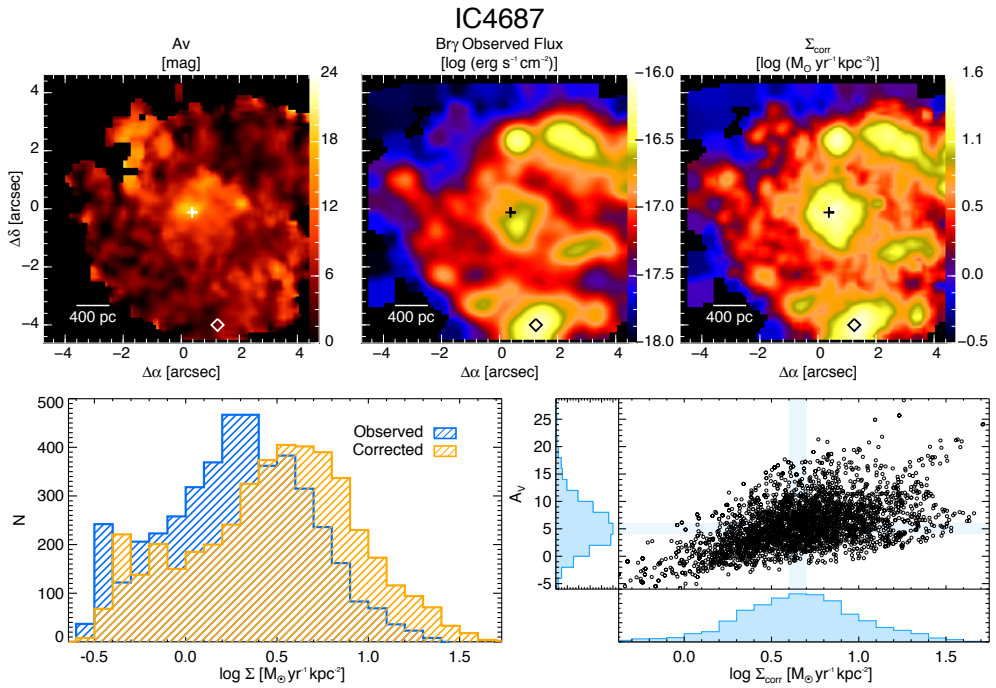

Figure D.1h: IC 4687 - Same as Fig. D.1a but for IC 4687.

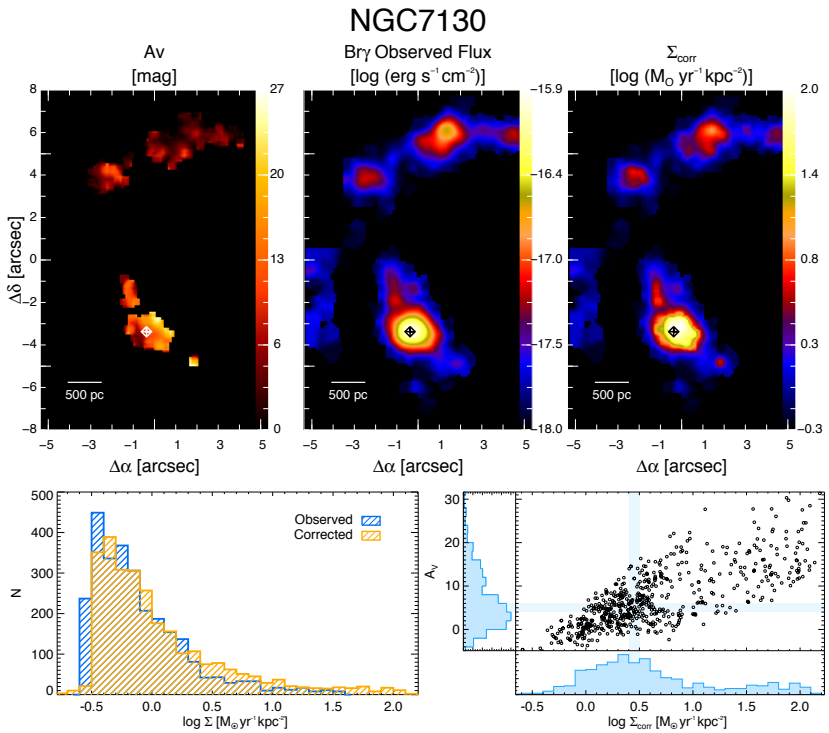

Figure D.1i: NGC 7130 - Same as Fig. D.1a but for NGC 7130.

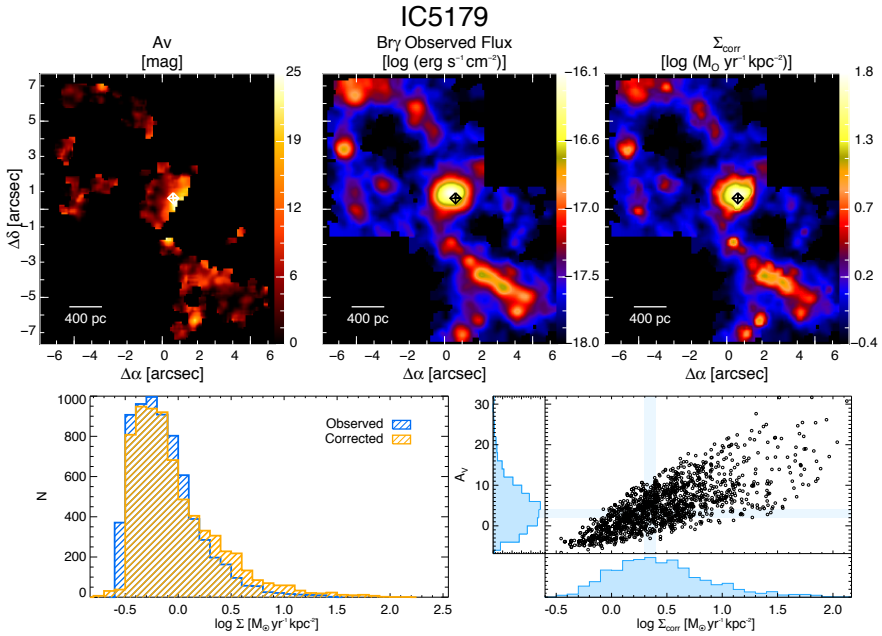

Figure D.1j: IC 5179 - Same as Fig. D.1a but for IC 5179.

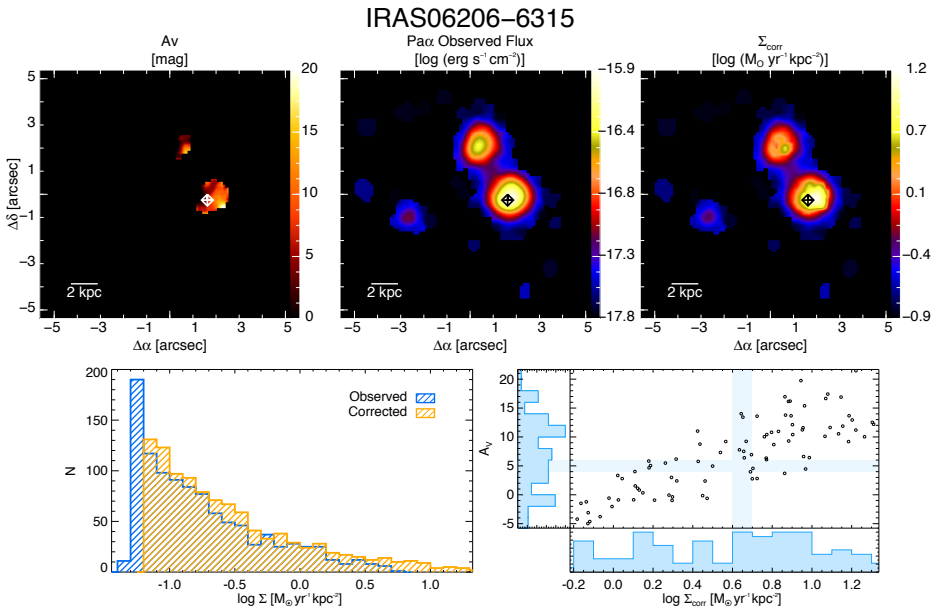

Figure D.2a: IRAS 06206-6315 - Top panels show the A_V map derived from the Paα λ1.876μm and Brγ λ2.166μm line ratio, the observed maps of the Paα emission, together with the star-formation rate surface density (Σ_{SFR}) map, corrected from extinction. The nucleus and Paα peak (see Chapter 6) are marked with a plus symbol (+) and a diamond ($\Diamond$), respectively. Bottom left panel shows the observed (blue histogram) and corrected from extinction (yellow histogram) Σ_{SFR} spaxel-by-spaxel distributions. The relationship between the corrected Σ_{SFR} values and the A_V is shown in the bottom right panel only for those points with a spaxel-by-spaxel correction of the extinction. The blue histograms show the projected distribution onto each axis, and are arbitrarily normalised, whereas the blue lines are the median of each distribution.

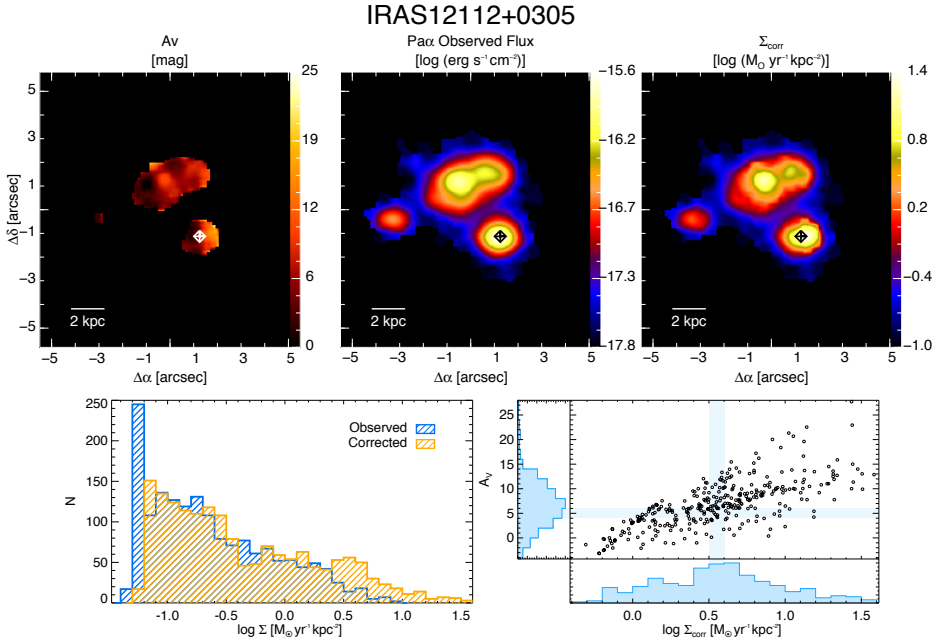

Figure D.2b: IRAS 12112+0305 - Same as Fig. D.2a but for IRAS 12112+0305.

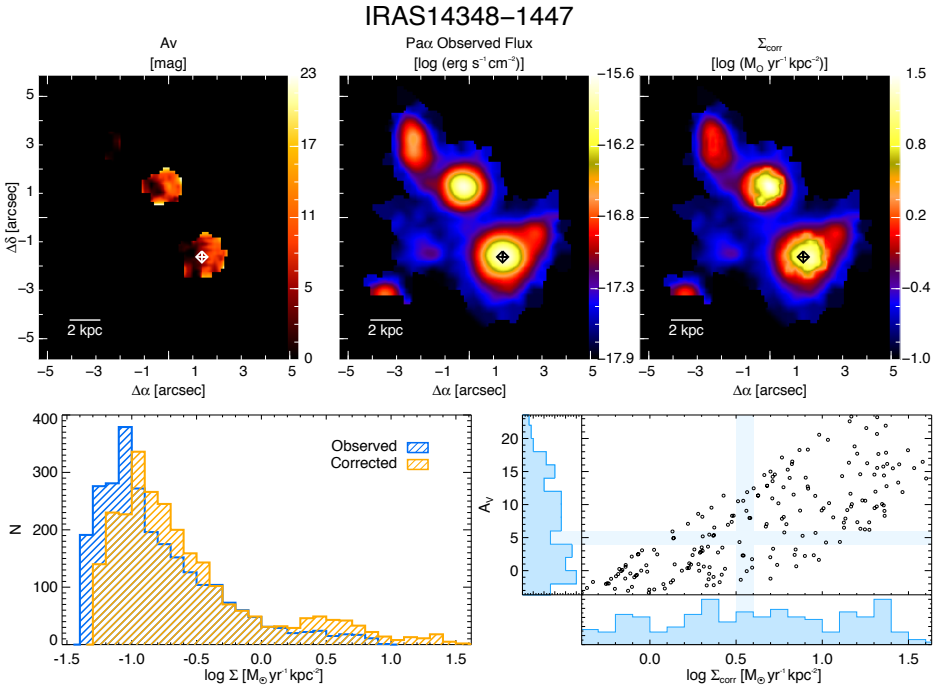

Figure D.2c: IRAS 14348-1447 - Same as Fig. D.2a but for IRAS 14348-1447.

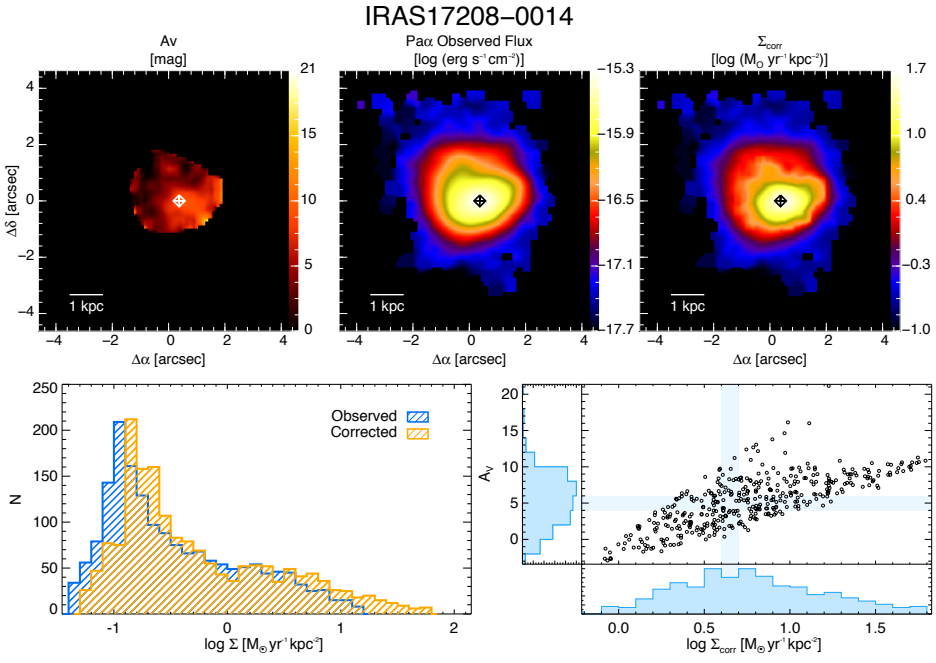

Figure D.2d: IRAS 17208-0014 - Same as Fig. D.2a but for IRAS 17208-0014.

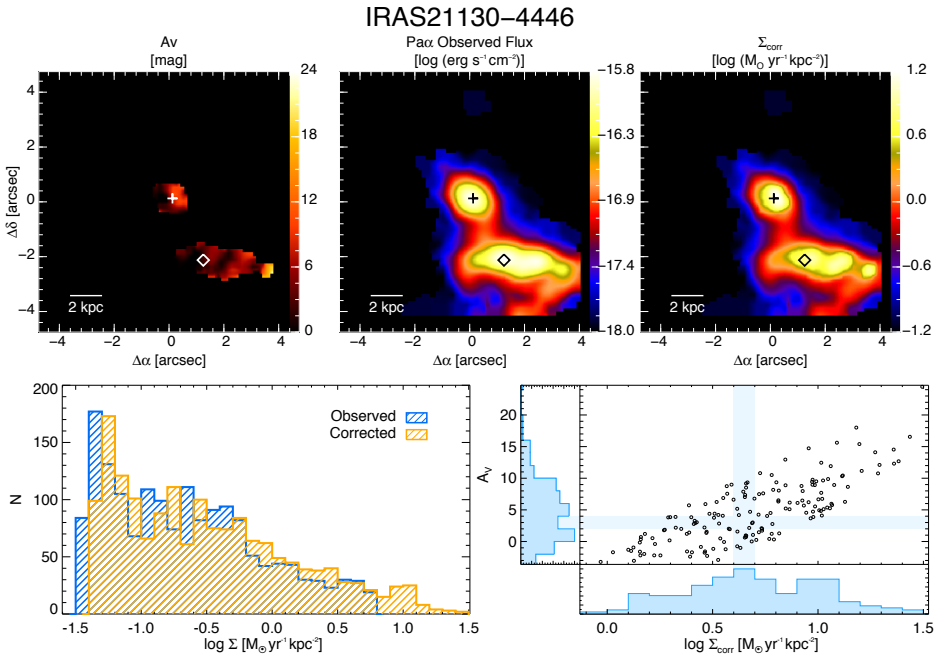

Figure D.2e: IRAS 21130-4446 - Same as Fig. D.2a but for IRAS 21130-4446.

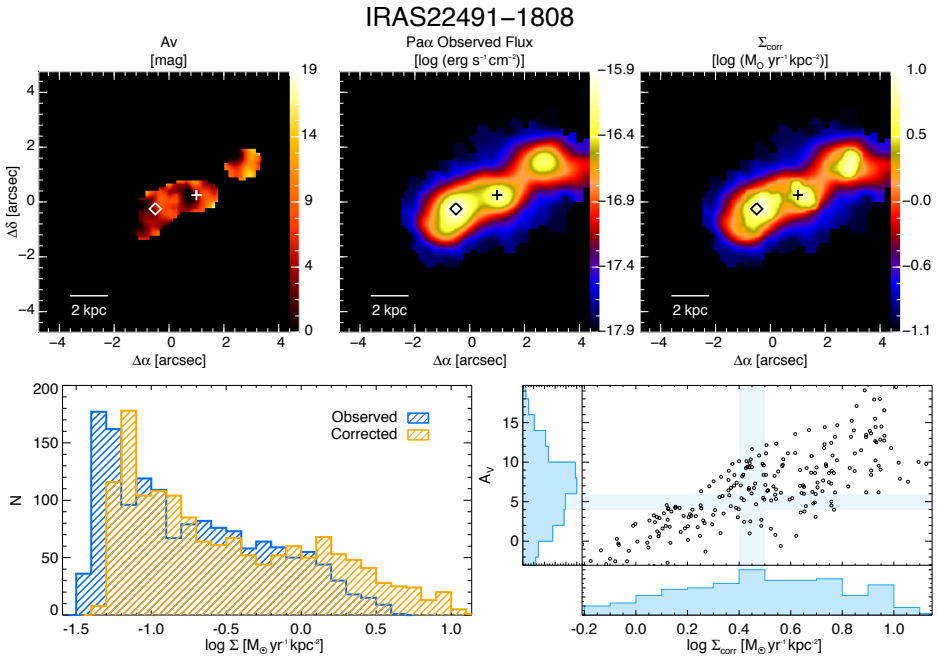

Figure D.2f: IRAS 22491-1808 - Same as Fig. D.2a but for IRAS 22491-1808.

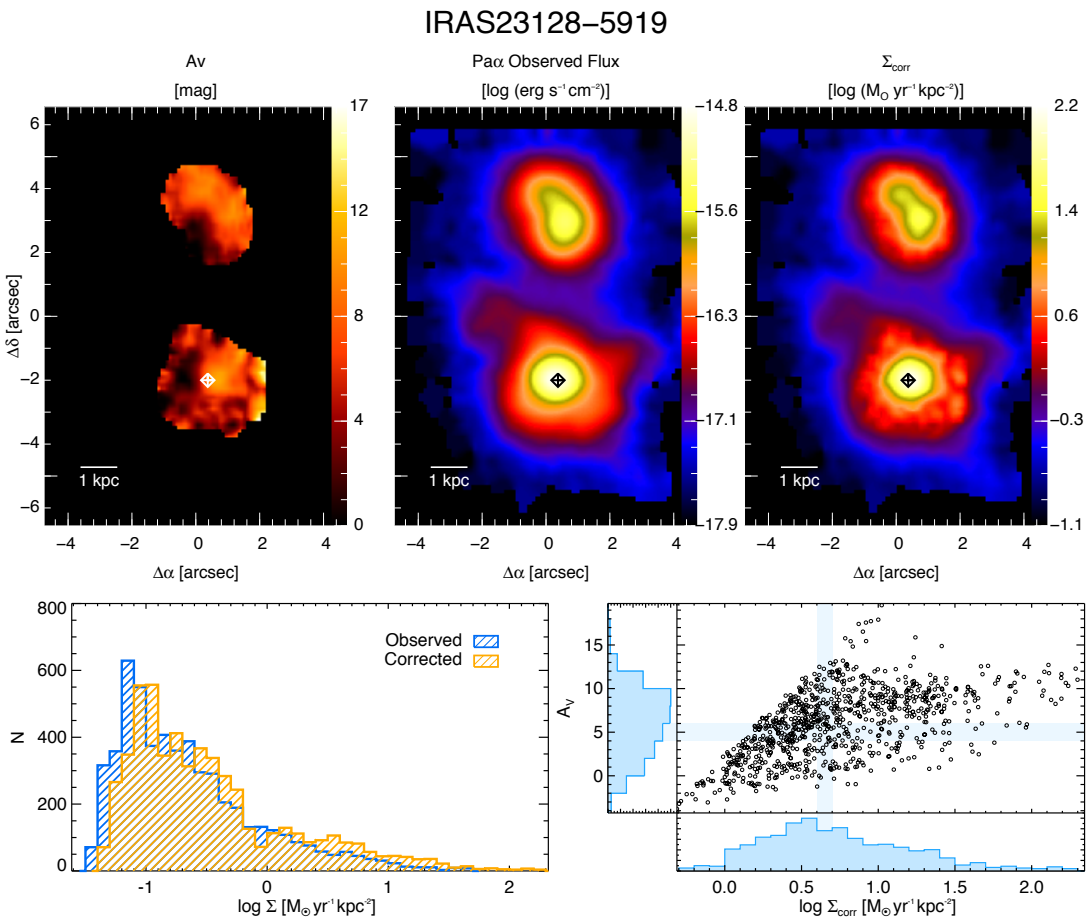

Figure D.2g: IRAS 23128-5919 - Same as Fig. D.2a but for IRAS 23128-5919.

Publications

Referred publications

- *Outflow of hot and cold molecular gas from the deeply buried secondary nucleus of NGC 3256*

  Emonts, B.; **Piqueras López**, J.; Colina, L.; Arribas, S.; Villar-Martin, M.; Pereira-Santaella, M.; Garcia-Burillo, S.; 2014; Astronomy & Astrophysics, submitted.

- *Spatially resolved kinematics, galactic wind, and quenching of star formation in the Luminous InfraRed Galaxy IRAS F11506-3851*

  Cazzoli, S.; Arribas, S.; Colina, L.; **Piqueras López, J.**; Bellocchi, E.; Emonts, B.; Maiolino, R.; Villar-Martin, M.; 2014, Astronomy & Astrophysics, submitted.

- *Warm molecular gas temperature distribution in local infrared bright Seyfert galaxies*

  Pereira-Santaella, M.; Spinoglio, L.; van der Werf, P. P.; **Piqueras López, J.**; 2014, Astronomy & Astrophysics, accepted.

- *Fueling the central engine of radio galaxies III. The molecular gas and star formation efficiency of 3C 293*

  Labiano, A.; Garcia-Burillo, S.; Combes, F.; Usero, A.; Soria-Ruiz, R.; **Piqueras López, J.**; Fuente, A.; Morganti, R.; Neri, R.; Hunt, L.; 2014, Astronomy & Astrophysics, accepted (arXiv:1402.7208)

- *VLT-SINFONI integral field spectroscopy of low-z luminous and ultraluminous infrared galaxies. II. 2D extinction structure and distance effects*

  Piqueras López, J.; Colina, L.; Arribas, S.; Alonso-Herrero, A.; 2013; Astronomy & Astrophysics, Volume 553, id.A85, 18 pp

- *VLT-SINFONI integral field spectroscopy of low-z luminous and ultraluminous infrared galaxies. I. Atlas of the 2D gas structure*

  Piqueras López, J.; Colina, L.; Arribas, S.; Alonso-Herrero, A.; Bedregal, A. G.; 2012; Astronomy & Astrophysics, Volume 546, id.A64, 38 pp.

- *Spatially Resolved Kinematics of the Central Regions of M83: Hidden Mass Signatures and the Role of Supernovae*

  Piqueras López, J.; Davies, R.; Colina, L.; Orban de Xivry, G.; 2012; The Astrophysical Journal, Volume 752, Issue 1, article id. 47, 13 pp.

Non-referred publications

- *A 2D near-infrared study of a sample of local LIRGs and ULIRGs*

  Piqueras López, J.; Colina, L.; Bedregal, A. G.; Alonso-Herrero, A.; Arribas, S.; Azzollini, R.. Proceedings of *Extreme Starbursts in the Local Universe*, Instituto de Astrofísica de Andalucia, Granada, June 2010; arXiv:1008.2107

References

Alaghband-Zadeh, S., Chapman, S. C., Swinbank, A. M., et al. 2012, MNRAS, 424, 2232 117, 145, 147, 155

Alonso-Herrero, A., García-Marín, M., Monreal-Ibero, A., et al. 2009, A&A, 506, 1541 8, 66, 67, 99

Alonso-Herrero, A., Pereira-Santaella, M., Rieke, G. H., & Rigopoulou, D. 2012, ApJ, 744, 2 3, 66, 104, 109

Alonso-Herrero, A., Rieke, G. H., Rieke, M. J., et al. 2006, ApJ, 650, 835 3, 8, 68, 73, 78, 86, 91, 104, 113, 114, 124, 142, 143, 165, 166, 169, 170

Alonso-Herrero, A., Rieke, G. H., Rieke, M. J., & Kelly, D. M. 2003, AJ, 125, 1210 11, 83

Alonso-Herrero, A., Rieke, M. J., Rieke, G. H., & Ruiz, M. 1997, ApJ, 482, 747 85

Arribas, S., Bushouse, H., Lucas, R. A., Colina, L., & Borne, K. D. 2004, AJ, 127, 2522 66

Arribas, S., Carter, D., Cavaller, L., et al. 1998, SPIE, 3355, 821 68

Arribas, S. & Colina, L. 2003, ApJ, 591, 791 168

Arribas, S., Colina, L., Alonso-Herrero, A., et al. 2012, A&A, 541, A20 67, 105, 110, 111, 113, 127, 130, 148

Arribas, S., Colina, L., & Borne, K. D. 2000, ApJ, 545, 228 8

Arribas, S., Colina, L., Monreal-Ibero, A., et al. 2008, A&A, 479, 687 8, 14, 66, 68, 139, 167

Barnes, J. E. & Hernquist, L. 1996, Astrophysical Journal v.471, 471, 115 4

Barnes, J. E. & Hernquist, L. E. 1991, ApJ, 370, L65 4

Barth, A. J., Strigari, L. E., Bentz, M. C., Greene, J. E., & Ho, L. C. 2009, ApJ, 690, 1031 57

Bastian, N., Emsellem, E., Kissler-Patig, M., & Maraston, C. 2006, A&A, 445, 471 144, 145, 146, 153

Basu-Zych, A. R., Gonçalves, T. S., Overzier, R., et al. 2009, ApJ, 699, L118 57

Beckman, J. E., Rozas, M., Zurita, A., Watson, R. A., & Knapen, J. H. 2000, AJ, 119, 2728 146

Bedregal, A. G., Colina, L., Alonso-Herrero, A., & Arribas, S. 2009, ApJ, 698, 1852 7, 8, 12, 71, 78, 86, 92, 93, 104, 106, 167, 168

Bellocchi, E., Arribas, S., Colina, L., & Miralles-Caballero, D. 2013, A&A, 557, A59 7, 9, 13, 156

Blain, A. W., Smail, I., Ivison, R. J., Kneib, J. P., & Frayer, D. T. 2002, PhR, 369, 111 117

Blietz, M., Cameron, M., Drapatz, S., et al. 1994, ApJ, 421, 92 96

Borne, K. D., Bushouse, H., Lucas, R. A., & Colina, L. 2000, ApJ, 529, L77 4, 8, 66

Bothwell, M. S., Kennicutt, Jr., R. C., & Lee, J. C. 2009, MNRAS, 400, 154 6

Bouché, N., Cresci, G., Davies, R., et al. 2007, ApJ, 671, 303 6

Bournaud, F., Combes, F., Jog, C. J., & Puerari, I. 2005a, A&A, 438, 507 62

Bournaud, F., Jog, C. J., & Combes, F. 2005b, A&A, 437, 69 4

Burton, M. G., Hollenbach, D. J., Haas, M. R., & Erickson, E. F. 1990, ApJ, 355, 197 53, 54

Bushouse, H. A., Borne, K. D., Colina, L., et al. 2002, ApJS, 138, 1 165, 171

Calzetti, D. 2001, PASP, 113, 1449 118

Calzetti, D. 2012, arXiv 122, 123

Calzetti, D., Armus, L., Bohlin, R. C., et al. 2000, ApJ, 533, 682 106, 118, 128, 141, 144

Calzetti, D., Kennicutt, R. C., Engelbracht, C. W., et al. 2007, ApJ, 666, 870 125, 142, 143, 144

Calzetti, D., Kennicutt, R. C. J., Bianchi, L., et al. 2005, ApJ, 633, 871 142

Calzetti, D., Wu, S.-Y., Hong, S., et al. 2010, ApJ, 714, 1256 124

Cappellari, M. & Copin, Y. 2003, MNRAS, 342, 345 35, 42, 72

Cappellari, M. & Emsellem, E. 2004, PASP, 116, 138 41, 78

Cerviño, M., Valls-Gabaud, D., Luridiana, V., & Mas-Hesse, J. M. 2002, A&A, 381, 51 123

REFERENCES

Chabrier, G. 2003, PASP, 115, 763 125

Cicone, C., Maiolino, R., Sturm, E., et al. 2014, A&A, 562, 21 7, 13

Cohen, M., Wheaton, W. A., & Megeath, S. T. 2003, AJ, 126, 1090 28, 40, 57, 71

Colina, L. 1993, ApJ, 411, 565 11, 58, 83

Colina, L., Arribas, S., & Borne, K. D. 1999, ApJ, 527, L13 8

Colina, L., Arribas, S., Borne, K. D., & Monreal, A. 2000, ApJ, 533, L9 104, 167

Colina, L., Arribas, S., & Monreal-Ibero, A. 2005, ApJ, 621, 725 67, 168

Comte, G. 1981, A&AS, 44, 441 38

Cortese, L., Boselli, A., Franzetti, P., et al. 2008, MNRAS, 386, 1157 125

Crocker, A. F., Calzetti, D., Thilker, D. A., et al. 2012, ApJ, 762, 79 123

Crosthwaite, L. P., Turner, J. L., Buchholz, L., Ho, P. T. P., & Martin, R. N. 2002, AJ, 123, 1892 48

Cui, J., Xia, X.-Y., Deng, Z.-G., Mao, S., & Zou, Z.-L. 2001, AJ, 122, 63 169, 170

Daddi, E., Dickinson, M., Morrison, G., et al. 2007, ApJ, 670, 156 6, 7

Daddi, E., Elbaz, D., Walter, F., et al. 2010, ApJ, 714, L118 6

Dale, D. A., Cohen, S. A., Johnson, L. C., et al. 2009, ApJ, 703, 517 62

Dale, D. A., Roussel, H., Contursi, A., et al. 2004, ApJ, 601, 813 85

Dasyra, K. M., Tacconi, L. J., Davies, R. I., et al. 2006, ApJ, 651, 835 66

Davies, R. 2008, The 2007 ESO Instrument Calibration Workshop. Proceedings of the ESO Workshop held in Garching, 249 33, 34, 43

Davies, R., Förster Schreiber, N. M., Cresci, G., et al. 2011, ApJ, 741, 69 41

Davies, R. I. 2007, MNRAS, 375, 1099 24, 40, 70

Davies, R. I., Sternberg, A., Lehnert, M., & Tacconi-Garman, L. E. 2003, ApJ, 597, 907 12, 51, 84

Davies, R. I., Sternberg, A., Lehnert, M. D., & Tacconi-Garman, L. E. 2005, ApJ, 633, 105 12, 84

Díaz, R. J., Dottori, H., Aguero, M. P., et al. 2006, ApJ, 652, 1122 38, 39, 50, 60, 61

Díaz-Santos, T., Alonso-Herrero, A., Colina, L., et al. 2010, ApJ, 711, 328 170

Díaz-Santos, T., Alonso-Herrero, A., Colina, L., et al. 2008, ApJ, 685, 211 73, 114

Doherty, R. M., Puxley, P. J., Lumsden, S. L., & Doyon, R. 1995, MNRAS, 277, 577 85

Dopita, M. A., Blair, W. P., Long, K. S., et al. 2010, ApJ, 710, 964 45, 53

Dopita, M. A., Groves, B. A., Sutherland, R. S., & Kewley, L. J. 2003, ApJ, 583, 727 123

Dopita, M. A. & Sutherland, R. S. 1995, ApJ, 455, 468 53

Dopita, M. A. & Sutherland, R. S. 1996, ApJS, 102, 161 53

Draine, B. T. 2003, ARA&A, 41, 241 124

Duc, P.-A., Mirabel, I. F., & Maza, J. 1997, A&AS, 124, 533 69, 165

Eisenhauer, F., Abuter, R., Bickert, K., et al. 2003, SPIE, 4841, 1548 8

Elbaz, D., Daddi, E., Le Borgne, D., et al. 2007, A&A, 468, 33 7

Elbaz, D., Dickinson, M., Hwang, H. S., et al. 2011, A&A, 533, A119 7

Eldridge, J. J. & Relaño, M. 2010, MNRAS, 411, 235 123

Elmegreen, D. M., Chromey, F. R., & Warren, A. R. 1998, AJ, 116, 2834 38, 48

Epinat, B., Tasca, L., Amram, P., et al. 2012, A&A, 539, A92 9, 13, 67

Erwin, P. 2004, A&A, 415, 941 166

Farrah, D., Afonso, J., Efstathiou, A., et al. 2003, MNRAS, 343, 585 69, 170

Farrah, D., Bernard-Salas, J., Spoon, H. W. W., et al. 2007, ApJ, 667, 149 3

Fathi, K., Beckman, J. E., Lundgren, A. A., et al. 2008, ApJ, 675, L17 48

Ferland, G. J., Fabian, A. C., Hatch, N. A., et al. 2008, MNRAS, 386, L72 84

Feruglio, C., Fiore, F., Maiolino, R., et al. 2013, A&A, 549, 51 7

Förster Schreiber, N. M. 2000, AJ, 120, 2089 77

Förster Schreiber, N. M., Genzel, R., Bouché, N., et al. 2009, ApJ, 706, 1364 9, 41, 67, 117

Förster Schreiber, N. M., Genzel, R., Lehnert, M. D., et al. 2006, ApJ, 645, 1062 9, 67

Förster Schreiber, N. M., Shapley, A. E., Erb, D. K., et al. 2011a, ApJ, 731, 65 9, 67, 117

Förster Schreiber, N. M., Shapley, A. E., Genzel, R., et al. 2011b, ApJ, 739, 45 117

García-Marín, M., Colina, L., & Arribas, S. 2009a, A&A, 505, 1017 9, 67, 78, 91, 104, 105, 109, 113, 139, 140, 141

García-Marín, M., Colina, L., Arribas, S., Alonso-Herrero, A., & Mediavilla, E. 2006, ApJ, 650, 850 104

García-Marín, M., Colina, L., Arribas, S., & Monreal-Ibero, A. 2009b, A&A, 505, 1319 9, 66

Genzel, R., Lutz, D., Sturm, E., et al. 1998, ApJ, 498, 579 104

Genzel, R., Newman, S., Jones, T., et al. 2011, ApJ, 733, 101 117, 144, 146, 148, 153, 155

Genzel, R., Tacconi, L. J., Gracia-Carpio, J., et al. 2010, MNRAS, 407, 2091 145

Goldader, J. D., Joseph, R. D., Doyon, R., & Sanders, D. B. 1995, ApJ, 444, 97 8, 9, 104

Green, A. W., Glazebrook, K., McGregor, P. J., et al. 2010, Natur, 467, 684 155

Grimm, H.-J., Gilfanov, M., & Sunyaev, R. 2003, MNRAS, 339, 793 59

Haan, S., Surace, J. A., Armus, L., et al. 2011, AJ, 141, 100 4, 66

Hägele, G. F., Díaz, Á. I., Cardaci, M. V., Terlevich, E., & Terlevich, R. 2009, MNRAS, 396, 2295 57

Harris, J., Calzetti, D., Gallagher, J. S., Conselice, C. J., & Smith, D. A. 2001, arXiv 55

Harrison, C. M., Alexander, D. M., Swinbank, A. M., et al. 2012, MNRAS, 426, 1073 117

Heckman, T. M., Lehnert, M. D., Strickland, D. K., & Armus, L. 2000, ApJS, 129, 493 155

Hirashita, H., Inoue, A. K., Kamaya, H., & Shibai, H. 2001, A&A, 366, 83 124

Hopkins, P. F. & Quataert, E. 2010, MNRAS, 405, L41 62

Houghton, R. C. W. & Thatte, N. 2008, MNRAS, 385, 1110 60

Imanishi, M., Dudley, C. C., Maiolino, R., et al. 2007, ApJS, 171, 72 109, 113

Inoue, A. K. 2001, AJ, 122, 1788 123

Kartaltepe, J. S., Sanders, D. B., Le Floc'h, E., et al. 2010, ApJ, 721, 98 3, 4

Kennicutt, Jr., R. C. & Evans, II, N. J. 2012, ARA&A, 50, 531 11, 123, 124, 125

Kennicutt, R. C. J. 1979, ApJ, 228, 696 128

Kennicutt, R. C. J. 1998, ARA&A, 36, 189 6, 7, 90, 122, 123, 124, 125

Kennicutt, R. C. J., Armus, L., Bendo, G., et al. 2003, PASP, 115, 928 142

Kennicutt, R. C. J., Hao, C.-N., Calzetti, D., et al. 2009, ApJ, 703, 1672 125

Kewley, L. J., Geller, M. J., Jansen, R. A., & Dopita, M. A. 2002, AJ, 124, 3135 142

Kewley, L. J., Heisler, C. A., Dopita, M. A., & Lumsden, S. 2001, ApJS, 132, 37 171

Kim, D.-C., Sanders, D. B., Veilleux, S., Mazzarella, J. M., & Soifer, B. T. 1995, ApJS, 98, 129 8

Kleinmann, D. E. & Low, F. J. 1970a, ApJ, 161, L203 1

Kleinmann, D. E. & Low, F. J. 1970b, ApJ, 159, L165 1

Knapen, J. H., Sharp, R. G., Ryder, S. D., et al. 2010, MNRAS, 408, 797 38, 61, 62

Kotilainen, J. K., Moorwood, A. F. M., Ward, M. J., & Forbes, D. A. 1996, A&A, 305, 107 73, 114

Kovács, A., Chapman, S. C., Dowell, C. D., et al. 2006, ApJ, 650, 592 117

Krist, J. E., Hook, R. N., & Stoehr, F. 2011, Optical Modeling and Performance Predictions V. Edited by Kahan, 8127, 16 34

Kroupa, P. 2001, MNRAS, 322, 231 125

Labrie, K. & Pritchet, C. J. 2006, ApJS, 166, 188 83

REFERENCES

Larkin, J., Barczys, M., Krabbe, A., et al. 2006, in Astronomical Telescopes and Instrumentation, ed. I. S. McLean & M. Iye (SPIE), 62691A–62691A–5 8

Law, D. R., Steidel, C. C., Erb, D. K., et al. 2009, ApJ, 697, 2057 67

Le Floc'h, E., Papovich, C., Dole, H., et al. 2005, ApJ, 632, 169 x, xiv, 4, 5

Lee, J. C., Gil de Paz, A., Tremonti, C., et al. 2009, ApJ, 706, 599 123

LeFèvre, O., Saisse, M., Mancini, D., et al. 2003, SPIE, 4841, 1670 68

Lehnert, M. D., Nesvadba, N. P. H., Tiran, L. L., et al. 2009, ApJ, 699, 1660 154

Leitherer, C., Schaerer, D., Goldader, J. D., et al. 1999, ApJS, 123, 3 13, 55, 83, 92, 98

Leroy, A. K., Walter, F., Sandstrom, K., et al. 2013, AJ, 146, 19 158

Lípari, S., Díaz, R., Taniguchi, Y., et al. 2000, AJ, 120, 645 86, 166

Lípari, S. L., Díaz, R. J., Forte, J. C., et al. 2004, MNRAS, 354, L1 166

Liu, G., Calzetti, D., Kennicutt, R. C. J., et al. 2013, ApJ, 772, 27 144, 145, 146

Lonsdale, C. J., Farrah, D., & Smith, H. E. 2006, Astrophysics Update 2, 285 x, xiv, 2, 66, 104

Low, J. & Kleinmann, D. E. 1968, AJ, 73, 868 1

Lumsden, S. L., Puxley, P. J., & Hoare, M. G. 2001, MNRAS, 320, 83 85

Lumsden, S. L., Puxley, P. J., Hoare, M. G., Moore, T. J. T., & Ridge, N. A. 2003, MNRAS, 340, 799 85

Lutz, D., Veilleux, S., & Genzel, R. 1999, ApJ, 517, L13 69

Magnelli, B., Elbaz, D., Chary, R. R., et al. 2011, A&A, 528, A35 5

Magnelli, B., Popesso, P., Berta, S., et al. 2013, A&A, 553, A132 x, xiv, 4, 5

Maraston, C. 1998, MNRAS, 300, 872 13, 83

Maraston, C. 2005, MNRAS, 362, 799 13, 57, 83

Marconi, A. & Hunt, L. K. 2003, ApJ, 589, L21 59

Markwardt, C. B. 2009, Astronomical Data Analysis Software and Systems XVIII ASP Conference Series, 411, 251 72

Martin, C. L. 2005, ApJ, 621, 227 7

Martin, C. L. 2006, ApJ, 647, 222 7

Mast, D., Díaz, R. J., & Agüero, M. P. 2006, AJ, 131, 1394 38, 39, 44, 60

McCrady, N. & Graham, J. R. 2007, ApJ, 663, 844 57

Menéndez-Delmestre, K., Blain, A. W., Smail, I., et al. 2009, ApJ, 699, 667 117

Menéndez-Delmestre, K., Blain, A. W., Swinbank, M., et al. 2013, ApJ, 767, 151 117

Mihos, J. C. & Hernquist, L. 1996, Astrophysical Journal v.464, 464, 641 4

Monreal-Ibero, A., Arribas, S., Colina, L., et al. 2010, A&A, 517, 28 9, 67

Morganti, R., Frieswijk, W., Oonk, R. J. B., Oosterloo, T., & Tadhunter, C. 2013, A&A, 552, L4 7

Mouri, H., Kawara, K., & Taniguchi, Y. 2000, ApJ, 528, 186 83, 85

Murphy, T. W., Armus, L., Matthews, K., et al. 1996, AJ, 111, 1025 4, 8, 66

Murphy, T. W. J., Soifer, B. T., Matthews, K., Armus, L., & Kiger, J. R. 2001, AJ, 121, 97 3

Naab, T. & Burkert, A. 2003, ApJ, 597, 893 4

Nardini, E., Risaliti, G., Salvati, M., et al. 2008, MNRAS, 385, L130 x, xiv, 3, 4

Nardini, E., Risaliti, G., Watabe, Y., Salvati, M., & Sani, E. 2010, MNRAS, 405, 2505 3, 66, 104

Nesvadba, N. P. H., Lehnert, M. D., Genzel, R., et al. 2007, ApJ, 657, 725 117

Neugebauer, G., Becklin, E. E., Oke, J. B., & Searle, L. 1976, ApJ, 205, 29 1

Neugebauer, G., Habing, H. J., van Duinen, R., et al. 1984, ApJ, 278, L1 1

Onodera, S., Kuno, N., Tosaki, T., et al. 2010, ApJ, 722, L127 158

Osterbrock, D. E. 1989, Astrophysics of Gaseous Nebulae and Active Galactic Nuclei. University Science Books, Mill Valley, USA 106

Osterbrock, D. E. & Ferland, G. J. 2006, Astrophysics of gaseous nebulae and active galactic nuclei, 2nd. ed. Sausalito, CA: University Science Books 122, 125, 127, 135, 143

Pellegrini, E. W., Oey, M. S., Winkler, P. F., et al. 2012, ApJ, 755, 40 123

Peng, C. Y., Ho, L. C., Impey, C. D., & Rix, H.-W. 2010, AJ, 139, 2097 59

Pereira-Santaella, M., Alonso-Herrero, A., Rieke, G. H., et al. 2010, ApJS, 188, 447 99, 109, 113

Pereira-Santaella, M., Alonso-Herrero, A., Santos-Lleo, M., et al. 2011, A&A, 535, A93 69, 142

Pérez-González, P. G., Rieke, G. H., Egami, E., et al. 2005, ApJ, 630, 82 x, xiv, 2, 5, 66

Piqueras López, J., Colina, L., Arribas, S., & Alonso-Herrero, A. 2013, A&A, 553, A85 xii, xvi, 15, 83, 125, 126, 127, 128

Piqueras López, J., Colina, L., Arribas, S., Alonso-Herrero, A., & Bedregal, A. G. 2012a, A&A, 546, 64 xi, xv, 10, 15, 105, 113, 127

Piqueras López, J., Davies, R., Colina, L., & Orban de Xivry, G. 2012b, ApJ, 752, 47 xi, xv, 14

Planesas, P., Colina, L., & Perez-Olea, D. 1997, A&A, 325, 81 144, 145

Prieto, M. A., Marco, O., & Gallimore, J. 2005, MNRAS, 364, L28 93

Puxley, P. J., Hawarden, T. G., & Mountain, C. M. 1990, ApJ, 364, 77 55

Raymond, J. C. 2001, SSRv, 99, 209 54

Relaño, M., Kennicutt, Jr, R. C., Eldridge, J. J., Lee, J. C., & Verley, S. 2012, MNRAS, 423, 2933 123

Relaño, M., Peimbert, M., & Beckman, J. 2002, ApJ, 564, 704 123

Rich, J. A., Kewley, L. J., & Dopita, M. A. 2011, ApJ, 734, 87 114

Rieke, G. H. 1978, ApJ, 226, 550 1

Rieke, G. H., Alonso-Herrero, A., Weiner, B. J., et al. 2009, ApJ, 692, 556 143

Rieke, G. H. & Lebofsky, M. J. 1978, ApJ, 220, L37 1

Rieke, G. H. & Low, F. J. 1972, ApJ, 176, L95 1

Rieke, G. H. & Low, F. J. 1975, ApJ, 200, L67 1

Riffel, R., Rodríguez-Ardila, A., Aleman, I., et al. 2013, MNRAS, 430, 2002 12

Riffel, R. A., Storchi-Bergmann, T., & Nagar, N. M. 2010, MNRAS, 404, 166 12, 85, 96

Rodighiero, G., Daddi, E., Baronchelli, I., et al. 2011, ApJ, 739, L40 6, 7

Rodrigues, I., Dottori, H., Díaz, R. J., Agüero, M. P., & Mast, D. 2009, AJ, 137, 4083 38, 39, 60

Rodríguez-Ardila, A., Pastoriza, M. G., Viegas, S., Sigut, T. A. A., & Pradhan, A. K. 2004, A&A, 425, 457 96

Rodríguez-Ardila, A., Prieto, M. A., Portilla, J. G., & Tejeiro, J. M. 2011, ApJ, 743, 100 84

Rodríguez-Ardila, A., Prieto, M. A., Viegas, S., & Gruenwald, R. 2006, ApJ, 653, 1098 7, 93

Rodríguez-Ardila, A., Riffel, R., & Pastoriza, M. G. 2005, MNRAS, 364, 1041 12, 85, 96

Rodriguez-Zaurín, J., Arribas, S., Monreal-Ibero, A., et al. 2011, A&A, 527, 60 9, 67, 139, 140, 141

Rodriguez-Zaurín, J., Tadhunter, C. N., Rose, M., & Holt, J. 2013, MNRAS, 432, 138 7, 13

Rosales-Ortega, F. F., Arribas, S., & Colina, L. 2012, A&A, 539, 73 75

Rosenberg, M. J. F., van der Werf, P. P., & Israel, F. P. 2012, A&A, 540, 116 83

Roth, M. M., Kelz, A., Fechner, T., et al. 2005, PASP, 117, 620 68

Rousselot, P., Lidman, C., Cuby, J.-G., Moreels, G., & Monnet, G. 2000, A&A, 354, 1134 23

Rozas, M., Richer, M. G., López, J. A., Relaño, M., & Beckman, J. E. 2006, A&A, 455, 539 153

Rupke, D. S. & Veilleux, S. 2005, ApJ, 631, L37 7

Rupke, D. S., Veilleux, S., & Sanders, D. B. 2005a, A&A, 632, 751 7, 13

Rupke, D. S., Veilleux, S., & Sanders, D. B. 2005b, ApJS, astro-ph, 115 7

Rupke, D. S. N. & Veilleux, S. 2013a, ApJ, 775, L15 7, 8

Rupke, D. S. N. & Veilleux, S. 2013b, ApJ, 768, 75 13

Saikia, D. J., Pedlar, A., Unger, S. W., & Axon, D. J. 1994, MNRAS, 270, 46 54

REFERENCES

Sakamoto, K., Matsushita, S., Peck, A. B., Wiedner, M. C., & Iono, D. 2004, ApJ, 616, L59 38, 42, 62

Salpeter, E. E. 1955, ApJ, 121, 161 122

Sandage, A. & Tammann, G. A. 1974, ApJ, 190, 525 128

Sanders, D. B., Egami, E., Lípari, S., Mirabel, I. F., & Soifer, B. T. 1995, AJ, 110, 1993 68

Sanders, D. B., Mazzarella, J. M., Kim, D.-C., Surace, J. A., & Soifer, B. T. 2003, AJ, 126, 1607 69

Sanders, D. B. & Mirabel, I. F. 1996, ARA&A, 34, 749 x, xiv, 2, 66, 69, 104

Sargent, M. T., Béthermin, M., Daddi, E., & Elbaz, D. 2012, ApJ, 747, L31 x, xiv, 2, 66

Savage, B. D. & Mathis, J. S. 1979, ARA&A, 17, 73 141

Schmidt, M. 1959, A&A, 129, 243 7

Schmidt, M. 1963, ApJ, 137, 758 7

Scoville, N. Z., Evans, A. S., Thompson, R., et al. 2000, AJ, 119, 991 8, 104, 107

Scoville, N. Z., Polletta, M., Ewald, S., et al. 2001, AJ, 122, 3017 146

Shields, J. C. 1993, ApJ, 419, 181 11, 85

Skrutskie, M. F., Cutri, R. M., Stiening, R., et al. 2006, AJ, 131, 1163 28, 40, 59, 71

Soifer, B. T., Boehmer, L., Neugebauer, G., & Sanders, D. B. 1989, AJ, 98, 766 68

Soifer, B. T. & Neugebauer, G. 1991, AJ, 101, 354 4

Soifer, B. T., Neugebauer, G., Helou, G., et al. 1984, ApJ, 283, L1 1, 66, 104

Soifer, B. T., Sanders, D. B., Madore, B. F., et al. 1987, AJ, 320, 238 5

Soria, R. & Wu, K. 2002, A&A, 384, 99 53, 54, 59

Spoon, H. W. W., Armus, L., Marshall, J. A., et al. 2009, ApJ, 693, 1223 7

Surace, J. A., Sanders, D. B., & Evans, A. S. 2000, ApJ, 529, 170 167

Swinbank, A. M., Smail, I., Chapman, S. C., et al. 2010, MNRAS, 405, 234 117

Swinbank, A. M., Smail, I., Sobral, D., et al. 2012, ApJ, 760, 130 144, 145, 146, 147, 148, 155

Takata, T., Sekiguchi, K., Smail, I., et al. 2006, ApJ, 651, 713 117, 145

Thatte, N., Tecza, M., & Genzel, R. 2000, A&A, 364, L47 38, 39, 49, 57, 59, 60, 61

Toomre, A. & Toomre, J. 1972, ApJ, 178, 623 4

Tremaine, S. 1995, AJ, 110, 628 62

Tremaine, S., Gebhardt, K., Bender, R., et al. 2002, ApJ, 574, 740 59

U, V., Medling, A., Sanders, D., et al. 2013, ApJ, 775, 115 7, 8

Valencia-S, M., Zuther, J., Eckart, A., et al. 2012, arXiv 85, 96

van der Werf, P. P. 2000, arXiv 84

van Dokkum, P. G. 2001, PASP, 113, 1420 29

Veilleux, S., Kim, D.-C., Rupke, D. S. N., et al. 2009, A&A, 701, 587 104

Veilleux, S., Kim, D.-C., & Sanders, D. B. 1999, ApJ, 522, 113 2

Veilleux, S., Kim, D.-C., & Sanders, D. B. 2002, ApJS, 143, 315 4, 66

Veilleux, S., Kim, D.-C., Sanders, D. B., Mazzarella, J. M., & Soifer, B. T. 1995, ApJS, 98, 171 2, 3, 8, 170

Vergani, D., Epinat, B., Contini, T., et al. 2012, A&A, 546, 118 9, 67

Véron-Cetty, M.-P. & Véron, P. 2006, A&A, 455, 773 69

Walcher, C. J., van der Marel, R. P., McLaughlin, D., et al. 2005, ApJ, 618, 237 57

Wamsteker, W., Prieto, A., Vitores, A., et al. 1985, A&AS, 62, 255 69

West, R. M. 1976, A&A, 46, 327 169

Westmoquette, M. S., Clements, D. L., Bendo, G. J., & Khan, S. A. 2012, MNRAS, 424, 416 7, 13

Wiklind, T., Lundgren-Andersson, A., & Olofsson, H. 2004, The Interplay among Black Holes, 222, 219 50, 59

Winge, C., Riffel, R. A., & Storchi-Bergmann, T. 2009, ApJS, 185, 186 41, 78

Wisnioski, E., Glazebrook, K., Blake, C., et al. 2012, MNRAS, 422, 3339 130, 146, 153, 154, 155

Wisnioski, E., Glazebrook, K., Blake, C., et al. 2011, MNRAS, 417, 2601 67

Wright, C. O., Egan, M. P., Kraemer, K. E., & Price, S. D. 2003, AJ, 125, 359 28, 40, 71

Wright, E. L. 2006, PASP, 118, 1711 69

Wright, S. A., Larkin, J. E., Law, D. R., et al. 2009, ApJ, 699, 421 67

Wuyts, S., Förster Schreiber, N. M., Lutz, D., et al. 2011, ApJ, 738, 106 7, 117

Yao, L., Seaquist, E. R., Kuno, N., & Dunne, L. 2003, ApJ, 588, 771 7

Yuan, T. T., Kewley, L. J., & Sanders, D. B. 2010, ApJ, 709, 884 2, 3

Glossary

2MASS Two Microns All Sky Survey

ACS Advanced Camera for Surveys

AGB Asymptotic Giant Branch

AGN Active Galactic Nucleus

AO Adaptive Optics

BB Black Body

BGS Bright Galaxy Survey

BPT Baldwin, Phillips and Terlevich

COSMOS Cosmological Evolution Survey

ESO European Southern Observatory

EsoRex ESO Recipe Execution Tool

EW Equivalent Width

FITS Flexible Image Transport System

FoV Field of View

FWHM Full Width at Half Maximum

HST Hubble Space Telescope

IFS Integral Field Spectroscopy/Spectrograph

IFU Integral Field Unit

IMF Initial Mass Function

IR Infrared

IRAS Infrared Astronomical Satellite

ISM Interstelar medium

KS Kennicutt-Schmidt

La3D 3D Laplacian Edge Detection

LGS Laser Guide Star

LINER Low-Ionization Nuclear Emission-line Region

LIRG Luminous Infrared Galaxy

MASSIV Mass Assembly Survey with SINFONI in VVDS

MS Main Sequence

NED NASA/IPAC Extragalactic Database

NFGS Nearby Field Galaxy Survey

NGC New General Catalogue

NGS Natural Guide Star

NICMOS Near Infrared Camera and Multi-Object Spectrometer

NLR Narrow Line Region

OSIRIS OH-Suppressing Infra-Red Imaging Spectrograph

PDR Photon-Dominated Region

PMAS Potsdam MultiAperture Spectrophotometer

pPXF Penalized Pixel-Fitting

PSF Point Spread Function

QSO Quasi Stellar Object

S/N Signal-to-Noise

SED Spectral Energy Distribution

SFR Star Formation Rate

SINFONI Spectrograph for INtegral Field Observations in the Near Infrared

SINGS Spitzer Infrared Nearby Galaxies Survey

SINS Spectroscopic Imaging survey in the Near-infrared with SINFONI

SMG Sub-Millimetre Galaxy

SN Supernova

SNR Supernova Remnant

SOF Set-of-Frames

sSFR Specific Star Formation Rate

TIR Total Infrared

TTS Tip-Tilt Star

ULIRG Ultraluminous Infrared Galaxy

GLOSSARY

UV Ultraviolet

VIMOS VIsible MultiObject Spectrograph

VLT Very Large Telescope

VVDS The VIMOS VLT Deep Survey

WFPC2 Wide-Field Planetary Camera 2

WHT William Herschel Telescope

WYFFOS Wide Field Fibre Optical Spectrograph

List of Figures

LIST OF FIGURES

List of Tables